Mechanical
Engineering Advances

https://ojs.acad-pub.com/index.php/mea

ACADEMIC
ACADEMIC PUBLISHING PTE LTD

2025 VOLUME 3 ISSUE 2
ISSN: 3029-1232 (Online)

2

ACADEMIC
ACADEMIC PUBLISHING PTE LTD

Editorial Board

Editor-in-Chief

Prof. Chunsheng Lu
Curtin University
Australia

Associate Editor

Prof. Huachao Yang
Zhejiang University
China

Editorial Board Members

Dr. Che Zhang
University of Melbourne
Australia

Prof. Shaowei Wang
Shandong University
China

Dr. Xiang Peng
Zhejiang University of Technology
China

Prof. Guosheng Wang
Beijing University of Technology
China

Prof. Bin Ji
Central South University
China

Dr. Hongye Pan
Southwest Jiaotong University
China

Dr. Hongwei Guo
The Hong Kong Polytechnic University
China

Prof. Chunlei Li
South China University of Technology
China

Dr. Liaqat Ali
Xi'an Technological University
China

Prof. Xinhua Liu
Imperial College London
United Kingdom

Prof. Gleb A. Turichin
Saint Petersburg State Marine Technical University
Russia

Assoc. Prof. Tibor Krenicky
Technical University of Kosice
Slovakia

Prof. Francesco Freddi
Università di Parma
Italy

Prof. Stefanos Papanikolaou
National Centre of Nuclear Research
Poland

Dr. Marian Grigoras
National Institute of Research and
Development for Technical Physics
(NIRDTP)
Romania

Prof. Stan Chirita
Alexandru Ioan Cuza University of Iasi
Romania

Dr. Araliya Mosleh
University of Porto
Portugal

Dr. Tianzhu Sun
University of Warwick
United Kingdom

Prof. Serguei Murzin
Samara National Research University
Russia

Prof. Rosario Sinatra
Università degli Studi di Catania
Italy

Prof. Hitesh Panchal
Government Engineering College
India

Prof. Mohsen Sheikholeslami Kandelousi
Babol Noshirvani University of Technology
Iran

Assoc. Prof. Emilian Florin Mosnegutu
"Vasile Alecsandri" University of Bacau
Romania

Dr. Ahmad Serjouei
Nottingham Trent University
United Kingdom

Prof. Van-Tu Nguyen
Pusan National University
Korea

Prof. Mohammad Zaman Kabir
Department of Civil and Environmental
Engineering
Iran

Prof. José Manoel Balthazar
Universidade Tecnológica Federal do
Paraná
Brazil

Prof. Sohail Ahmad Khan
Quaid-i-Azam University
Pakistan

Prof. Freddie Liswaniso Inambao
University of KwaZulu-Natal
South Africa

Dr. Sajad Saraygord Afshari
University of Manitoba
Canada

Prof. Eurico Augusto Rodrigues de Seabra
University of Minho
Portugal

Prof. K.K. Viswanathan
Samarkand State University
Uzbekistan

Prof. Angelo Aloisio
Università degli Studi dell'Aquila
Italy

Prof. Hosein Naderpour
Toronto Metropolitan University
Canada

Prof. Vinícius Piccirillo
Federal Technological University of Parana
Brazil

Prof. Ali Nikkhoo
University of Science and Culture
Iran

Prof. Hassaine Daouadji Tahar
University of Tiaret Algeria
Algeria

Prof. Gilberto Santos
Polytechnic Institute Cavado Ave
Portugal

Dr. Mohammad Molla-Alipour
University of Mazandaran
Iran

Volume 3 Issue 2 • 2025

Mechanical Engineering Advances

Editor-in-Chief

Prof. Chunsheng Lu

Curtin University, Australia

ACADEMIC

ACADEMIC PUBLISHING PTE LTD

2025 | Volume 3 | Issue 2

Mechanical Engineering Advances

https://ojs.acad-pub.com/index.php/MEA

Contents

Articles

Mechanical Engineering Advances 2025, 3(2), 2145.
https://doi.org/10.59400/mea2145

Article

Traffic-based methodology to develop peak Heat Release Rate probability distributions for sizing road tunnels ventilation systems when using a probabilistic approach

Sonia Fernandez[1,*], **Charles Fleischmann**[2], **Daniel Nilsson**[2], **Alberto Fraile**[3]

[1] Sociedad Ibérica de Construcciones Eléctricas S.A. (SICE), 28108 Madrid, Spain
[2] Department of Civil & Natural Resources Engineering, University of Canterbury, Christchurch 8041, New Zealand
[3] Universidad Politécnica de Madrid, 28040 Madrid, Spain
*** Corresponding author:** Sonia Fernandez, sfernandezmartin@gmail.com

CITATION

Fernandez S, Fleischmann C, Nilsson D, Fraile A. Traffic-based methodology to develop peak Heat Release Rate probability distributions for sizing road tunnels ventilation systems when using a probabilistic approach. Mechanical Engineering Advances. 2025; 3(2): 2145. https://doi.org/10.59400/mea2145

ARTICLE INFO

Received: 26 November 2024
Accepted: 28 February 2025
Available online: 2 April 2025

COPYRIGHT

Copyright © 2025 by author(s). *Mechanical Engineering Advances* is published by Academic Publishing Pte. Ltd. This work is licensed under the Creative Commons Attribution (CC BY) license. https://creativecommons.org/licenses/by/4.0/

Abstract: Road tunnels are a crucial part of today's transport infrastructures worldwide. Among the installed systems, the tunnel ventilation is key, as in the case of fire, it establishes and keeps appropriate conditions for self-evacuation and emergency services operations. Recent works propose using a probabilistic approach to assess road tunnels ventilation systems' capacity for fire scenarios. Under this approach, key design variables are defined based on probability distributions. From these distributions, the analysis uses the different possible values of the variables, including lower and upper limits as well as mean and characteristic values. The results obtained with this proposed probabilistic approach allow not only designers, but also tunnel operators and administrations, to quantify the reliability of the capacity of the ventilation system, assess its probability of failure, and define safety levels. This paper illustrates a methodology to define the design fire as a probability distribution for sizing road tunnels ventilation systems when applying the above-mentioned probabilistic approach. The methodology uses traffic information (crucial in road tunnels) and correlates it to peak Heat Release Rate (HRR) values from published reports by PIARC to obtain the design fire variable in terms of peak HRR probability distributions. The methodology is applied to two case study tunnels with different characteristics. The obtained results for the two tunnels are then compared and analyzed to peak HRR values normally recommended and used when sizing road tunnels ventilation systems to understand the uncertainty and sensitivity of the results.

Keywords: road tunnels; tunnel ventilation; stochastic analysis; probability distributions; design fire; traffic statistics

1. Introduction: Overview of important previous research

Road tunnels are a crucial part of today's transport infrastructures, contributing to the transportation system both from the economic and practical point of view.

To operate a road tunnel safely and efficiently, an integrated design of Mechanical, Electrical and Intelligent Transportation Systems (ME&I) is required. Among these ME&I systems, the tunnel ventilation system is key, as in case of fire it establishes and keeps appropriate conditions for self-evacuation and emergency services operations.

Traditionally, a deterministic approach has been adopted when sizing road tunnels ventilation systems, using prescriptive requirements and design criteria from standards and industry guidance to obtain an acceptable design solution from a fire safety point of view. The result of this design approach is given as a single outcome (for the most onerous design scenario considered) in terms of the capacity of the ventilation system to be installed.

Recent works propose the use of a probabilistic approach when sizing road tunnels ventilation systems (refer to references [1–5]). Under this approach, key design variables are defined using probability distributions to quantify the reliability of the system, assess its failure probability, and define safety levels. One of these critical variables is the design fire expressed as peak Heat Release Rate (HRR).

The outcome of the probabilistic approach documented in a recent published work from the corresponding author [4] for sizing road tunnel longitudinal ventilation systems provides an indicator of the residual risk associated with the capacity of the system expressed as a failure probability. This probabilistic approach uses a 1D steady-state model based on pressure loss calculations, supported by a Monte Carlo Simulation (MCS) method to perform a large number of simulations. For each of the simulations a deterministic calculation using the balance equation in Equation (1) is carried out for the different combinations of the design variables values, including those traditionally considered in a deterministic analysis (most onerous design scenario).

$$\Delta H_v \geq \Delta H_f + \Delta H_s + \Delta H_p + \Delta H_{ch} + \Delta H_{atm} \tag{1}$$

where:

- ΔH_v: Jet fans thrust;
- ΔH_f: Pressure loss generated by air friction along the tunnel;
- ΔH_s: Pressure loss generated by the air drag along the tunnel because of shape changes (turbulence zones);
- ΔH_p: Resistance generated by the stopped traffic;
- ΔH_{ch}: Pressure loss generated by the hot smoke buoyancy along the tunnel (upwards propagation of smoke);
- ΔH_{atm}: Natural draught (combined effects of wind and pressures).

The model used considers both the conservation of mass and the air as an ideal gas, it also accounts for the fire effects through air density changes (inversely proportional to those in the absolute temperature), and provides the air temperature downstream of the fire as the result of the balance of the heat released from the fire and the absorbed heat by the tunnel walls.

This probabilistic approach is an extension of the traditional deterministic one, as it considers and provides outcomes not only for the most onerous design scenario but also for all other possible combinations. It gives the result of the analysis as a failure probability function associated with the ventilation thrust, providing crucial information about the design criteria to assist administrations, tunnel operators, and designers.

The defined failure function (Equation (2)) depends on the installed ventilation thrust and the pressure losses. It defines the unsafe zone ($g(x) < 0$) as all those situations where the ventilation thrust is not enough to prevent smoke back-layering upstream of the fire (critical velocity not achieved). And the safe zone ($g(x) > 0$) is those situations where the capacity of the ventilation system is greater than the losses, and therefore there would be no back-layering as the obtained air velocity would be equal to or greater than the critical velocity.

$$g(x) = \Delta H_v - (\Delta H_f + \Delta H_s + \Delta H_p + \Delta H_{ch} + \Delta H_{atm}) \tag{2}$$

With this in mind, the failure probability is defined as the percentage of times that the pressure losses exceed the capacity of the installed ventilation system.

Figure 1, extracted from reference [4] and obtained with the mentioned probabilistic approach, shows the results for different tunnel lengths in terms of the installed ventilation thrust for different failure probability curves. In the figure, results show how the estimated probability of failure, based on the same design requirements, is different for the different tunnel lengths.

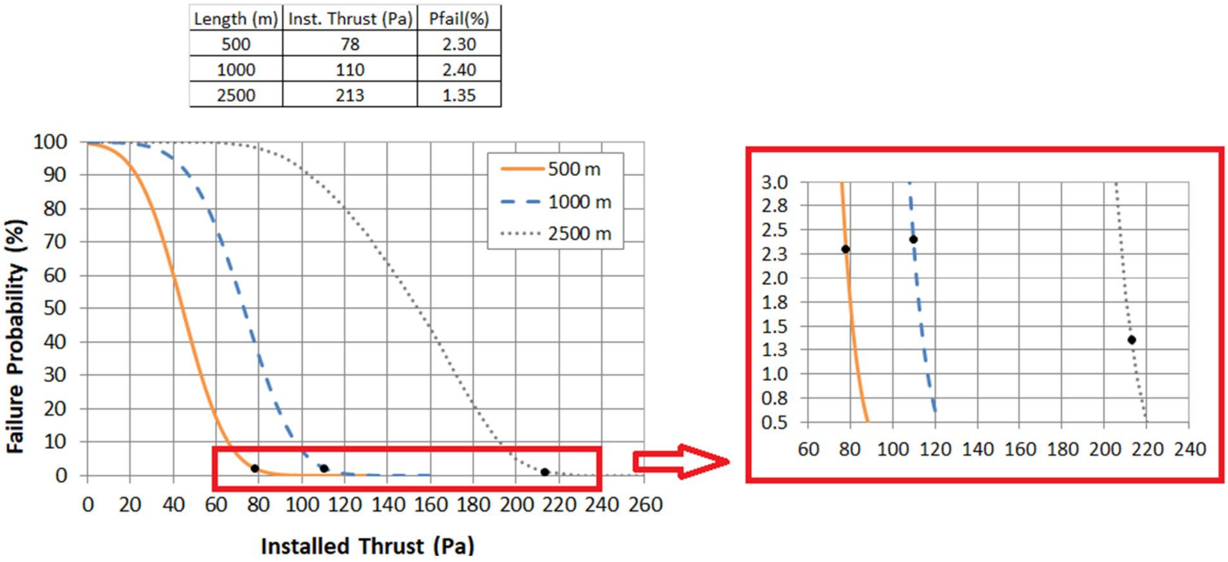

Length (m)	Inst. Thrust (Pa)	Pfail(%)
500	78	2.30
1000	110	2.40
2500	213	1.35

Figure 1. Failure probability curves for tunnel lengths.

Reproduced from reference [4].

For more detail on this probabilistic approach for sizing road tunnel longitudinal ventilation systems (and its comparison with the traditional deterministic approach), please refer to reference [4].

2. Design variables for tunnel ventilation sizing: Design fire

The design variables to evaluate the terms shown in Equation (1) for the pressure loss calculations in the 1D steady-state model to size a longitudinal ventilation system are:

- Geometry variables: Length, grade, friction and singular losses coefficients, cross section, number of lanes, hydraulic diameter.
- Fans: Installed thrust under ambient air conditions (with installation efficiencies), location and jet fan outflow velocity (at full speed).
- Traffic variables: Density, volume, percentage of each type of vehicle, aerodynamic coefficient of the stopped vehicles and their cross-sectional area (for each type of vehicle).
- Atmospheric/ambient conditions: Air temperature, air density and specific heat Cp.
- Fire scenario-related variables: Peak Heat Release Rate (HRR), critical velocity and fire location.

From these variables, the choice of the design fire is key, as it affects not only the design of the ventilation system but also the structural design and other systems designs, such as traffic management, fire detection, alarm, and suppression, as well as operations (incident response plans and evacuation strategies).

When sizing ventilation systems, the design fire can be considered as a time-dependent fire curve (refer to reference [6]) or as a single constant value defined as the peak HRR (refer to references [7–9]). And, generally, the selection of the fire HRR must be done accounting for the traffic fleet and whether the transport of Dangerous Goods is allowed or not.

A summary of peak HRR values from different international standards and guidelines is captured in **Table 1**.

Table 1. Peak HRR (MW) & vehicle type. International standards/recommendations.

Vehicle type	**French Guid. [10]**	**German Stand. [11]**	**USA Stand. [7]**	**UPTUN WP2 fire scenarios [12]**	**PIARC [8]**
Car	---	5–10	5–10	5	5–10
Several cars	8	5-10	10-20	10-20	---
Light duty vehicle	15	---	---	---	15
Bus, coach	---	20–30	20–30	30	20
HGV (< 25 T), lorry	30	30–30	70–200	50–150	30–50
HGV (25–50 T)	30	20–30	70–200	50–150	70–150
Tanker	200	50–100	200–300	200 or higher	200–300

3. Traffic-based peak HRR probability distribution development methodology

Based on the probabilistic approach mentioned in Section 1, the work presented in this paper shows a methodology to define the design fire variable as a peak HRR probability distribution, based on traffic information, to be used in that approach.

The analysis presented in the paper is applied to a case study for two different tunnels. It uses real traffic data from the two tunnels, including traffic volume (and its relationship with speed), the percentage of Heavy Goods Vehicles (HGV) and the allowance of Dangerous Goods (DG) traffic, which is correlated to peak HRR values collected from the literature [8] and fitted using the @Risk Distribution Fitting tool to four different probability distributions.

It is worth noting that the work is focused only on defining design fires to assist in road tunnel ventilation systems sizing. Other tunnel features/systems' designs (e.g., suppression or detection systems) where other parameters of the design fire (e.g., growth rate, species production, gas temperatures, etc.) would need to be considered separately are not within the scope of this paper.

It is not the intent of this work to provide standardized design fire probability distributions, but rather to demonstrate the application of the proposed traffic-based methodology using the data compiled for the analysis in a case study for two different tunnels.

When applying the probabilistic approach for sizing a tunnel ventilation system, the probability distribution of the design fire is one of the input design variables and it helps to understand the uncertainty and sensitivity of the peak HRR values to be used in the analysis. Additionally, when applying a deterministic approach, this aid is also valid, as discussed in Section 4.

For this case study, traffic data from two tunnels, including a total of 744 traffic data points per tunnel (vehicles/h and HGV percentage for each hour of each day of a whole month), was analyzed.

Note that an extended amount of data, in terms of the number of tunnels and time (more than one month of traffic data), should be explored in future work in order to obtain standardized design fire probability distributions.

3.1. Traffic data analysis

Tunnel operators were approached to provide real traffic data from tunnels with different characteristics, including location (rural/urban), traffic direction (bidirectional/unidirectional), and Dangerous Goods presence (allowed/not allowed). Real traffic data obtained from two tunnels was analyzed. Although the source (and therefore the name of the tunnels) cannot be disclosed, **Table 2** presents the main characteristics of the two tunnels (Tunnel A and Tunnel B).

Table 2. General characteristics of analyzed tunnels.

	Tunnel A	**Tunnel B**
Length (km)	8.5	2.5
Number of tubes	Single	Twin
Number of lanes (per tube)	2	3
Traffic type	Bidirectional	Unidirectional
Dangerous Goods (DG) allowed	Yes	No

For this study, traffic data from one month during the end of the winter season with no holiday periods was analyzed. The analyzed traffic data included hourly numbers of total vehicles, Passenger Cars (PC) and Heavy Good Vehicles (HGV). **Figure 2** presents hourly total numbers of vehicles during the whole month. The graphs in **Figure 2** show the difference in the number of vehicles driving through each of the tunnels, which aligns with the different locations of the tunnels (Tunnel A, mountain rural tunnel and Tunnel B, urban tunnel).

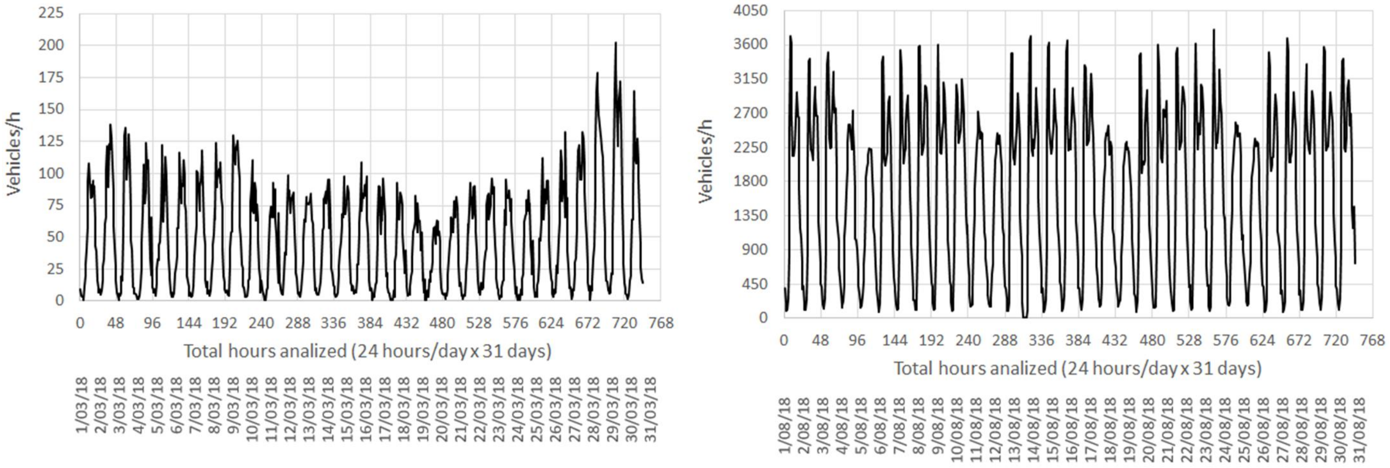

(a) **(b)**

Figure 2. Number of vehicles per hour per day during a month, **(a)** Tunnel A; **(b)** Tunnel B.

The proposed framework analyzes the traffic volume in terms of percentage instead of the traffic numbers, as these can be significantly different between tunnels (e.g., a maximum of 202 vehicles/h in Tunnel A and 3798 in Tunnel B). The percentage of traffic volume is calculated in relation to the maximum hourly total traffic value for each hourly total traffic value during the period of time analyzed (a total of 744 h, or data points included in the analysis). This standardization of the traffic volume in terms of percentage for the two tunnels analyzed is presented in **Figure 3**. These percentages of traffic volumes were the ones used during the peak HRR fitting step (as per **Table 3**).

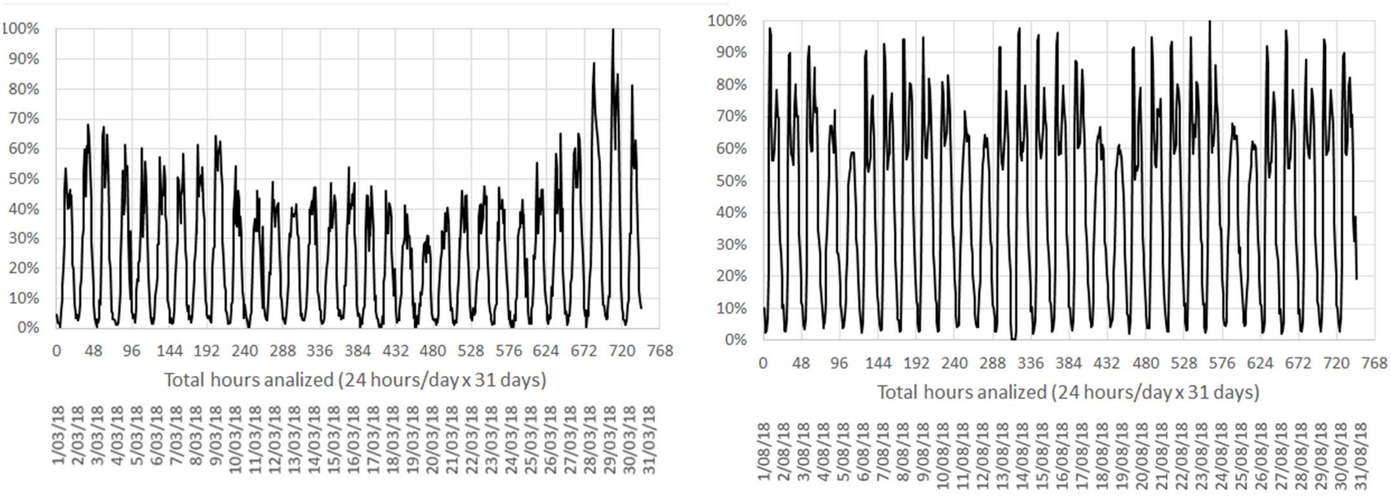

(a) **(b)**

Figure 3. Standardized traffic volume per hour in %, **(a)** Tunnel A; **(b)** Tunnel B.

The other traffic data analyzed was the percentage of HGV driving through the tunnel. As shown in **Figure 4** for each of the tunnels.

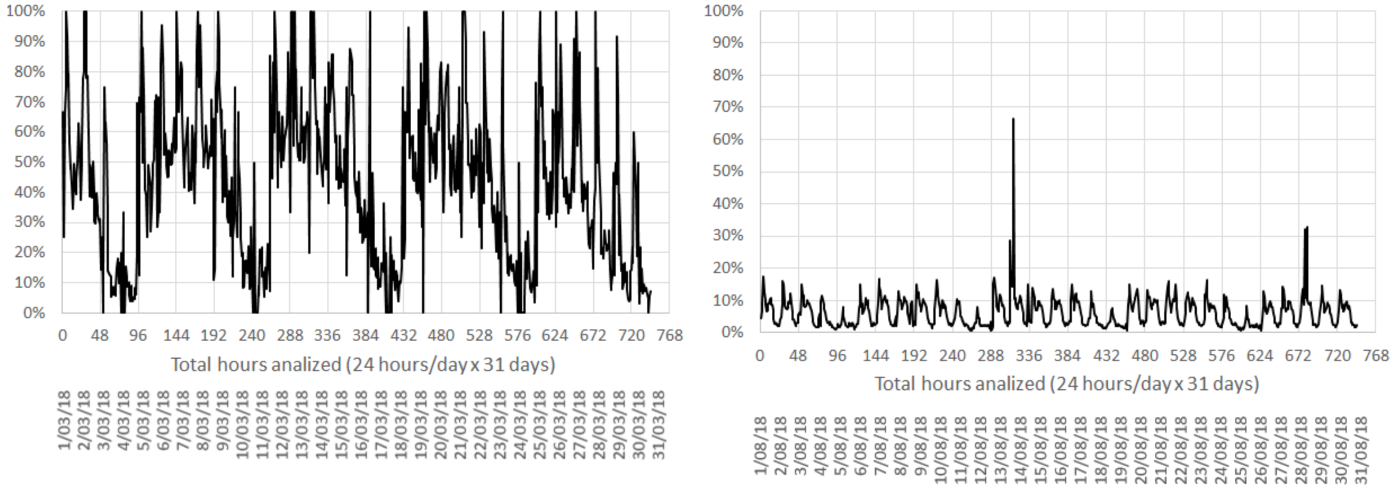

(a) **(b)**

Figure 4. Standardized % of HGV per hour, **(a)** Tunnel A; **(b)** Tunnel B.

The graphs in **Figure 4** show the difference between the tunnels, with the average percentage of HGVs in Tunnel A around 45% while in Tunnel B is around 6%. This difference in the percentage of HGV aligns with the fact that Tunnel A is a rural tunnel, part of a freight transport route, and Tunnel B is a city tunnel.

3.2. Probability distribution fitting process

Over the years, fire tests on different road vehicles burned under different conditions (calorimeter hood, inside a tunnel, or in a car park) have been carried out to estimate the peak HRR and the time to reach the peak. An overview of peak HRR values for vehicle fires in road tunnels (including PC, HGV, buses and Dangerous Goods vehicles) is captured in the literature (refer to references [6,9,12–14,15]).

In this section, different probability distributions have been fitted to peak HRR values using the @Risk Distribution Fitting tool. @Risk is a commercial piece of software for risk analysis that uses the Microsoft Excel environment. It is a tool that provides features to help assess the fitting results (i.e., comparison, P-P and Q-Q plots) and includes delimiters on graphs to allow quick assessment of the probabilities associated with the values in the fitted distributions. The fact that the software is a commercial one, the data used for the fitting was in Excel, and @Risk Distribution Fitting automatically updates the distribution when the data is updated were the main reasons to select this fitting tool.

The HRR values correlated to the traffic data that are captured in **Table 3** have been based on the following:

- Incident frequency/occurrence. The frequency/occurrence of a fire incident is not variable. The probability distributions are meant to be used to size road tunnel ventilation systems and therefore the fact of a fire is taken as the starting point.
- Peak HRR value. The peak HRR values used for fitting the probability distributions are based on data captured in the literature and shown in **Table 1** (e.g., car fires HRR between 5–10 MW). It is not part (nor the aim) of the study

to analyze the conditions, physics or how the tunnel configuration influences/affects the HRR (fire size) when obtaining the peak values.

- Percentage of traffic volume. The traffic volume in tunnels is not constant; it varies along the day and with the day of the week (traffic volume is not the same on weekends or holidays or working days, nor during peak or low hours). To help understand the traffic profile, an average hourly percentage of total vehicles during the weekdays and the weekend days was calculated for both tunnels, as shown in **Figure 5**.

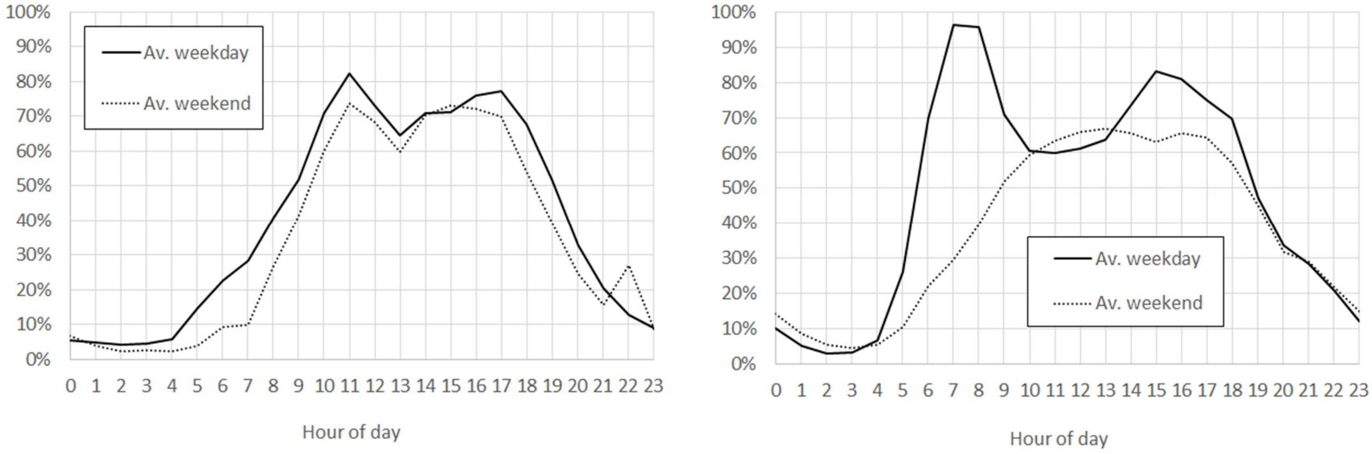

(a) **(b)**

Figure 5. Average % of traffic volume per hour, **(a)** Tunnel A; **(b)** Tunnel B.

Based on these profiles, the analysis divided the percentage of traffic volumes into five bands to cover the different traffic volumes (as per **Table 3**). For example, for Tunnel B’s weekday profile, traffic volumes less than 5% correspond to the early hours of the day (1:00–4:00), while traffic volume percentages between 80%–100% correspond to the morning and evening peaks (7:00–9:00 and 16:00–18:00, respectively).

- Traffic speed in relation to traffic volume as shown in **Figure 6**. Based on the fundamental relations of traffic flow, the flow is zero either because there are too many and they cannot move or because there are no vehicles. On the other hand, when the flow is maximum, the speed is between zero and free flow speed [16].

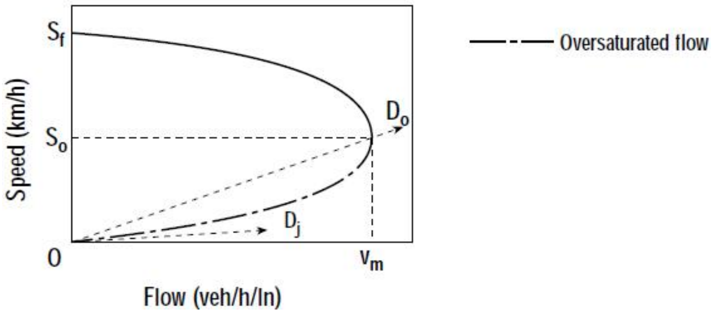

Figure 6. Generalized speed-flow curve.

Reproduced from reference [16].

Since high traffic volumes tend to reduce traffic speeds and with it the nature of the incidents tends to be less serious [17], the correlated peak HRR values for higher traffic volume percentages have been considered to be less than those with smaller traffic volumes.

- Percentage of HGV. The analysis has divided the percentage of HGV in six bands (as per **Table 3**). Since the HRR value for fires involving HGV is higher than for those involving Passenger Cars, the peak HRR has been considered to be larger for higher HGV percentages.
- Allowing or not allowing DG traffic. The assumed peak HRR value is greater when the traffic of DG vehicles is allowed (as per **Table 3**). The maximum peak HRR value considered when DG is allowed goes up to 300 MW, while when DG is not allowed, it goes up to 200 MW.
- DG traffic through the tunnel. Based on information provided by the tunnel operators of the tunnel allowing DG's traffic analyzed for the case study, if the traffic volume is high, then the traffic of DG vehicles is less likely to be allowed during that time.

Table 3. Peak HRR based on the proposed traffic-based framework for the case study.

Traffic Volume (%)	**HGV (%)**	**HRR (MW)**	
		DG allowed	**DG not allowed**
< 5%	< 5%	30	5
	5%–< 10%	30	20
	10%–< 25%	30	30
	25%–< 50%	50	50
	50%–< 70%	150	70
	70%–100%	200	150
5%–< 15%	< 5%	30	10
	5%–< 10%	50	15
	10%–< 25%	50	30
	25%–< 50%	70	50
	50%–< 70%	150	70
	70%–100%	300	200
15%–< 50%	< 5%	15	15
	5%–< 10%	30	30
	10%–< 25%	50	50
	25%–< 50%	70	70
	50%–< 70%	150	150
	70%–100%	300	200

Table 3. (*Continued*).

Traffic Volume (%)	HGV (%)	HRR (MW)	
		DG allowed	DG not allowed
50%–< 80%	< 5%	20	20
	5%–< 10%	30	30
	10%–< 25%	70	70
	25%–< 50%	100	100
	50%–< 70%	150	150
	70%–100%	200	150
80%–100%	< 5%	30	30
	5%–< 10%	50	50
	10%–< 25%	70	70
	25%–< 50%	100	100
	50%–< 70%	150	150
	70%–100%	200	150

Each of the traffic data points, which include traffic volume percentage, HGV percentage and criteria of allowance of DG traffic was correlated/assigned a peak HRR value. This correlation was based on the above considerations (as per **Table 3**) and generated a 744 peak HRR database for each tunnel of the study case (as shown in **Figure 7**).

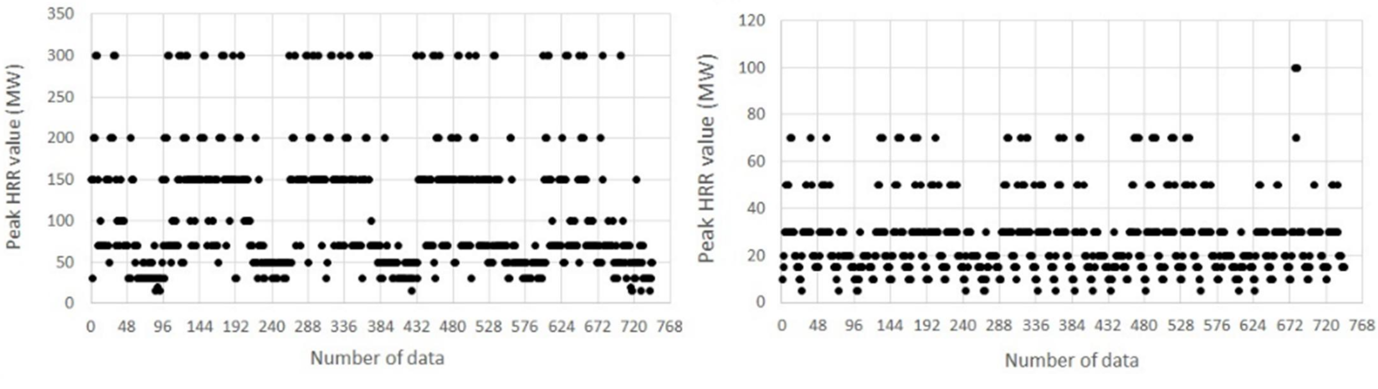

(a) **(b)**

Figure 7. Correlated peak HRR values database for distribution fitting, **(a)** Tunnel A; **(b)** Tunnel B.

To clarify the process followed and the peak HRR values in **Table 3**, a few points of the obtained database are presented and compared below:

- For a percentage of traffic volume of 2%, with 0% of HGV and DG traffic allowed, the peak HRR value correlated is 30 MW. Meanwhile for a percentage of traffic volume of 41%, with 4% of HGV and DG traffic allowed, the peak HRR value correlated is 15 MW. The difference in these cases is based on the traffic volume percentage (2% vs. 41%) and its relationship with the traffic speed and the likelihood of DG being allowed to drive through. It has been assumed that with low traffic volume the traffic speed and the likelihood of DG passing through will be higher.

- For a percentage of traffic volume of 4.8%, with 4.9% of HGV and no DG traffic allowed, the peak HRR value correlated is 5 MW. It has been assumed that even if the traffic speed could be high with the low traffic volume and low percentage of HGV it is likely that the possible incident would involve a passenger car.
- For a percentage of traffic volume of 41%, with 4% of HGV and DG traffic allowed, the peak HRR value correlated is 15 MW. Meanwhile, for a percentage of traffic volume of 25% (the same traffic volume band as for 41%) but with 59% of HGV and DG traffic allowed, the peak HRR value correlated is 150 MW. The difference in these cases is based on the percentage of HGV (4% vs. 59%) and the HRR values for PCs and HGVs. It has been assumed that with a low percentage of HGV it is more likely in the case of a fire occurrence to be related to PCs and therefore the difference in HRR value.
- For a percentage of traffic volume of 65%, with 33% of HGV and DG traffic allowed, the peak HRR value correlated is 100 MW. For a percentage of traffic volume of 71%, with 33% of HGV and no DG traffic allowed, the peak HRR value correlated is 100 MW. The HRR value assumed in these two cases is the same, as both the traffic volume and HGV percentages are similar, and it has been assumed that when the traffic volume is high, the traffic of DG vehicles would be less likely to be allowed.

This database represented in **Figure 7** was used with @Risk Distribution Fitting tool to fit four probability distributions for each tunnel. The reason for assessing different types of distributions was to see the differences based on the type of distribution and which distribution would give a better fit of the data. The fitted distributions are Beta, Weibull, Gamma and Lognormal distributions. For the fitting process in @Risk, the fitting options used for all the distributions included fixing the lower bound at zero. For the Beta distribution, also a fixed upper bound at 500 MW was used. The rest of the fitting options were the ones by default in @Risk.

To compare the fit from these four distributions, @Risk provides a goodness of fit measurement to see how the fitted distribution matches the data, and therefore the goodness of the fit. For continuous data, @RISK provides five methods for obtaining the goodness of the fit: The Bayesian Information Criteria (BIC), the Akaike Information Criteria (AIC), the Chi-Squared (Chi-Sq), the Anderson-Darling (AD) and the Kolmogorov-Smirnov (K-S).

The A-D, K-S and Chi-Sq methods were developed as tests for fit validation but not as tools for deciding between different distributions (although they can be used for this purpose when the number of data values is very large). The AIC and BIC methods ("Information Criteria" methods) were developed for model selection and they consider, among other criteria, the number of free parameters of the fitted distribution. Both AIC and BIC methods are very similar and rely on Bayesian analysis, although the AIC method tends to penalize less the number of parameters than the BIC method. Based on this, in this paper the AIC method has been chosen for comparing each potential distribution, where a smaller AIC value indicates a better fit.

Tunnel A peak HRR distribution fitting:

A summary of the outcomes of the @RISK Distribution Fitting process is captured in **Table 4** and shows the parameters defining each distribution, the mean, standard deviation, percentiles (5th and 95th) and the obtained AIC values.

Table 4. @Risk outcomes summary (Tunnel A).

	Mean	Std. Dev.	5% Pert	95% Pert	AIC Value	Rank based on AIC
Beta (1.62, 4.87, 0, 450)	112	71	18	247	8301	4
Weibull (1.53, 122.79)	111	74	18	252	8296	3
Gamma (2.24, 49.13)	110	73	22	252	8261	2
Lognorm (110.68, 88.68)	111	89	27	275	8228	1

Figure 8 shows the frequency data and fitted distributions (density and cumulative functions) for the peak HRR (MW) values related to the traffic for Tunnel A.

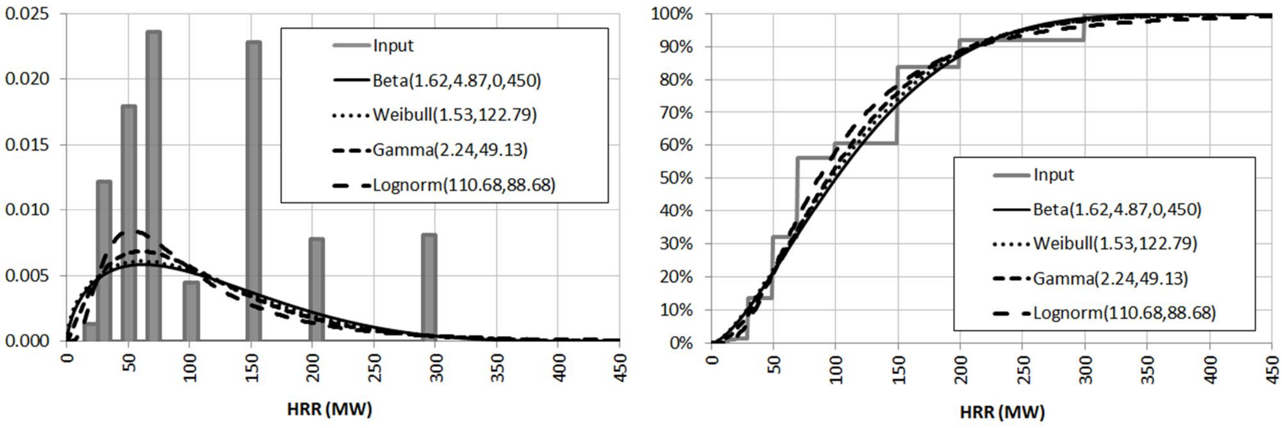

(a) **(b)**

Figure 8. Frequency data and fitted distributions (Tunnel A), **(a)** density function; **(b)** cumulative function.

Tunnel B peak HRR distribution fitting:

A summary of the outcomes of the @RISK Distribution Fitting process for Tunnel B is captured in **Table 5** and shows the parameters defining each distribution, the mean, standard deviation, percentiles (5th and 95th), and the obtained AIC values.

Table 5. @Risk outcomes summary (Tunnel B).

	Mean	Std. Dev.	5% Pert	95% Pert	AIC Value	Rank based on AIC
Beta (2.73, 12.67, 0, 150)	27	14	7	53	5947	3
Weibull (1.84, 29.82)	26	15	6	54	5982	4
Gamma (3.45, 7.62)	26	14	8	53	5905	2
Lognorm (26.36, 15.73)	26	16	9	56	5873	1

Figure 9 shows the frequency data and fitted distributions (density and cumulative functions) for the HRR (MW) values related to the traffic for Tunnel B.

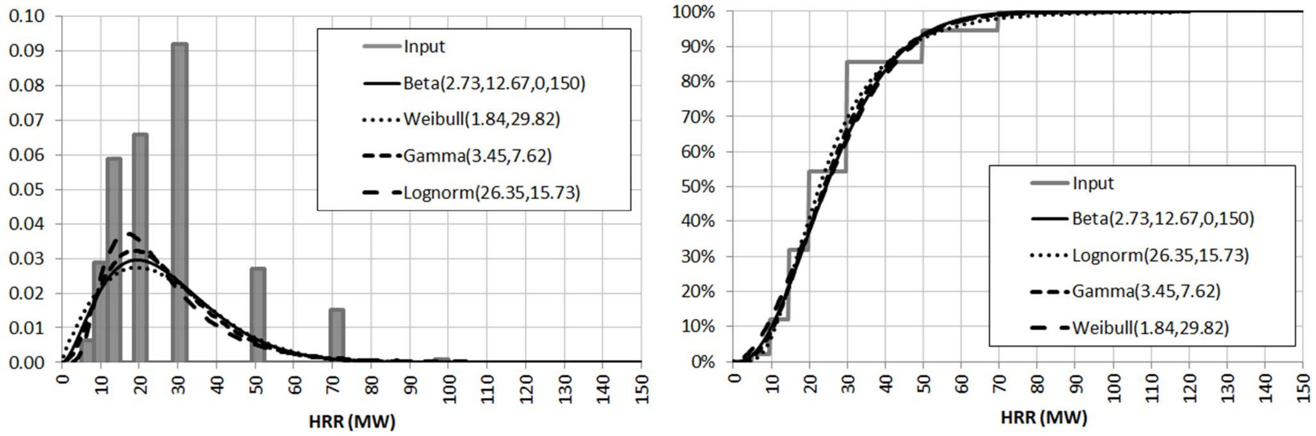

(a) **(b)**

Figure 9. Frequency data and fit distributions (Tunnel B), **(a)** density function; **(b)** cumulative function.

4. Discussion

A comparison between the design fire probability distributions (obtained with the proposed methodology) and representative peak HRR values normally used when sizing road tunnels ventilation systems applying a deterministic approach (see **Table 1**), can be made to help understand the sensitivity of the values.

This has been done with the results obtained for the case study presented in this manuscript. **Table 6** compares the representative peak HRR values, and their corresponding probability based on the results obtained for the two tunnels assessed.

Table 6. Probability distributions and representative peak HRR values comparison.

Representative peak HRR value when sizing road tunnel ventilation systems design	Tunnel A probability distributions	Tunnel B probability distributions
10 MW	0%–2%	7%–13%
20 MW	2%–6%	37%–42%
30 MW	7%–11%	63%–70%
50 MW	20%–22%	92%–93%
100 MW	50%–59%	99%–100%
200 MW	87%–88%	100%

Note that when sizing the ventilation system based on a deterministic approach, the probability distributions on their own don't dictate the specific value to be used. When statistical information is available for a design parameter (like the one provided by the probability distributions), the designer selects the specific percentile to use in the design (percentile approach). Generally, when considering upper values, the recommended percentile varies from 80th (refer to reference [18]) to 95th (refer to references [10,18,19]).

Assuming a 95th percentile approach and based on the obtained probability distributions (refer to **Tables 4** and **5**), for Tunnel A this would mean a design fire value of 247–275 MW (per PIARC's recommendations in the middle range of the peak

HRR for petrol tanker fires) and for Tunnel B 53–56 MW (per PIARC's recommendations, the upper bound of the peak HRR for HGV up to 25 T).

This comparison shows how the obtained probability distributions would cover the different peak HRR values that are normally recommended and used when sizing road tunnels ventilation systems with a deterministic approach.

Note that a comparison between the obtained distributions with other probability distributions used and/or proposed in/for other frameworks (e.g., risk assessments/models) where other properties or features are considered (e.g., time to reach peak HRR and frequency and consequences of the events) has not been done and is not within the scope of the study. The distributions obtained based on the proposed methodology are meant as an input for sizing tunnel ventilation systems following a probabilistic approach as the one presented in recent published works (refer to reference [4]).

Defining the design fire in terms of a probability distribution and using a probabilistic approach to size the tunnel ventilation system assesses the capacity of the system based on the different design fire values covered by the distribution (i.e., lower and upper limits as well as mean and characteristic values), not only the most onerous one (as per a deterministic approach-based design).

The outcome obtained from using a probabilistic approach gives an indicator of the residual risk associated with the capacity of the system expressed as a failure probability (refer to reference [4]).

In other engineering fields, such as structural engineering, the use of a probabilistic approach is widely used, and it is an entire field of research in performance-based safety engineering.

Note that it is not the aim of the work to provide standardized probability distributions, but rather, to demonstrate the application of the proposed traffic-based methodology using a limited amount of data. An extended amount of data, in terms of the number of tunnels and time (more than one month of traffic data), should be explored to obtain standardized design fire probability distributions.

5. Conclusions

This paper illustrates, through a case study, a methodology to define design fires (peak HRR) for sizing road tunnel ventilation systems in terms of probability distributions based on traffic data.

Peak HRR data obtained from the literature has been correlated to real traffic data for two tunnels following assumptions based upon the percentage of total traffic volume, percentage of HGVs, traffic speed in relation to the traffic volume and whether DG traffic is allowed or not. Using the @Risk Distribution Fitting tool, four probability distributions have been fitted to characterize the design fire.

The analysis shows how the probability distributions would cover the different peak HRR values that are normally recommended and used when sizing road tunnels ventilation systems with a deterministic approach, which helps to understand the uncertainty and sensitivity of the values.

The results presented in this paper are based on a case study and are intended only for illustrating the proposed process to obtain design fire probability distributions for sizing road tunnel ventilation systems based on traffic data. It is not the intent of the study to provide standardized probability distributions for general road tunnel assessments, nor propose the use of a specific design fire percentile value.

It is worth noticing that the probability distributions on their own don't dictate the design fire value to be used. As per Section 4, when sizing the ventilation system based on a deterministic approach, the designer can select a specific percentile to be used in the design (percentile approach).

When using a probabilistic approach (as the one captured in reference [4]), the capacity of the system is based on the different design fire values covered by the distribution (i.e., lower and upper limits as well as mean and characteristic values), not only the most onerous one (as per the deterministic approach). The probabilistic approach is an extension of the traditional deterministic one, as it considers and provides outcomes not only for the most onerous design scenario but also for all other possible combinations.

Although in both approaches the peak HRR values represent the same, in terms of sizing the ventilation system, the probabilistic one provides important information about the design criteria to assist administrations, designers, and tunnel operators.

Based on the results obtained from recent published works [4], the information obtained with the probabilistic approach can compensate for unbalances derived from the application of the common deterministic practice (where for similar conditions and the same design criteria, different residual risk is allowed). This is important for national highway administrations and/or tunnel operators, since the fact of not having a comparative and consistent criterion (residual risk) for all the tunnels can imply an uneven and inefficient use of resources.

Author contributions: Conceptualization, SF and CF; methodology, SF; software, CF; validation, SF, CF and AF; formal analysis, SF; investigation, SF; resources, SF; data curation, SF; writing—original draft preparation, SF; writing—review and editing, DN; visualization, SF; supervision, AF; project administration, CF. All authors have read and agreed to the published version of the manuscript.

Acknowledgments: The authors would like to thank the Tunnel Operators who provided the traffic data analyzed and presented in this paper.

Conflict of interest: The authors declare no conflict of interest.

References

1. Steunpunt T. Recommendations for ventilation of traffic tunnels (Dutch). Thieme GrafiMedia Groep; 2005.
2. Fernández S, Fraile A, Del Rey I, et al. Probabilistic approach for longitudinal ventilation system design in fire situations. In: Proceedings of the 15th International Symposium on Aerodynamics, Ventilation & Fire in Tunnels; 18–20 September 2013; Barcelona, Spain.
3. Pachera M, Weyenberge BV, Deckers X. Development of a full probabilistic risk model to assess the performance of longitudinal ventilation system for fires in tunnel. In: Proceedings of the Tunnel Safety and Ventilation—9th International Conference; 12–14 June 2018; Graz, Austria.
4. Fernandez Martin S, del Rey Llorente I, de Lerma AF. Tunnel Ventilation Analysis Using a Probabilistic Approach: Case Study, Fire in Road Tunnels with Longitudinal Ventilation. Fire Technology. 2020; 57.
5. Fernandez Martin S. Application of Probabilistic Methods for the Optimization of Ventilation Systems in Road Tunnels [PhD thesis]. Polytechnic University of Madrid; 2023.

6. Ingason H, Li YZ, Lonnermark A. Tunnel Fire Dynamics. Springer; 2015. pp. 1–134.
7. National Fire Protection Association. NFPA 502, Standard for Road Tunnels, Bridges, and Other Limited Access Highways. National Fire Protection Association; 2017.
8. PIARC. Design Fire Characteristics for Road Tunnels. PIARC; 2017.
9. Carvel R, Beard A. The Handbook of Tunnel Fire Safety. Thomas Telford; 2005.
10. CETU. The Pilot Files, Ventilation (France). Ministère de l'Équipement, des Transports, du Logement, du Tourisme et de la Mer direction des routes; 2003.
11. RABT. Guidelines for the equipment and operation of road tunnels (German). Research Society for Road and Traffic Engineering; 2006.
12. NCHRP. Design Fires in Road Tunnels. NCHRP; 2011.
13. Carvel R. Fire size in tunnels [PhD thesis]. Heriot-Watt University; 2004.
14. Bouwdienst Rijkswaterstaat. Project 'Safety Test': Fire Test Report (Dutch). Bouwdienst Rijkswaterstaat; 2002.
15. Ingason H. State of the Art of Tunnel Fire Research. Fire Safety Science. 2008; 9.
16. TRB. Highway Capacity Manual. Transportation Research Board; 2000.
17. PIARC. Experience with significant incidents in road tunnels. PIARC; 2017.
18. Hadjisophocleous GV, Mehaffey JR. Fire Scenarios. In: SFPE Handbook of Fire Protection Engineering. Springer; 2016.
19. Meacham, B. Toward next generation performance-based building regulatory systems. In: Proceedings of SFPE 11th Conference on performance-based codes and fire safety design methods; 23-25 May 2016; Warsaw, Poland.

Mechanical Engineering Advances 2025, 3(2), 2534.
https://doi.org/10.59400/mea2534

Article

Effect of inverse-square heat absorption on MHD natural convection flow in a vertical concentric annulus with radial and induced magnetic fields

Muhammad Yusuf Muhammad[1,*], **Yusuf Ya'u Gambo**[2], **Muhammad Auwal Lawan**[1]

[1] Department of Mathematics, Aliko Dangote University of Science and Technology, Kano 713103, Nigria
[2] Department of Mathematics, North West University, Kano 713103, Nigeria
*** Corresponding author:** Muhammad Yusuf Muhammad, muhammadyusufmuhammad@kustwudil.edu.ng

CITATION

Muhammad MY, Gambo YY, Lawan MA. Effect of inverse-square heat absorption on MHD natural convection flow in a vertical concentric annulus with radial and induced magnetic fields. Mechanical Engineering Advances. 2025; 3(2): 2534. https://doi.org/10.59400/mea2534

ARTICLE INFO

Received: 9 January 2025
Accepted: 17 February 2025
Available online: 3 April 2025

COPYRIGHT

Copyright © 2025 by author(s). *Mechanical Engineering Advances* is published by Academic Publishing Pte. Ltd. This work is licensed under the Creative Commons Attribution (CC BY) license. https://creativecommons.org/licenses/by/4.0/

Abstract: This study investigates the impact of inverse-square heat absorption on steady, fully developed laminar MHD natural convection flow within an infinite vertical concentric annulus under the influence of applied radial and induced magnetic fields. The governing transport equations in the model were transformed into a non-dimensional form, allowing for the derivation of unified analytical solutions for the velocity, temperature, magnetic field, and induced current density distributions for both isothermal and iso-flux on the inner cylinder of concentric annuli. The influence of key physical parameters in the model is illustrated through a comprehensive analysis of graphs and tables. The findings reveal that increasing the heat absorption parameter intensifies thermal gradients near the inner cylinder, while stronger magnetic fields suppress fluid motion, reducing mass flux and enhancing flow resistance. Mass flux and induced current density decrease as Hartmann number and heat absorption parameter increase, demonstrating the combined influence of thermal and electromagnetic forces. The magnetic field distributions and associated current densities exhibit pronounced attenuation near the inner cylinder under a higher Hartmann number. These findings highlight the intricate interaction between thermal and electromagnetic forces, offering valuable insights for applications in nuclear reactors, MHD power generation, and advanced cooling technologies. This study contributes to refining MHD-driven thermal management approaches for Advanced engineering systems.

Keywords: MHD; natural convection; heat generation; vertical concentric annulus; Hartmann number; inverse-square heat generation

1. Introduction

The study of magnetohydrodynamic (MHD) natural convection in annular geometries is crucial for engineering applications such as power generation, nuclear cooling systems, and metallurgical processes. When a conducting fluid is exposed to an externally applied uniform magnetic field, an induced magnetic field is generated due to fluid motion and interaction with the applied field. The interaction between these fields affects heat transfer and flow stability, making it essential to distinguish their separate and combined influences.

There are numerous applications for studying natural convective flow along a vertical cylinder in fields like technology, agriculture, oceanography, and geothermal power generation. Applications in solar power collectors, magnetohydrodynamic power generator design, and oil thermal recovery have drawn attention to the study of transport phenomena with annular geometry.

The analysis and design of heat exchangers often rely on annular geometries due to their extensive applications in geophysics and engineering fields. These applications include magnetohydrodynamic (MHD) power generation, geothermal energy systems, treatment of nuclear fuel debris, and solidification of metals and alloys. Notably, natural convective flows along vertical cylinders have found uses in solar power collection, geothermal energy extraction, and oil recovery. The integration of heat sources or sinks within a concentric annulus enhances fluid flow efficiency and overall system performance Kumar and Singh [1].

Magnetohydrodynamics, which bridges fluid mechanics and electromagnetism, facilitates the control and propulsion of electrically conducting fluids via Lorentz forces generated from interactions between magnetic fields and electric currents. In the context of vertical concentric annuli, studying MHD-natural convection interactions is critical for optimizing cooling systems in nuclear reactors, enhancing safety and operational efficiency [2]. Additionally, understanding the effects of radial and induced magnetic fields has practical implications for geothermal energy systems Kefayati and Ahmadi [3] and industrial processes such as MHD propulsion and metal solidification [4,5].

Heat generation and absorption significantly impact natural convection flows by altering temperature distributions and flow patterns. These effects are vital in various applications, including nuclear reactor cores, semiconductor manufacturing, and combustion modeling. Employing an inverse-square heat absorption model provides a realistic framework for simulating heat transfer in such systems, addressing a gap in the literature where most studies have focused on constant or linear heat sources.

The influence of radial magnetic fields on flow stability and heat transfer in annular geometries has been highlighted by several researchers Smith and Johnson [6], Brown et al. [7]. These studies reveal that magnetic fields induce additional fluid motion, thereby improving convective heat transfer rates. For instance, Gupta and Sharma [8] demonstrated that radial magnetic fields reduce boundary layer thickness, enhancing heat transfer efficiency near the cylinder walls. Conversely, ignoring the induced magnetic field underestimates velocity and current density in MHD flows, emphasizing its critical role [9–11].

Studying the combined effects of radial and induced magnetic fields on fluid flow is crucial for advancing technologies in fields like metallurgy, nuclear fusion, and space science, where control over electrically conducting fluids is important. These magnetic fields influence flow patterns, turbulence, and heat transfer, enabling precise regulation in applications such as cooling systems in nuclear reactors and metal casting processes. In astrophysics, they help explain plasma behavior in phenomena like solar flares and accretion disks. Moreover, understanding their interactions improves plasma confinement in fusion reactors, enhances the accuracy of computational models for MHD, and even finds biomedical applications in targeted drug delivery and diagnostic imaging.

The concept of inverse-square heat absorption refers to a scenario where the rate of heat absorption decreases in proportion to the square of the distance from a heat source. This spatial variation in heat absorption significantly impacts the temperature distribution and fluid flow patterns within the system.

Hasanuzzaman et al. [11] have explored the effects of heat absorption on MHD natural convection flows. This research has investigated the role of heat absorption or production on time-dependent free MHD convective transport over a vertical porous plate with thermal radiation, highlighting the importance of heat absorption in modifying flow characteristics and thermal profiles. Mabood et al. [12] examined the impact of heat generation and absorption on thermally stratified MHD flow over an inclined stretching surface and found that heat absorption significantly alters the temperature distribution within the boundary layer, affecting the velocity and thermal profiles of the fluid. Additionally, the role of heat absorption in MHD flows with chemical reactions has been investigated where homogeneous-heterogeneous chemical reactions and heat absorption effects on a two-dimensional steady hydromagnetic Newtonian fluid. The results demonstrated that heat absorption significantly influences concentration profiles, which is essential for processes involving chemical species transport [13]. Moreover, the combined impact of heat generation/absorption and Joule heating on the MHD flow of Ag-H_2O nanofluid into a porous stretching/shrinking sheet was studied. The research indicated that heat absorption plays a critical role in enhancing or diminishing heat transfer rates, depending on the flow configuration [14]. Another investigation focused on MHD natural convective flow of a polar fluid with Newtonian heat transfer in vertical concentric annuli. The study analyzed the effects of transverse magnetic fields and Newtonian heating on velocity distribution and flow stability, offering valuable data for applications involving polar fluids in annular geometries [15].

Key parameters such as the Hartmann number, annular gap, and heat absorption parameter have been extensively studied in MHD flows. Chamkha and Issa [16] showed that heat absorption decreases the Nusselt number, while [17] demonstrated that constant iso-flux heating alters the thermal energy distribution in vertical annuli. Despite this, the combined effects of inverse-square heat absorption, radial magnetic fields, and induced magnetic fields on MHD natural convection in vertical concentric annuli remain underexplored.

The mathematical modeling and exact solutions for predicting flow behavior in these systems have gained increasing attention due to their relevance in industrial applications. Numerous studies have examined natural convection in vertical annuli under isothermal or iso-flux conditions. Kumar and Singh [1] analyzed the effects of heat sources, sinks, and induced magnetic fields on natural convection flows in vertical concentric annuli with radial magnetic fields using analytical methods. Similarly, Muhammad et al. [18] investigated heat absorption in natural convection along vertical coaxial cylinders under constant iso-flux conditions. Other notable works include El-Shaarawi et al. [3], who studied laminar flow dynamics in open-ended annuli, and Joshi [19], who provided insights into free convection in isothermal vertical annuli. Furthermore, El-Shaarawi and Sarhan [20] presented an analytical solution for developing natural convection flow in open-ended vertical concentric annuli, considering four different thermal boundary conditions and providing a closed-form solution for each. The impact of an induced magnetic field on fully developed convection flow in an annular microchannel was examined by Jha and Aina [21].

The behavior of electrically conductive fluids has also attracted considerable interest due to its importance in battery design and power generation systems. Early works, such as Rossow [22], established foundational theories, while later studies, including Ramamoorthy [23] and Arora [24], expanded the understanding of MHD flows in coaxial cylinders under magnetic fields. Moalem [25] suggested that heat generation could be inversely related to temperature. Several other studies have explored heat generation or absorption in vertical concentric cylinders [26–30]. Several practical physical phenomena, such as convection within the Earth's mantle, heat dissipation following accidents, fire and combustion modeling, exothermic and endothermic chemical reactions in fluids, the development of metal waste from spent nuclear fuel, and various applications in nuclear energy, are strongly affected by the properties associated with heat absorption and generation. Jha [15] explored the impact of heat-generating or absorbing fluids on heat transfer and the resulting flow behavior to better understand this class of fluid dynamics. This is particularly important because the volumetric heat generation or absorption term can significantly influence heat transfer processes as temperatures increase. Investigations into fluid flow within open-ended vertical concentric annuli shed light on the intricate fluid mechanics crucial for applications in MHD propulsion [31]. Magnetohydrodynamics (MHD) integrates principles of classical electromagnetism with fluid dynamics, enabling the manipulation and propulsion of conducting fluids using Lorentz forces. These forces emerge from the interaction between electric currents and magnetic fields when an external magnetic field is applied. However, the motion of an electrically conducting fluid perpendicular to the magnetic field is significantly impeded due to the strong influence of these interactions [32–34].

The growing demand for efficient heat transfer management has spurred research into heat-generating and heat-absorbing fluids. While earlier models assumed constant heat generation rates [28,35], subsequent studies explored spatially dependent heat sources and sinks [4,22]. Recent research, such as that by Oni et al. [36], examines the effects of radially varying magnetic fields and heat sources in vertical annuli. Ferdousi and Alim [37] investigated the impact of magnetic fields on mixed convection within a rectangular enclosure featuring a trapezoidal heated obstacle and two semi-circular wall heaters. The study employs the finite element method to analyze fluid flow and temperature distribution, focusing on parameters such as Hartmann number, buoyancy ratio, and Richardson number. The findings indicate that the heat transfer rate along the right semi-circular wall heater surpasses that of the left heater as both Hartmann number and buoyancy ratio increase. Also, more related work to this study is [38–40].

This study aims to address these gaps by investigating the effects of inverse-square heat absorption on MHD natural convection flow in a vertical concentric annulus. Special attention is given to the interplay between radial and induced magnetic fields. Analytical solutions to the governing equations provide insights into the influence of critical parameters, Hartmann number, heat absorption, and annular gap on temperature, velocity, and magnetic field distributions. The findings have practical applications in optimizing MHD systems for engineering purposes, such as nuclear reactors, geothermal systems, and electromagnetic propulsion.

2. Mathematical formulation

The fundamental hydrodynamic equations, together with Maxwell's electromagnetic equations, describe the steady-state flow of electrically charged fluids [1,18]. In vector form, these equations are expressed as follows.

2.1. Continuity equation

$$\nabla \cdot \mathbf{V} = 0 \tag{1}$$

2.2. Momentum equation

$$\rho(\mathbf{V} \cdot \nabla)\mathbf{V} = -\nabla P + \mu(\nabla^2 \mathbf{V}) + (\mathbf{J} \times \mathbf{B}) + \rho g \tag{2}$$

2.3. Magnetic field equation

$$(\boldsymbol{\eta} \boldsymbol{\nabla}^{\mathbf{2}} \mathbf{H}) + \boldsymbol{\nabla} \times (\mathbf{V} \times \mathbf{H}) = \mathbf{0} \tag{3}$$

2.4. Energy equation

$$(\mathbf{V} \cdot \nabla)T = \frac{k}{\rho C_p} \nabla^2 T + \frac{Q_0}{\rho C_p} \tag{4}$$

2.5. Configuration of the study

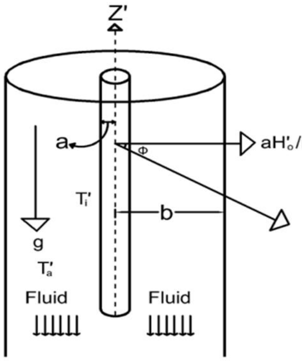

Figure 1. Geometry of the model [18].

The configuration of the study as illustrated in **Figure 1**, involves a fully developed natural convection flow of steady, viscous, incompressible electrically conducting fluid within a vertical concentric annulus of infinite length. The z' axis is oriented along the axis of coaxial cylinders is measured in the vertically upward direction, while R' represents the radial direction, measured outward from the axis of the cylinder. The applied magnetic field represented as ${}^{aH'_o}\!/_{R'}$ is directed radially outward. The temperatures T'_i and T'_a denote the temperature at the outer surface of the inner cylinder and the ambient temperature, respectively. The radii of the inner and outer cylinders are denoted by a and b, respectively. The velocity components are $U'_{R'}$, U'_θ and $U'_{z'}$ in the direction R', θ and z' direction respectively. For fully developed flow, $U'_{R'} = U'_\theta = 0$ with flow direction along the z'-axis. The flow depends solely on R' due to the fully developed nature and infinite length of the cylinders. For the considered model, the velocity and magnetic field components are given as $(0, 0U')$ and $({}^{aH'_o}\!/_{R'}, 0\,, H'_{z'})$ respectively [18].

The study assumes an axisymmetric, parallel, and fully developed flow in the flow direction, with the fluid being Newtonian and incompressible. Additionally, the pressure remains constant along the flow direction. Utilizing the assumptions and applying ∇^2 and ∇ laplacian and gradient operators to the velocity and magnetic field, we obtained the following equations.

$$\nabla^2 H = \left[\frac{1}{R'}\frac{d}{dR'}\left(R'\frac{dU'(R')}{dR'}\right)\right] \tag{5}$$

$$\nabla^2 V = \left[\frac{1}{R'}\frac{d}{dR'}\left(R'\frac{dH'_{z'}(R')}{dR'}\right)\right] \tag{6}$$

Also, the term $(\boldsymbol{J} \times \boldsymbol{B})$ and using Ampere's law for a steady state ($\nabla \times B = \mu_e J$) and the relation $B = \mu_e H$ [18]we get:

$$(J \times B)_z = [\mu_e(\nabla \times H) \times H]_z = \frac{a\mu_e H'_o}{R'}\left(\frac{dH'_{z'}}{dR'}\right) \tag{7}$$

Similarly,

$$[(\nabla \times V) \times H]_z = \frac{aH'_o}{R'}\left(\frac{dU'}{dR'}\right) \tag{8}$$

The non-dimensional governing equations for the flow formation, based on Equations (5)–(8) and Equations (1)–(4) under the Boussinesq approximation, are as follows:

$$\nu\left[\frac{1}{R'}\frac{d}{dR'}\left(R'\frac{dU'}{dR'}\right)\right] + g\beta(T' - T'_a) + \frac{a\mu_e H'_o}{\rho R'}\frac{dH'_{z'}}{dR'} = 0 \tag{9}$$

$$\eta\left[\frac{1}{R'}\frac{d}{dR'}\left(R'\frac{dH'_{z'}}{dR'}\right)\right] + \frac{aH'_0}{R'}\frac{dU'}{dR'} = 0 \tag{10}$$

$$\frac{k}{\rho C_p}\left[\frac{1}{R'}\frac{d}{dR}\left(R'\frac{dT'}{dR'}\right)\right] + \frac{Q_o}{\rho C_p} = 0 \tag{11}$$

The boundary conditions for Equations (9)–(11) are:

$$\begin{cases} U' = H'_{z'} = 0; T' = T'_i / \dfrac{dT'}{dR'} = -\dfrac{q}{k} at R' = a \\ U' = H'_{z'} = 0; T' = T'_a at R' = b \end{cases} \tag{12}$$

In these equations, the following symbols represent various physical quantities: Fluid velocity U', gravitational acceleration g, coefficient of volume expansion β, magnetic permeability μ_e, fluid density ρ, magnetic diffusivity η, thermal conductivity of the fluid k, specific heat capacity at constant pressure C_p, fluid temperature T', ambient temperature T'_a, heat generation/absorption parameter respectively $Q_0 > 0$ and $Q_0 < 0$.

Rendering Equations (9)–(12) to the following non-dimensional variables and parameters.

$u = \frac{U^{'}}{U_o}, R = \frac{R'}{a}, \theta = \frac{(T^{'} - T_a^{'})}{(T_i^{'} - T_a^{'})}, H = \frac{H_{Z'}^{'}}{\sigma a \mu_e H_o^{'} U_0} \lambda = \frac{b}{a}, Q_o = \frac{Q_o^* a^2 (T^{'} - T_a^{'})}{R^{'2}}$ (radially-dependent heat generation/absorption function), $S = -\frac{Q_o^* a^2}{k}$ (heat generation/absorption parameter), $U_o = \frac{g a^2 \beta (T_i^{'} - T_a^{'})}{\nu}$ (characteristic velocity) and $Ha = a \mu_e H_o^{'} [\sigma / \rho \nu]^{\frac{1}{2}}$ (Hartmann number), we obtained the following dimensionless equaions:

$$\left[\frac{1}{R}\frac{d}{dR}\left(R\frac{du}{dR}\right)\right] + \theta + Ha^2\left[\frac{1}{R}\frac{dH}{dR}\right] = 0 \tag{13}$$

$$\left[\frac{1}{R}\frac{d}{dR}\left(R\frac{dH}{dR}\right)\right] + \left[\frac{1}{R}\frac{du}{dR}\right] = 0 \tag{14}$$

$$\left[\frac{1}{R}\frac{d}{dR}\left(R\frac{d\theta}{dR}\right)\right] - \frac{S}{R^2}\theta = 0 \tag{15}$$

$$\begin{cases} u = H = 0; \theta = 1/\frac{d\theta}{dR} = -1 at R = 1 \\ u = H = 0; \theta = 0 at R = \lambda \end{cases} \tag{16}$$

3. Method

This study's methodology is comparable to that described in [18]. By using non-dimensional boundary conditions to solve the dimensionless governing linear simultaneous ordinary differential equations, the exact solutions for the velocity, induced magnetic field, induced current density, and temperature field are obtained, along with corresponding numerical values for skin friction, mass flux, induced current flux, and Nusselt number, which are also obtained for both isothermal and iso-flux conditions.

Analytical solution

Solving Equations (13)–(16), the velocity, skin friction, mass flux, induced magnetic field, induced current density, induced current flux, temperature, and Nusselt number were determined analytically, subject to boundary conditions (16) as follows:

$$u(R) = E_1 R^{Ha} + E_2 R^{-Ha} + E_3 - \frac{E_5}{(2+\sqrt{S})^2 - Ha^2} R^{(2+\sqrt{S})} - \frac{E_6}{(2-\sqrt{S})^2 - Ha^2} R^{(2-\sqrt{S})} \tag{17}$$

$$\tau_1 = \left.\frac{du}{dR}\right|_{R=1} = Ha(E_1 - E_2) - \frac{E_5(2+\sqrt{S})}{((2+\sqrt{S})^2 - Ha^2)} - \frac{E_6(2-\sqrt{S})}{((2-\sqrt{S})^2 - Ha^2)} \tag{18}$$

$$\tau_\lambda = -\left.\frac{du}{dR}\right|_{R=\lambda} = -Ha(E_1\lambda^{Ha-1} - E_2\lambda^{-Ha-1}) + \frac{E_5(2+\sqrt{S})}{((2+\sqrt{S})^2 - Ha^2)}\lambda^{(1+\sqrt{S})} + \frac{E_6(2-\sqrt{S})}{((2-\sqrt{S})^2 - Ha^2)}\lambda^{(1-\sqrt{S})} \tag{19}$$

$$Q = 2\pi\int_1^\lambda R\,u(R)dR = 2\pi\left[\frac{E_1}{(Ha+2)}(\lambda^{Ha+2} - 1) + \frac{E_2}{(2-Ha)}(\lambda^{2-Ha} - 1) + \frac{E_3}{2}(\lambda^2 - 1) + E_7 + E_8\right] \tag{20}$$

$$H(R) = -\frac{1}{Ha}\left[E_1 R^{Ha} - E_2 R^{-Ha}\right] + \frac{E_5}{\left(2+\sqrt{S}\right)\left[(2+\sqrt{S})^2 - Ha^2\right]} R^{(2+\sqrt{S})} + \frac{E_6}{\left(2-\sqrt{S}\right)\left[(2-\sqrt{S})^2 - Ha^2\right]} R^{(2-\sqrt{S})} + E_4 + E_3\, ln(R) \tag{21}$$

$$J_\theta = -\frac{dH}{dR} = E_1 R^{Ha-1} - E_2 R^{-Ha-1} - \frac{E_3}{R} + E_{13} R^{1+\sqrt{S}} + E_{14} R^{1-\sqrt{S}} \tag{22}$$

$$J = \int_1^\lambda J_\theta\, dR = \frac{1}{Ha}\left[E_1(\lambda^{Ha} - 1) - E_2(1 - \lambda^{-Ha})\right] + E_{15} + E_{16} + E_{17} \tag{23}$$

$$\theta(R) = \frac{R^{\sqrt{S}} - \lambda^{2\sqrt{S}} R^{-\sqrt{S}}}{(1 - \lambda^{2\sqrt{S}})} \tag{24}$$

$$Nu_1 = -\left.\frac{d\theta}{dR}\right|_{R=1} = -\sqrt{S}(E_5 - E_6) \tag{25}$$

$$Nu_\lambda = -\left.\frac{d\theta}{dR}\right|_{R=\lambda} = -\sqrt{S}\left(E_5 \lambda^{\sqrt{S}-1} - E_6 \lambda^{-\sqrt{S}-1}\right) \tag{26}$$

The constants in the Equations (17)–(26) are given in Appendix A.

4. Results

To investigate the fluid flow dynamics, the governing equations were solved analytically, with the results visualized through MATLAB-generated plots. The study focused on three key parameters: Heat absorption strength, radii ratio, and Hartmann number. Each parameter was independently varied while the others remained constant to produce the plots shown in **Figures 1–16**. Comparison and numerical results corresponding to Equations (18)–(20), (23), (25), and (26) are detailed in **Tables 1–6** The Hartmann number was evaluated over a range consistent with prior studies, including those by [12,14,17]. The trends in velocity, induced magnetic field, induced current density, and temperature profiles, as depicted in **Figures 1–16**, demonstrate a clear dependency on the annular region, heat absorption parameter, and Hartmann number, aligning well with previously reported findings.

Figures and tables

Here we present a detailed analysis of the results obtained through graphical and tabular representations. The figures illustrate the influence of key parameters such as Hartmann number (Ha), heat absorption strength (S), and the annular gap ratio (λ) on the temperature, velocity, magnetic field, and induced current density profiles. The tables provide a comprehensive summary of numerical values, highlighting trends and correlations among the studied variables. Together, these figures and tables offer a clear visualization of the physical phenomena and validate the theoretical findings of the study.

Table 1. Comparison between the study [36] and this study for isothermal.

		Oni, et al. [17] $Ha = 3$			**Current study $Ha = 3$**		
S	λ	τ_1	τ_λ	Q	τ_1	τ_λ	Q
0.5	1.6	0.1751	0.0648	0.0531	0.1751	0.0648	0.0531
0.5	1.8	0.2177	0.0743	0.1189	0.2177	0.0743	0.1189
0.5	2	0.2535	0.0806	0.2191	0.2535	0.0806	0.2191
0.5	2.2	0.2837	0.0849	0.3577	0.2837	0.0849	0.3577
1.5	1.6	0.1724	0.0631	0.0519	0.1724	0.0631	0.0519
1.5	1.8	0.2127	0.0711	0.1145	0.2127	0.0711	0.1145
1.5	2	0.2455	0.0758	0.2078	0.2455	0.0758	0.2078
1.5	2.2	0.2723	0.0784	0.3340	0.2723	0.0784	0.3340
3	1.6	0.1686	0.0606	0.0501	0.1686	0.0606	0.0501
3	1.8	0.2056	0.0668	0.1085	0.2056	0.0668	0.1085
3	2	0.2346	0.0695	0.1928	0.2346	0.0695	0.1928
3	2.2	0.2573	0.0701	0.3033	0.2573	0.0701	0.3033

Table 2. Comparison between the study [36] and this study for iso-flux.

		Oni, et al. [17] $Ha = 3$			**Current study $Ha = 3$**		
S	λ	τ_1	τ_λ	Q	τ_1	τ_λ	Q
0.5	1.6	0.0794	0.0294	0.0241	0.0794	0.0294	0.0241
0.5	1.8	0.1211	0.0413	0.0661	0.1211	0.0413	0.0661
0.5	2	0.1629	0.0518	0.1407	0.1629	0.0518	0.1407
0.5	2.2	0.2031	0.0608	0.2561	0.2031	0.0608	0.2561
1.5	1.6	0.0731	0.0268	0.022	0.0731	0.0268	0.0220
1.5	1.8	0.1071	0.0358	0.0577	0.1071	0.0358	0.0577
1.5	2	0.1384	0.0428	0.1172	0.1384	0.0428	0.1172
1.5	2.2	0.1660	0.0478	0.2037	0.1660	0.0478	0.2037
3	1.6	0.0654	0.0235	0.0194	0.0654	0.0235	0.0194
3	1.8	0.0913	0.0297	0.0482	0.0913	0.0297	0.0482
3	2	0.1129	0.0334	0.0928	0.1129	0.0334	0.0928
3	2.2	0.1304	0.0355	0.1537	0.1304	0.0355	0.1537

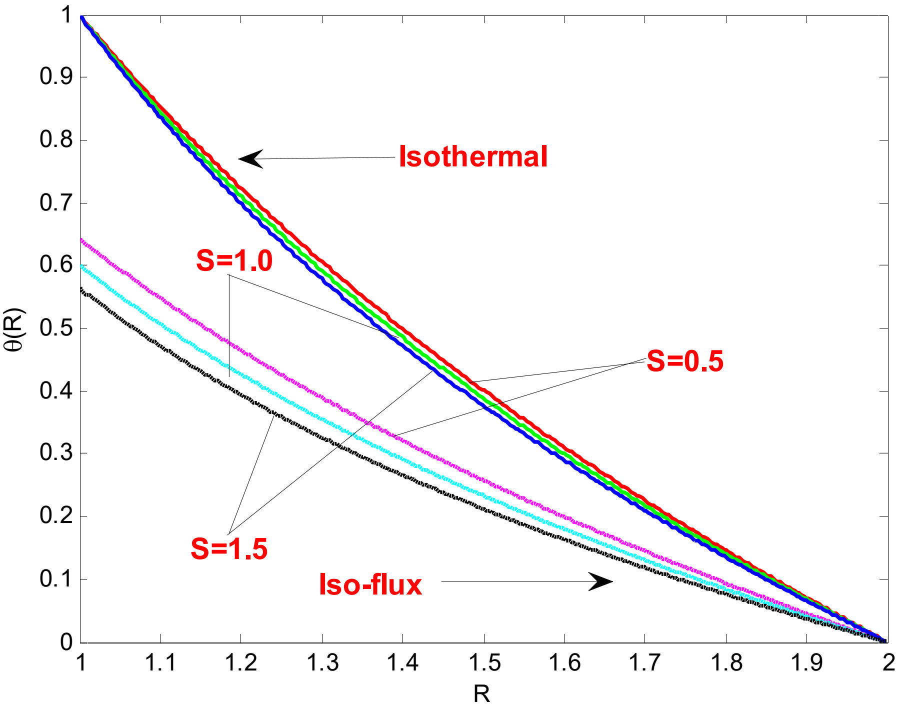

Figure 1. Temperature profile for different values of (S) at $\lambda = 2$.

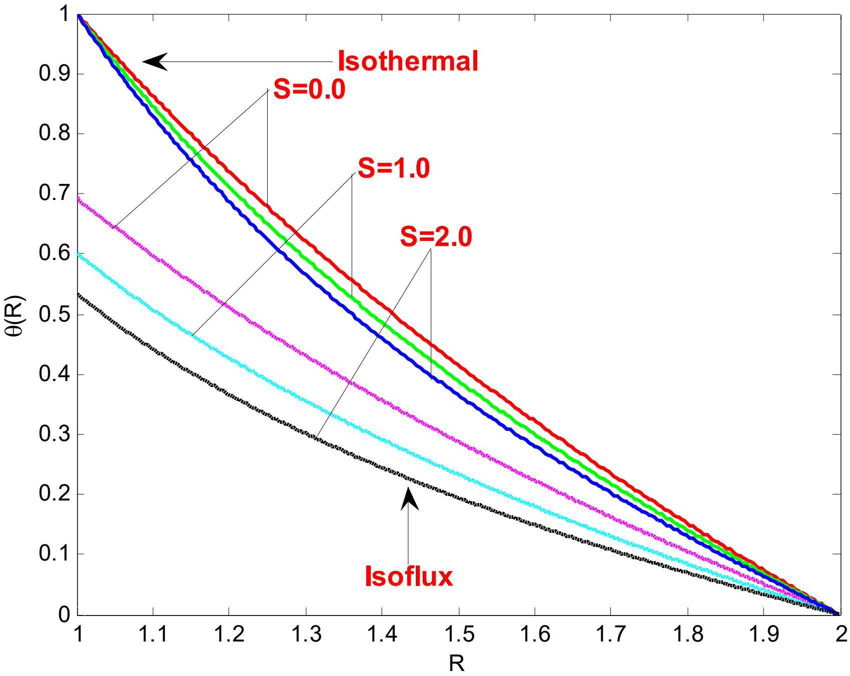

Figure 2. Temperature profile for $S = 0.0, 1, 2$ at $\lambda = 2$.

Table 3. Numerical values of isothermal and iso-flux for different values of Ha and λ.

		Isothermal $S \to 0$			**Iso-flux $S \to 0$**		
Λ	**Ha**	**τ_1**	**τ_λ**	**Q**	**τ_1**	**τ_λ**	**Q**
1.8	0.5	0.2684	0.1005	0.1583	0.1578	0.0590	0.0930
	1	0.2632	0.0978	0.1542	0.1547	0.0575	0.0906
	1.5	0.2552	0.0936	0.1479	0.1500	0.0550	0.0869
2	0.5	0.3365	0.1197	0.3205	0.2332	0.0829	0.2221
	1	0.3273	0.1153	0.3092	0.2268	0.0799	0.2143
	1.5	0.3134	0.1088	0.2922	0.2172	0.0754	0.2025
3	0.5	0.6839	0.2002	2.9988	0.7511	0.2199	3.2932
	1	0.6359	0.1844	2.7548	0.6984	0.2025	3.0253
	1.5	0.5711	0.1632	2.4262	0.6272	0.1792	2.6644

Table 4. Numerical values of dimensionless τ_1, τ_λ, and Q for isothermal and iso-flux conditions for different values of Ha, S and λ.

			Isothermal			**Iso-flux**		
Ha	**S**	**λ**	**τ_1**	**τ_λ**	**Q**	**τ_1**	**τ_λ**	**Q**
2	1	1.8	0.238715	0.084548	0.134700	0.126114	0.044667	0.071162
3			0.215138	0.072668	0.11666	0.113658	0.038391	0.061632
4			0.190662	0.060628	0.098248	0.100727	0.032030	0.051904
2	1	2	0.285891	0.094799	0.257033	0.171535	0.056879	0.154220
3			0.249374	0.078145	0.213257	0.149624	0.046887	0.127954
4			0.214392	0.062646	0.172206	0.128635	0.037587	0.103324
2	1	3	0.459881	0.119962	1.806018	0.367905	0.09597	1.444815
3			0.353006	0.086147	1.281521	0.282405	0.068918	1.025217
4			0.275470	0.062300	0.912339	0.220376	0.04984	0.729871
2	2	1.8	0.233007	0.081053	0.129823	0.112227	0.039039	0.062529
3			0.210207	0.069617	0.112429	0.101245	0.033531	0.054151
4			0.186523	0.058033	0.094676	0.089838	0.027951	0.045600
2	2	2	0.276517	0.089388	0.244159	0.147267	0.047606	0.130034
3			0.241646	0.073595	0.202541	0.128695	0.039195	0.107869
4			0.208200	0.058910	0.16352	0.110882	0.031374	0.087087
2	2	3	0.425563	0.103698	1.589418	0.275157	0.067048	1.027671
3			0.329597	0.074060	1.126108	0.213108	0.047885	0.728109
4			0.259502	0.053265	0.800449	0.167786	0.03444	0.517547

Table 5. Numerical values of dimensionless induced current flux (J) for different Ha, S, and λ.

			Isothermal	Iso-flux
S	λ	Ha	J	J
1	1.8	2	0.1091644	0.0576718
		3	0.0462127	0.0244142
		4	0.0235330	0.0124325
1	2	2	0.1244444	0.0746667
		3	0.0512146	0.0307287
		4	0.0253968	0.0152381
1	3	2	0.1800000	0.0144000
		3	0.0655856	0.0524685
		4	0.0297909	0.0238328
2	1.8	2	0.1152914	0.0555296
		3	0.0476403	0.0229457
		4	0.0239789	0.0115494
2	2	2	0.1305719	0.0695396
		3	0.0525273	0.0279748
		4	0.0257751	0.0137272
2	3	2	0.1826348	0.1180864
		3	0.0656708	0.0424661
		4	0.0297198	0.0192160

Table 6. Numerical Nusselt numbers for various values of S and λ.

		Isothermal		Iso-flux	
S	λ	Nu_1	Nu_λ	Nu_1	Nu_λ
1	2	1.66667	0.66667	1.00000	0.40000
2	2	1.87766	0.61758	1.00000	0.32891
1	3	1.25000	0.25000	1.00000	0.20000
2	3	1.54662	0.20871	1.00000	0.13495

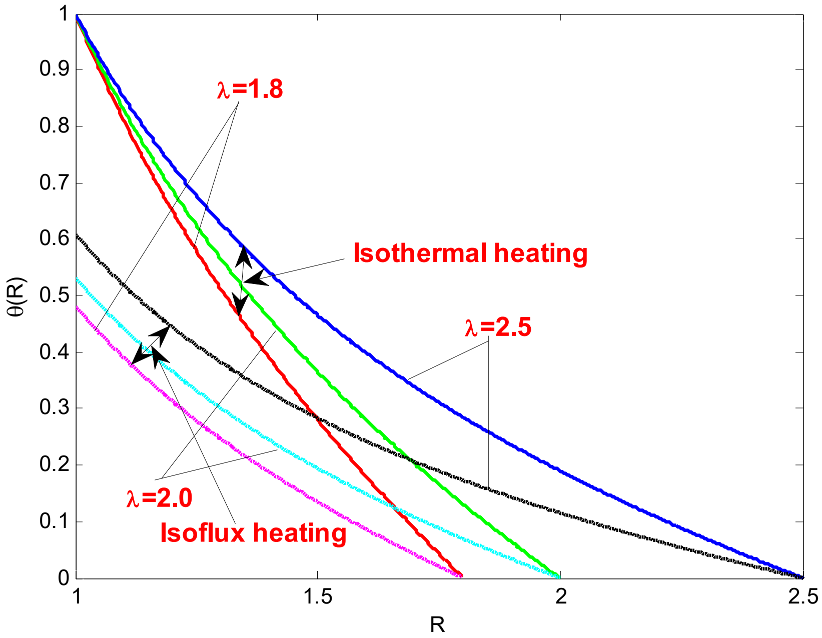

Figure 3. Temperature profile for different values λ at $S = 2$.

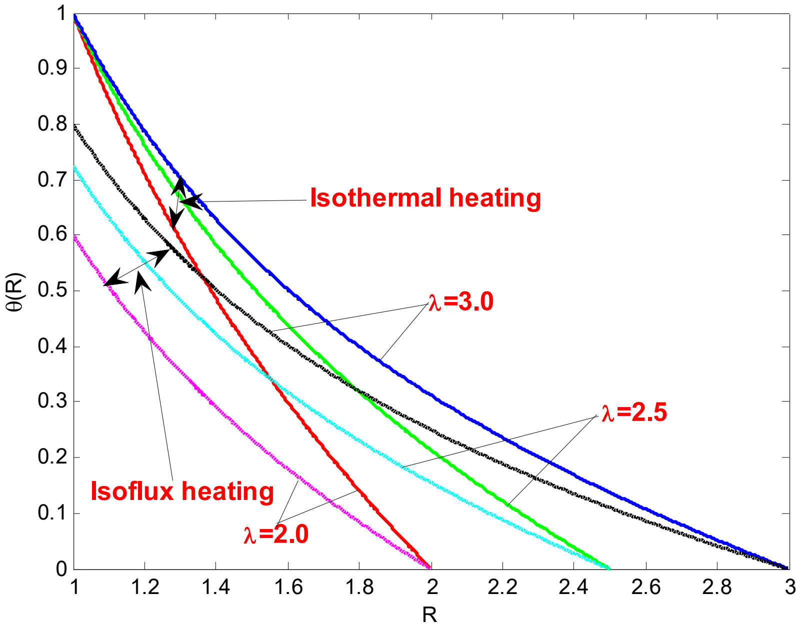

Figure 4. Temperature profile for $\lambda = 2.0, 2.5, 3$ at $S = 1$.

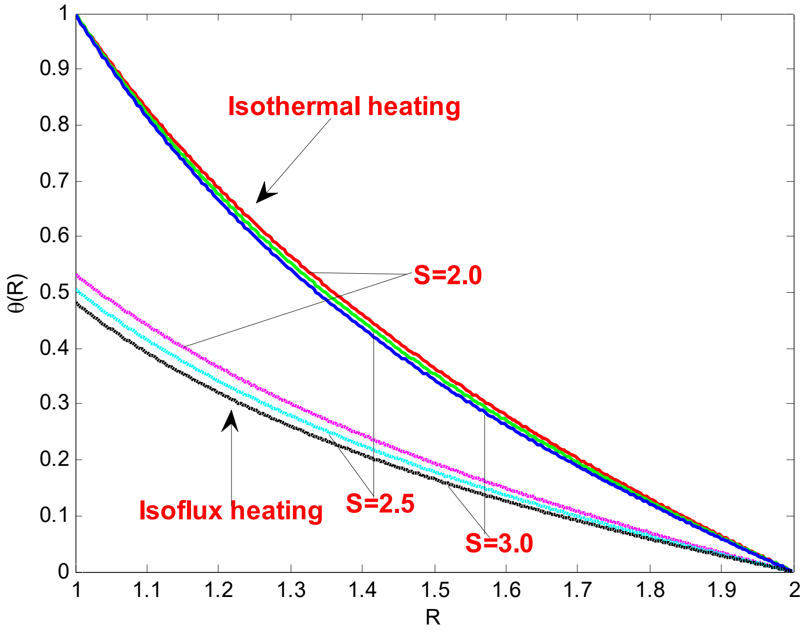

Figure 5. Temperature profile for S = 2.0, 2.5, 3 at λ = 2.

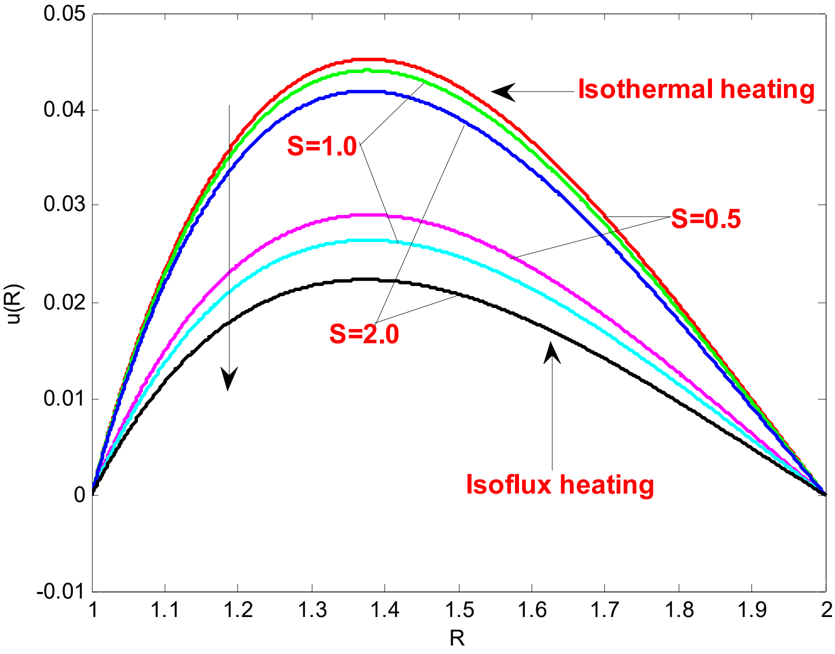

Figure 6. Velocity profile for different values of S at Ha = 2 and λ = 2.

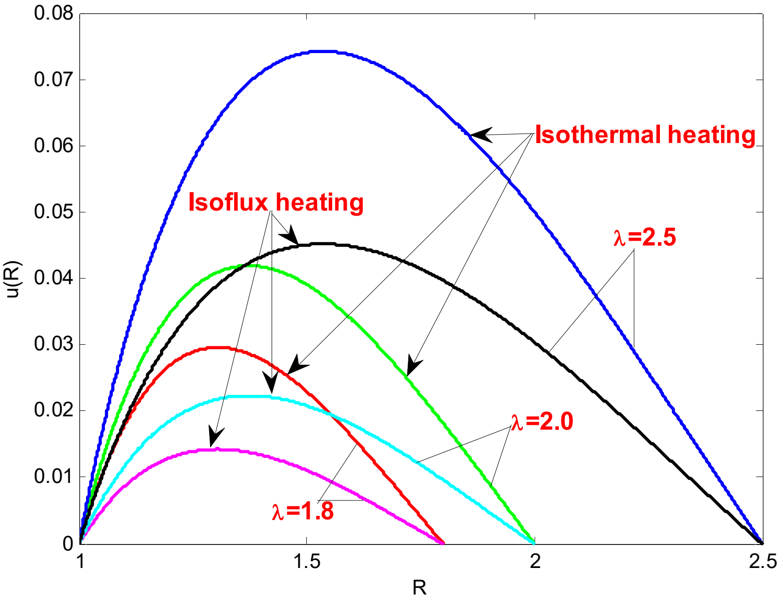

Figure 7. Velocity profile for different values of λ at $Ha = 2$ and $S = 2$.

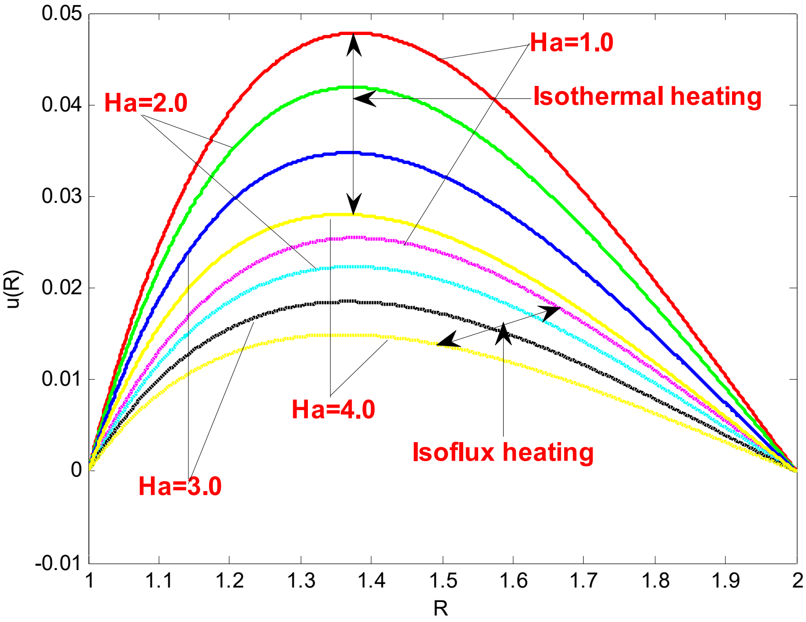

Figure 8. Velocity profile for different values of Ha at $\lambda = 2$ and $S = 2$.

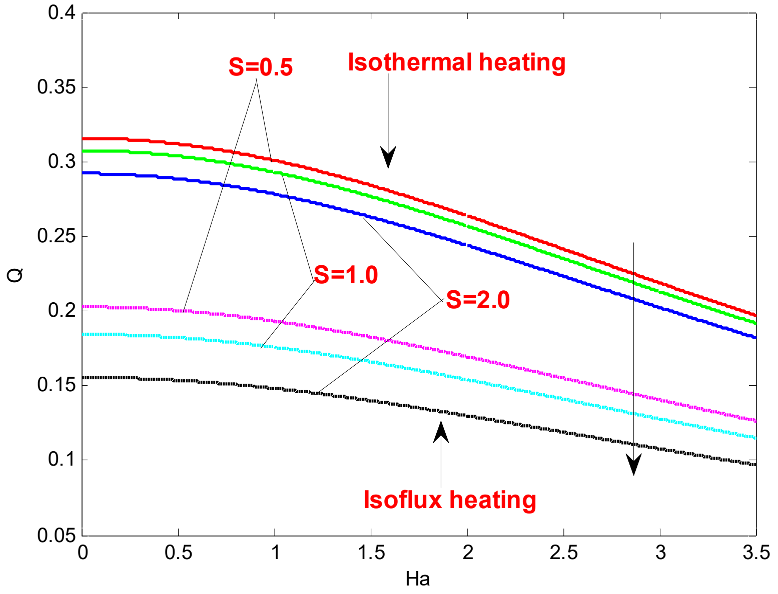

Figure 9. Mass flux for different values Ha and S at $\lambda = 2$.

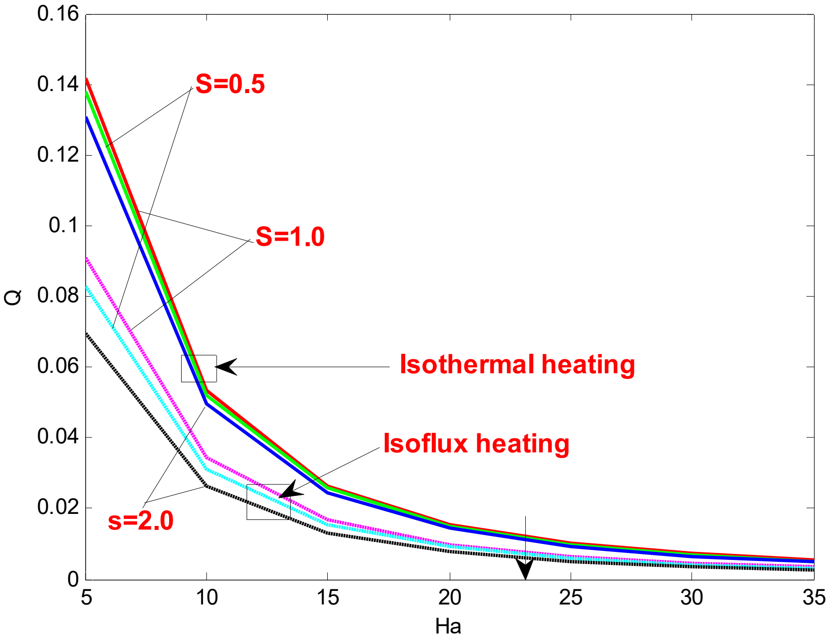

Figure 10. Mass flux for different values Ha and S at $\lambda = 2$.

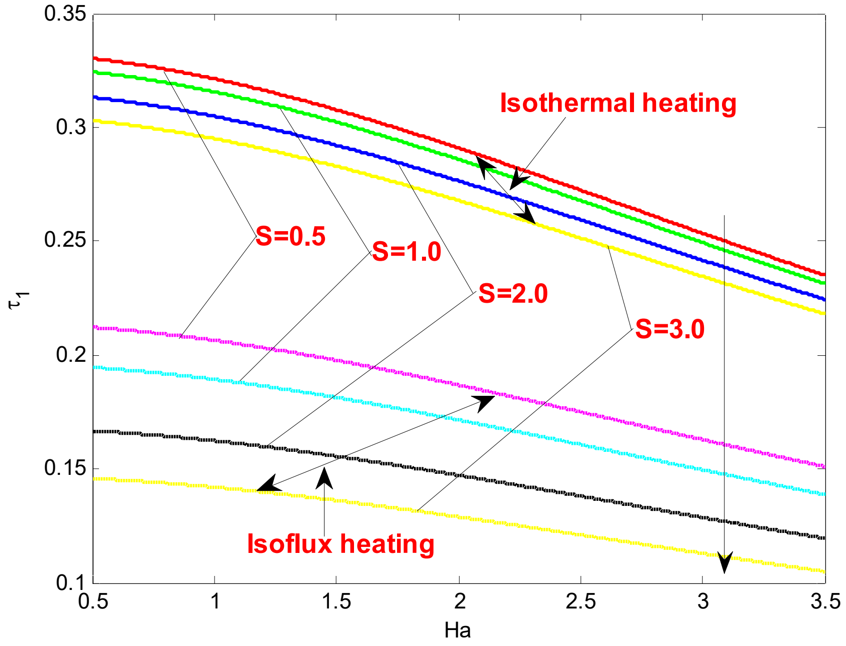

Figure 11. Skin friction (at inner cylinder) for different values of Ha and S at $\lambda = 2$.

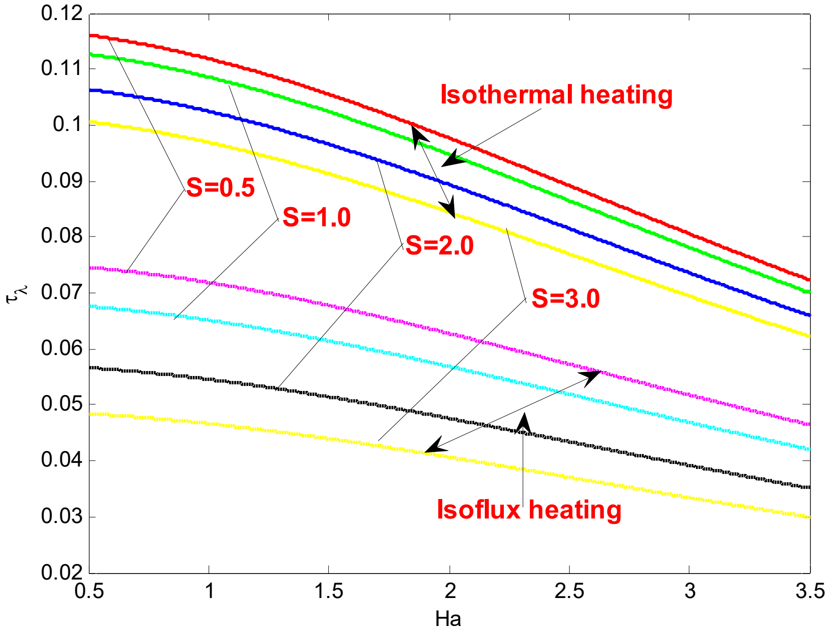

Figure 12. Skin friction (at outer cylinder) for different values of Ha and S at $\lambda = 2$.

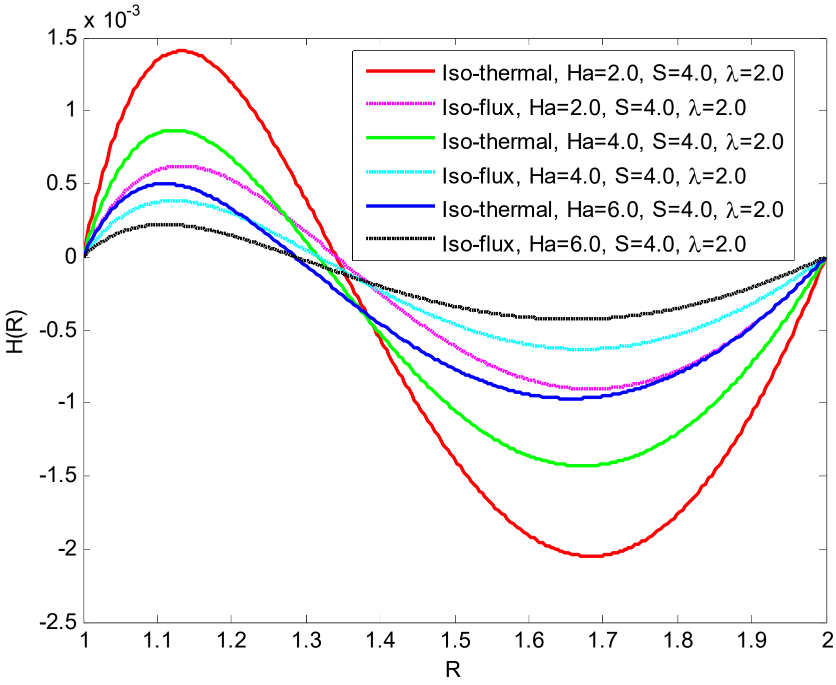

Figure 13. Magnetic field for different values of Ha at S = 4 and λ = 2.

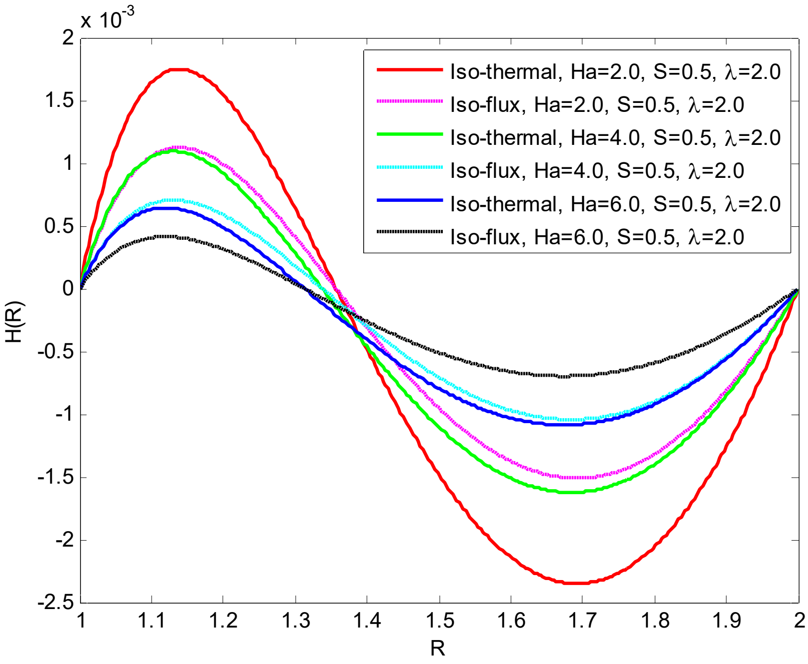

Figure 14. Magnetic field for different values of Ha at S = 0.5 and λ = 2.

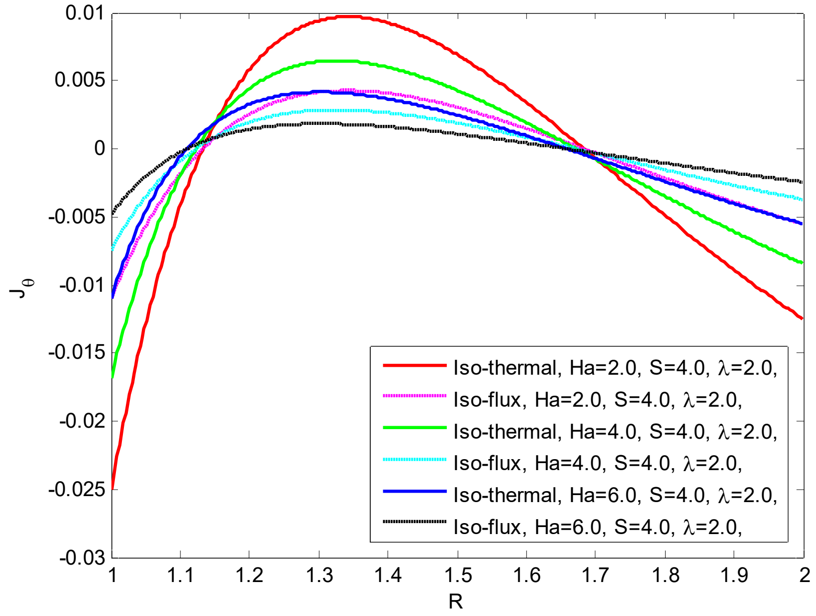

Figure 15. Induced current density for different values of Ha at S = 4 and λ = 2.

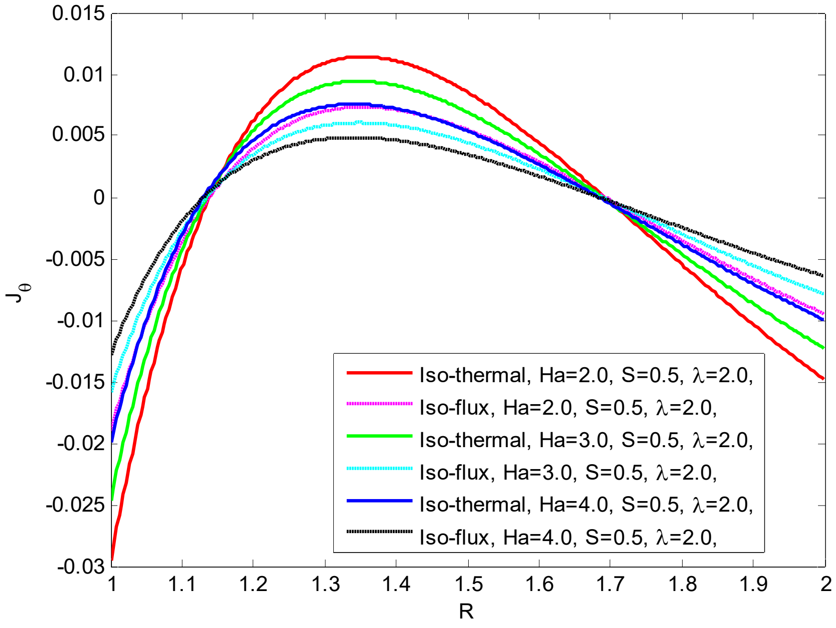

Figure 16. Induced current density for different values of Ha at S = 0.5 and λ = 2.

5. Discussion

The results presented in **Tables 1–6** offer a comprehensive comparison and numerical analysis of isothermal and iso-flux conditions for various parameters. **Tables 1** and **2** provide comparative data between the studies of Oni et al. [17] and the current investigation, detailing the dimensionless parameters under isothermal and iso-flux boundary conditions. The values show a consistent trend of increasing magnitudes with varying heat absorption parameter (S) and constant Hartmann numbers (Ha), reflecting the influence of magnetic fields on heat absorption characteristics. **Table 3** further elaborates on the numerical results for both conditions, considering variations in the annular gap (λ) and (Ha), emphasizing the dependency of heat transfer rates on these physical parameters. **Table 4** extends this analysis to dimensionless quantities such as skin friction at the inner cylinder (τ_1), skin friction at the outer cylinder (τ_λ), and mass flux Q for different Hartmann numbers and heat absorption parameter, illustrating a declining trend with increasing (Ha) under both boundary conditions. Finally, **Table 5** presents the induced current flux (J) values, showcasing the magnetic field's effect on the electrical current distribution in the medium. **Table 6** presents numerical Nusselt numbers (Nu_1 and Nu_λ) under isothermal and iso-flux conditions for varying heat absorption parameters (S) and annulus radius ratios (λ). The results show that increasing S enhances heat transfer at the inner boundary (Nu_1) while reducing it at the outer boundary (Nu_λ), indicating stronger internal heat generation effects. Increasing λ weakens heat transfer at both boundaries due to a reduced temperature gradient. Under iso-flux conditions, Nu_1 remains constant at 1.0, while Nu_λ is consistently lower than in the isothermal case, suggesting greater stability in heat transfer behavior. These results highlight the complex interplay between conduction and convection in heat transfer systems, underscoring the importance of optimizing both S and λ for maximizing heat transfer efficiency in systems governed by isothermal and isoflux conditions.

Figure 1 depicts the temperature profile at $\lambda = 2$ for different values of S for iso-thermal and iso-flux boundary conditions and shows that for higher values of S (e.g., $S = 1.5$), the temperature profile is elevated, indicating stronger heat generation within the annulus. This effect is more pronounced under the isothermal condition compared to the iso-flux case, where temperature gradients appear more stable. The isothermal profiles exhibit a steeper decline near the outer boundary, suggesting enhanced heat loss at larger radii. In contrast, the iso-flux curves show a smoother transition, implying a more uniform heat transfer mechanism. **Figure 2** illustrates the temperature distribution at $\lambda = 2$ for different values of S. Similar to **Figure 1**, this reinforces the effect of S on temperature. Higher values of S correspond to greater thermal diffusion from the inner to the outer cylinder, showing isothermal and iso-flux conditions showings distinct profiles. In **Figures 3** and **4**, the influence of the annular region at $S = 2$ and $S = 1$ for different values of λ is depicted. Increasing λ broadens the gap between the cylinders, leading to an extended thermal boundary layer and reduced temperature gradients near the wall. But for smaller heat generation strength, the temperature profiles are less steep, indicating a weaker influence of λ when S is reduced. This **Figure 5** consolidates the effect of S on temperature for isothermal and iso-flux conditions. It emphasizes the significant role of heat generation strength in thermal behavior for higher S values. **Figure 6**, depicts the influence of S on velocity distributions. Velocity distribution decreases with increasing S due to the combined damping effects of heat absorption and magnetic fields. Iso-flux conditions exhibit slightly lower velocities compared to isothermal. In this **Figure 7**, in this figure, the velocity profile for different values of λ. As λ increases, the velocity magnitude reduces, highlighting the influence of geometry on flow dynamics. Larger λ values introduce more resistance to fluid motion due to enhanced magnetic effects. **Figure 8** demonstrates the effect of Ha on the velocity profile. Velocity profile reduces with an increase in Ha, attributed to the Lorentz force acting as a resistive mechanism. This trend is consistent for both isothermal and iso-flux conditions. **Figures 9** and **10** depict mass flux for values of Ha and S. Q decreases with increasing Ha, demonstrating the suppressive effect of the magnetic field on fluid motion. Higher S values further reduce Q, emphasizing the combined influence of magnetic and thermal forces. Isothermal conditions exhibit marginally higher flux values than iso-flux. **Figures 11** and **12** show the effects of skin friction at both inner and outer cylinders for varying Ha and S. In both cases, skin friction decreases as Ha increases, indicating that a stronger magnetic field suppresses wall shear stress. Higher values of S further reduce skin friction, suggesting that buoyancy forces weaken the flow resistance at the cylinder walls. Additionally, isothermal heating (solid lines) consistently results in higher skin friction compared to isoflux heating (dashed lines), likely due to stronger thermal gradients influencing the flow. The inner cylinder (τ_1) experiences greater skin friction than the outer cylinder (τ_λ), which aligns with expectations given the annular flow structure. **Figures 13** and **14** illustrate the variation of the magnetic field $H(R)$ for different values of the Hartmann number (Ha) under both isothermal and iso-flux boundary conditions at $\lambda = 2$, with **Figure 14** corresponding to $S = 4$ and **Figure 15** to $S = 2$. In both figures, the magnetic field exhibits a similar trend, with an initial increase followed by a decline before reaching a minimum and then rising again towards the outer boundary. The impact of Ha is evident, as increasing Ha leads to a reduction in the amplitude of $H(R)$, signifying stronger Lorentz forces that suppress the induced magnetic field. The isothermal condition generally results in higher peak values compared to the iso-flux condition. Comparing **Figures 14** and **15**, the effect of decreasing S from 4 to 0.5 is noticeable, as the amplitude of $H(R)$ increases, particularly for lower Ha values, highlighting the role of the heat source parameter in influencing the magnetic field distribution. **Figures 15** and **16** demonstrate the influence of induced current density for different values of Ha at $S = 4$ and $S = 0.5$. J_θ decreases with higher Ha, especially near the boundaries. For lower S the induced current density is significantly reduced due to weaker thermal and magnetic interactions. Iso-flux conditions show slightly higher values than isothermal. All symbol used are given in Appendix B

Physical significance of the study

This study provides valuable insights into the dynamics of MHD natural convection flow within a vertical concentric annulus. The inclusion of inverse-square heat absorption is particularly significant, as it models practical scenarios where thermal energy dissipates with distance, akin to radiative heat transfer in astrophysical and industrial applications. The effects of radial and induced magnetic fields add another layer of complexity, reflecting realistic electromagnetic interactions in engineering systems like fusion reactors and MHD generators. The parameters explored, Hartmann number (Ha), heat absorption strength (S), and radii ratio (λ) provide insights into how electromagnetic forces influence thermal and flow behavior in constrained geometries. Radial magnetic fields exert a Lorentz force that suppresses fluid velocity and reduces turbulence, particularly near the inner cylinder, leading to laminarization of flow patterns. Induced magnetic fields, generated by fluid motion in a conducting medium, further modify thermal gradients and current density distributions, reducing heat transfer rates and mass flux as magnetic field strength increases. The combined influence of radial and induced magnetic fields results in enhanced flow resistance and suppressed convective heat transfer, which is critical in optimizing thermal management in systems like fusion reactors and MHD generators. Additionally, induced magnetic fields can generate magnetic pressure gradients that impact the overall pressure distribution, affecting flow separation points and boundary layer development in channels and annuli. These fields also interact with electric currents generated within the fluid, leading to complex behaviors such as magnetic braking and magnetically driven recirculation. Ultimately, radial and induced magnetic fields play a pivotal role in controlling fluid motion, reducing turbulence, and influencing heat transfer efficiency in MHD systems, with critical applications in nuclear reactor cooling, liquid metal flows in fusion reactors, and metallurgical processes.

The findings aligned with established MHD principles, particularly the damping effect of magnetic fields on velocity profiles and the thermal boundary layer thickening observed under increased heat absorption.

6. Conclusion

This research offers an analytical approach to understanding MHD natural convection flow with radially varying temperature within a vertical concentric annulus, influenced by both radial and induced magnetic fields. We have investigated the effects of Hartmann number (Ha), annular region, and heat absorption parameter on free convective flow of an electrically conducting fluid by imposing a mixed type of thermal conditions on the surface of the inner cylinder in the presence of an applied uniform and induced amagnetic field. The key findings are summarized as follows:

- The inverse-square heat absorption model significantly influences thermal gradients, with higher absorption intensifying heat transfer effects near the inner cylinder.
- Heat absorption strength S significantly affects temperature profiles, with higher S amplifying thermal gradients near the inner cylinder. The annular gap (λ) further modifies the thermal boundary layer, emphasizing geometric dependence.
- The Lorentz force generated by magnetic fields suppresses fluid velocity as (Ha) increases. Heat absorption (S) also contributes to flow resistance, highlighting the combined impact of thermal and electromagnetic forces.
- Mass flux (Q) decreases with Ha and S, reflecting restricted flow under stronger magnetic and thermal forces. Skin friction near the inner cylinder decreases with S, indicating the shear stress effects of heat absorption.
- The magnetic field and induced current density diminish with increasing Ha, particularly under strong heat absorption conditions. This interaction emphasizes the interconnected relationship between electrical and thermal dynamics.
- Magnetic fields significantly influence heat and mass transfer, with stronger fields suppressing heat transfer rates and current flux.

- The heat absorption parameter (S), Hartmann number (Ha), and annular gap (λ) impact thermal and electrical behavior, with implications for optimizing magnetic field strength for thermal management in engineering systems.
- As the heat absorption parameter S increases, the isothermal Nusselt numbers Nu_1 and Nu_λ decrease, indicating a reduction in thermal efficiency due to enhanced heat absorption and for iso-flux Nu_1 remains constant at -1.0, signifying that the convective flux is predominantly governed by conduction rather than convection under the given conditions.

Overall, this study provides novel insights into the effects of inverse-square heat absorption on MHD flows in constrained geometries, bridging gaps in existing literature. By examining the range of parameters, the results pave the way for optimizing heat transfer in engineering applications involving MHD systems.

7. Future research directions

- Investigating transient effects and time-dependent variations in heat absorption for dynamic thermal systems.
- Extending the model to non-Newtonian fluids to explore complex industrial applications.
- Incorporating turbulence modeling to examine flow instabilities under varying magnetic field strengths.
- Exploring the impact of variable thermal conductivity on energy dissipation and heat transfer efficiency.
- Extending the study to alternative annular geometries, such as elliptical or rectangular cross-sections, to optimize heat transfer efficiency.

This research establishes a foundational framework for further studies in MHD heat transfer optimization, enabling more precise control over energy dissipation in high-performance engineering systems.

Author contributions: Conceptualization, MYM and YYG; methodology, MYM; software, MYM; validation, MYM, YYG and MAL; formal analysis, MYM, YYG and MAL; resources, MYM; writing—original draft preparation, MYM; writing—review and editing, MYM; visualization, MYM, YYG and MAL; supervision, YYG and MAL. All authors have read and agreed to the published version of the manuscript.

Conflict of interest: The authors declare no conflict of interest.

References

1. Kumar D, Singh AK. Effects of heat source/sink and induced magnetic field on natural convective flow in vertical concentric annuli. Alexandria Engineering Journal. 2016; 55(4): 3125–3133. doi: 10.1016/j.aej.2016.08.019
2. Cheng L, Zhang L, Chen Z. Magnetohydrodynamic natural convection heat transfer of a conducting fluid in an open-ended concentric annulus with inner moving core. International Journal of Heat and Mass Transfer. 2019; 138: 501–516.
3. Kefayati GR, Ahmadi G, Daryasafar A. Analysis of natural convection in a vertical annulus filled with a conducting fluid under a radial magnetic field using lattice Boltzmann method. Journal of Magnetism and Magnetic Materials. 2017; 427: 276–286.
4. Oztop HF, Baytas AC. Magnetohydrodynamic mixed convection in an open-ended vertical cylindrical annulus. Journal of Magnetism and Magnetic Materials. 2018; 448: 305–317.

5. Jain RK, Mehta KN. Laminar hydromagnetic flow in an annulus with porous walls. The Physics of Fluids. 1962; 5(10): 1207–1211. doi: 10.1063/1.1706506
6. Smith J, Johnson R. Effect of radial magnetic field on MHD natural convection in concentric cylinders. International Journal of Magnetohydrodynamics. 2023; 12: 87–102.
7. Brown A, Smith J, Johnson R, Williams M. Conducted numerical simulations to investigate the behavior of MHD natural convection flow with radial magnetic fields. Journal of Fluid Mechanics. 2023; 75: 123–135.
8. Gupta S, Sharma M. Analysis of heat transfer enhancement in MHD natural convection flow with radial magnetic field. Heat Transfer Engineering. 2023; 38: 487–502.
9. Sastry VUK, Bhadram CVV. Hydromagnetic convective heat transfer in vertical pipes. Flow, Turbulence and Combustion. 1978; 34(2–3): 117–125. doi: 10.1007/bf00418859
10. Raptis A, Singh AK. MHD free convection flow past an accelerated vertical plate. Int. Comm. Heat and Mass Transfer. 1983; 4: 313–321.
11. Jha BK. Transient free Convection flow in a vertical channel with heat sinks. Int J Appl Mech Eng. 2001; 6(1): 279–289.
12. Jha BK, Apere CA. Combined effect of hall and ion-slip currents on unsteady MHD couette flows in a rotating system. Journal of the Physical Society of Japan. 2010; 79(10): 104401. doi: 10.1143/jpsj.79.104401
13. Nayak MK, Mohapatra M. Effect of magnetic field on steady MHD natural convection flow between vertical concentric cylinders with asymmetric heat fluxes. Ain Shams Engineering Journal. 2016; 7: 1401–1411.
14. Oudina FM, Bessaïh R. Effect of the Geometry on the MHD Stability of Natural Convection Flows. Institute of Thermo mechanics. 2014; 3(2): 159–161.
15. Hasanuzzaman M, Labony MA, Hossain MM. Heat generation and radiative effects on time-dependent free MHD convective transport over a vertical permeable sheet. Heliyon. 2023; 9(10): e20865. doi: 10.1016/j.heliyon.2023.e20865
16. Chamkha AJ, Issa C. Effects of heat generation/absorption and thermophoresis on hydromagnetic flow with heat and mass transfer over a flat surface. International Journal of Numerical Methods for Heat & Fluid Flow. 2000; 10(4): 432–449. doi: 10.1108/09615530010327404
17. Singh RK, Singh AK. Effect of induced magnetic field on natural convection in vertical concentric annuli. Acta Mechanica Sinica. 2012; 28(2): 315–323. doi: 10.1007/s10409-012-0052-4
18. Muhammad YM, Lawan MA, Gambo YY. Heat absorption effects of magneto-natural convection flow in vertical concentric annuli with influence of radial and induced magnetic field. Sci Rep. 2024; 14: 15165.
19. Joshi HM. Fully developed natural convection in an isothermal vertical annular duct. Int Commun Heat Mass Transfer. 1987; 14(6): 657–664.
20. El-Shaarawi MAI, Al-Nimr MA. Fully developed laminar natural convection in open-ended vertical concentric annuli. Int J Heat Mass Transfer. 1990; 33(9): 1873–1884.
21. Jha BK, Aina B. Impact of induced magnetic field on magnetohydrodynamic natural convection flow in a vertical annular micro-channel in the presence of radial magnetic field. Propuls Power Res. 2018; 7: 171–181.
22. Rossow VJ. On flow of electrically conducting fluids over a flat plate in the presence of a transverse magnetic field. NACA Technical Note. 1958.
23. Ramamoorthy P. Flow between two concentric rotating cylinders with a radial magnetic field. The Physics of Fluids. 1961; 4(11): 1444–1445. doi: 10.1063/1.1706237
24. Arora KL, Gupta PR. Magnetohydrodynamic flow between two rotating coaxial cylinders under radial magnetic field. The Physics of Fluids. 1972; 15(6): 1146–1148. doi: 10.1063/1.1694041
25. Moalem D. Steady state heat transfer within porous medium with temperature dependent heat generation. Int J Heat Mass Transfer. 1976; 19(5): 529–537.
26. Jha BK, Ajibade AO. Free convective flow of heat generating/absorbing fluid between vertical porous plates with periodic heat input. International Communications in Heat and Mass Transfer. 2009; 36(6): 624–631. doi: 10.1016/j.icheatmasstransfer.2009.03.003
27. Jha BK, Oni MO, Aina B. Steady fully developed mixed convection flow in a vertical micro-concentric-annulus with heat generating/absorbing fluid: An exact solution. Ain Shams Engineering Journal. 2018; 9(4): 1289–1301. doi: 10.1016/j.asej.2016.08.005

28. Oni MO. Combined effect of heat source, porosity and thermal radiation on mixed convection flow in a vertical annulus: An exact solution. Engineering Science and Technology, An International Journal. 2017; 20(2): 518–527. doi: 10.1016/j.jestch.2016.12.009
29. Singh SK, Jha BK, Singh AK. Natural convection in vertical concentric annuli under a radial magnetic field. Heat and Mass Transfer. 1997; 32(5): 399–401. doi: 10.1007/s002310050137
30. Samuel Taiwo Y. Exact solution of an MHD natural convection flow in vertical concentric annulus with heat absorption. International Journal of Fluid Mechanics & Thermal Sciences. 2017; 3(5): 52–61. doi: 10.11648/j.ijfmts.20170305.12
31. Nandkeolyar R, Mahatha B, Mahato G, Sibanda P. Effect of Chemical Reaction and Heat Absorption on MHD Nanoliquid Flow Past a Stretching Sheet in the Presence of a Transverse Magnetic Field. Magnetochemistry. 2018; 4(1): 18. doi: 10.3390/magnetochemistry4010018
32. Mabood F, Bognár G, Shafiq A. Impact of heat generation/absorption of magnetohydrodynamics Oldroyd-B fluid impinging on an inclined stretching sheet with radiation. Scientific Reports. 2020; 10(1). doi: 10.1038/s41598-020-74787-2
33. Mishra A, Pandey AK, Chamkha AJ, et al. Roles of nanoparticles and heat generation/absorption on MHD flow of Ag–H2O nanofluid via porous stretching/shrinking convergent/divergent channel. Journal of the Egyptian Mathematical Society. 2020; 28(1). doi: 10.1186/s42787-020-00079-3
34. Panigrahi L, Panda JP, Dash GC. MHD natural convective flow of a polar fluid with Newtonian heat transfer in vertical concentric annuli. International Journal of Ambient Energy. 2020; 43(1): 3410–3417. doi: 10.1080/01430750.2020.1831953
35. Inman RM. Experimental study of temperature distribution in laminar tube flow of a fluid with internal heat generation. Int J Heat Mass Transfer. 1962; 5(11): 1053–1058.
36. Oni MO, Jha BK, Abba JM, Adebayo OH. Influence of radially varying magnetic fields and heat sources/sinks on mhd free-convection flow within a vertical concentric annulus. Power Engineering and Engineering Thermophysics. 2024; 3(1): 27–44. doi: 10.56578/peet030103
37. Ferdousi SF, Alim MdA. Effects on two semi-circular wall heaters attached with a rectangular enclosure containing trapezoidal heated obstacle in presence of magnetohydrodynamics. International Journal of Research and Innovation in Social Science. 2024; Ⅷ(XI): 2479–2487. doi: 10.47772/ijriss.2024.8110192
38. Mishra SK, Chandra H, Arora A. Effects on Heat Transfer and Radial Temperature Profile of Non-Isoviscous Vibrational Flow with Varying Reynolds Number. Journal of Applied Fluid Mechanics. 2019; 12(1): 135–144. doi: 10.29252/jafm.75.253.28952
39. Sukariya VK, Anurag, Jakhar A, et al. Effect of Hall current generated by a radial magnetic field on transient natural convection between vertical annuli. The European Physical Journal Plus. 2024; 139(11). doi: 10.1140/epjp/s13360-024-05786-9
40. Ojemeri G, Hamza MM, Tambuwal BH, et al. Influence of Soret and Radial Magnetic Field on Natural Convection of a Chemically Reactive Fluid in an Upright Porous Annulus. UMYU Scientifica. 2023; 2(3): 108–120. doi: 10.56919/usci.2323.017

Appendix A

$$E_5 = \frac{1}{1-\lambda^{2\sqrt{S}}}, E_6 = -\frac{\lambda^{2\sqrt{S}}}{1-\lambda^{2\sqrt{S}}}$$

$$\boldsymbol{E_1} = \frac{-\boldsymbol{E_3}\left(\mathbf{1}-\boldsymbol{\lambda}^{-\boldsymbol{Ha}}\right) + \frac{\boldsymbol{E_5}}{(\mathbf{2}+\sqrt{\boldsymbol{S}})^{\mathbf{2}} - \boldsymbol{Ha}^{\mathbf{2}}}\left(\boldsymbol{\lambda}^{(\mathbf{2}+\sqrt{\boldsymbol{S}})} - \boldsymbol{\lambda}^{-\boldsymbol{Ha}}\right) + \frac{\boldsymbol{E_6}}{(\mathbf{2}-\sqrt{\boldsymbol{S}})^{\mathbf{2}} - \boldsymbol{Ha}^{\mathbf{2}}}\left(\boldsymbol{\lambda}^{(\mathbf{2}-\sqrt{\boldsymbol{S}})} - \boldsymbol{\lambda}^{-\boldsymbol{Ha}}\right)}{\boldsymbol{\lambda}^{\boldsymbol{Ha}} - \boldsymbol{\lambda}^{-\boldsymbol{Ha}}}$$

$$E_2 = -E_3 + \frac{E_5}{(2+\sqrt{S})^2 - Ha^2} + \frac{E_6}{(2-\sqrt{S})^2 - Ha^2} - E_1$$

$$E_3 = -\frac{1}{ln(\lambda)}[-\frac{1}{Ha}[E_1(\lambda^{Ha}-1) - E_2(\lambda^{-Ha}-1)] + E_9 + E_{10}]$$

$$E_4 = \frac{1}{Ha}(E_1 - E_2) + E_{11} + E_{12}, E_7 = -\frac{E_5}{(4+\sqrt{S})\left[(2+\sqrt{S})^2 - Ha^2\right]}\left[\lambda^{(4+\sqrt{S})} - 1\right]$$

$$E_8 = -\frac{E_6}{\left(4-\sqrt{S}\right)\left[(2-\sqrt{S})^2 - Ha^2\right]}\left[\lambda^{(4-\sqrt{S})} - 1\right], E_9 = \frac{E_5}{\left(2+\sqrt{S}\right)\left[(2+\sqrt{S})^2 - Ha^2\right]}\left(\lambda^{2+\sqrt{S}} - 1\right)$$

$$\mathrm{E}_{10} = \frac{\mathrm{E}_6}{\left(2-\sqrt{\mathrm{S}}\right)\left[(2-\sqrt{\mathrm{S}})^2 - \mathrm{Ha}^2\right]}\left(\lambda^{2-\sqrt{\mathrm{S}}} - 1\right), \mathrm{E}_{11} = -\frac{\mathrm{E}_5}{\left(2+\sqrt{\mathrm{S}}\right)\left[(2+\sqrt{\mathrm{S}})^2 - \mathrm{Ha}^2\right]}$$

$$E_{12} = -\frac{E_6}{\left(2-\sqrt{S}\right)\left[(2-\sqrt{S})^2 - Ha^2\right]}, E_{13} = -\frac{E_5}{\left[(2+\sqrt{S})^2 - Ha^2\right]}, E_{14} = -\frac{E_6}{\left[(2-\sqrt{S})^2 - Ha^2\right]}$$

$$E_{15} = -E_3\, ln(\lambda), E_{16} = \frac{E_{13}}{\left(2+\sqrt{S}\right)}\left(\lambda^{2+\sqrt{S}} - 1\right), E_{17} = \frac{E_{14}}{(2-\sqrt{S})}\left(\lambda^{2-\sqrt{S}} - 1\right)$$

Appendix B

Nomenclature

Table B1. Roman symbols.

Symbol	Description
a	Inner cylinder radius (m)
b	Outer cylinder radius (m)
g	Gravitational acceleration (m/s^2)
H_o'	Applied magnetic field (A/m)
$H_{z'}'$	Magnetic field induced in the z'-direction (A/m)
H	Dimensionless induced magnetic field in z-direction
C_P	Specific heat at constant pressure (J/(kg·K))
J_θ	Induced current density along h-direction (A/m^2)
Ha	Hartmann number (dimensionless)
r', θ', z'	Cylindrical coordinates (m)
R	Dimensionless radial distance
T'	Fluid Temperature (K)
θ	Dimensionless fluid temperature
T_a'	Temperature of the surroundings (K)
T_i'	Temperature of the inner cylinder at the surface (K)
U	Dimensionless velocity of the fluid along the axial direction
U'	Fluid velocity along the axial direction (m/s)
U_o	Characteristic fluid velocity (m/s)
Nu_1	Nusselt number at the inner cylinder (dimensionless)
Nu_λ	Outer cylinder Nusselt number (dimensionless)
Q_o	Rate of heat generation per unit volume (W/m^3)
S	Heat source/sink parameter (dimensionless)

Table B2. Greek symbols.

Symbol	Description
β	Thermal expansion coefficient (K^{-1})
k	Fluid thermal conductivity (W/(m·K))
μ_e	Magnetic permeability (H/m)
ν	Fluid kinematic viscosity (m^2/s)
η	Magnetic diffusivity (m^2/s)
ρ	Fluid Density (kg/m^3)
λ	Annular gap (dimensionless)
σ	Fluid Conductivity (s/m)
τ_1	Inner cylinder skin friction coefficient (dimensionless)
τ_λ	Outer cylinder skin friction coefficient (dimensionless)

Mechanical Engineering Advances 2025, 3(2), 2474.
https://doi.org/10.59400/mea2474

Article

Design method for intelligent robots applied to traditional CNC processing plants: An integrated system based on mechanical, circuit, and image recognition technologies

Yung-Hsiang Chen*, **Sheng-Yan Pan**

Department of Mechanical Engineering, National Pingtung University of Science and Technology, Pingtung 912301, Taiwan
*** Corresponding author:** Yung-Hsiang Chen, yhchen@mail.npust.edu.tw

CITATION

Chen YH, Pan SY. Design method for intelligent robots applied to traditional CNC processing plants: An integrated system based on mechanical, circuit, and image recognition technologies. Mechanical Engineering Advances. 2025; 3(2): 2474.
https://doi.org/10.59400/mea2474

ARTICLE INFO

Received: 30 December 2024
Accepted: 28 February 2025
Available online: 7 April 2025

COPYRIGHT

Copyright © 2025 by author(s). *Mechanical Engineering Advances* is published by Academic Publishing Pte. Ltd. This work is licensed under the Creative Commons Attribution (CC BY) license.
https://creativecommons.org/licenses/by/4.0/

Abstract: This study aims to design an automated production assistance device for small to medium-sized traditional CNC factories. The goal is to provide a cost-effective auxiliary production tool that integrates seamlessly into existing machining environments. The design encompasses mechanical, circuit, and software components. Mechanically, the device features a robotic arm equipped with a camera for object recognition and gripping, utilizing real-time image processing to enhance efficiency and stability. The circuit design employs embedded devices and microcontrollers to create a low-power, high-performance control system that manages motor drive, sensor data collection, and image recognition. On the software front, the system uses OpenCV and You Only Look Once (YOLO) for object detection and identification to tackle complex industrial scenarios. The design also considers economic feasibility, making it suitable for effective application in small and medium-sized enterprises. Through detailed theoretical analysis and multi-stage system simulations, the intelligent robot system has been thoroughly validated for overall stability and practicality. The final product is an intelligent self-propelled cart with capabilities, supporting efficient automated production and the intelligent upgrade of traditional manufacturing industries. Such a system is expected to significantly enhance production line efficiency in variable environments, reduce reliance on manual labor, and promote the intelligent transformation of traditional factories.

Keywords: mechanical design; circuit design; software design; YOLO; image recognition

1. Introduction

In the context of rapid industrial automation, continuous technological innovation has driven the deep integration of robotics, autonomous vehicles, and artificial intelligence (AI). This integration is pivotal in enhancing manufacturing efficiency, flexibility, and productivity. Traditional factories heavily rely on manual operations and fixed processes, leading to inefficiencies, lack of flexibility, and low precision, especially in complex production environments prone to human error [1–4].

According to market research data, the global market size of the CNC industry is expected to be approximately USD 100.7 billion in 2024 and is projected to grow at a compound annual growth rate (CAGR) of 7.8% until 2029. This growth trend indicates that with the continuous upgrading of global manufacturing and the advancement of Industry 4.0, the demand for industrial automation will keep expanding. To meet the increasing market demand, the application of CNC machines will continue to rise, further driving the rapid development of smart manufacturing and automation technologies.

Despite the potential for CNC machining plants to adopt automation equipment, the high costs and maintenance expenses remain prohibitive. Consequently, small to medium-sized enterprises (SMEs) struggle to afford these investments, posing significant challenges to their technological upgrades and automation processes. Additionally, the complexity of existing equipment and the lack of tailored solutions for SMEs hinder their ability to improve efficiency and reduce labor dependency. Therefore, this study proposes a design methodology based on mechanical, circuit, and image recognition techniques to create cost-effective and easy-to-maintain equipment.

Intelligent robots integrate multiple cutting-edge technologies, including robotic arms, autonomous vehicles, and image recognition systems, to complete complex tasks without human intervention. These systems utilize technological synergy to adapt to changing production requirements and execute tasks precisely. Moreover, these robots can collaborate with other automated equipment, moving the manufacturing environment closer to intelligent goals [5,6]. For example, robotic arms are designed to balance performance and safety, where human-friendly drive technology and high-precision calibration methods significantly enhance operational stability and accuracy [7,8]. For the needs of object detection and localization, deep learning provides advantages in real-time processing and small object recognition, offering strong support for intelligent robot applications [9–11].

This study proposes an intelligent robot system aimed at providing efficient, flexible, and sustainable solutions for small to medium-sized factories. The core design of this system is based on a six-degree-of-freedom robotic arm, paired with an autonomous vehicle for material transport, integrated with advanced image recognition technology for positioning and operations [12–14]. Such a design demonstrates superior adaptability in dynamic production environments, ensuring high operational accuracy and stability, thus achieving precise production control [15–17].

This research will delve into the mechanical design, circuit design, and software development of the intelligent robot, showcasing its application value and future development prospects in industrial environments. Through this study, we aim to provide practical references and technical support for the advancement of intelligent industrial development [18–20].

2. Intelligent robot design

The design of the intelligent robot integrates robotic arms, self-propelled vehicles, and image recognition technology to enhance the flexibility, efficiency, and intelligence of factory operations. The system can autonomously operate in complex environments and collaborate with other factory equipment to achieve a high level of integration between smart manufacturing and production lines.

2.1. Mechanism design

The system architecture of the intelligent robot is divided into three key components: a robotic arm, a mobile platform (self-propelled vehicle), and a visual recognition system. Each component plays a crucial role in the overall system, collaborating to achieve efficient and precise tasks.

2.1.1. The robotic arm design of the intelligent robot

The design of the robotic arm features a lightweight structure, with the main frame made of aluminum alloy 6061-T6, which offers high load-bearing capacity and rigidity. As shown in **Figure 1**, the structural design not only enhances stability but also ensures flexible operation under high loads. To improve control accuracy and power output, the mechanism incorporates a harmonic reducer (**Figure 2**) and a time-gauge pulley transmission system. The harmonic reducer, known for its high precision, small size, and high transmission efficiency, combines with the stable power transmission and seismic performance of the time-gauge pulley to ensure more accurate and stable overall mechanism operation. The design is based on a six-degree-of-freedom mechanism, enabling the robotic arm to have a wide operating range and high flexibility, capable of performing various precision operations according to actual needs. The arm's movement is driven by a precise servo motor, ensuring efficient and precise operation.

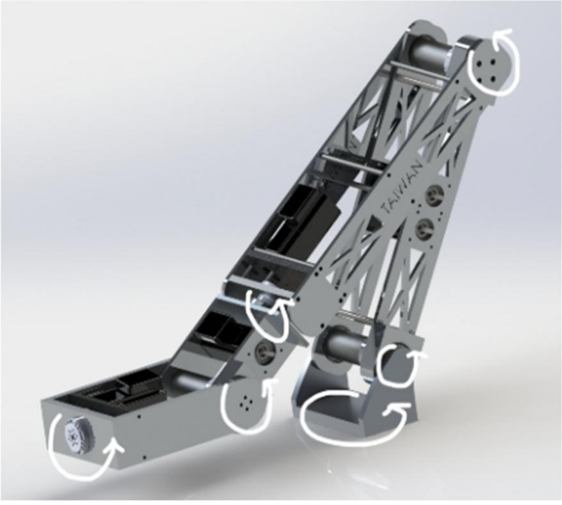

Figure 1. Six-axis robotic arm design schematic diagram.

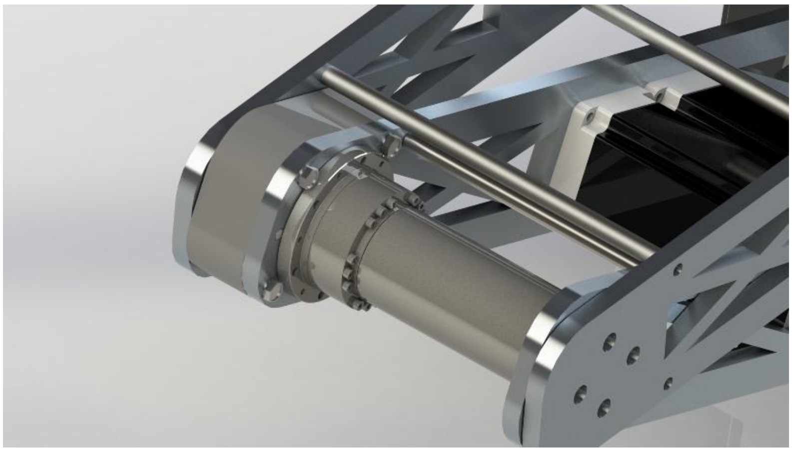

Figure 2. Schematic diagram of harmonic reducer.

The use of a harmonic reducer and timing belt transmission can obtain the following advantages at the same time:

- Effectively reduces shock and absorbs vibration, improving reliability.

- Power can be transmitted over a long distance, and at the same time, it can be decelerated by relying on harmonic reducers.
- High degree of freedom in structural design.
- High-precision transmission capability.

2.1.2. Design of self-propelled vehicles for intelligent robots

The design of the self-propelled vehicle mechanism in this study employs welding techniques to fabricate the structure, as shown in **Figure 3**. This approach aims to create a high-strength and integrated chassis. The application of welding technology ensures the chassis has superior structural integrity and durability. Even when the self-propelled vehicle carries various loads during operation, its structure remains stable, avoiding deformation or damage due to external forces or load changes. This chassis design not only enhances the rigidity and reliability of the overall mechanism but also effectively extends the service life of the self-propelled vehicle to meet the needs of diverse and complex environments.

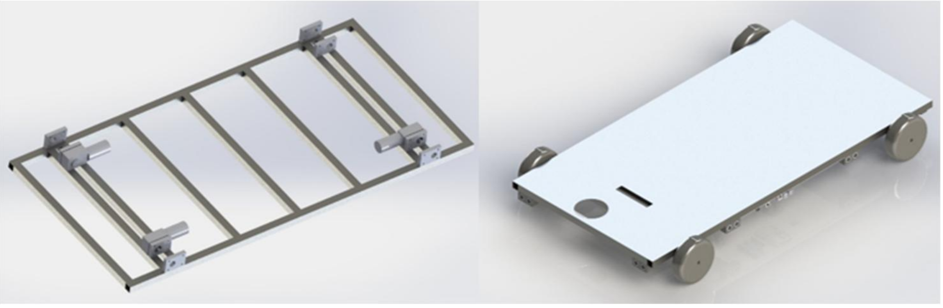

Figure 3. Self-propelled vehicle chassis structure diagram.

2.2. Circuit design of intelligent robot

In this study, multiple electronic components were utilized to form the overall system architecture, as shown in **Figure 4**. Given that image recognition applications are employed in both the robotic arm and the self-propelled vehicle mechanisms, two sets of Raspberry Pi are used to control the movement of the self-propelled vehicle and the robotic arm, respectively. These Raspberry Pi units can communicate with each other to achieve collaborative operation.

In the self-propelled vehicle mechanism, an Arduino acts as an intermediary, receiving data from ultrasonic sensors, radars, electronic compasses, and GPS. This data is packaged and transmitted to the Raspberry Pi for analysis, which then issues action commands back to the Arduino to drive motor movements. Once the movement command is executed and the destination is reached, communication is established between the Raspberry Pi of the self-propelled vehicle and the Raspberry Pi of the robotic arm. The next task is subsequently completed by the Raspberry Pi controlling the robotic arm, which is also equipped with a camera to detect the position of the workpiece, enabling precise movements.

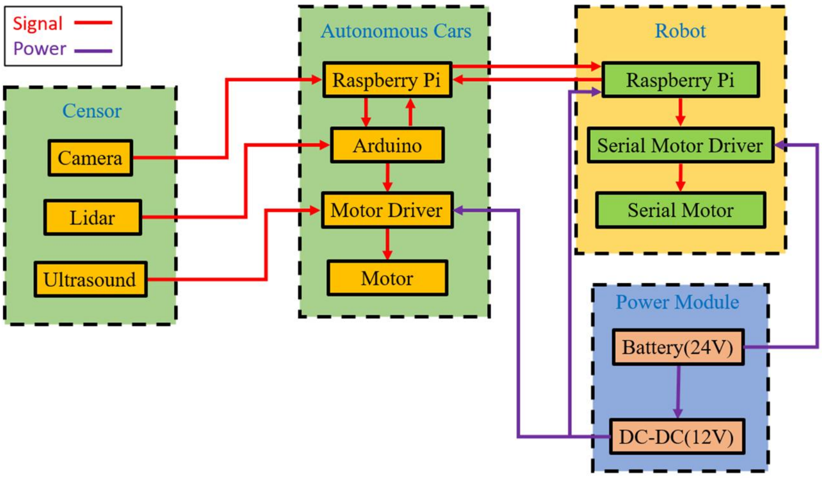

Figure 4. Overall system architecture of intelligent robots.

2.3. Software design of intelligent robot

The control system in this study primarily utilizes Raspberry Pi running Python as the core controller, responsible for coordinating the operations of the robotic arm and the self-propelled vehicle. The Raspberry Pi collects environmental data through sensors, conducts real-time path planning, and controls the motor to perform actions based on the path instructions. Additionally, it manages the servo motor to lift the robotic arm for picking up or placing down workpieces.

2.3.1. Control design

The entire system is illustrated in **Figure 5**, with a Raspberry Pi serving as the core controller, responsible for coordinating the operations of the robotic arm and the self-propelled vehicle. The Raspberry Pi collects environmental data through sensors, performs real-time calculations and path planning, and sends instructions to the servo motors and drive modules to execute operations. The workflow of the system is as follows: First, the self-propelled vehicle receives the destination information and begins navigation. After reaching the designated position, the robotic arm commences materials. Upon completing the task, both the self-propelled vehicle and the robotic arm return to their initial positions, ready to perform the next task.

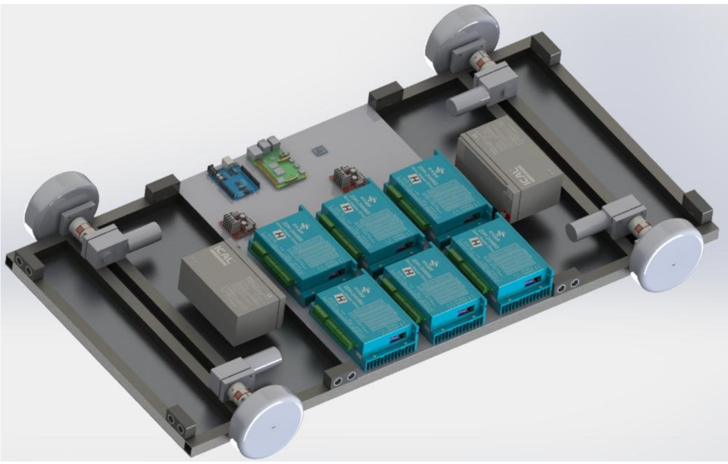

Figure 5. Intelligent robot control parts architecture diagram.

2.3.2. System operation process design

The system operation process of this study is divided into two parts: the system operation of the self-propelled vehicle and the robotic arm, and the interoperability is achieved through serial communication, as shown in **Figure 6**, and the overall process is as follows:

a) The operation process of the self-propelled vehicle:
  - Receive Navigation Destination: The self-propelled vehicle receives the navigation destination set by the user.
  - Path planning: Sensors (such as ultrasonic sensors, radars, electronic compasses, and GPS) are used to sense the environment, and the Raspberry Pi executes Python to set the walking path.
  - Perform the task: follow the planned path and receive sensor data to change direction and adjust speed
  - Arrive at the destination: Complete the task and notify the robot arm to perform the task.

b) The operation process of the robotic arm:
  - Task Receiving: Receive the task execution command sent by the Shumei faction and start executing the task.
  - Image inspection: The position of the workpiece is detected by the camera to ensure that it can be accurately positioned.
  - Grip and Place: Control the servo motor to operate the robotic arm to grip or lower the workpiece, and continuously use the camera to compensate for the position to achieve more accurate positioning in the process.
  - Complete the task: When the task is over, a command is sent to notify the self-propelled car Shumei faction to execute the next command.

c) Collaborative work:
  - The self-propelled vehicle and the robotic arm are synchronized through serial communication to ensure the continuity of navigation and tasks.
  - After executing a work, return to the initial position and wait for the next task order, which is distributed by the two Shumei factions.

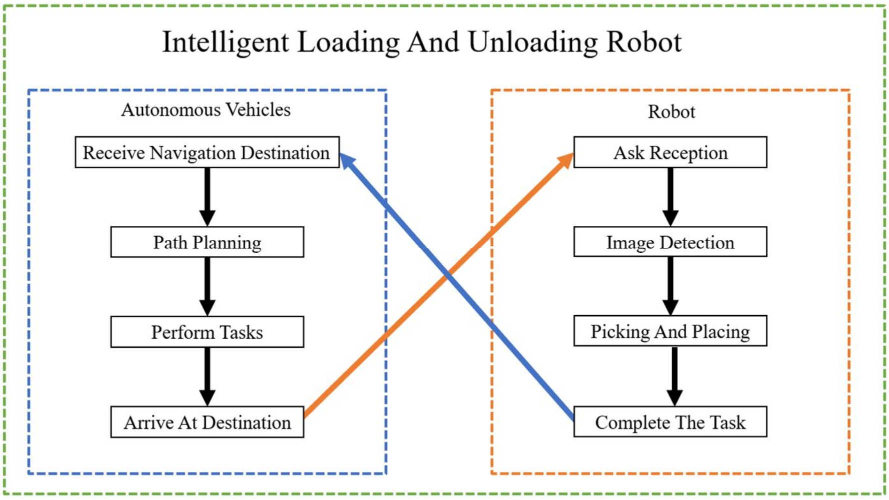

Figure 6. Flow chart of the operation of the intelligent robot.

2.3.3. Image recognition process

The image recognition system is a core function of the intelligent robot, primarily used to detect and identify the position and characteristics of workpieces. This ensures that the robotic arm can accurately perform operations. The system employs the YOLO (You Only Look Once) algorithm for real-time object detection and integrates OpenCV for image preprocessing and feature analysis. The entire image recognition process can be divided into the following stages, as illustrated in **Figure 7**:

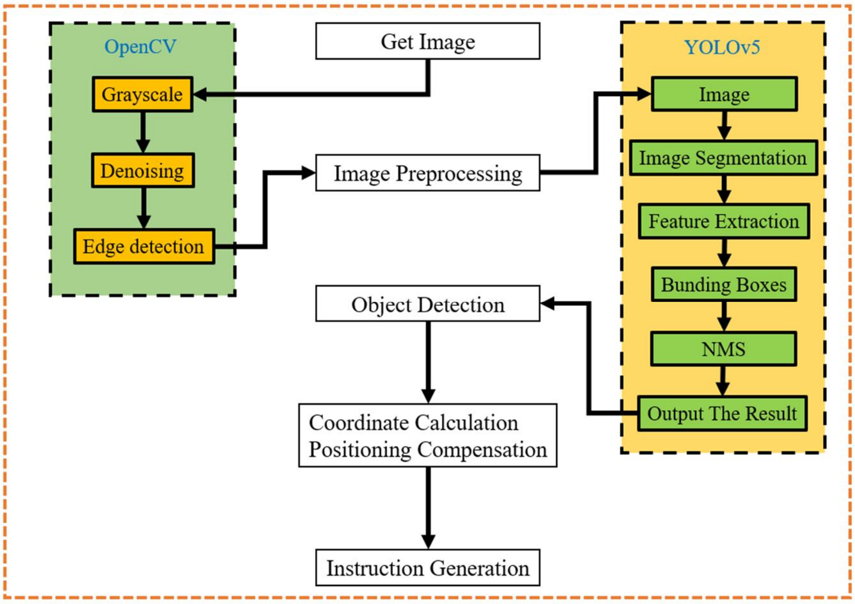

Figure 7. Image detection flow chart.

a) Image Acquisition:

Use a camera to capture images of the environment and transfer the data to the Raspberry Pi via USB or serial communication for processing. The camera is positioned in a carefully adjusted position to ensure that the field of view covers the area.

b) Image pre-processing:

Image pre-processing via OpenCV, including:

- Grayscale processing: Reduce the complexity of image data and improve processing efficiency.
- Denoising: Apply Gaussian blur or median filtering to reduce the impact of environmental interference on identification.
- Edge Detection: Enhance object contours with Canny edge detection to improve the accuracy of object detection.

c) Object detection: Input the preprocessed image data into the YOLO algorithm for object detection, run the following steps:

- Load the pretrained model (YOLOv5).
- Extract feature points in the image and generate candidate boxes.
- The final detection frame is screened by non-maximal suppression (NMS) to ensure that only the most relevant targets are labeled.

d) Coordinate Calculation and Positioning Compensation:

Based on the correction parameters of the camera, the image coordinates are converted to world coordinates to ensure that the robotic arm can be accurately positioned according to the detection results. A multi-point calibration method is used to eliminate the effects of lens distortion.

e) Command generation and run:

The Raspberry Pi generates control instructions based on the recognition results and transmits them to the servo motor and robotic arm controller through serial communication. The robotic arm completes the clamping or placing operation of the target object according to the instructions.

2.3.4. Object detection YOLO model training

In order to enable the intelligent robot to accurately identify workpieces, the YOLO (You Only Look Once) object detection algorithm was used in this study, and the model was trained and adjusted for industrial scenarios, as shown in **Figure 8**, and the specific process is as follows:

a) Data preparation
   - Dataset collection: Collect high-resolution images covering the features of the workpiece, including different viewing angles, lighting conditions and background environment, to improve the generalization ability of the model.
   - Data annotation: Use LabelImg to label images, including the position and category of the workpiece’s rectangular box.

b) Model settings
   - Select model version: This study chooses to use YOLOv5 as the core algorithm of object detection to train the model, which has the advantages of framework simplicity, which is easier to apply and develop, and the model can choose YOLOv5-L, YOLOv5-M, YOLOv5-S, etc., and the appropriate model size can be selected according to the development equipment.
   - Model configuration: training and test data, artifact category name, total artifact category.

c) Model training
   - Training Environment Settings: Use the Python environment to build the YOLO training framework.
   - Execute training: Set training parameters, including image size, batch size, number of training rounds, etc., and execute commands to start training.
   - Training Monitoring and Optimization: Monitor model loss, mAP, and other metrics in real time.

d) Model validation and testing
   - Validate the dataset: Validate model performance using a test dataset, checking metrics including: mAP, Precision, Recall.
   - Model Fine-tuning: Fine-tune the model based on the validation results, including optimizing the anchor point size or adjusting the input resolution to further improve detection accuracy.

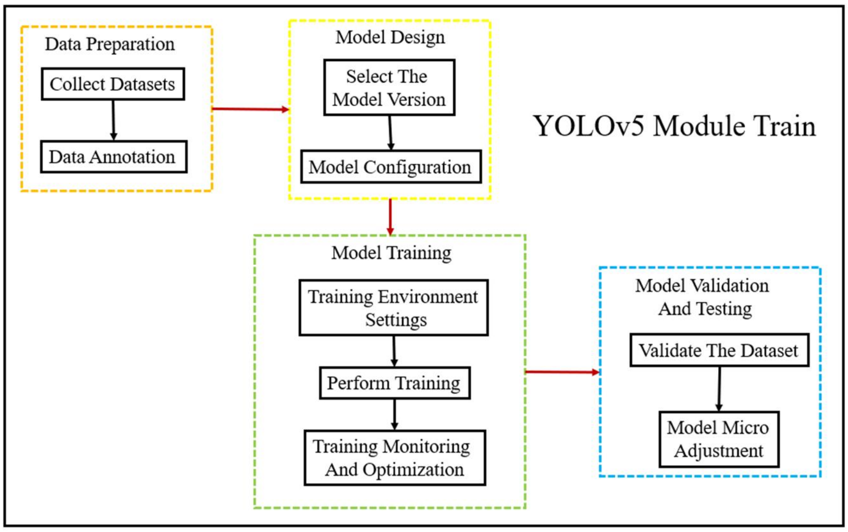

Figure 8. YOLOv5 model training.

3. Results

This study designed an intelligent robot system, illustrated in **Figure 9**. The system combines a self-propelled vehicle, a robotic arm, and advanced image recognition technology, aiming to assist traditional industries in transitioning towards industrial automation. The intelligent robot provides high mobility, allowing it to navigate various complex work environments, and it is equipped with a robotic arm capable of gripping items or performing other tasks, meeting diverse production line needs.

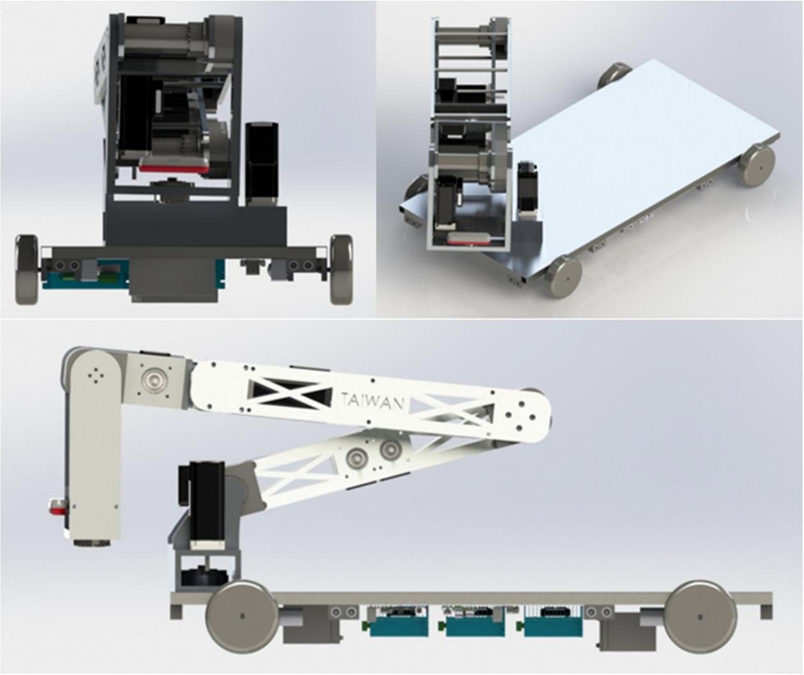

Figure 9. Intelligent robot design drawing.

Through rigorous theoretical analysis and experimental validation, the system demonstrated design reliability and practicality. Overall, the robot developed in this study is efficient and practical, capable of significantly improving productivity in small to medium-sized traditional industries and offering new possibilities for the future of intelligent manufacturing. Moreover, the system uses a Raspberry Pi as the controller, which is cost-effective compared to solutions from large enterprises. The design prioritizes commonly available components, reducing maintenance costs and further enhancing economic efficiency.

3.1. Expected performance of system functions

The intelligent robot has completed a number of technologies, and the expected results are shown in **Table 1**. In the operation, the system relies on a six-axis robotic arm with a camera to carry out real-time detection of the position of the workpiece and operations such as gripping and placement. This process ensures the stability and accuracy of the clamping process, reduces the risk of damage to the workpiece during operation, and improves the finishing efficiency of the production line. At the same time, the self-propelled vehicle system combines GPS, Lidar, ultrasonic and other sensors to collect environmental information, achieve autonomous navigation and be able to respond flexibly to the environment. In addition, in order to ensure the stability, continuity and cost of the system, the system uses two groups of Raspberry Pi to control the self-propelled vehicle and the robotic arm respectively, and through communication to achieve collaborative operation, through real-time transmission of task information, can complete complex processes collaboratively or interactively, shorten the production cycle and improve work efficiency.

Table 1. The expected effect of the intelligent robot.

Functional categories	Description of the function	Key technologies	What to expect
operations	Detection of position Complete gripping and placement	Six-axis robotic arm camera	Improve efficiency
Autonomous navigation Dynamic obstacle avoidance	Plan routes and avoid obstacles according to environmental routes	GPS, Lidar, Ultrasonic Sensors	Ensure transportation performance and safety in complex environments
Intelligent collaboration	Instant communication between the self-propelled vehicle and the robotic arm ensures the continuity of operations	Shumeipai embedded system and communication module	Improve the operation of the system.

The expected performance specifications of the intelligent robot in this study are shown in **Table 2**. In this study, the robotic arm has six degrees of freedom and the end of the arm is expected to lift a workpiece of about 5 kg, and the positioning accuracy is expected to reach ± 0.1 mm, and the camera can complete high-precision grasping work and other tasks, and in the conveying process, sensors are used to collect environmental data to navigate. The expected effect is that when the load reaches 45 kg, the workpiece can still be transported stably. The system uses Raspberry Pi to collaborate with UART, Wireless and other communication technologies to complete the goal of collaboration.

Table 2. Expected performance specifications of intelligent.

Project	Specification
Robotic arm degrees of freedom	6 DOF
robotic arm maximum payload	5 kg
precision	± 0.1 mm
Navigation	GPS, Lidar, Ultrasound
vehicle weight	30 kg
Carrying capacity	40 kg
Image recognition technology	YOLO (you Only Look Once)
Control system	Raspberry Pi
Methods of Communication	UART, Wireless
Energy supply	24 V 34 Ah Battery
Applicable environment	Temperature range 0 °C to 50 °C

3.2. Structural design analysis

Figure 10 shows the stress analysis diagram of the load knot in the self-propelled vehicle used in this study. We used a square tube of ASTM A36 material, welded it and applied a 50~80 kg force on the surface to carry out the simulation analysis. The color distribution ranged from blue to red, indicating the limit value of the descent strength.

The subsidence strength of ASTM A36 steel is about 250 Mpa. When the stress is greater than this value, the material may be permanently deformed or fail. According to the analysis diagram, the maximum stress is about 167 MPa, which is lower than the subsidence strength of ASTM A36 steel. This means that when a force of 45KG is applied, this structure is safe and has not yet reached the yield point of structural stress. To ensure safety, the maximum load should consider the factor of safety. If the safety factor is set at 1.5, the maximum allowable stress is as shown in Equation (1):

$$\sigma_{max} = \frac{subsidence\ strength}{Safety} = \frac{250MPa}{1.5} \approx 167MPa \tag{1}$$

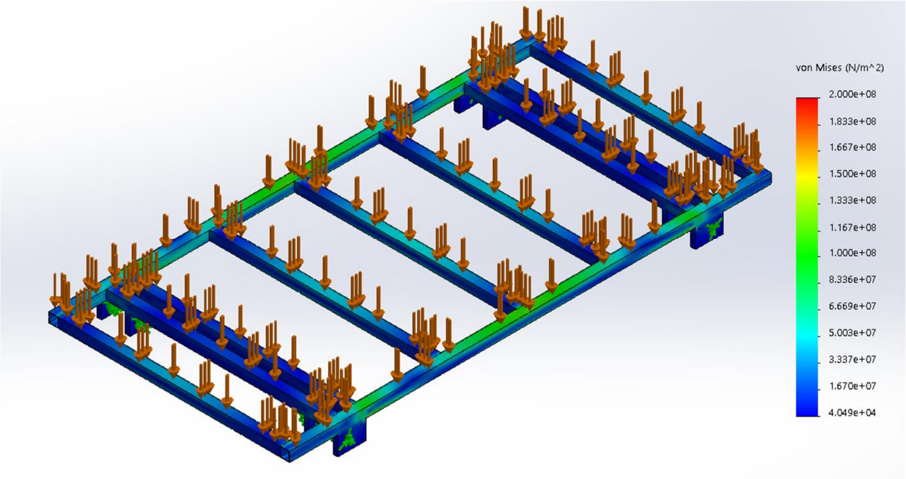

Figure 10. The static stress distribution diagram of 45 kg.

When a simulated force of 70 kg is applied, as shown in **Figure 11**, the maximum stress distribution value reaches approximately 183 MPa. This exceeds the allowable safety factor range and approaches the critical value of the material subsidence strength, indicating the potential for permanent deformation or failure under this load. To ensure the stability and reliability of the structure in long-term use, it is recommended that the load limit be set to less than 50 kg.

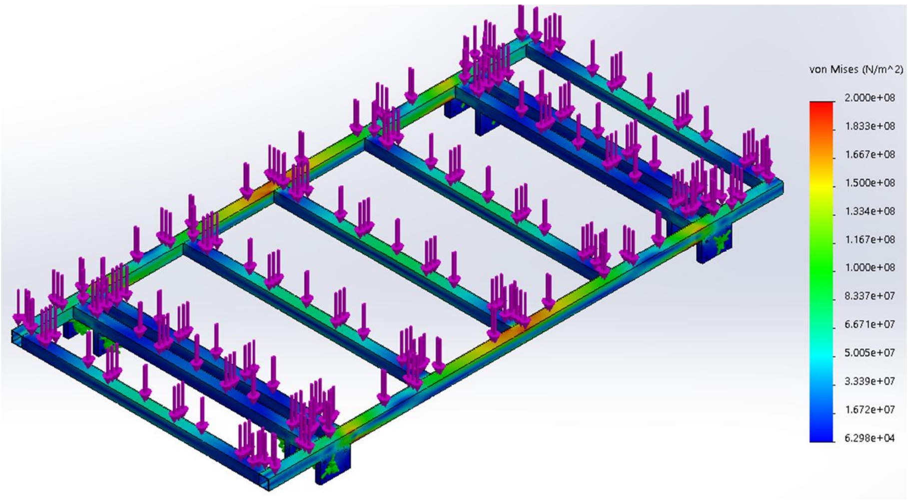

Figure 11. The application of 70 kg static stress analysis diagram.

When a force of about 80 kg is applied, as shown in **Figure 12**, the stress distribution has been clearly red area, which means that the force generated at this time has exceeded the limit that the material can bear, so it can be seen that the chassis structure of the self-propelled vehicle in this study can withstand the force of less than 80 kg when it exceeds the safety factor range.

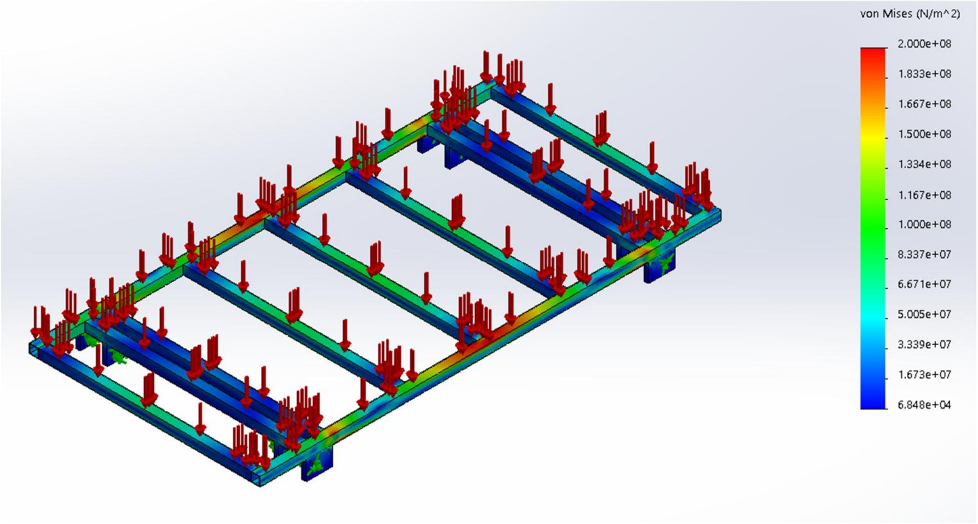

Figure 12. The application of 80 kg static stress analysis diagram.

3.3. Model training results

This study initially utilized approximately 50 images of workpieces in diverse environments for training. Post-optimization, the performance indicators are shown in **Table 3**. Through evaluation with the test set, the model swiftly determined the workpiece's location in the environment. Furthermore, the YOLOv5 model was deployed on a Raspberry Pi. Given the option to select model files, we chose YOLOv5-s. The model achieved real-time operational performance in an embedded system. After multiple rounds of testing, this study developed a target detection system for workpieces. This system assists intelligent robots in accomplishing automated tasks, thereby enhancing the manufacturing and production capabilities of traditional factories.

Table 3. Performance metrics for image recognition models.

Index	**Number**
mAP	94%
Precision	93%
Recall	91%
Inference frame	18 Fps

4. Conclusion

This study addresses the automation needs of small and medium-sized traditional manufacturing plants by proposing an intelligent robot tailored for industrial automation. The design integrates mechanical engineering, circuitry design, and software development. The robotic system consists of a six-degree-of-freedom robotic arm and a mobile platform to ensure high flexibility and stability. Additionally, the system incorporates cameras and YOLO (You Only Look Once) technology for accurate object recognition. The circuitry design, based on Raspberry Pi and Arduino control architecture, effectively integrates various sensors and communication modules, ensuring efficient collaborative operations. The software design leverages OpenCV and YOLO algorithms, enhancing image recognition accuracy and the ability to handle complex industrial scenarios.

Although a prototype of the intelligent robot was not physically constructed, the theoretical design verified the system's feasibility and potential benefits. The proposed system can shorten production cycles, improve operational precision, and adapt to diverse industrial environments. Future research should focus on actual prototype development and testing to further validate the system's stability and performance. Additionally, optimizing computational efficiency and reliability can further enhance the system's capability to handle complex industrial scenarios.

Author contributions: Conceptualization, YHC and SYP; methodology, YHC and SYP; software, SYP; validation, YHC and SYP; formal analysis, YHC and SYP; investigation, YHC and SYP; resources, YHC; data curation, YHC and SYP; writing—original draft preparation, YHC and SYP; writing—review and editing, YHC; visualization, YHC and SYP; supervision, YHC; project administration, YHC and SYP; funding acquisition, YHC. All authors have read and agreed to the published version of the manuscript.

Conflict of interest: The authors declare no conflict of interest.

References

1. Mabkhot MM, Al-Ahmari AM, Salah B, et al. Requirements of the Smart Factory System: A Survey and Perspective. Machines. 2018; 6(2): 23. doi: 10.3390/machines6020023
2. Kalsoom T, Ramzan N, Ahmed S, et al. Advances in Sensor Technologies in the Era of Smart Factory and Industry 4.0. Sensors. 2020; 20(23): 6783. doi: 10.3390/s20236783
3. Zinn M, Roth B, Khatib O, et al. A New Actuation Approach for Human Friendly Robot Design. The International Journal of Robotics Research. 2004; 23(4-5): 379-398. doi: 10.1177/0278364904042193
4. Zhang Y, Guo Z, Wu J, et al. Real-Time Vehicle Detection Based on Improved YOLO v5. Sustainability. 2022; 14(19): 12274. doi: 10.3390/su141912274
5. Mahdi E, Eltai E, Alabtah FG, et al. Mechanical Characterization of AA 6061-T6 MIG Welded Aluminum Alloys Using a Robotic Arm. Key Engineering Materials. 2022; 913: 271-278. doi: 10.4028/p-rhrr3n
6. Garzón Quiroz MQ. Inductive Machine Learning with Image Processing for Objects Detection of a Robotic Arm with Raspberry PI. In Technology Trends; 2019. doi: 10.1007/978-3-030-05532-5_45
7. Zhao Y, Liu X, Cao J, et al. A calibration and compensation method for an industrial robot with high accuracy harmonic reducers. Science China Technological Sciences. 2024; 67(3): 725-739. doi: 10.1007/s11431-023-2526-2
8. Cheng HT, Sun Z, Zhang P. Real-Time Imitative Robotic Arm Control for Home Robot Applications. In: Proceedings of the IEEE International Conference on Robotics and Automation; 2011.
9. Lu L, Liu B, Mao E, et al. Design and Optimization of High Ground Clearance Self-Propelled Sprayer Chassis Frame. Agriculture. 2023; 13(2): 233. doi: 10.3390/agriculture13020233
10. Srivastava S. Raspberry Pi Controlled Robotic Arm. International Journal of Research. 2015.
11. Kadir WMHW, Samin RE, Ibrahim BSK. Internet Controlled Robotic Arm. Procedia Engineering. 2012; 41: 1065-1071. doi: 10.1016/j.proeng.2012.07.284
12. Calvo I, Gil-García J, Recio I, et al. Building IoT Applications with Raspberry Pi and Low Power IQRF Communication Modules. Electronics. 2016; 5(3): 54. doi: 10.3390/electronics5030054
13. Viswanatha V, Chandana RK, & Ramachandra AC. Real-Time Object Detection System with YOLO and CNN Models: A Review. arXiv preprint arXiv:2208.00773; 2022.
14. Hu H, Yu L, Wo Tsui P, et al. Internet-based robotic systems for teleoperation. Assembly Automation. 2001; 21(2): 143-152. doi: 10.1108/01445150110388513
15. Somarathna RN. Path Planning and Obstacle Avoidance Scheme for Autonomous Robots using Raspberry Pi. arXiv preprint arXiv:2012.10863; 2020.
16. Redmon J, Divvala S, Girshick R, et al. You Only Look Once: Unified, Real-Time Object Detection. In: Proceedings of the 2016 IEEE Conference on Computer Vision and Pattern Recognition (CVPR); 2016.
17. Wang Z, Li C, Xu H, & Zhu X. Mamba YOLO: SSMs-Based YOLO for Object Detection. arXiv preprint arXiv:2406.05835; 2024.
18. Terven J, Córdova-Esparza DM, Romero-González JA. A Comprehensive Review of YOLO Architectures in Computer Vision: From YOLOv1 to YOLOv8 and YOLO-NAS. Machine Learning and Knowledge Extraction. 2023; 5(4): 1680-1716. doi: 10.3390/make5040083
19. Zhong Y, Wang J, Peng J, et al. Anchor Box Optimization for Object Detection. 2020 IEEE Winter Conference on Applications of Computer Vision (WACV). Published online March 2020: 1275-1283. doi: 10.1109/wacv45572.2020.9093498
20. Deng C, Wang M, Liu L, Liu Y. Extended feature pyramid network for small object detection. arXiv preprint arXiv:2004.00950; 2020.

Mechanical Engineering Advances 2025, 3(2), 2486.
https://doi.org/10.59400/mea2486

Article

The SG6043 airfoil optimization for low Reynolds number applications in wind turbines

Hossein Seifi Davari[1], Mohammad Yaghoub Abdollahzadeh Jamalabadi[1,*], Mohsen Seify Davari[2]

[1] Ocean Engineering Department, Chabahar Maritime University, Chabahar 99717, Iran
[2] Germi Department, Islamic Azad University, Germi 56911, Iran
*** Corresponding author:** Mohammad Yaghoub Abdollahzadeh Jamalabadi, my.abdollahzadeh@cmu.ac.ir, muhammad_yaghoob@yahoo.com

CITATION

Davari HS, Jamalabadi MYA, Davari MS. The SG6043 airfoil optimization for low Reynolds number applications in wind turbines. Mechanical Engineering Advances. 2025; 3(2): 2486. https://doi.org/10.59400/mea2486

ARTICLE INFO

Received: 31 December 2024
Accepted: 7 March 2025
Available online: 8 April 2025

COPYRIGHT

Copyright © 2025 by author(s). *Mechanical Engineering Advances* is published by Academic Publishing Pte. Ltd. This work is licensed under the Creative Commons Attribution (CC BY) license. https://creativecommons.org/licenses/by/4.0/

Abstract: This study focuses on optimizing the SG6043 airfoil for small wind turbines (SWTs) operating at low Reynolds numbers (Re = 100,000 to 600,000). Using XFOIL software, 71 airfoils were analyzed, and the SG6043 airfoil demonstrated the highest lift-to-drag ratio (C_L/C_D). Three modified airfoils were designed by varying the thickness-to-camber ratio (t/c) between 0.5 and 1.5. The SG6043 modified 1 airfoil achieved a maximum C_L/C_D of 184.85 at Re = 600,000, outperforming other airfoils. These findings provide valuable insights for designing more efficient SWTs for low wind speed applications. At first, 71 airfoils, including some symmetrical National Advisory Committee for Aeronautics (NACA) 4-digit, NACA 5-digit, Eppler series, Selig series, and other airfoils with higher aerodynamic performance at Reynolds numbers (Re) of 100,000 to 600,000 (the operation range for small wind turbines, SWTs), were chosen and analyzed in XFOIL software to determine their lift-to-drag ratio (C_L/C_D). The results showed that the SG6043 airfoil had the highest maximum C_L/C_D when compared to the other airfoils. To investigate and enhance the shape modification of the airfoil utilizing variations in thickness-to-camber ratio (t/c) and to determine the ideal t/c at Re of 100,000 to 600,000, the SG6043 airfoil was used. Based on the findings, 0.5 to 1.5 was the optimum t/c at Re of 100,000 to 600,000 for the development of the SG6043 airfoil, which had the maximum C_L/C_D. Then, three airfoils with varying thicknesses and cambers were designed and analyzed at the mentioned Re, with the optimal t/c being between 0.5 and 1.5. The findings indicated that when the Re increased, the SG6043 modified airfoil's aerodynamic efficiency enhanced. SG6043 modified 1 airfoil presented the greatest C_L/C_D of 184.85 at a Re of 600,000. For the SG6043 modified 2 airfoil, the maximum stall angle (AoA_{stall}) of 13° was demonstrated for Re of 300,000 to 600,000. Maximum C_L/C_D values for SG6043 modified 1, SG6043 modified 3, and SG6043 modified 2 were 184.85, 182.36, and 177.25, respectively. SG6043 modified 2, SG6043 modified 1, and SG6043 modified 3 had peak lift coefficients (C_L) of 1.798, 1.79, and 1.788, respectively. SG6043 modified airfoils performed well in the drag bucket when initial lift increases were accompanied by either steady or decreasing drag.

Keywords: modified airfoil; Reynolds numbers; aerodynamic; lift-to-drag; optimization; XFOIL software

1. Introduction

Small wind turbines (SWTs) are increasingly used for decentralized power generation, particularly in remote areas with low wind speeds. However, SWTs operate at low Reynolds numbers (Re), which poses challenges for aerodynamic efficiency. Most airfoil designs are optimized for large wind turbines operating at higher Re, making them unsuitable for SWTs. This study aims to optimize the SG6043 airfoil for low Re applications by varying the thickness-to-camber ratio (t/c) to improve aerodynamic performance. The results provide a foundation for designing more efficient SWTs for low wind speed conditions. A device that transforms wind power into electrical energy is a wind turbine (WT). Depending on the demands and purposes, WTs can be put in oceans and on beaches to generate power for residential homes [1]. SWTs operate at low Re due to their small size and position. Airfoils are crucial to the efficacy of WTs, and for greater efficiency, airfoils must be employed. It has also been demonstrated that SWTs function at Re below 500,000 and that lower wind speeds also function within this range. WT efficiency will decrease if low-aerodynamic-efficiency airfoils are employed [2]. As well as, study results have demonstrated that airfoils made for giant wind turbines are inappropriate for SWTs. WTs must operate well to have high aerodynamic efficiency since it depends on the C_L, drag coefficient (C_D), C_L/C_D, drag bucket, and AoA_{stall} [3]. A number of studies have been investigated recently to improve the effectiveness of VAWTs using a variety of airfoils and methods, as follows:

Seifi et al. [4] used the XFOIL software to conduct studies on several NACA and Selig airfoil types at low Re. Their results demonstrated that the NACA0015 airfoil surpassed other airfoils regarding maximum C_L/C_D. The NACA0015 airfoil's shape, camber, and thickness were then modified, and a novel airfoil was developed and compared to the original airfoil. Their research showed that for the NACA0015 modified airfoil at Re of 35780 and 53670, the maximum C_L/C_D increased by 34.01% and 17.94%, respectively. Giguere et al. [5] proved that thinner airfoils were more efficient than thicker airfoils, and as the Re increased, the C_L/C_D of airfoils increased.

Using the Class Deformation Method (CST) and the Parametric Cross Section Parameterization Method (PARSEC), Akram et al. [6] were able to raise the C_L and C_L/C_D by 11.8% and 9.6%, respectively. Martel et al. [7] used a multi-objective Non-Dominated Sorting Genetic Algorithm (SGA) to optimize the airfoil of a UAV in their research. Then, the optimization algorithm was combined with an updated CST parameterization to enhance aerodynamic efficiency by increasing C_L/C_D. Their results showed an enhancement in aerodynamic efficiency of up to 65.3% in C_L/C_D at an AoA of 8° compared to the base airfoil.

Wu et al. [8] studied the standard aerodynamic shape optimization with the proposed POD-based CST airfoil-dependent process, and their findings showed that the developed parametric method was able to closely correspond to the initially high-dimensional CST method's capacity to include the potential airfoils with significantly fewer parameters, which was capable of resolving the conflict between the high-dimensional design parameters and an increase in optimization challenges.

The optimum airfoil for VAWTs at low tip speed ratios (TSR), when dynamic stall existed, was investigated by Tirandaz et al. [9]. To determine the overall design space, their study used an integrated evaluation of three shape-defining parameters, notably the airfoil's greatest thickness and its location, in addition to the leading-edge radius. Their findings demonstrated an entirely related effect between the three shape-defining parameters on the WT power and thrust coefficients.

The Initial Dolphin Airfoil, the Smooth Transition Dolphin Airfoil, and the Deflected Dolphin Airfoil were three different novel airfoils that were developed by Huang et al. [10] after studying the motion behavior of dolphins. After that, CFD simulations were used to compare the aerodynamic efficiency of these three novel airfoils with the NACA0018 profile. Their findings demonstrated that, in comparison to the NACA0018 profile, the aerodynamic capabilities of all three kinds of dolphin-head-shaped airfoils were considerably dissimilar due to variations in the curvature and leading edge radius. Osei et al. [11] were able to enhance the maximum C_L/C_D of the EYO7-8, EYO8-8, and EYO9-8 airfoils by 134, 131, and 127, respectively, by introducing three airfoils by altering the shape of the SG6043 airfoil with XFOIL software. Additionally, they revealed in the follow-up research that the aerodynamic efficiency of the airfoils under study improved as the Re rose [12].

Hu et al. [13] utilized the free-form deformation method to modify the airfoil shape using control points and sensitivity analysis to condense the size of the control variables. Since altering the geometry of the airfoil was able to offer both stability and the highest C_L/C_D, it was similar to doing single-objective optimization while under a constraint. Their findings demonstrated that static stability height and C_L/C_D were sensitive to abrupt changes around the leading edge, one-quarter chord point, and trailing edge. The deformed ideal airfoil with an S-shape camber line decreased the C_L/C_D to achieve sufficient static stability.

Santos et al. [14] investigated the advantages of the Bézier-GAN as an airfoil parameterization approach for H-Darrieus turbines in an effort to eliminate these shortcomings. They employed sensitivity evaluation, metamodeling, and optimization techniques in addition to computational fluid dynamics (CFD) models. Their findings demonstrated that the Bézier-GAN integrated well with the framework under investigation and significantly reduced the study's overall cost of computation. Shape optimization is a significant phase in aerodynamics, yet it is computationally costly to use CFD simulation programs in the optimization procedure by Achour et al. [15].

As well as, to enhance convergence, Lim et al. [16] investigated multi-objective aerodynamic optimization problems using a hybrid evolutionary-adaptive directional localization method. Their findings revealed that the adaptive directional search process significantly improves convergence for issues where the directional search was effective and minimizes computational spending for cases where the directional search did not produce competitive findings.

Findings by Guo et al. [17] showed that an improved shuttle-shaped airfoil was able to further efficiently reduce the aerodynamic C_D and at the same time enhance the prototype blade's performance in tests when compared to elliptical airfoils. The aim of Boudis et al.'s [18] optimization process was to enhance the WT output power, and the aim was to pick the S809 airfoil C_L/C_D with three Re of 3×10^5, 4.8×10^5, and 10^6 at $AoAs$ between 0° to 20°. Their finding showed that (i) the C_L/C_D of the optimized airfoils was noticeably enhanced compared to the original S809 airfoil; (ii) this enhancement was sensitive to the Re; and (iii) the C_L/C_D was moreover enhanced for AoA values.

Particle swarm optimization was used by Echavarria et al. [19] along with XFOIL software and the free and open-source CFD OpenFOAM to optimize the airfoil form as parameterized by the NACA 4-digit equations. Then an analysis and comparison of the XFOIL software and CFD simulation followed. In addition to having an effect on the best feasible aerodynamic effectiveness, their findings indicated a linear link between the desired C_L and the highest possible camber of the ideal airfoil. Rangriz et al. [20] used the enhanced geometric parameter method, which was a state-of-the-art airfoil design methodology, along with the non-dominated SGA for the optimization of airfoils for WT utilization. Then, Pareto-optimal fronts and corresponding optimal airfoil profiles at various peak thickness ratios were acquired. Their results showed that the optimized airfoils were designed in a shape reminiscent of flapped airfoils, which indicated a multi-element airfoil design.

Turbine blade optimization is crucial for several reasons, as it directly impacts the performance, efficiency, durability, and cost-effectiveness of turbines used in various industries, such as aerospace, power generation, and marine propulsion. Here are the key reasons why turbine blade optimization is important:

1) Improved efficiency

Turbine blades are critical components in converting fluid or gas energy into mechanical energy. Optimizing their shape, material, and design enhances aerodynamic efficiency, reducing energy losses and improving overall turbine performance.

Better efficiency translates to higher power output for the same input energy, which is particularly important in power plants and aircraft engines.

2) Reduced fuel consumption

In gas turbines (e.g., jet engines or power plants), optimized blades reduce fuel consumption by improving combustion efficiency and minimizing energy losses.

Lower fuel consumption reduces operational costs and environmental impact, making turbines more sustainable.

3) Enhanced durability and reliability

Turbine blades operate under extreme conditions, including high temperatures, pressures, and mechanical stresses. Optimization ensures they can withstand these conditions without failure.

Improved durability reduces the risk of blade fatigue, cracking, or erosion, leading to longer operational lifespans and fewer maintenance requirements.

4) Cost savings

Optimized blades reduce manufacturing and maintenance costs by minimizing material waste and extending the lifespan of components.

Efficient turbines also lower operational costs by reducing fuel consumption and downtime.

5) Environmental impact

Optimized turbine blades contribute to lower emissions by improving combustion efficiency and reducing fuel consumption.

This is particularly important in industries like aviation and power generation, where reducing carbon footprints is a priority.

6) Higher performance in extreme conditions

Turbine blades in jet engines or power plants must perform reliably at high temperatures and rotational speeds. Optimization ensures they maintain performance under these conditions.

Advanced cooling techniques and materials can be incorporated into optimized designs to handle extreme thermal stresses.

7) Weight reduction

In aerospace applications, reducing the weight of turbine blades without compromising strength or performance is critical. Lighter blades improve fuel efficiency and aircraft performance.

Optimization techniques, such as topology optimization, help achieve the ideal balance between weight and strength.

8) Noise reduction

Optimized blade designs can reduce noise generated by turbines, which is particularly important in aviation and wind turbines located near residential areas.

Improved aerodynamics and blade shapes minimize turbulence and noise emissions.

9) Adaptability to advanced technologies

Optimization allows for the integration of advanced materials (e.g., composites, single-crystal alloys) and manufacturing techniques (e.g., additive manufacturing) to create blades with superior performance characteristics.

It also enables the use of computational fluid dynamics (CFD) and finite element analysis (FEA) to simulate and refine designs before physical prototyping.

10) Competitive advantage

Companies that invest in turbine blade optimization gain a competitive edge by offering more efficient, reliable, and cost-effective products.

In industries like aerospace and energy, even small improvements in turbine performance can lead to significant market advantages.

In conclusion, turbine blade optimization is essential for maximizing efficiency, reducing costs, improving durability, and minimizing environmental impact. It enables turbines to operate more effectively under demanding conditions, making it a critical focus area for engineers and researchers in the field of turbomachinery.

As already mentioned, SWTs work at low Re, and several investigations have been carried out in this Re. However, the appropriate *t*/*c* of airfoils in the Re range of 100,000 to 600,000, where airfoils have higher aerodynamic efficiency, has not been researched and ignored. Hence, it was chosen to investigate present research. The objective of the current study is to use the airfoil's *t*/*c* to improve the aerodynamic performance of the airfoil at Re between 100,000 and 600,000. At first, 71 symmetrical NACA 4-digit, NACA 4-digit, NACA 5-digit, Eppler series, Selig series, and other airfoils with greater aerodynamic performance at Re of 100,000 to 600,000 were studied for the current purpose using the XFOIL software. The next step was to develop three new airfoils with the ideal *t*/*c*. Finally, the modified airfoils in the Re above were evaluated in comparison to the SG6043 airfoil and the newly developed airfoils of the EYO-Series airfoils.

In the present study, the aerodynamic efficiency characteristics of the SG6043 modified (SG6043 modified 1, SG6043 modified 2, and SG6043 modified 3) airfoils were investigated at a scope of Re between 10^5 to 6×10^5, in order to identify their improved aerodynamic productivity features within the range of Re and to determine their aerodynamic efficiency features across the spectrum. The results of this study serve as a starting point for the creation of other low Re airfoils and illustrate important aerodynamic features of the SG6043 modified airfoils. The following section describes the procedures used to carry out this study.

2. Methodology

2.1. Selection and investigation of airfoils

Seventy-one airfoils, including NACA 4-digit, NACA 5-digit, Eppler, and Selig series, were selected for analysis. These airfoils were chosen based on their performance at low Re, which is typical for SWTs. The SG6043 airfoil was identified as the most efficient and was selected for further optimization. A gradient-based form optimization approach is developed in the current study to enhance WT blades. The 2D potential airflow solver with viscous effects, XFOIL software, was utilized with the blade element momentum (BEM) approach. The goal function of the gradient-based optimization procedure was the power output of the WT, which was calculated by the BEM analysis. A number of researchers utilized XFOIL software to develop and design airfoils, and it was demonstrated that it was in good agreement with the experimental results [21–25].

Firstly, 71 commonly used airfoils that have been tested in recent studies were chosen and analyzed in XFOIL software to determine their C_L/C_D at Re of 100,000 to 600,000. A summary of the airfoil selection procedure is shown in **Figure 1**, followed by an analysis using the XFOIL software. The selected airfoils were from symmetrical NACA 4-digit (NACA0010, NACA0012, NACA0015, NACA0018, NACA0020, NACA0021, NACA0022, NACA0025, and NACA0030), NACA 4-digit (NACA2415, NACA2421, NACA3530, NACA4412, NACA4415, NACA4418, NACA5513, NACA6712, and NACA8412), NACA 5-digit (NACA23012, NACA23015, NACA23018, NACA23024, NACA24012, NACA24015, NACA24020, NACA63018, and NACA63415), Selig airfoils (S809, S814, S818, S821, S822, S823, S825, S828, S85, S1046, S1223, S2027, S4083, S5010, S6063, S7012, S8036, S8052, SA7035, SA7038, SD2030, SD6060, SD7003, SD7032, SD7037, SD7062, SD7080, SG6040, SG6041, SG6042, SG6043, SG6050, and SG6051), Eppler airfoils (E231, E374, E387, E423, and ESA40), and BW-3, FX63-137, FX74-Cl5-140, PSU94-097, RG15, and USNPS4.

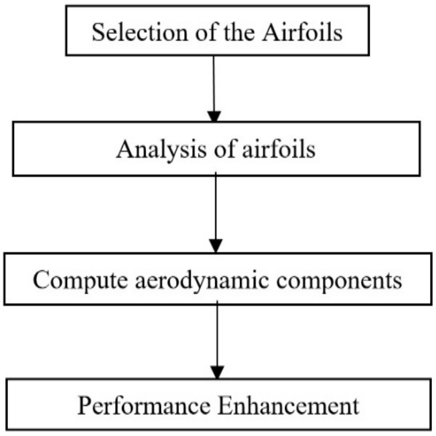

Figure 1. Abstract of XFOIL software for airfoils selection.

2.2. Comparison of the C_L/C_D of airfoils at Rey of 100,000 to 600,000

The aerodynamic performance of the selected airfoils was analyzed using XFOIL software, which is widely used for low Re airfoil analysis due to its accuracy and efficiency. The lift-to-drag ratio (C_L/C_D) was calculated for each airfoil at Re ranging from 100,000 to 600,000. **Figure 2** compares the maximum C_L/C_D for some different airfoils at Re between 100,000 and 600,000. The symmetrical NACA 4-digit airfoils are presented in **Figure 2a**. The greatest maximum C_L/C_D for the NACA0015 airfoil at Re of 100,000 was 37.32, whereas the lowest maximum C_L/C_D for the NACA0030 airfoil was 12.89. For the airfoils NACA0018, NACA0012, NACA0020, NACA0021, NACA0010, NACA0022, and NACA0025, the maximum C_L/C_D were, respectively, 37.30, 36.6, 36.58, 36.21, 35.71, 35.69, and 32.86. At a Re of 200,000, the NACA0018 and NACA0030 airfoils achieved the highest and lowest maximum C_L/C_D , respectively, at 50.17 and 29.53. NACA0015, NACA0020, NACA0021, NACA0012, NACA0022, NACA0010, and NACA0025 airfoils all had maximum C_L/C_D , respectively, of 49.62, 48.51, 47.63, 47.3, 46.15, 44.81, and 40.09. The highest and lowest maximum C_L/C_D were measured at Re of 300,000, NACA0018, and NACA0030, respectively, and they were 57.21 and 32.05. The corresponding airfoils for the NACA0015, NACA0020, NACA0012, NACA0021, NACA0022, NACA0010, and NACA0025 were 56.83, 54.9, 53.56, 52.43, 50.8, 49.77, and 43.

The highest and lowest maximum C_L/C_D for NACA0015 and NACA0030 airfoils were 62.56 and 35.02, respectively, at a Re of 400,000. The maximum C_L/C_D for the airfoils NACA0018, NACA0020, NACA0012, NACA0021, NACA0022, NACA0010, and NACA0025 were 61.87, 58.9, 57.82, 56.28, 54.67, 53.14, and 45.66, respectively. The highest and lowest C_L/C_D for the NACA0015 and NACA0030 airfoils were 66.44 and 37.21 at a Re of 500,000, respectively. The NACA0018, NACA0020, NACA0021, NACA0012, NACA0022, NACA0010, and NACA0025 airfoils' greatest and lowest maximum C_L/C_D were measured at 66.44, 65.83, 61.89, 61.31, 58.31, 56.39, and 50.16, respectively.

Finally, at the Re of 600,000, the highest and lowest maximum C_L/C_D for the NACA0015 and NACA0030 airfoils were 69.60 and 40.35, respectively. The NACA0018, NACA0020, NACA0012, NACA0021, NACA0022, NACA0010, and NACA0025 airfoils' greatest and lowest maximum C_L/C_D were determined at 68.60, 66.70, 65, 63.70, 61.12, 59.8, and 53.3, respectively. Hence, for the NACA0015 airfoil, the greatest maximum C_L/C_D was recorded at Re of 100,000, 400,000, 500,000, and 600,000, and for the NACA0018 airfoil, the greatest maximum C_L/C_D was recorded at Re of 200,000 and 300,000. Also, the NACA0030 airfoil achieved the lowest maximum C_L/C_D in the range Re of 100,000 to 600,000.

The 4-digit NACA airfoils are depicted in **Figure 2b**. The greatest maximum C_L/C_D for the NACA5513 airfoil at Re of 100,000 was 55.21, while the lowest maximum C_L/C_D for the NACA3530 airfoil was 3.11. NACA4412, NACA6712, NACA4412, NACA2415, NACA8412, NACA2421, and NACA4418 airfoils, in that order, with maximum C_L/C_D of 55.45, 52.81, 46.73, 46.55, 41.52, 36.93, and 35.77. At a Re of 200,000, the NACA5513 and NACA3530 airfoils recorded the highest and lowest maximum C_L/C_D, with values of 85.85 and 36.50, respectively. The maximum C_L/C_D of the airfoils NACA6712, NACA8412, NACA4412, NACA4415, NACA4418, NACA2415, and NACA2421 were, respectively, 79.08, 78.53, 78, 71.9, 64.91, 64.82, and 57.48.

The highest and lowest maximum C_L/C_D were measured at Re of 300,000, NACA5513, and NACA3530, respectively, and they were 103.21 and 41.64. The maximum C_L/C_D airfoils for the NACA8412, NACA4412, NACA4415, NACA6712, NACA4418, NACA2415, and NACA2421 were 95.8, 91.33, 85.74, 82.75, 78.37, 74.9, and 67.13. The greatest and lowest maximum C_L/C_D for NACA5513 and NACA3530 airfoils were 115.69 and 43.28, respectively, at a Re of 400,000. The maximum C_L/C_D for the NACA8412, NACA4412, NACA6712, NACA4415, NACA4418, NACA2415, and NACA2421 airfoils were 106.71, 101.3, 98.53, 96.56, 86.78, 82.54, and 72.35, respectively. The greatest and lowest maximum C_L/C_D for the NACA5513 and NACA3530 airfoils at Re of 500,000 were 124.59 and 44.92, respectively. The NACA8412, NACA4412, NACA4415, NACA6712, NACA4418, NACA2415, NACA2421, and NACA0025 airfoils' maximum C_L/C_D were measured at 116.07, 109.23, 103.63, 102.78, 94.74, 88.89, and 77.37, respectively.

In addition, at the Re of 600,000, the greatest and lowest maximum C_L/C_D for the NACA5513 and NACA3530 airfoils were 131.57 and 46.8, respectively. The NACA6712, NACA8412, NACA4412, NACA4415, NACA4418, NACA2415, and NACA2421 airfoils had a maximum C_L/C_D of 128.93, 122.71, 115.78, 109.56, 100.24, 93.34, and 82.43, respectively. Thus, the NACA5513 airfoil's greatest maximum C_L/C_D was recorded at Re of 100,000 to 600,000, whereas the NACA350030 airfoil had the lowest maximum C_L/C_D at Re of 100,000 to 600,000.

The NACA 5-digit airfoils are displayed in **Figure 2c**. The greatest maximum C_L/C_D for the NACA24012 airfoil at Re of 100,000 was 37.4, whereas the lowest maximum C_L/C_D for the NACA23024 airfoil was 32.06. NACA63415, NACA63018, NACA24015, NACA23012, NACA23015, NACA23018, and NACA24020 airfoils had a maximum C_L/C_D of 36.4, 36.32, 36.3, 35.85, 35.42, and 33.8. The highest and lowest maximum C_L/C_D were achieved by the NACA24012 and NACA23024 airfoils at 56.9 and 43.13, respectively, at a Re of 200,000.

NACA24015, NACA24020, NACA23012, NACA23015, NACA23018, NACA63018, and NACA63415 airfoils' maximum C_L/C_D were 53.5, 50.55, 50.09, 49.18, 48.57, 45.41, and 45.22, respectively. The highest and lowest maximum C_L/C_D were measured at Re of 300,000, NACA24012, and NACA23024, respectively, at 68.87 and 46. The maximum C_L/C_D of the airfoils for the NACA24015, NACA23012, NACA24020, NACA23015, NACA23018, NACA63415, and NACA63018 were 64.77, 61.35, 59.55, 58.39, 56.54, 49.94, and 49.85. The greatest and lowest maximum C_L/C_D for NACA24012 and NACA23024 airfoils were 77.27 and 48.13, respectively, at a Re of 400,000. The maximum C_L/C_D for the NACA24015, NACA23012, NACA23015, NACA24020, NACA23018, NACA63415, and NACA63018 airfoils were 73.19, 69.89, 66.08, 65.96, 63.17, 52.55, and 52.38, respectively.

The highest and lowest maximum C_L/C_D for the NACA24012 and NACA23024 airfoils were 84.06 and 49.95, respectively, at a Re of 500,000. The NACA24015, NACA23012, NACA23015, NACA24020, NACA23018, NACA63018, and NAC63415 airfoils' maximum C_L/C_D were measured at 80.31, 77.7, 72.47, 71.33, 68.86, and 58.14, respectively. Finally, at a Re of 600,000, the greatest and lowest maximum C_L/C_D for the NACA24012 and NACA23024 airfoils were 89.49 and 52.68, respectively. The NACA24015, NACA23012, NACA23015, NACA24020, NACA23018, NACA63415, and NACA63018 airfoils' maximum C_L/C_D were measured at 86.25, 83.4, 78.64, 74.95, 73.7, 63.38, and 63.29, respectively. Hence, the NACA24012 airfoil's greatest maximum C_L/C_D was recorded at Re of 100,000 to 600,000, whereas the NACA23024 airfoil's lowest maximum C_L/C_D was reported at Re of 100,000 to 600,000.

Several of the Selig airfoils are shown in **Figure 2d**. The S825 airfoil had the greatest maximum C_L/C_D of 48.84 at a Re of 100,000, while the S818 airfoil had the lowest maximum C_L/C_D of 14.73. For the airfoils S822, S823, S835, S821, S814, S828, and S809, the maximum C_L/C_D were 41.02, 40.73, 34.17, 33.85, 30.97, 29, and 22.12. At a Re of 200,000, the S825 and S809 airfoils achieved the highest and lowest maximum C_L/C_D, respectively, at 70.12 and 44.41. S822, S823, S814, S835, S818, S821, and S828 airfoils had a maximum C_L/C_D of 67.89, 62.38, 56.3, 54.35, 52.47, 52.3, and 46.87, respectively.

The highest and lowest maximum C_L/C_D were measured at Re of 300,000, S825, and S828, respectively, and they were 81.7 and 48.36. The maximum values for the S822, S823, S814, S818, S835, S821, and S809 airfoils were 75.12, 73.8, 68.45, 67.69, 66.03, 63.07, and 55.35. The maximum C_L/C_D for the S825 and S828 airfoils was 91.98 and 58.09, respectively, at a Re of 400,000. The maximum C_L/C_D for the airfoils S822, S823, S814, S818, S835, S821, and S809 were 86.69, 82.11, 79.32, 75.72, 73.52, 69.82, and 68.01, respectively.

The maximum C_L/C_D for the S825 and S809 airfoils was 96.79 and 73.09, respectively, at the Re of 500,000. The S822, S823, S818, S814, S835, S821, and S828 airfoils' greatest and lowest maximum C_L/C_D were measured at 94.06, 87.96, 85.23, 84.97, 79.06, 75.09, and 74.87, respectively.

Finally, at a Re of 600,000, the S825 and S809 airfoils' highest and lowest maximum C_L/C_D were 104.9 and 74.9, respectively. The S822, S823, S818, S814, S835, S821, and S828 airfoils' maximum C_L/C_D, respectively, were 101.4, 93.4, 91.8, 90.5, 81.9, 79.4, and 77.14. Therefore, the S825 airfoil's greatest maximum C_L/C_D was measured at Re of 100,000 to 600,000, whereas the S809 airfoil's lowest maximum C_L/C_D was measured at Re of 100,000, 200,000, 500,000, and 600,000. Additionally, at Re of 300,000 and 400,000, the S828 airfoil had the lowest maximum C_L/C_D.

Figure 2e shows a number of the Selig airfoils. The S1223 airfoil had the greatest maximum C_L/C_D of 52.47 at a Re of 100,000, while the S1046 airfoil had the lowest maximum C_L/C_D of 33.67. S4083, S7012, S8036, S8052, S5010, S6063, and S2027 airfoils had maximum C_L/C_D of 51.89, 51.1, 47.46, 47.33, 44.91, 42.58, and 42.54. At a Re of 200,000, the S4083 and S6063 airfoils recorded the maximum C_L/C_D with values of 74.28 and 49.18, respectively. For the S1223, S8036, S7012, S2027, S8052, S5010, and S1046 airfoils, the maximum C_L/C_D were 71.18, 69.75, 69.36, 65.36, 64.3, and 54.67, respectively.

The highest and lowest maximum C_L/C_D were measured at Re of 300,000, S4083, and S6063, respectively, and they were 86.55 and 49.78. The maximum C_L/C_D of the airfoils for the S2027, S1223, S7012, S8036, S5010, S8052, and S1046 were equal to 83.57, 82.66, 78.52, 77.87, 73.46, 72.97, and 64.78. The greatest and lowest maximum C_L/C_D for S4083 and S6063 airfoils were 95.96 and 51.5 at Re of 400,000, respectively. The maximum C_L/C_D for the airfoils S2027, S1223, S7012, S8036, S5010, S8052, and S1046 were 93.7, 92.1, 84.38, 83.59, 79.71, 78.35, and 70.9, respectively.

The greatest and lowest maximum C_L/C_D for the S2027 and S6063 airfoils were 102.43 and 55.5, respectively, at a Re of 500,000. S4083, S1223, S8036, S7012, S5010, S8052, and S1046 airfoils' maximum C_L/C_D were measured at 102.02, 98.3, 88.73, 86.55, 84.5, 82.24, and 74.6, respectively. Finally, at the Re of 600,000, the maximum

C_L/C_D for the S2027 and S6063 airfoils were 107.8 and 59.88, respectively. The S2027, S1223, S8036, S7012, S5010, S8052, and S1046 airfoils' greatest and lowest maximum C_L/C_D were measured at 107.8, 102.6, 92.7, 89.1, 88.69, 84.03, and 77.63, respectively.

Hence, the S1223 airfoil recorded the highest maximum C_L/C_D at a Re of 100,000. Additionally, with a Re of 200,000 to 300,000, the S4083 airfoil had the highest maximum C_L/C_D. The S2027 airfoil had the highest maximum C_L/C_D at Re of 400,000 to 600,000, whereas the S1046 airfoil achieved the lowest maximum C_L/C_D at Re of 100,000. Additionally, the S6063 airfoil had the lowest maximum C_L/C_D at Re of 200,000 to 600,000.

A number of Selig airfoils are displayed in **Figure 2f**. The SD2030 airfoil had the highest maximum C_L/C_D of 56.07 at Re of 100,000, whereas the SD7003 airfoil had the lowest maximum C_L/C_D of 43.12. For the airfoils SA7038, SD7032, SD7037, SA7035, SD7080, SD6060, and SD7062, the maximum C_L/C_D were 55.75, 55.33, 54.56, 52.57, 52.03, 49.78, and 44.6, respectively. At a Re of 200,000, the SD7032 and SD7003 airfoils obtained the highest and lowest maximum C_L/C_D, respectively, at 78.21 and 57.87.

For the SA7038, SD2030, SD7037, SA7035, SD7080, SD7062, and SD6060 airfoils, the maximum C_L/C_D were 77.06, 76.67, 74.78, 71.37, 70.19, 69.89, and 69.44, respectively. The highest and lowest maximum C_L/C_D were measured at Re of 300,000, SD7032, and SD7003, respectively, and they were 91.65 and 66.44. The respective values are 88.53, 88.17, 85.86, 84.04, 82.64, 81.24, and 80.20 for the SA7038, SD2030, SD7037, SD7062, SA7035, SD6060, and SD7080 airfoils.

The greatest and lowest maximum C_L/C_D for the SD7032 and SD7003 airfoils were 100.08 and 74.03 at a Re of 400,000, respectively. The maximum C_L/C_D for the airfoils SD2030, SA7038, SD7037, SD7062, SA7035, SD6060, and SD7080 were 97.39, 97.24, 94.68, 92.43, 90.27, 87.6, and 85.49, respectively. The highest and lowest maximum C_L/C_D for the SD7032 and SD7003 airfoils were 107.39 and 78.49, respectively, at a Re of 500,000. The SD2030, SA7038, SD7062, SD7037, SA7035, SD6060, and SD7080 airfoils' maximum C_L/C_D were measured at 103.46, 103.17, 101.47, 98.63, 95.46, 93.53, and 89.08, respectively.

In the end, at the Re of 600,000, the highest and lowest maximum C_L/C_D for the SD7032 and SD7003 airfoils were 112.87 and 82.36, respectively. The SD7062, SA7038, SD2030, SD7037, SA7035, SD6060, and SD7080 airfoils' maximum C_L/C_D were measured at 107.93, 107.52, 106.66, 102.07, 100.37, 97.78, and 94.16, respectively. Thus, the SD2030's highest maximum C_L/C_D was recorded at Re of 100,000, and the SD7032's was recorded at Re of 200,000 to 600,000. Furthermore, at Re between 100,000 and 600,000, the SD7003 airfoil had the lowest maximum C_L/C_D.

The SG6040, SG6041, SG6042, SG6043, SG6050, SG605, PSU94-097, and RG15 airfoils are depicted in **Figure 2g**. At Re of 100,000, the SG6043 airfoil had the highest maximum C_L/C_D, measuring 65.68, and the SG6050 airfoil had the lowest maximum, measuring 48.19. For the airfoils PSU94-097, SG6051, SG6041, RG15, and SG6040, the maximum C_L/C_D were 63.15, 59.3, 55.57, 53.4, 51.81, and 51.03, respectively. The highest and lowest maximum C_L/C_D were obtained by the SG6043 and SG15 airfoils at 97.21 and 68.9, respectively, at a Re of 200,000.

PSU94-097, SG6042, SG6051, SG6050, SG6040, and SG6041 airfoils' the greatest and lowest maximum C_L/C_D were 90.47, 89.01, 80.61, 73.89, 72.85, and 72.5, respectively. The maximum C_L/C_D for the SG6043 and RG15 airfoils at Re of 300,000 were 117.41 and 78.3, respectively. The maximum C_L/C_D airfoils for the PSU94-097, SG6042, SG6051, SG6050, SG6040, and SG6041 were equal to 106.92, 105.09, 95.7, 88.81, 83.82, and 82.61. The highest and lowest maximum C_L/C_D for the SG6043 and RG15 airfoils were 132.89 and 84.88, respectively, at a Re of 400,000. The maximum C_L/C_D for the PSU94-097, SG6042, SG6051, SG6050, SG6040, and SG6041 airfoils was 119.08, 115.78, 104.48, 98.63, 92.17, and 88.34, respectively.

The highest and lowest maximum C_L/C_D for the SG6043 and RG15 airfoils were 143.47 and 89.99, respectively, at a Re of 500,000. The PSU94-097, SG6042, SG6051, SG6050, SG6040, and SG6041 airfoils had the maximum C_L/C_D of 126.1, 123.77, 113.62, 106.16, 97.84, and 91.14, respectively. Finally, at a Re of 600,000, the highest and lowest maximum C_L/C_D for the SG6043 and RG15 airfoils were 153.09 and 92.5, respectively. The PSU94-097, SG6042, SG6051, SG6050, SG6040, and SG6041 airfoils had a maximum C_L/C_D of 135.1, 131.19, 119.59, 111.67, 103.2, and 93.4, respectively. The SG6043 airfoil had the highest maximum C_L/C_D, which was measured at Re of 100,000 to 600,000, while the SG6050 airfoil had the lowest maximum C_L/C_D, measured at Re of 100,000, and the RG15 airfoil at Re of 200,000 to 600,000.

The E231, USNPS4, E387, BW-3, E374, ESA40, E423, FX63-137, and FX74-Cl5-140 airfoils are depicted in **Figure 2h**. The BW-3 airfoil had the highest maximum C_L/C_D of 58.7 at a Re of 100,000, while the E423 airfoil had the lowest maximum C_L/C_D of 12.94. Respectively, the maximum C_L/C_D for E387, USNPS4, FX63-137, E374, E231, FX74-Cl5-140, and ESA40 airfoils were 57.19, 54.93, 54.42, 53.02, 52.77, 33.09, and 24.17.

At a Re of 200,000, the FX63-137 and ESA40 airfoils obtained the highest and lowest maximum C_L/C_D, respectively, at 90.29 and 37.04. E387, E231, USNPS4, E374, FX74-Cl5-140, BW-3, and E423 airfoils had maximum C_L/C_D that were, respectively, 81.97, 76.84, 74, 73.31, 72.74, and 72.04 and 60.75. The highest and lowest maximum C_L/C_D were measured at Re of 300,000 for the FX63-137 and ESA airfoils, respectively, at 107.31 and 50.36. The E387, FX74-Cl5-140, E423, E231, USNPS4, E374, and BW-3 airfoils were equal to 93.82, 93.33, 91.08, 88, 84.79, 84.47, and 75.4, respectively.

At a Re of 400,000, the highest and lowest maximum C_L/C_D for the FX63-137 and ESA40 airfoils were 119.4 and 60.24, respectively. The maximum C_L/C_D for the airfoils E423, FX74-Cl5-140, E387, E374, USNPS4, E231, and BW-3 were 109.46, 108, 99.95, 94.17, 91.27, 91, and 78.03, respectively. The greatest and lowest maximum C_L/C_D for the FX63-137 and EAS40 airfoils at Re of 500,000 were 129.64 and 67.72, respectively. The E423, FX74-Cl5-140, E387, E374, USNP4, E231, and BW-3 airfoils' maximum C_L/C_D was measured at 122.94, 119.16, 106, 97.47, 95.38, 94.05, and 84.31, respectively.

Finally, at the Re of 600,000, the highest and lowest maximum C_L/C_D for the FX63-137 and ESA40 airfoils were 135.28 and 73.3, respectively. The E423, FX74-Cl5-140, E387, E374, USNPS4, E231, and BW-3 airfoils' maximum C_L/C_D were measured at 132.9, 129.12, 109.2, 103.1, 99.94, 94.5, and 87.6, respectively. The BW-

3 airfoil's highest maximum C_L/C_D was measured at Re of 100,000, and the FX63-137's was between Re 200,000 to 600,000. Additionally, the E423 airfoil at Re of 100,000 and the ESA40 airfoil at Re of 200,000 to 600,000 achieved the lowest maximum C_L/C_D.

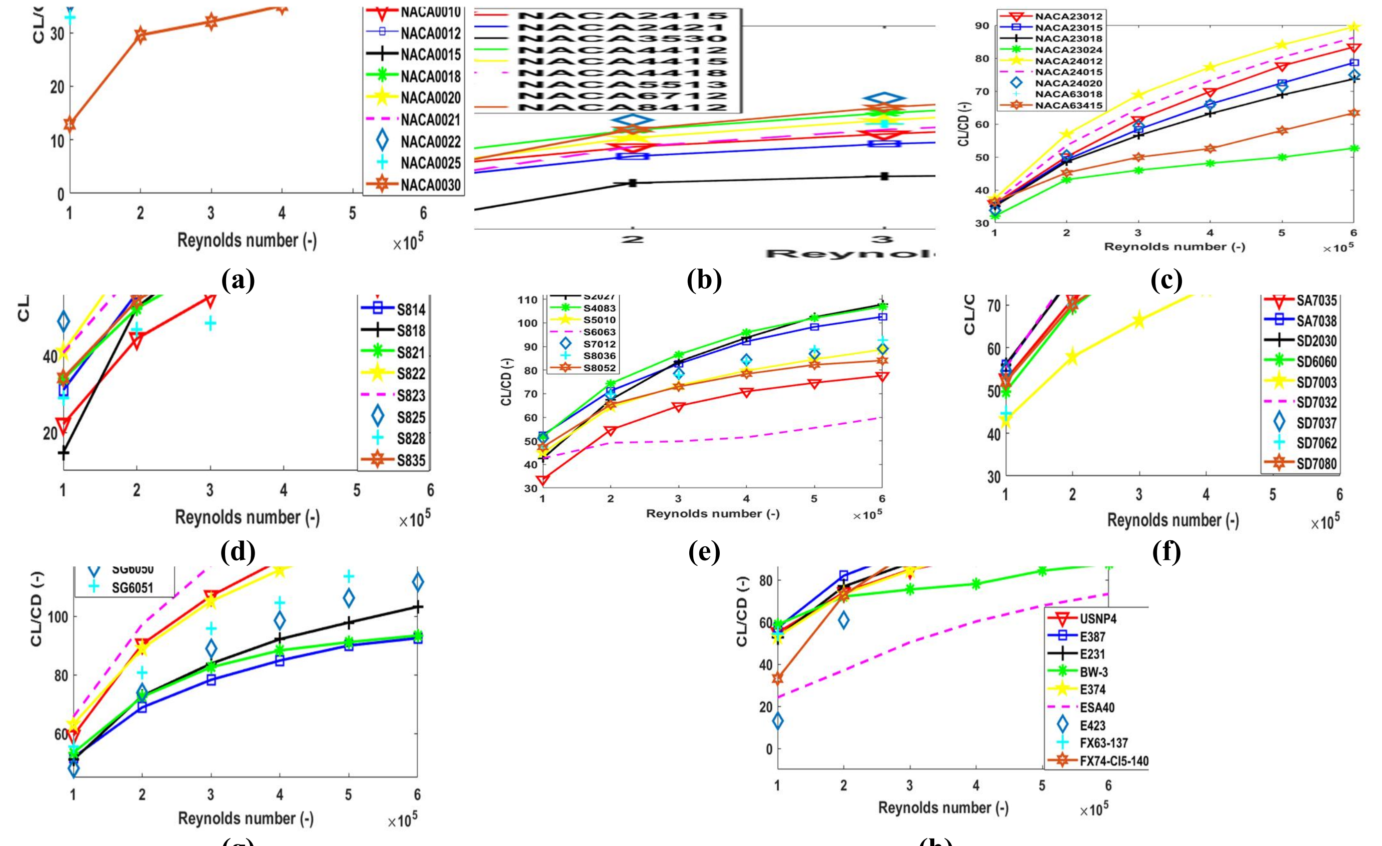

(a) **(b)** **(c)**

(d) **(e)** **(f)**

(g) **(h)**

Figure 2. Analyzing the maximum C_L/C_D of selected airfoils at Reynolds numbers (Re) ranging from 100,000 to 600,000. **(a)** Symmetrical NACA 4-digit airfoils; **(b)** other NACA 4-digit airfoils; **(c)** NACA 5-digit airfoils; **(d)** Selig airfoils (3-digit); **(e)** Selig airfoils (4-digit); **(f)** Selig airfoils (SA/SD series); **(g)** SG604x and related airfoils; **(h)** Eppler and other airfoils.

As a consequence, the SG6043 airfoil revealed the highest maximum C_L/C_D when compared to the other 71 airfoils evaluated at Re from 100,000 to 600,000. To investigate and enhance the form modification of the airfoil utilizing variations in *t*/*c* and to determine the ideal *t*/*c* at Re of 10,000 to 600,000, the SG6043 airfoil was used. We can develop another airfoil by modifying the shape variations in the *t*/*c* using the XFOIL software. At each *t*/*c* configuration, research was carried out on the most suitable new airfoil for optimum C_L/C_D at Re ranging from 10^5 to 6×10^5. Then, utilizing the zone of *t*/*c* with the more significant value C_L/C_D, the geometrical parameters of the SG6043 modified airfoils were found.

Aerodynamic efficiency metrics for the novelty-modified airfoils, including C_L, C_D, C_L/C_D, AoA_{stall}, and drag buckets, were determined and investigated with the baseline airfoil at a Re of 10^5 to 6×10^5 and for the AoA range from 0° to 20°. A summary of the procedure used for the novel airfoil under investigation in XFOIL software is shown in **Figure 3a**.

Turbine blades are critical components in converting fluid or gas energy into mechanical energy. Optimizing their shape, material, and design enhances aerodynamic efficiency, reducing energy losses and improving overall turbine performance. As well better efficiency translates to higher power output for the same input energy, which is particularly important in power plants and aircraft engines. The optimization process of XFOIL is shown in **Figure 3b**. The effectiveness standards for innovative airfoils were changed, and Section 3 presents the effective methods. simplified version of the XFOIL optimization flowchart is shown in Algorithm 1 as below:

Algorithm 1 Airfoil optimization

```
1:   Start
2:   Define Airfoil Geometry
3:     - Input initial airfoil shape parameters.
4:   Set Flow Conditions
5:     - Specify Reynolds number, Mach number, and angle of attack.
6:   Run XFOIL Analysis
7:     - Compute lift, drag, and moment coefficients.
8:   Evaluate Performance
9:     - Check if the performance meets the desired criteria.
10:  Optimization Loop
11:    - If not optimized:
12:      - Modify airfoil shape using optimization algorithm.
13:      - Return to step 3.
14:    - If optimized:
15:      - Proceed to next step.
16:  Output Optimized Airfoil
17:    - Save the final airfoil geometry and performance data.
18:  End
```

This is a high-level overview. The actual process can be more complex depending on the specific optimization algorithms and criteria used.

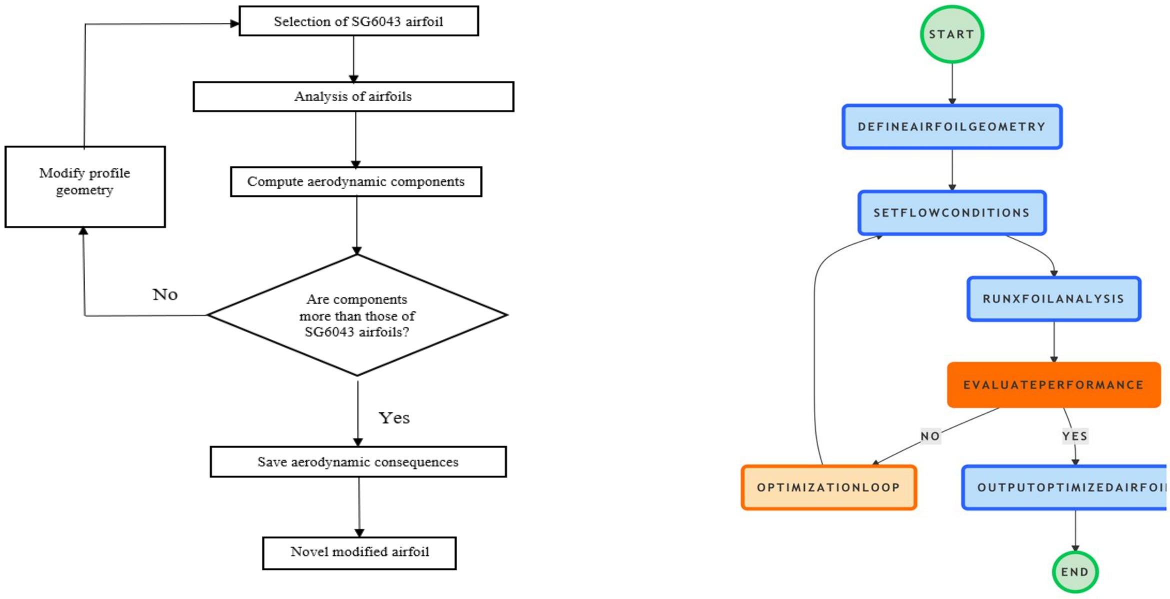

(a) **(b)**

Figure 3. (a) Abstract of XFOIL software process for profile experiment; **(b)** optimization process.

2.3. Theoretical framework

The SG6043 airfoil was modified by varying the thickness-to-camber ratio (*t*/*c*) between 0.5 and 1.5. Three modified airfoils (SG6043 modified 1, 2, and 3) were designed and analyzed to determine their aerodynamic performance. Equations (1)–(5) show the mathematical basis for investigating the aerodynamic characteristics of the airfoil [25,26].

$$Reynoldsnumber = \frac{\rho U_{rel} c}{\mu} = \frac{U_{rel} c}{\upsilon} \tag{1}$$

$$U_{rel} = \sqrt{[U(1-a)]^2 + [r\omega]^2} \tag{2}$$

$$L = C_l \frac{1}{2} \rho U^2 cl \tag{3}$$

$$D = C_d \frac{1}{2} \rho U^2 cl \tag{4}$$

$$\frac{L}{D} = \frac{(C_l \frac{1}{2} \rho U^2 cl)}{(C_d \frac{1}{2} \rho U^2 cl)} = \frac{C_l}{C_d} \tag{5}$$

Equation (1) defines a relationship between the speed of air, kinematic viscosity, airfoil chord length, and wind Re. The lift force (F_L) and drag force (F_D) of an airfoil can be calculated in Equations (3) and (4), respectively.

Equation (3) illustrates the relationship between the F_L and the C_L by including the air speed, density, chord length, and span. In Equation (4), the F_D on the airfoil is correlated with the C_D, speed of the wind, density, chord, and span. The C_L/C_D was provided by Equation (5).

2.4. SG6043 airfoil modified optimization

Based on initial design optimization findings, **Figure 4a** illustrates variations in reaching their highest C_L/C_D with *t*/*c* for the SG6043 airfoil for Re from 10^5 to 6×10^5. **Figure 4a** shows that the peak C_L/C_D had a dome-shaped relationship with the *t*/*c* for each Re, and that the efficiency of C_L/C_D generally improved with rising Re. The maximum peak CL/CD occurred within the *t*/*c* range of 0.50 to 1.50 for each Re. Hence, the top C_L/C_D was smaller outside of this *t*/*c* range. The *t*/*c* of the SG6043 airfoil was determined using the *t*/*c*, which was considered when generating the airfoils in the current research. The *t*/*c* ranged from 0.50 to 1.50.

SG6043 modified 1 airfoil was optimized to have a pick thickness of 7.05% at 17.20% of the chord and a pick camber of 7.72% at 49.80% of the chord, SG6043 modified 2 airfoils was optimized to have a pick thickness of 6.52% at 15.30% of the chord and a pick camber of 8.79% at 53.20% of the chord; and SG6043 modified 3 airfoils was optimized to have a pick thickness of 4.91% at 15.70% of the chord and a pick camber of 8.88% at 52.50% of the chord, as was represented graphically in **Figure 4b**. Moreover, the SG6043 airfoil had a peak thickness of 10.02% at 32.10% of the chord and a peak camber of 5.50% at 49.70% of the chord.

Hence, the *t*/*c* range for these parameters was between 0.50 and 1.50. This zone saw the development of three airfoils with the designations SG6043 modified 1, SG6043 modified 2, and SG6043 modified 3. According to **Figure 4b**, the significant variation between the SG6043 airfoil and the novelty-modified SG6043 modified airfoils was in the geometrical features of the thickness and camber airfoils. In comparison to the SG6043 airfoil, the SG6043 modified airfoils had thinner and more cambered geometries. As previously mentioned, the efficiency parameters of the novelty-designed airfoils and the SG6043 airfoil were calculated at a Re of 10^5 to 6×10^5.

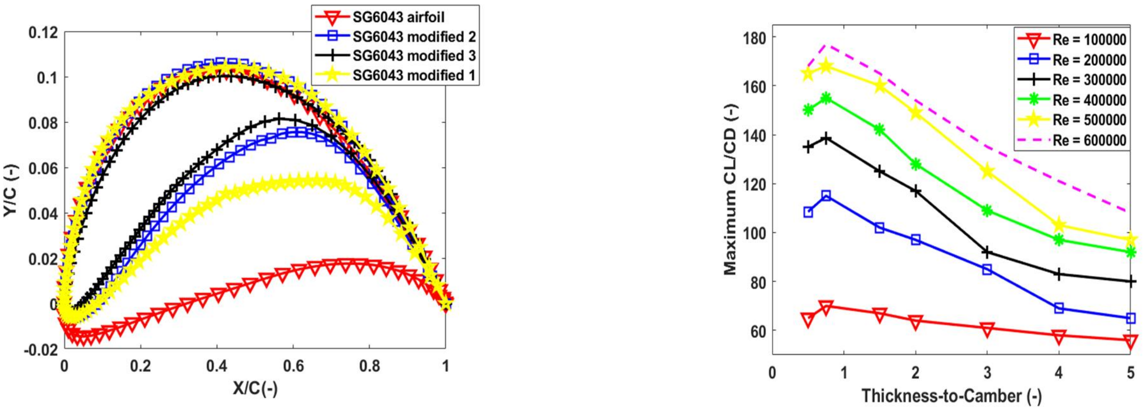

(a) **(b)**

Figure 4. Airfoil geometry variation for SG6043 airfoil optimization, **(a)** peak C_L/C_D at various thickness-to-camber ratios; **(b)** SG6043 and SG6043 modified airfoils.

3. Results and discussions

3.1. Validation data

As illustrated in **Figure 5a**,**b**, which compare the aerodynamic efficiency of the E387 airfoil as predicted by X-Foil at Re of 200,000 and 400,000 with the experiment and X-Foil data by Wei et al. [27] in order to confirm the correctness of the X-Foil software. The results from the experiment and X-Foil software are in strong agreement with one another, which can support the need for optimization.

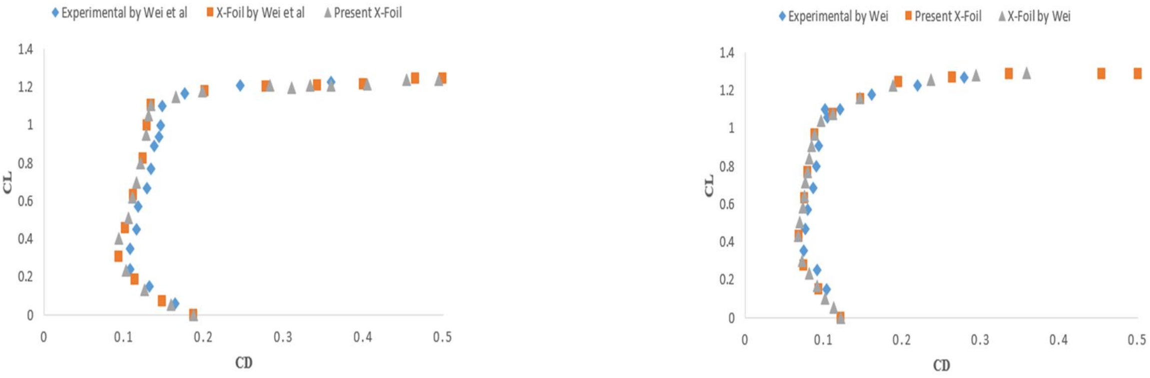

(a) **(b)**

Figure 5. Variation of aerodynamic parameters predicted by the XFOIL software data and experimental findings [27]. (**a**) Re = 200,000, (**b**) Re = 400,000.

3.2. Lift efficiency of SG6043, SG6043 modified 1, SG6043 modified 2, and SG6043 modified 3 airfoils

For Re between 100,000 and 600,000, the lift efficiency graphs for the base and modified SG6043 modified 1, SG6043 modified 2, and SG6043 modified 3 airfoils were illustrated in **Figures 6–9**, respectively. The value of the C_L had increased for the SG6043 airfoil as the Re had risen from 10^5 to 6×10^5; the lowest value of the C_L in the Re of 10^5 was equal to 1.604, and the highest value of the C_L in the Re of 6×10^5 was 1.769 (**Figure 6**).

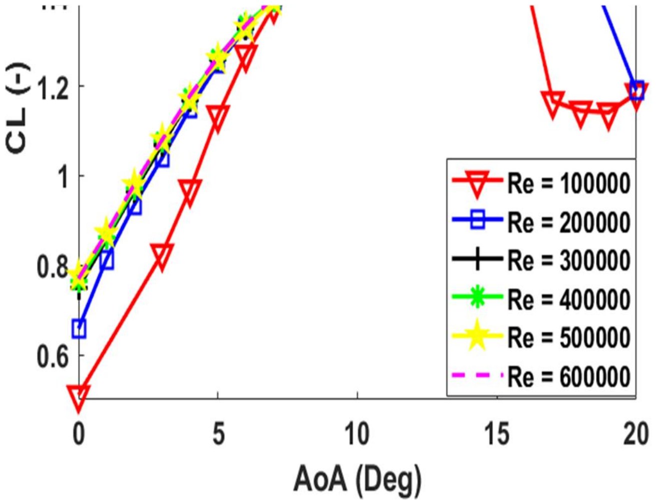

Figure 6. C_L graph for SG6043 airfoil.

The SG6043 modified 1 airfoil had the greatest peak C_L of 1.79 at a Re of 10^5. The lowest peak C_L of 1.72 equaled a Re of 3×10^5. The findings demonstrated that when the Re increased, C_L generally increased better. SG6043 modified 1 had near lift efficiency for Re between 2×10^5 and 5×10^5. Moreover, the C_L at Re of 3×10^5, 4×10^5, 5×10^5, and 6×10^5 equal to 1.72, 1.74, 1.75, and 1.772, respectively. This value had risen as Re from 3×10^5 to 6×10^5 had increased (**Figure 7**).

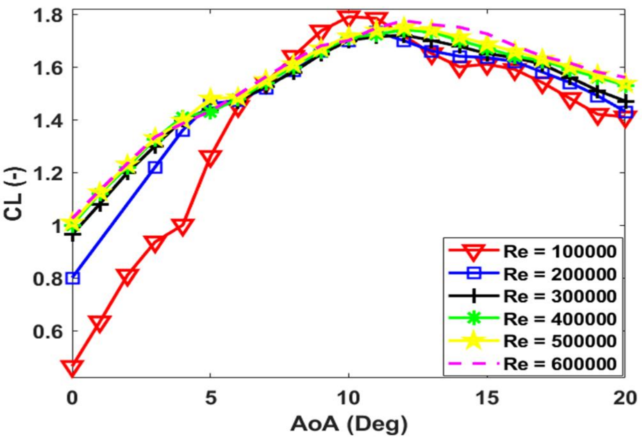

Figure 7. C_L graph for SG6043 modified 1 airfoil.

Figure 8 illustrates the lift efficiency graph for the SG6043 modified 2 airfoils at Re between 10^5 to 6×10^5. Similarly, as Re increased, C_L efficiency generally improved. For $AoAs$ less than 12° at Re of 10^5 to 6×10^5, the C_L efficiency was close to each other. At Re of 6×10^5 and 2×10^5, the SG6043 modified 2 airfoil had peaks C_L of 1.798 and 1.743, respectively, the most excellent and lowest values. Also, at a Re of 10^5, the greatest value of the C_L was equal to 1.748, which was more than a Re of 2×10^5 and less than a Re of 3×10^5 to 6×10^5.

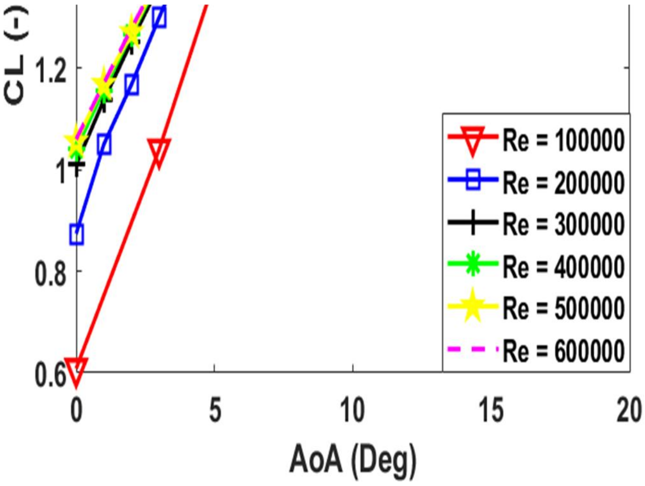

Figure 8. C_L graph for SG6043 modified 2 airfoil.

The lift efficiency graph for SG6043 modified 3 airfoils with a Re of 10^5 to 6×10^5 is indicated in **Figure 9**. The C_L efficiency was enhanced with an increment in Re, with relative efficiency for Re of 2×10^5, 3×10^5, 5×10^5, and 6×10^5. The SG6043 modified 3 airfoil had the greatest and least peak C_L of 1.788 and 1.697, respectively, at Re of 10^5 and a Re of 4×10^5, respectively. In addition, the peak C_L in Re of 2×10^5, 3×10^5, 5×10^5, and 6×10^5 equals 1.763, 1.781, 1.773, and 1.778.

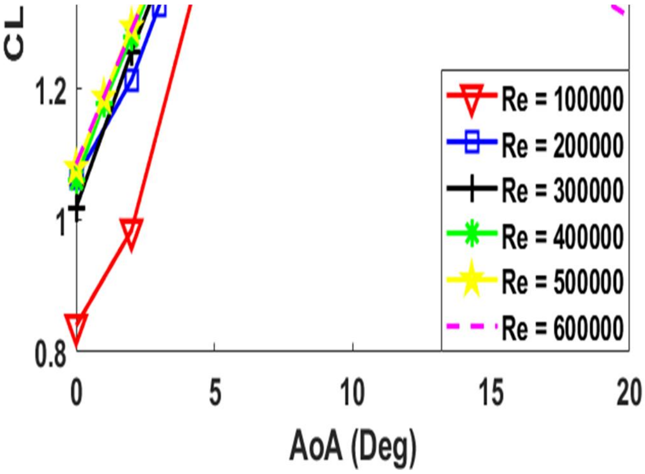

Figure 9. C_L graph for SG6043 modified 3 airfoil.

Typically, the peak C_L of modified airfoils in all Re was greater than the peak C_L of the SG6043 airfoil, and the enhancement in lift efficiency for an increment in Re was related to an incremented air velocity relevant to a higher Re.

Moreover, at each Re, the decrement in lift efficiency beyond the peak C_L was related to the airfoils encountering stall situations as a consequence of lift resistance from turbulence on the airfoil's suction surfaces. At a Re of 3×10^5, there was almost no discernible difference in lift efficiency between any airfoil. This near-efficiency attitude indicates that the lift efficiency of the airfoils was comparatively less susceptible to changes in Re from Re of 3 × 10^5 to 6 × 10^5. This effect was related to nonlinear aerodynamic properties frequently found in low Re airflow situations [28].

3.3. Stall efficiency of SG6043 modified 1, SG6043 modified 2, and SG6043 modified 3 airfoils

The stall efficiency of SG6043 modified 1, SG6043 modified 2, and SG6043 modified 3 airfoils at Re from 10^5 to 6 × 10^5 was investigated in **Table 1**. For the analysis, Re of 10^5 to 6 × 10^5, entire airfoils had AoA_{stall} between 9° to 13°.

Table 1. Stall performances for SG6043 modified airfoils.

Airfoils	Stall Angle (°)					
	Re = 10^5	Re = 2 × 10^5	Re = 3 × 10^5	Re = 4 × 10^5	Re = 5 × 10^5	Re = 6 × 10^5
SG6043 modified 1	10	11	12	12	12	12
SG6043 modified 2	12	12	13	13	13	13
SG6043 modified 3	9	10.5	10	11	9	9

SG6043 modified 1 airfoil had the lowest AoA_{stall} of 10° at Re of 10^5 and the greatest AoA_{stall} of 12° at Re of 3 × 10^5, 4 × 10^5, 5 × 10^5, and 6 × 10^5. Moreover, AoA_{stall} of 11° was presented at a Re of 2 × 10^5. The SG6043 modified 2 airfoil had the least AoA_{stall} of 12° at Re of 10^5 and 2 × 10^5. Moreover, SG6043 modified 2 airfoils had the most excellent AoA_{stall} of 13° at Re of 3 × 10^5, 4 × 10^5, 5 × 10^5, and 6 × 10^5, respectively.

The SG6043 modified 3 airfoil had the least AoA_{stall} of 9° at Re of 10^5, 5 × 10^5, and 6 × 10^5. Also, SG6043 modified 3 airfoils had the most significant AoA_{stall} of 11° at Re of 4 × 10^5. As well as, AoA_{stall} of 10.5° and 10° were presented at Re of 2 × 10^5 and 3 × 10^5. The AoA_{stall} demonstrates the crucial AoA beyond which the C_L efficiency starts to degrade due to resistance generated by turbulence on the airfoil's suction area for every airfoil under each Re flow regime.

The greatest AoA_{stall} of 13º and 12º for SG6043 modified 2 airfoil for nearly the entire Re demonstrated it was favorable for utilization over and across a comparatively wider AoA.

Figures 7–9's lift efficiency graphs showed that total airfoils often produced post-stall slow performance at Re of 200,000. The shape of the airfoils, which was developed for the most incredible C_L/C_D efficiency and was required for continuous aerodynamic efficiency at an extensive range of AoA without a short loss of lift, causes this slow post-stall feature. It was known that abrupt lift loss causes WT rotor efficiency to degrade quickly [28].

3.4. The C_L/C_D efficiency of SG6043 and SG6043 modified airfoils

The SG6043 modified 1 airfoil demonstrated the highest lift coefficient (C_L) of 1.79 at Re = 100,000, outperforming the original SG6043 airfoil. As Re increased, the C_L for all modified airfoils improved, with the SG6043 modified 2 airfoil achieving a peak C_L of 1.798 at Re = 600,000 (**Figure 6**). This improvement in lift efficiency is attributed to the optimized *t*/*c* ratio, which enhances airflow over the airfoil surface. The C_L/C_D efficiency graphs of SG6043, SG6043 modified 1, SG6043 modified 2, and SG6043 modified 3 airfoils for Re of 10^5 to 6 × 10^5 were illustrated in **Figures 10–13**, respectively. The C_L/C_D efficiency typically increased with increasing Re for airfoils and had a dome-shaped relationship with AoA for the entire Re. Throughout the whole AoA, the C_L/C_D efficiency was greatest at a Re of 6 × 10^5 and lowest at a Re of 10^5. According to **Figure 10**, at a Re of 6 × 10^5, the SG6043 airfoil's greatest peak C_L/C_D was 152.88 at an AoA of 3°. The least peak C_L/C_D at Re of 10^5 was 65.86 at an AoA of 7°. The highest C_L/C_D for the SG6043 airfoil was 97.21, 117.25, 132.5, and 143.33, respectively, for Re of 2 × 10^5, 3 × 10^5, 4 × 10^5, and 5 × 10^5, at AoA of 5°, 4°, 4°, and 3°.

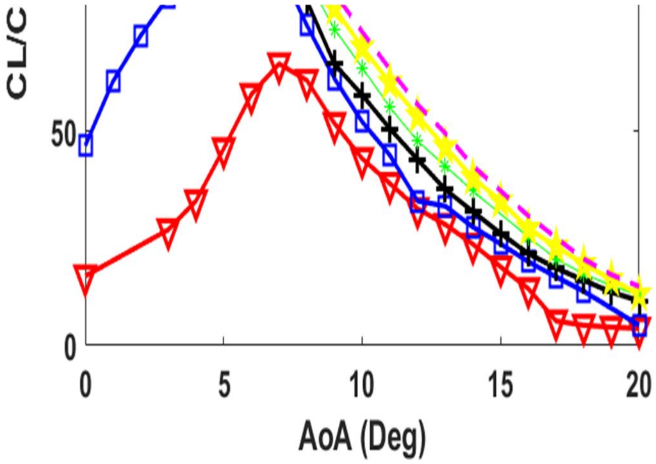

Figure 10. The C_L/C_D efficiency for SG6043 airfoil.

From **Figure 11**, at a Re of 6 × 10^5, the highest peak C_L/C_D for the SG6043 modified 1 airfoil was 184.85 at AoA = 3°. At a Re of 10^5, the least peak C_L/C_D was 69.48 at AoA = 6°. At Re of 2 × 10^5, 3 × 10^5, 4 × 10^5, and 5 × 10^5, the greatest values C_L/C_D for SG6043 modified 1 airfoil were 108.47, 135.59, 154.3, and 172.43, respectively, at $AoAs$ of 5°, 4°, 3°, and 3°.

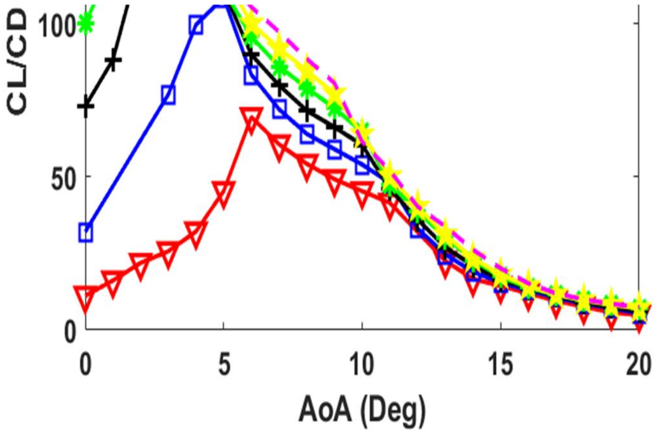

Figure 11. The C_L/C_D efficiency for SG6043 modified 1 airfoil.

From **Figure 12**, at a Re of 6 × 10^5, the greatest peak C_L/C_D for the SG6043 modified 1 airfoil was 177.25 at AoA = 3°. At a Re of 10^5, the least peak C_L/C_D was

73.08 at AoA = 7°. At Re of 2 × 10^5, 3 × 10^5, 4 × 10^5, and 5 × 10^5, the highest values of C_L/C_D for SG6043 modified 1 airfoil were 111.70, 138.67, 160.80, and 171.08, respectively, at $AoAs$ of 5°, 4°, 4°, and 4°.

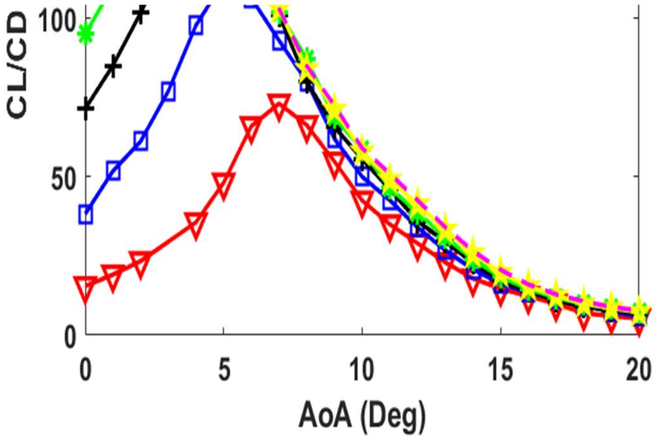

Figure 12. The C_L/C_D efficiency for SG6043 modified 2 airfoil.

According to **Figure 13**, at a Re of 6 × 10^5, the SG6043 modified 3 airfoil's greatest peak C_L/C_D was 182.36 at an AoA of 2°. The least peak C_L/C_D at a Re of 10^5 was 71.34 at an AoA of 6°. The highest C_L/C_D for the SG6043 modified 3 airfoil was 116.98, 145.02, 157.34, and 170.15, respectively, for Re of 2 × 10^5, 3 × 10^5, 4 × 10^5, and 5 × 10^5, at $AoAs$ of 4°, 3°, 3°, and 2°, respectively.

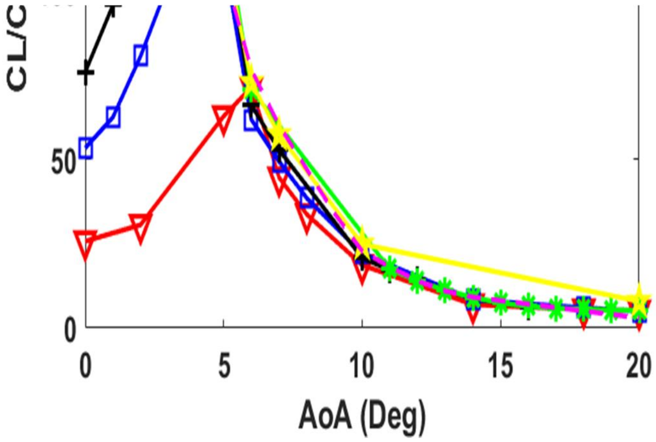

Figure 13. The C_L/C_D efficiency for SG6043 modified 3 airfoil.

The greatest C_L/C_D efficiency for each airfoil occurred at a Re of 6 × 10^5, which was related to a high energy flow and tried to produce a high lift. The maximum C_L/C_D efficiency for the SG6043 modified 1, SG6043 modified 2, and SG6043 modified 3 airfoils at Re of 3 × 10^5, respectively, was 135.59, 138.67, and 145.02, compared with further airfoils like the E387, SG6043, Go471a, and EYO-Series airfoils studied in other research [9,15,16,21].

3.5. Drag bucket performances of SG6043 and SG6043 modified airfoils

The SG6043 modified 2 airfoil exhibited the highest stall angle (AoA_{stall}) of 13° at Re = 300,000 to 600,000, making it suitable for a wider range of operating conditions (**Table 1**). This is a significant improvement over the original SG6043 airfoil, which had a stall angle of 12° at the same Re range. The drag bucket efficiency for the SG6043, SG6043 modified 1, SG6043 modified 2, and SG6043 modified 3 airfoils is shown in **Figures 14** and **15**, respectively. Typically, SG6043 and SG6043-modified airfoils had an increment in drag bucket efficiency with an incrementing Re. According to **Figure 14**, for the SG6043 airfoil and at a Re of 10^5, the first rise in the lift was accompanied by a slight decrease in drag up to a C_L of around 1.6. After this limit, there was a small drop in lift and a significant increase in drag. With no commensurate change in drag, the initial increment in C_L up to around 1.20 happened steadily at a Re of 6 × 10^5. Above C_L of 1.76, lift only was reduced while drag drastically increased. At Re of 2 × 10^5, 3 × 10^5, 4 × 10^5, and 5 × 10^5, there was a similar performance trend.

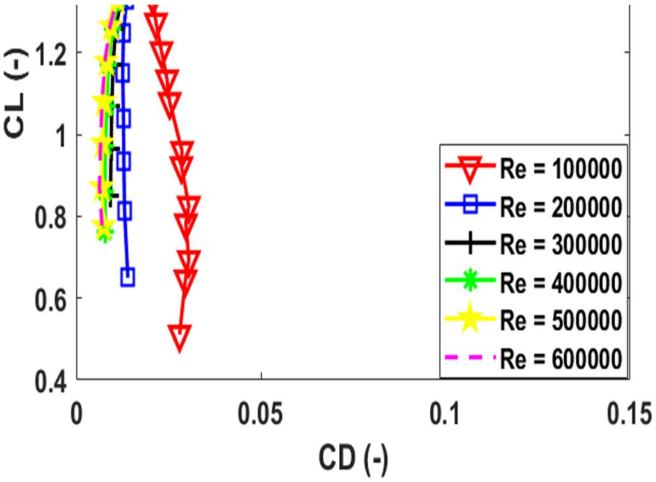

Figure 14. Drag bucket for SG6043 airfoil.

According to **Figure 15**, with the SG6043 modified 1 airfoil at a Re of 10^5, the primary rise in the lift was accompanied by a minor decrease in drag up to a C_L of around 1.78. After this amount, there was a slight drop in lift and a significant increase in drag. At a Re of 6 × 10^5, the C_L slowly increased at first, reaching a value of around 1.38, without any commensurate variation in drag. With only a modest reduction in lift, drag significantly rose above the C_L of 1.772. The efficiency trends for Re of 2 × 10^5, 3 × 10^5, 4 × 10^5, and 5 × 10^5 were comparable.

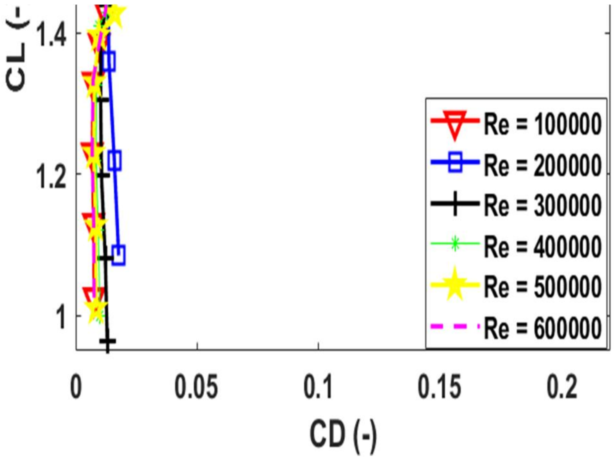

Figure 15. Drag bucket for SG6043 modified 1.

Figure 16 shows that for the SG6043 modified 2 airfoil at a Re of 10^5, the primary rise in the lift was accompanied by a minor decrease in drag up to a C_L of around 1.74. After this amount, there was a slight drop in lift and a significant increase in drag. At a Re of 6 × 10^5, the C_L slowly increased at first, reaching a value of around 1.53, without any commensurate variation in drag. With only a modest reduction in lift, drag significantly rose above the C_L of 1.798. The efficiency trends for Re of 2 × 10^5, 3 × 10^5, 4 × 10^5, and 5 × 10^5 were comparable.

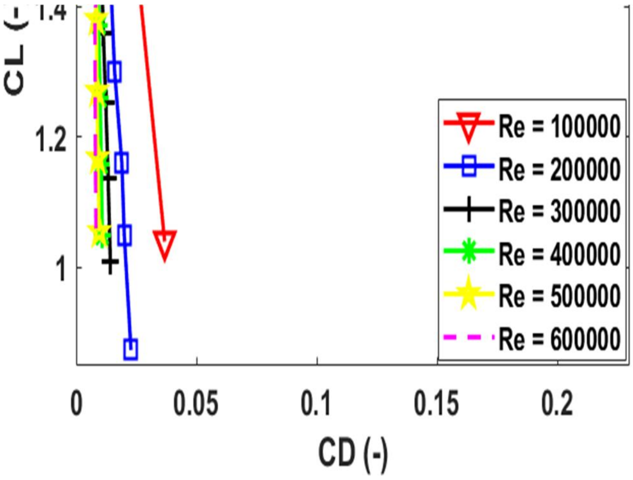

Figure 16. Drag bucket for SG6043 modified 2.

Figure 17 illustrates that with the SG6043 modified 3 airfoil at a Re of 10^5, the primary rise in the lift was accompanied by a minor decrease in drag up to a C_L of around 1.787. After this amount, there was a slight drop in lift and a significant increase in drag. At a Re of 6 × 10^5, the C_L slowly increased at first, reaching a value of around 1.47, without any commensurate variation in drag. With only a modest reduction in lift, drag significantly increased above the C_L of 1.778. The efficiency trends for Re of 2 × 10^5, 3 × 10^5, 4 × 10^5, and 5 × 10^5 were comparable.

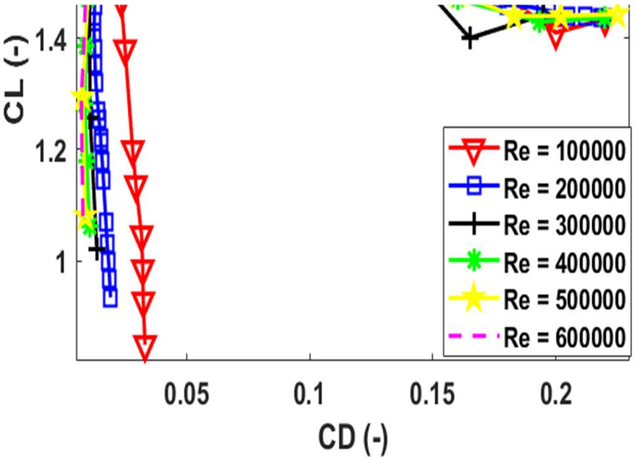

Figure 17. Drag bucket for SG6043 modified 3.

At the whole Re, every airfoil had its primary increment in C_L happening at either steady drag or decreasing drag up to around the region of peak C_L. This aerodynamic treatment resulted from how the airfoils were modified and developed for peak C_L/C_D

efficiency. The post-stall areas, where turbulence on the airfoil areas decreased lift generation and raised drag, include the area in the drag buckets beyond the peak C_L where the C_D incremented rapidly. The capability of the airfoils to increment lift efficiency to around the part of peak C_L while stabilizing or decreasing the surface of drag was a typically favorable feature of great-efficiency airfoils. All modified airfoils showed improved drag bucket performance, with the SG6043 modified 1 airfoil demonstrating the most significant reduction in drag at higher lift coefficients (**Figure 14**). This indicates that the modified airfoils are more efficient at maintaining lift while minimizing drag, which is critical for SWT performance.

3.6. Pressure distribution (C_P) of SG6043 modified airfoils

Figures 18–21 were illustrated, respectively, the upper and bottom surfaces C_P of the SG6043 modified 1, SG6043 modified 2, and SG6043 modified 3 airfoils at Re of 3×10^5 for the AoA of 0°, the angle at peak C_L/C_D, AoA_{stall}, and 20°. According to **Figure 18**, the modified airfoil had considerably bigger suction (negative pressures) on its upper area than on its bottom area at an AoA of 0°. Each airfoil's pressure loading along its chord length was almost consistent from the leading edge to the trailing edge. Due to the consistent pressure loading, it was possible to determine that the lift generated by the airfoils at an AoA of 0° was distributed uniformly from the leading to the trailing edges. For entire modified airfoils, the stagnation points (point of peak pressure) at an AoA of 0° were recorded at the leading edge.

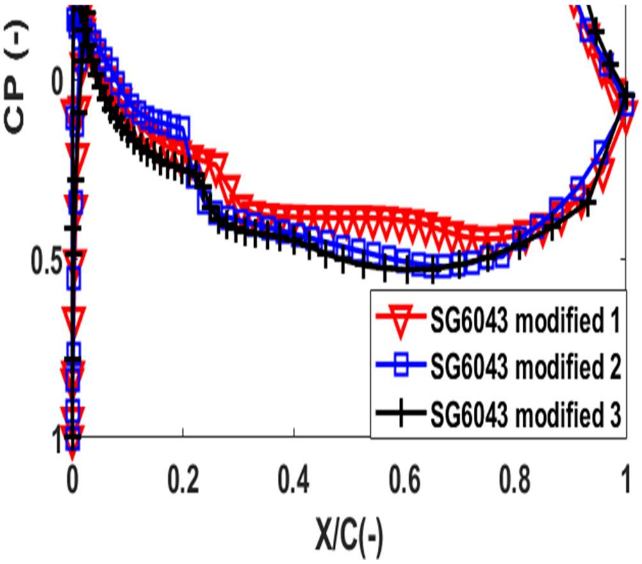

Figure 18. C_P of entire modified airfoils at an angle of attack of 0°.

According to **Figure 19**, a higher suction value on the upper area of all modified airfoils was localized towards the leading edge at the angle at peak C_L/C_D. Moreover, the pressure loading was higher towards the modified airfoils leading edge than their trailing edge. The results demonstrated that the surface immediately adjacent to the leading edge was primarily responsible for the lift efficiency of the airfoils at the angle at peak C_L/C_D. Leading edges were recorded as stagnation points for entire airfoils at angles at peak C_L/C_D.

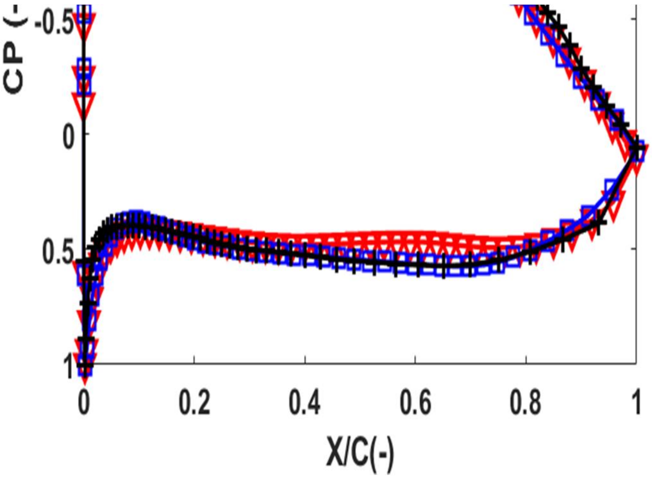

Figure 19. C_P of whole modified airfoils angle at peak C_L/C_D.

According to **Figures 20** and **21** for modified airfoils, the pressure loading was noticeably higher at the leading edge at an AoA_{stall} and an AoA of 20°, respectively. That demonstrated that the area closely adjacent to the leading edge contributed significantly to the lift efficiency of the airfoils at an AoA of 20°. For all the modified airfoils at both AoA investigated in **Figures 20** and **21**, the stagnation point was about 1% of the chord below the leading edge.

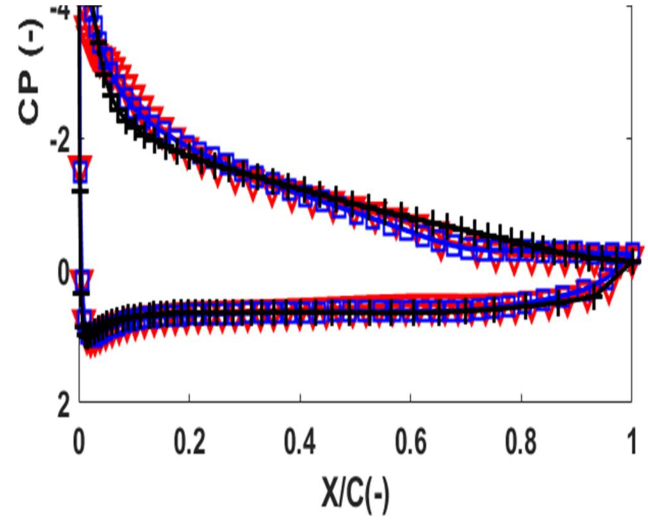

Figure 20. C_P of entire modified airfoils at AoA_{stall}.

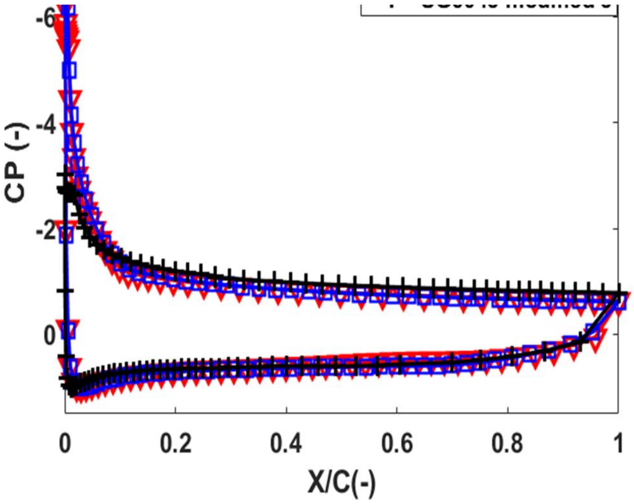

Figure 21. C_P of entire modified airfoils at an angle of attack of 20°.

On the low-pressure sides or top areas of the airfoils, greater F_L was typically correlated with a comparably more significant suction value. Consequently, the high C_L/C_D efficiency findings at that AoA were confirmed by the relatively wide suction pressure in the C_P data for the modified airfoils at an AoA of 4°.

4. Summary of performance analysis for modified airfoils

The C_L and C_L/C_D summary for the SG6043 modified 1, SG6043 modified 2, and SG6043 modified 3 airfoils were revealed in **Figures 22** and **23**, respectively. From **Figure 22**, the SG6043 modified 1 airfoil had the greatest peak C_L at the investigated Re of 10^5, while the SG6043 modified 2 airfoil had the lowest peak C_L. Plus, SG6043 modified 3 had the greatest maximum C_L at Re of 2×10^5, and 3×10^5 while SG6043 modified 1 had the lowest maximum C_L.

Moreover, SG6043 modified 2 had the greatest peak C_L at Re of 4×10^5 to 6×10^5, while SG6043 modified 1 had the lowest peak C_L. Moreover, the SG6043 modified 2 airfoil had the greatest AoA_{stall} at whole Re. At a Re of 10^5 and 2×10^5, the SG6043 modified 2 airfoil had an AoA_{stall} of 12°. Moreover, at Re of 3×10^5 to 6×10^5, SG6043 modified 2 airfoils had an AoA_{stall} of 13°.

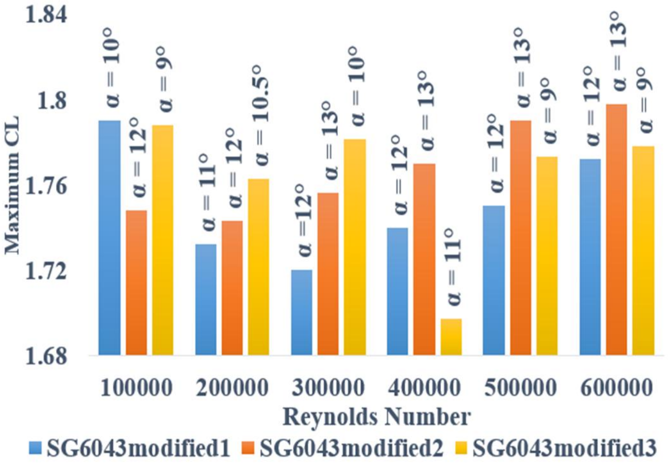

Figure 22. Lift and stall efficiency summary for modified airfoils.

According to **Figure 23**, the SG6043 modified 1 airfoil had the lowest values at a Re of 10^5 to 4 × 10^5, while the SG6043 modified 2 airfoil had the highest maximum C_L/C_D at a Re of 10^5 and 4 × 10^5. Moreover, the SG6043 modified 3 airfoil had the highest maximum C_L/C_Dat Re of 2 × 10^5 and 3 × 10^5. As well, the SG6043 modified 1 airfoil had the highest maximum C_L/C_D at Re of 5 × 10^5 and 6 × 10^5, while the SG6043 modified 3 and SG6043 modified 2 airfoils had the lowest values at Re of 5 × 10^5 and 6 × 10^5.

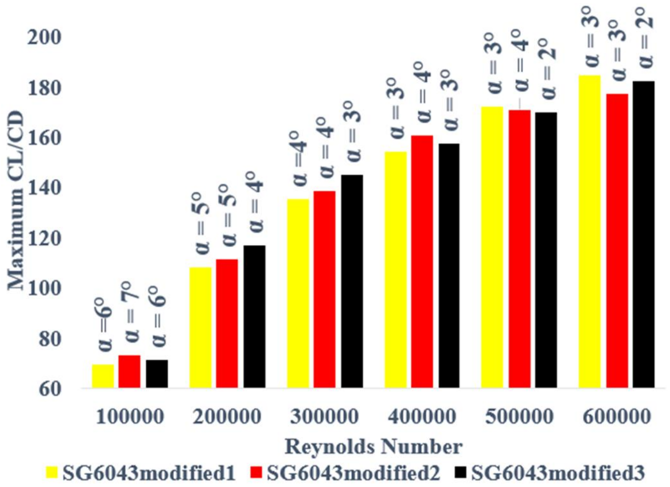

Figure 23. The C_L/C_D efficiency summary for modified airfoils.

The C_L/C_D at Re of 10^5 to 6 × 10^5 was indicated in **Figures 24–29** and was compared with the findings of other researchers [11,12,29,30] to determine the efficiency of the modified airfoils being compared to other airfoils designed by various studies for low Re and SWT usage.

The C_L/C_D efficiency of the SG6043 modified airfoils and their comparison with another low Re airfoil at Re of 10^5 were presented in **Figure 24**. The SG6043 modified airfoils were compared to the developed airfoils of the EYO-Series [12] at a Re of 10^5. The results revealed that the SG6043 modified airfoils had a higher peak C_L/C_D than the EYO-Series airfoils. Moreover, the SG6043 modified 2 airfoil was more efficient than other airfoils.

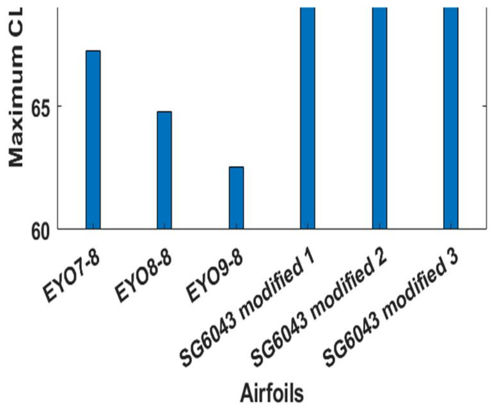

Figure 24. Comparison of SG6043 modified airfoils with EYO-Series airfoils [12] at Re of 10^5.

In **Figure 25**, at a Re of 2 × 10^5, the developed airfoils of the EYO-Series [12] were compared to the SG6043 modified airfoils, and the results demonstrated that the SG6043 modified airfoils had a greater peak C_L/C_D than the EYO-Series airfoils and had a higher efficiency than other airfoils. Additionally, compared to other airfoils, the SG6043 modified 3 airfoil had a higher C_L/C_D.

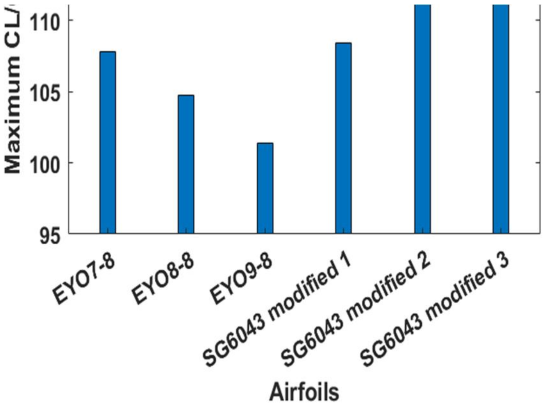

Figure 25. Comparison of SG6043 modified airfoils with EYO-Series airfoils [12] at Re of 2 × 10^5.

Also, at a Re of 3 × 10^5, the SG6043 modified airfoils outperformed the SG604x airfoil family, the EYO-Series airfoils [11,12], and others [9,22] in terms of peak C_L/C_D performance, according to the comparative result in **Figure 26**. Hence, the SG6043 modified 3 airfoils were more efficient than other airfoils.

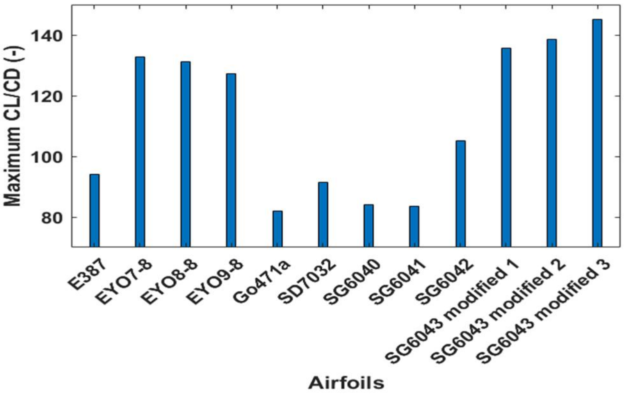

Figure 26. Comparison of SG6043 modified airfoils with EYO-Series [11,12], SG604x airfoil family, and other airfoils [9,22] at Re of 3 × 10^5.

The developed EYO-series [12] airfoils were compared to the SG6043 modified airfoils in **Figure 27** at a Re of 4 × 10^5. The results illustrated that the SG6043 modified airfoils had a higher peak C_L/C_D than the EYO-Series airfoils and higher efficiency than other airfoils. Additionally, compared to other airfoils, the SG6043 modified 2 airfoils were more efficient.

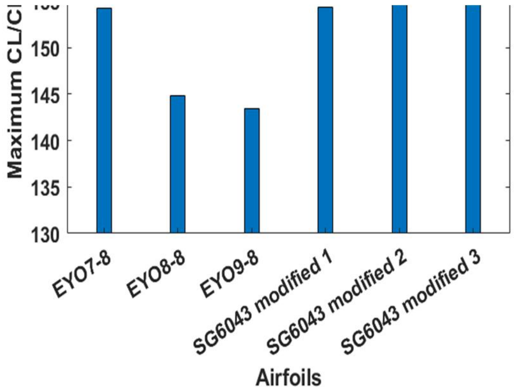

Figure 27. Comparison of SG6043modified airfoils with EYO-Series airfoils [12] at Re of 4 × 10^5.

The developed EYO-Series [12] airfoils were compared to the SG6043 modified airfoils in **Figure 28** at Re of 5 × 10^5. The results illustrated that the SG6043 modified airfoils had a higher peak C_L/C_D than the EYO-Series airfoils and higher efficiency than other airfoils. In addition, compared to other airfoils, the SG6043 modified 3 airfoil had a higher C_L/C_D at a Re of 5 × 10^5.

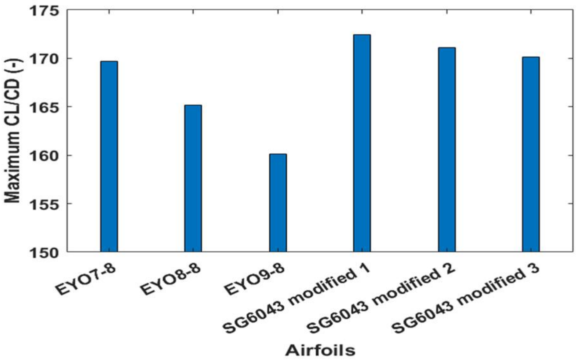

Figure 28. Comparison of SG6043 modified airfoils with EYO-Series airfoils [12] at Re of 5 × 10^5.

Likewise, compared to other airfoils, the SG6043 modified 3 airfoil had a greater C_L/C_D at a Re of 6 × 10^5 (**Figure 29**).

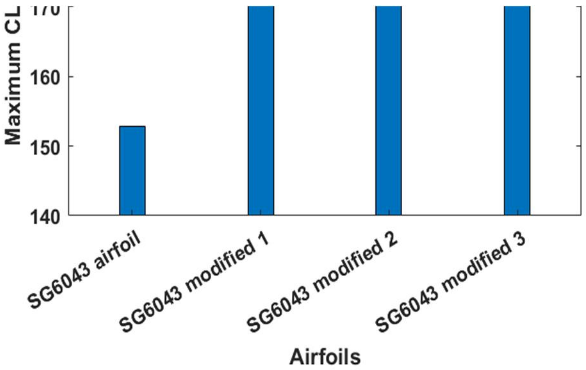

Figure 29. Comparison of SG6043 modified airfoils with SG6043 airfoil at Re of 6 × 10^5.

5. Conclusions

This study optimized the SG6043 airfoil for low Reynolds number applications by varying the thickness-to-camber ratio (*t*/*c*). The results showed that a *t*/*c* ratio between 0.5 and 1.5 significantly improved aerodynamic efficiency, with the SG6043 modified 1 airfoil achieving a maximum C_L/C_D of 184.85 at Re = 600,000. The modified airfoils also demonstrated improved stall angles and drag bucket performance, making them suitable for small wind turbines operating at low Re. Future work will include CFD computations, wind tunnel testing, and further optimization of airfoils for different Re ranges. The primary objective of the present research was to find the airfoil with the highest aerodynamic efficiency between 100,000 and 600,000. For the purpose of such a study, 71 effective airfoils from the symmetrical NACA 4-digit, NACA 5-digit, Selig airfoils, Eppler airfoils, and other airfoils were selected for study.

The results showed that the SG6043 airfoil had the greatest maximum C_L/C_D when compared to the other 71 airfoils evaluated at Re from 100,000 to 600,000. To investigate and enhance the form modification of the airfoil utilizing variations in *t*/*c* and to determine the ideal *t*/*c* at Re of 100,000 to 600,000, the SG6043 airfoil was used. The investigations occurred at Re between 10^5 and 6×10^5, within the usual range for SWT airfoils. According to the research results, efficiency generally improved as the Re increased. The study's major conclusions were as follows.

Based on the findings, 0.5 to 1.5 was the optimum *t*/*c* at Re of 100,000 to 600,000 for the development of the SG6043 airfoil, which had the maximum C_L/C_D.

Then, using the XFOIL software, three airfoils were generated with the optimal *t*/*c*, and the results revealed that the greatest maximum C_L/C_D values for SG6043 modified 1, SG6043 modified 3, and SG6043 modified 2 were 184.85, 182.36, and 177.25, respectively, at a Re of 6×10^5.

SG6043 modified 2, SG6043 modified 1, and SG6043 modified 3 had peaks C_L of 1.798, 1.79, and 1.788, respectively.

For SG6043 modified airfoils, the AoA_{stall} was from 9° to 13°. For the SG6043 modified 2 airfoil, a maximum AoA_{stall} of 13° was demonstrated for Re of 3×10^5, 4×10^5, 5×10^5, and 6×10^5.

At Re between 3×10^5 and 6×10^5, the airfoils behaved admirably regarding lift efficiency, with no notable changes.

According to the drag bucket analyses, S6043-modified airfoils enhanced lift efficiency to peak lift at either invariable or decreasing drag at all Re.

When compared to the SG6043 airfoil, the maximum C_L/C_D of the SG6043 modified 1, SG6043 modified 2, and SG6043 modified 3 airfoils improved by 5.49%, 10.96%, and 8.32%, respectively, at Re of 100,000.

The maximum C_L/C_D of the SG6043 modified 1, SG6043 modified 2, and SG6043 modified 3 airfoils enhanced in comparison to the SG6043 airfoil by 11.58%, 12.97%, and 20.33%, respectively, at Re of 200,000.

In comparison to the SG6043 airfoil, the maximum C_L/C_D of the SG6043 modified 1, SG6043 modified 2, and SG6043 modified 3 airfoils increased by 15.64%, 18.26%, and 23.68%, respectively, at a Re of 300,000.

The maximum C_L/C_D of the SG6043 modified 1, SG6043 modified 2, and SG6043 modified 3 airfoils enhanced in comparison to the SG6043 airfoil by 16.45%, 21.35%, and 18.83%, respectively, at Re of 400,000.

At a Re of 500,000, the maximum C_L/C_D of the SG6043 modified 1, SG6043 modified 2, and SG6043 modified 3 airfoils rose by 20.30%, 19.36%, and 18.71%, respectively, in comparison to the SG6043 airfoil.

At a Re of 600,000, the maximum C_L/C_D of the SG6043 modified 1, SG6043 modified 2, and SG6043 modified 3 airfoils increased by 20.91%, 16.26%, and 19.28%, respectively, compared to the SG6043 airfoil.

At a Re of 100,000, in comparison to the EYO7-8, EYO8-8, and EYO9-8 airfoils, the SG6043 modified 1 airfoil was able to improve the maximum C_L/C_D by 3.6%, 7.20%, and 11.07%, respectively.

The maximum C_L/C_D of the SG6043 modified 2 airfoil was enhanced by 8.63%, 12.76%, and 16.83% in comparison to the EYO7-8, EYO8-8, and EYO9-8 airfoils, at Re of 100,000.

Compared to the EYO7-8, EYO8-8, and EYO9-8 airfoils, the maximum C_L/C_D of the SG6043 modified 3 airfoil was improved by 6.05%, 12.76%, and 10.07%, respectively, at Re of 100,000.

The maximum C_L/C_D of the SG6043 modified 1 airfoil was increased by 0.64%, 3.59%, and 7.01%, respectively, at a Re of 200,000 when compared to the EYO7-8, EYO8-8, and EYO9-8 airfoils.

Comparing the SG6043 modified 2 airfoil to the EYO7-8, EYO8-8, and EY9-8 airfoils resulted in increases in the maximum C_L/C_D of 3.64%, 6.67%, and 10.20%, respectively, at Re of 200,000.

The maximum C_L/C_D increased by 8.54%, 11.71%, and 15.41%, respectively, at Re of 200,000 when comparing the SG6043 modified 3 airfoil to the EYO7-8, EYO8-8, and EY9-8 airfoils.

When comparing the SG6043 modified 1 airfoil to the EYO7-8, EYO8-8, and EY9-8 airfoils at Re of 300,000, the maximum C_L/C_D rose by 2.20, 3.33, and 6.52%, respectively.

By comparing the SG6043 modified 2 airfoil to the EYO7-8, EYO8-8, and EY9-8 airfoils at Re of 300,000, the maximum C_L/C_D increased by 4.52%, 5.68%, and 8.90%, respectively.

Comparing the SG6043 modified 3 airfoil to the EYO7-8, EYO8-8, and EY9-8 airfoils resulted in increases in the maximum C_L/C_D of 9.30%, 10.52%, and 13.92%, respectively, at Re of 300,000.

When comparing the EYO7-8, EYO8-8, and EY9-8 airfoils to the SG6043 modified 1 airfoil, the maximum C_L/C_D rose by 0.058%, 6.53%, and 7.54%, respectively, at a Re of 400,000.

The maximum C_L/C_D increased by 4.27%, 11.01%, and 12.79%, respectively, at Re of 400,000 when comparing the SG6043 modified 2 airfoil to the EYO7-8, EYO8-8, and EY9-8 airfoils.

At a Re of 400,000, when comparing the EYO7-8, EYO8-8, and EY9-8 airfoils to the SG6043 modified 3 airfoil, the maximum C_L/C_D improved by 2.02%, 8.63%, and 9.66%, respectively.

The maximum C_L/C_D was enhanced by 1.62%, 4.40%, and 7.70%, respectively, at Re of 500,000 when comparing the SG6043 modified 1 airfoil to the EYO7-8, EYO8-8, and EY9-8 airfoils.

The maximum C_L/C_D increased by 0.82%, 3.58%, and 6.85%, respectively, at Re of 500,000 when comparing the SG6043 modified 2 airfoil to the EYO7-8, EYO8-8, and EY9-8 airfoils.

When comparing the SG6043 modified 3 airfoil to the EYO7-8, EYO8-8, and EY9-8 airfoils at Re of 500,000, the maximum C_L/C_D improved by 0.27%, 3.02%, and 6.27%, respectively.

The results revealed that the newly developed EYO-Series airfoils had a lower maximum C_L/C_D than the SG6043 modified 1, SG6043 modified 2, and SG6043 modified 3 airfoils. Additionally, as compared to SG6043 and EYO-Series airfoils, they use fewer materials due to the optimal *t*/*c*, which lowers the cost of production and uses fewer natural resources. Hence, the SG6043 modified airfoils are appropriate for usage in SWT blades due to their aerodynamic performance results.

Furthermore, the modified airfoils at high Re will be compared to the SG6043 airfoil in the upcoming phase of the Solar Turbine Arta Energy (STAE) project. Moreover, a study into other airfoils using *t*/*c* at various Re will be carried out. As a sum up, for the construction of a three-bladed horizontal axis wind turbine, extensive CFD computations, PIV flow visualization, and wind tunnel testing will be carried out.

Author contributions: Conceptualization, HSD and MSD; methodology, MYAJ and MSD; software, MYAJ and MSD; validation, MYAJ, MSD and HSD; formal analysis, MYAJ, MSD and HSD; investigation, MYAJ, MSD and HSD; resources, MYAJ, MSD and HSD; data curation, MYAJ, MSD and HSD; writing—original draft preparation, MSD; writing—review and editing, MYAJ; visualization, MYAJ, MSD and HSD; supervision, MYAJ; project administration, MYAJ; funding acquisition, MSD. All authors have read and agreed to the published version of the manuscript.

Conflict of interest: The authors declare no conflict of interest.

Nomenclature

AoA	The angle of attack (Deg)
AoA_{stall}	stall angle (Deg)
c	chord length (m)
C_L	The lift coefficient (-)
C_D	drag coefficient (-)
D	drag force (N)
l	Airfoil span (m)
L	lift force (N)
L/D	lift-to-drag (-)
L/D_{max}	peak lift-to-drag (-)
Re	the Reynolds number (-)
U	Air velocity (m/s)
X/C	Relative chord position (-)

Greek letters

ρ	The density of the air (Kg/m^3)
υ	Kinematic viscosity (m^2 s^{-1})
μ	Dynamic viscosity (Kg m^{-1} s^{-1})

References

1. Seifi H, Kouravand S, Davary MS, Mohammadzadeh S. Numerical and Experimental study of the effect of increasing aspect ratio of self-starting force to vertical axis wind turbine. Journal of Renewable and New Energy. 2023; 10(1): 1–14. doi: 10.52547/jrenew.10.1.1
2. Singh RK, Ahmed MR. Blade design and performance testing of a small wind turbine rotor for low wind speed applications, Renewable Energy. 2013; 50: 812–819. doi: 10.1016/j.renene.2012.08.021
3. Akour SN, Al-Heymari M, Ahmed T, Khalil KA. Experimental and theoretical investigation of micro wind turbine for low wind speed regions. Renewable Energy. 2018; 116: 215–223. doi: 10.1016/j.renene.2017.09.076
4. Seifi Davari H, Kouravand S, Seify Davari M, Kamalnejad Z. Numerical investigation and aerodynamic simulation of Darrieus H-rotor wind turbine at low Reynolds numbers. Energy Sources, Part A: Recovery, Utilization, and Environmental Effects. 2023; 45(3): 6813–6833. doi: 10.1080/15567036.2023.2213670
5. Giguere P, Selig MS. Low Reynolds number airfoils for small horizontal axis wind turbines. Wind Engineering. 1997; 367–380.
6. Akram MT, Kim MH. Aerodynamic shape optimization of NREL S809 airfoil for wind turbine blades using Reynolds-averaged navier stokes model—Part II. Applied Sciences. 2021; 11: 2211. doi: 10.3390/app11052211
7. Longtin Martel S, Bashir M, Botez RM, Wong T. A Pareto Multi-Objective Optimization of a Camber Morphing Airfoil using Non-Dominated Sorting Genetic Algorithm. In: Proceedings of the AIAA SCITECH 2023 Forum; 23–27 January 2023; National Harbor, MD, USA. p. 1583.
8. Wu X, Zhang W, Peng X, Wang Z. Benchmark aerodynamic shape optimization with the POD-based CST airfoil parametric method. Aerospace Science and Technology. 2019; 84: 632–640. doi: 10.1016/j.ast.2018.08.005
9. Tirandaz MR, Rezaeiha A. Effect of airfoil shape on power performance of vertical axis wind turbines in dynamic stall: Symmetric Airfoils. Renewable Energy. 2021; 173: 422–441. doi: 10.1016/j.renene.2021.03.142
10. Huang S, Hu Y, Wang Y. Research on aerodynamic performance of a novel dolphin head-shaped bionic airfoil. Energy. 2021; 214: 118179. doi: 10.1016/j.energy.2020.118179
11. Osei EY, Opoku R, Sunnu AK, Adaramola MS. Development of high performance airfoils for application in small wind turbine power generation. Journal of Energy. 2020; 1–9. doi: 10.1155/2020/9710189
12. Osei EY, Opoku R, Sunnu AK, et al. Aerodynamic performance characteristics of EYO-Series low Reynolds number airfoils for small wind turbine applications. Alexandria Engineering Journal. 2022; 61: 12301–12310. doi: 10.1016/j.aej.2022.05.049
13. Hu H, Zhang G, Li D, et al. Shape optimization of airfoil in ground effect based on free-form deformation utilizing sensitivity analysis and surrogate model of artificial neural network. Ocean Engineering. 2022; 257: 111514. doi: 10.1016/j.oceaneng.2022.111514
14. Santos GB, Pantaleão AV, Salviano LO. Using deep generative adversarial network to explore novel airfoil designs for vertical-axis wind turbines. Energy Conversion and Management. 2023; 282: 116849. doi: 10.1016/j.enconman.2023.116849
15. Achour G, Sung WJ, Pinon-Fischer OJ, Mavris DN. Development of a conditional generative adversarial network for airfoil shape optimization. In: Proceedings of the AIAA Scitech 2020 Forum; 6–10 January 2020; Orlando, FL, USA. p. 2261.
16. Lim H, Kim H. Multi-objective airfoil shape optimization using an adaptive hybrid evolutionary algorithm. Aerospace Science and Technology. 2019; 87: 141–153. doi: 10.1016/j.ast.2019.02.016
17. Guo G, Zhu W, Sun Z, et al. Drag reducer design of wind turbine blade under flap-wise fatigue testing. Composite Structures. 2023; 318: 117094. doi: 10.1016/j.compstruct.2023.117094
18. Boudis A, Hamane D, Guerri O, Bayeul-Lainé AC. Airfoil Shape Optimization of a Horizontal Axis Wind Turbine Blade using a Discrete Adjoint Solver. Journal of Applied Fluid Mechanics. 2023; 16(4): 724–738. doi: 10.47176/JAFM.16.04.1493

19. Echavarria C, Hoyos JD, Jimenez JH, et al. Optimal airfoil design through particle swarm optimization fed by CFD and XFOIL. Journal of the Brazilian Society of Mechanical Sciences and Engineering. 2022; 44(11): 561. doi: 10.1007/s40430-022-03866-4
20. Rangriz S, Kheiri M. Design of optimal airfoils for airborne wind energy applications. In: Proceedings of the AIAA SCITECH 2023 Forum; 23–27 January 2023; National Harbor, MD, USA. p. 1155.
21. Kumar S, Narayanan S. Airfoil thickness effects on flow and acoustic characteristics. Alexandria Eng. J. 2022; 61: 4679–4699. doi: 10.1016/j.aej.2021.10.022
22. Song Q, Lubitz WD. Design and testing of a new small wind turbine blade. Journal of Solar Energy Engineering. 2014; 136(3): 4. doi: 10.1115/1.4026464
23. Akuffo FO, Brew-Hammond A, Antonio J, et al. Solar and Wind Energy Resource Assessment (SWERA). Energy Commission Ghana; 2003.
24. Bai CJ, Wang WC, Chen PW, Chong WT. System integration of the horizontal-axis wind turbine: The design of turbine blades with an axial-flux permanent magnet generator. Energies. 2014; 7(11): 7773–7793. doi: 10.3390/en7117773
25. Renganathan SA, Maulik R, Ahuja J. Enhanced data efficiency using deep neural networks and Gaussian processes for aerodynamic design optimization. Aerospace Science and Technology. 2021; 111: 106522. doi: 10.1016/j.ast.2021.106522
26. Acarer S. Peak lift-to-drag ratio enhancement of the DU12W262 airfoil by passive flow control and its impact on horizontal and vertical axis wind turbines. Energy. 2020; 201: 117659. doi: 10.1016/j.energy.2020.117659
27. Wei X, Wang X, Chen S. Research on parameterization and optimization procedure of Low-Reynolds-number airfoils based on genetic algorithm and Bezier curve. Advances in Engineering Software. 2020; 149: 102864. doi: 10.1016/j.advengsoft.2020.102864
28. Singh RK, Ahmed MR, Zullah MA, Lee Y. Design of a low Reynolds number airfoil for small horizontal axis wind turbines. Renewable Energy. 2012; 42: 66–76. doi: 10.1016/j.renene.2011.09.014
29. Giguere P, Selig MS. New airfoils for small horizontal axis wind turbines. J. Sol. Energy Eng. 1998; 120: 108–114. doi: 10.1115/1.2888052
30. Meana-Fernández A, Díaz-Artos L, Fernández Oro JM, Velarde-Suárez S. An optimized airfoil geometry for vertical-axis wind turbine applications. International Journal of Green Energy. 2020; 17: 181–195. doi: 10.1080/15435075.2020.1712211

Mechanical Engineering Advances 2025, 3(2), 2878.
https://doi.org/10.59400/mea2878

Article

Semi-analytical solution for nonlinear Von Kármán swirling fluid flow via the hybrid analytical and numerical method

Ali Ahmadi Azar

Department of Mechanical Engineering, North Tehran Branch, Islamic Azad University, Tehran, Iran; aliahmadiazar.mech@gmail.com, a.ahmadi.azar@iau-tnb.ac.ir

CITATION

Ahmadi Azar A. Semi-analytical solution for nonlinear Von Kármán swirling fluid flow via the hybrid analytical and numerical method. Mechanical Engineering Advances. 2025; 3(2): 2878. https://doi.org/10.59400/mea2878

ARTICLE INFO

Received: 1 March 2025
Accepted: 1 April 2025
Available online: 10 April 2025

COPYRIGHT

Copyright © 2025 by author(s). *Mechanical Engineering Advances* is published by Academic Publishing Pte. Ltd. This work is licensed under the Creative Commons Attribution (CC BY) license. https://creativecommons.org/licenses/by/4.0/

Abstract: This study investigates the nonlinear and classical problem of Von Kármán's viscous swirling fluid flow caused by a single rotating disk. Despite over a century since this problem was first introduced, recent advancements enable more accurate calculations and practical results than previously possible. The core innovation of this paper lies in the application of the Hybrid Analytical and Numerical method (HAN method), which facilitates the derivation of a semi-analytical solution to complex nonlinear differential equations. The HAN method combines numerical and analytical approaches to solve nonlinear problems. Initially, the system of nonlinear differential equations is solved using an arbitrary numerical method. The numerical solution then aids in extracting the analytical solution, which can take forms such as polynomial solutions with constant and unknown coefficients. Since boundary conditions lack the capacity to generate a sufficient number of algebraic equations, the numerical solution provides the additional required equations. The flexibility of the HAN method stems from its ability to leverage various numerical methods, making it a robust approach for solving nonlinear differential equations. Using this methodology, the Von Kármán problem is analytically calculated with remarkable accuracy. Furthermore, this study provides highly precise calculations of several physical and practical outputs, including the thickness of the layer, the slope of flow lines at the wall in the peripheral direction, the peripheral component of wall shear stress, the moment on one side of the wetted disk, the dimensionless moment coefficient for both sides of the disk, Reynolds number as a function of the disk's finite radius, volume flux, and mechanical power. This research contributes to two main perspectives: first, the mathematical aspect, which demonstrates the ability of the HAN method to solve various nonlinear problems; second, the practical-physical perspective, showcasing the enhanced accuracy and reliability of the obtained results in analyzing fluid flow mechanics.

Keywords: Von Kármán swirling viscous flow; semi-analytical solution; the Hybrid Analytical and Numerical Method; the HAN-method

1. Introduction

In fluid mechanics, rotating flows are a common phenomenon due to many industrial, mechanical, and environmental applications such as rotary pumps, fans, turbines, boilers and chemical storage, cyclone separators, and rotating disks of nuclear reactors, and have attracted considerable attention [1]. The Von Kármán rotational viscous flow is a well-known classical problem in fluid mechanics, and Von Kármán [2], in this famous problem, investigated the viscous fluid flow resulting from the rotation of a disk in such a way that the fluid far from the disk is stationary and introduced new variables called similarity transformations that allowed PDEs to be converted to ODEs, which later were called the Von Kármán similarity variables. More recent results were obtained by the Cochran [3] with a modification of the Von Kármán problem. Von Kármán’s answers contained errors that Cochran corrected. Bödewadt [4] was also the first to present a problem in which the disk is stationary and the fluid flow is the result of fluid rotation from a distance away from the disk. Just like rotating the coffee in the cup, the bottom of the cup is fixed, but by rotating the coffee, the fluid rotation is transferred everywhere. This form of fluid flow was later called Bödewadt flow, and Fettis [5] was one of the first to use Bödewadt flow. Rogers and Lance [6] studied the case where the fluid rotates at infinity with different uniform velocities in the same direction as the disc velocity, and the results of Von Kármán [2] and Bödewadt [4] were obtained in special cases. Batchelor [7] studied the problem in which the fluid is flowing due to the rotation of the disc with different uniform velocities and also different velocities of the fluid at certain distances. Specific distances mean both the infinite distance, which means the distance far from the disk, and the specified distances or close to the disk. Batchelor [7] studied the problem in which the fluid flows with different uniform velocities at certain distances and the rotation of the disk with different uniform velocities. Certain distances mean both infinite distance, which means far from the disk, and certain distances or close to the disk. Benton [8] extended Von Kármán’s rotating disc problem to a transient problem and also solved Von Kármán’s steady-state problem for more accuracy. Zandbergen and Dijkstra [9] presented a review paper of the studies [3,5,6,8], and also, in the mentioned studies [3–8], Von Kármán similarity variables have been used to convert the PDEs of the governing equations into ODEs. Tien and Tsuji [10] made theoretical inferences using numerical methods for the temperature distribution and heat transfer results due to the forced laminar motion on a non-isothermal rotating plate. Evans and Greif [11] analyzed the flow between two parallel plates. One is porous, unheated, and stationary, and the other is impermeable, heated, and rotating. The PDEs were reduced into a set of nonlinear ODEs via similarity transformation, and then the ODEs were solved numerically. By using the perturbation method, Sharma [12] investigated the fluid flow that is constrained by two infinitely swirling plates for three cases: the first case is when the plates have the same angular velocity, the second case is when the plates have different angular velocities, and the third case is when one plate has angular velocity and the other is at rest. Kumari et al. [13] investigated the asymmetric motion produced by the flow of a conductive fluid in a rotating infinite plate. There is also a magnetic field perpendicular to the plane. Similarity transformation is also considered for reducing the governing equations into a set of ODEs and solved numerically by the shooting method. Ozetkin and Brown [14] studied the viscometric motion of the viscoelastic fluid that is between two swirling parallel disks. Deshpande and Ghosh [15] studied the unsteady fluid flow that was caused by an infinite swirling disk numerically. Choudhury and Das [16] investigated the fluid motion that is constrained between two spinning disks, which has the elastic-viscous property. Shevchuk and Buschmann [17] investigated the fluid that co-rotates with the spinning disk. The governing equations were reduced into a set of ODEs by the similarity transformation, and then the ODEs were solved numerically. The heat transfer problem studied by aus der Wiesche [18] when the air flow passes from a swirling disk numerically. Hayat et al. [19] studied the MHD swirling flow of a fluid in a porous medium where the fluid model obeys the modified Darcy’s law. The Hall effect was also considered for this model, and finally, ODEs were solved by the HAM. Yang and Liao [20] solved the classical problem of Von Kármán [2] analytically by the HAM and compared the analytical results with the previous numerical solutions. Attia [21] investigated non-Newtonian, incompressible, and viscous fluid and considered the motion of this fluid on a stretchable swirling disk. The governing equations of the steady-state fluid flow were reduced into nonlinear ODEs, and they were solved numerically by the finite difference method. Bessaïh et al. [22] analyzed the stability of the swirling flow of liquid metal between two disks filled in a cylindrical chamber. One of the disks rotates at a certain temperature, while the other remains stationary at a different temperature. The governing equations were in PDE form and were solved numerically through FVM. Rahman and Postelnicu [23] investigated the thermal effects of the fluid flow caused by a rotating disk with a temperature different from the environment and then solved the equations numerically. Similar to Yang and Liao [20], Abdou [24] solved the classical problem of Von Kármán [2] analytically with the homotopy perturbation method. Turkyilmazoglu [25] investigated a boundary layer problem that is concerned with the motion of the fluid created by the rotation of a disk that disk injection or suction ability. Turkyilmazoglu [26] studied the fluid boundary layer that was caused by a swirling disk in a steady-state condition and solved by the analytical method of homotopy analysis. The results of the homotopy analysis technique compared with the numerical method of Runge-Kutta. Rashidi et al. [27] analyzed the second law of thermodynamics for nanofluid flow on a rotating disk. The vertical magnetic field is also presented in the problem. The governing equations were reduced to ODEs by converting to similarity, and then the ODEs were solved numerically. The study of Alam et al. [28] concerned the transient forced convective fluid flow that resulted from a swirling disk. The particles of fluid flow were assumed to be of micro size. The governing equations were transformed into the ODEs by the similarity transformation and solved numerically. Hayat et al. [29] analyzed the problem of ferrofluid flow bounded by two parallel planes, which are infinite planes but have different angular velocities. The governing equations were converted to ODEs by similarity transformation and converted to ODEs by the HAM. Doh et al. [30] studied micropolar fluid flow created by a rotating plate. A magnetic field perpendicular to that plane is also applied. The PDEs of the governing equations were converted into ODEs using similarity transformation and solved numerically. Das and Sahoo [31] studied the Reiner-Rivlin fluid flow problem confined between two parallel rotating infinite disks. The governing equations were transformed into a set of ODEs by similarity transformation and then solved using the homotopy method. Kumar et al. [32] carried out a numerical investigation on the problem of rotating flow of a Rainer-Rivlin fluid, where the surface of a rotating disk satisfies the Navier velocity slip condition in the presence of a magnetic field. Temperature jump conditions because of incomplete liquid-solid energy matching are also considered. Visuvasam and Alotaibi [33] did analytical research on the problem related to the rotating Von Kármán flow of a viscous incompressible fluid due to a rotating disk electrode. The governing equations are based on four nonlinear coupled differential equations and were solved by homotopy analysis. Ali et al. [34] investigated the problem of non-transient and incompressible convective flow of Rainer-Rivlin nanofluid through a rotating disk with different slip conditions. The governing equation was reduced to five coupled nonlinear ODEs with the help of similarity variables and solved through the BVP4c numerical method. In a recent study, a new semi-analytical method known as the Hybrid Analytical and Numerical Method (HAN method) was introduced for the first time by Jalili et al. [35]. This method was employed to solve the equations addressing the heat and mass transfer of a viscous, incompressible, laminar axisymmetric flow of a micropolar fluid in the presence of a magnetic field, constrained between two stretchable disks. To enhance the credibility and relevance of the HAN method, the article incorporates references to additional published studies [36–39] where this method has been effectively applied to solve governing equations similar to those addressed in the current study. In a recent study, the Hybrid Analytical and Numerical Method (HAN method), initially introduced by A. Ahmadi Azar, was applied as a semi-analytical technique to analyze the non-transient forced motion of a non-Newtonian MHD Reiner-Rivlin viscoelastic fluid confined between two plates [36]. The model included the presence of a magnetic field. The governing equations, initially in partial differential equation (PDE) form, were transformed into a set of ordinary differential equations (ODEs) using the Von Kármán similarity variables. The HAN method was then applied to solve the ODEs and their associated boundary conditions analytically. For validation, the results obtained from the HAN method were compared with those derived from the Homotopy Perturbation Method (HPM) and the numerical Runge-Kutta technique. Additionally, new quantitative results were extracted from the HAN solutions. Another study explored the steady, laminar, incompressible, and two-dimensional flow of a micropolar fluid between two disks [37]. In this analysis, the upper disk was assumed to be porous, while the lower one was non-porous. Body forces and body couples were disregarded, and the flow was considered fully developed. The governing equations were transformed into a set of ordinary differential equations (ODEs) using Von-Kármán's similarity variables. Since these ODEs had not been previously solved analytically, the Modified Akbari-Ganji Method (Modified AGM) and the Hybrid Analytical and Numerical Method (HAN method) were employed to obtain semi-analytical solutions. A primary novelty of the study was the application of these methods to achieve such solutions, although much of the innovation lay in the physical insights derived from the analytical results. The impacts of various slip coefficients, Reynolds numbers, and micropolar parameters—such as vortex viscosity, spin gradient viscosity, and microinertia density—were examined on profiles of normal velocity, streamwise velocity, and microrotation. The validity of the solutions was demonstrated through comparison with previously published results, with both methods producing nearly identical findings in all cases, indirectly confirming the reliability of the results. In another study [38], the Hybrid Analytical and Numerical Method (HAN method) was employed to solve nonlinear coupled ordinary differential equations (ODEs), investigating the effects of structural changes such as variations in the stretching rate and the distance between two disks on key physical quantities. The study demonstrated that an increased stretching rate significantly raised the temperature and Nusselt number, while increasing the distance between the disks led to a substantial reduction in microrotation and wall couple stress. By redefining parameters such as the magnetic parameter, Eckert number, stretching Reynolds number, and micropolar parameters, the research focused on analyzing physical quantities impacted by these structural changes. The findings were validated through comparisons with prior studies, ensuring accuracy and reliability. In another study [39], the HAN method was used to find an exact solution for the Von Kármán swirling viscous fluid flow caused by a rotating disk with uniform suction. Three cases were considered: swirling flow at infinity with directions opposite and similar to the angular velocity of the rotating disk, no swirling flow with suction on the disk's surface, and both swirling flow and suction on the disk. The findings revealed that when the angular velocity of the fluid at infinity decreased relative to the angular velocity of the disk, the skin friction coefficient reached its maximum, while an increase in fluid angular velocity led to its reduction. For the second case, higher surface suction caused an increase in the skin friction coefficient, making it greater on porous disks than on non-porous ones. Additionally, under specific conditions where both swirling flow and suction were absent, the pressure distribution depended solely on the distance above the disk. These results demonstrated the effectiveness of the HAN method in solving complex fluid flow scenarios and analyzing skin friction and pressure distributions in varying conditions. However, the HAN method is not limited to studies related to swirling flow due to the one or two disks [40–49]. Xu and Liao [50] studied the unsteady motion of a conducting viscous fluid driven by a rapidly spinning infinite disk. They employed the HAM to derive analytical solutions, first converting the governing Navier-Stokes equations into a system of nonlinear PDEs through novel similarity transformations. Their approach yielded convergent series solutions that remained valid across all time scales ($0 \leq \tau < \infty$) and throughout the entire flow domain ($0 \leq \eta < \infty$). This represented a significant advancement, as such comprehensive analytical solutions hadn't been achieved before. The work also quantified how magnetic field strength influenced the fluid's velocity characteristics. Mehmood et al. [51] employed the HAM to obtain analytical solutions for unsteady Von Kármán swirling flow induced by a suddenly rotating infinite disk, presenting complete closed-form solutions valid across all time ($0 \leq \tau \leq \infty$) and space ($0 \leq \eta \leq \infty$). Their results showed excellent agreement with Yang and Liao's [20] steady-state solution ($\tau \to \infty$) and revealed that flow velocity gradually increases over time until reaching steady-state conditions, while the hydrodynamic boundary layer thickness initially grows before stabilizing at a constant value. These analytical solutions serve as valuable benchmarks for numerical simulations in applications like helicopter rotor aerodynamics, rotating electrochemical systems, and turbine blade flow analysis. Sadiq [52] investigated unsteady viscous flow over a decelerating, rotating, stretchable disk. The study transformed the governing nonlinear partial differential equations into ordinary differential equations using similarity transformations, then solved them analytically using the HAM. The research demonstrated the convergence of HAM solutions and validated results through comparison with numerical solutions. Key findings included the effects of disk stretching and unsteadiness parameters on flow characteristics. The work provides analytical solutions for this complex rotating flow system with practical applications in rotating machinery and industrial processes involving stretchable surfaces. Finally, the analytical studies about the transient fluid flows due to one disk are developed by Bég et al. [53]. They investigated transient nanofluid flow around a time-dependent spinning sphere for coating applications, transforming the governing equations into a ninth-order nonlinear system using similarity variables. They solved this computationally challenging problem using the

HAM, verifying results with Adomian decomposition (ADM), and analyzed how acceleration, rotation, Brownian motion, thermophoresis, Lewis and Prandtl numbers affect shear stress, heat/mass transfer, and boundary layer behavior. The study demonstrated HAM's effectiveness in handling this complex nanofluid system, providing accurate solutions with good convergence that advance understanding of rotating-body nanofluid dynamics for industrial applications.

In this study, the classical problem of Von Kármán [2] that concerned the three-dimensional steady, laminar, axially-symmetric viscous fluid flow caused by an infinite radius disk with uniform angular velocity about z-axis. The partial governing differential equations of the problem are in a cylindrical coordinate system, and they are reduced into a system of coupled nonlinear ODEs with the help of Von Kármán similarity variables. Despite all these years since the introduction of this problem, Von Kármán's equations have not been approximated with great accuracy. Since the introduction of this problem in fluid mechanics, it has been solved many times by numerical methods [2,3]. But with the computers available to researchers today, these equations can be obtained with much greater accuracy than previously published numerical results. Also, various analytical solutions were presented [20,24], but the weak points of these analytical solutions are the large number of solution sentences. Therefore, according to these weaknesses of published analytical and numerical solutions, it is possible to compensate for the deficiencies of the past, and for this purpose, the HAN method is one of the most appropriate methods to achieve an accurate analytical solution. So, the innovation of this article is to show the application of the semi-analytical method of HAN in approximating the equations of a classic problem analytically with high accuracy.

2. Methodology

This part of the article belongs to the derivation of dimensionless Von Kármán's equations from the governing equations of conservation of mass and momentum in three directions by using the similarity variable introduced by Von Kármán [2]. **Figure 1** shows a geometric schematic of the problem, which represents a three-dimensional flow and shows the rotational motion of the fluid resulting from the uniform swirling of a disk with infinite radius.

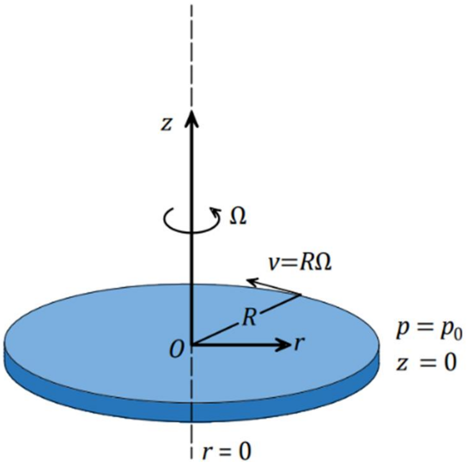

Figure 1. Geometric schematic of the problem.

In this problem and according to **Figure 1**, the disk is rotating with a constant angular velocity of Ω, and due to the viscosity of the fluid and the lack of fluid slip on the surface, the fluid rotates with the disk and causes a rotational flow. According to the figure, it can be said that the highest rotational velocity is near the disk, and the rotational velocity causes the rotating fluid to be pushed out along the radius of the disk, which is denoted by r. The fluid pushed around the disk creates a vacuum, and the vacuum itself causes fluid suction along the disk's axis of rotation. So, it can be said that the rotation of the disk is like a three-dimensional pump that sucks the fluid from above and pushes it along the radius of the disk. The steady governing partial differential equations of momentum and mass in the cylindrical coordinate system for the laminar, axially symmetric, viscous, and incompressible fluid flow are as follows:

The equation of conservation of mass [20,24]:

$$\frac{1}{r}\frac{\partial(rV_r)}{\partial r}+\frac{1}{r}\frac{\partial V_\theta}{\partial \theta}+\frac{\partial V_z}{\partial z}=0 \tag{1}$$

The equation of conservation of momentum along r-axis [20,24]:

$$V_r\frac{\partial V_r}{\partial r}+V_z\frac{\partial V_z}{\partial z}-\frac{V_\theta^2}{r}=\nu\left[\frac{\partial^2 V_r}{\partial r^2}+\frac{1}{r}\frac{\partial V_r}{\partial r}+\frac{\partial^2 V_r}{\partial z^2}-\frac{V_r}{r^2}\right]-\frac{1}{\rho}\frac{\partial p}{\partial r} \tag{2}$$

The equation of conservation of momentum along θ-axis [20,24]:

$$V_r\frac{\partial V_\theta}{\partial r}+V_z\frac{\partial V_\theta}{\partial z}+\frac{V_\theta V_r}{r}=\nu\left[\frac{\partial^2 V_\theta}{\partial r^2}+\frac{1}{r}\frac{\partial V_\theta}{\partial r}+\frac{\partial^2 V_\theta}{\partial z^2}-\frac{V_\theta}{r^2}\right] \tag{3}$$

The equation of conservation of momentum along z-axis [20,24]:

$$V_r\frac{\partial V_z}{\partial r}+V_z\frac{\partial V_z}{\partial z}=\nu\left[\frac{\partial^2 V_z}{\partial r^2}+\frac{1}{r}\frac{\partial V_z}{\partial r}+\frac{\partial^2 V_z}{\partial z^2}\right]-\frac{1}{\rho}\frac{\partial p}{\partial z} \tag{4}$$

where ρ is fluid density, ν is the kinematic viscosity, r, θ, and z are cylindrical coordinate components, p is the pressure, V_θ, V_r, and V_z are the velocity components along the azimuthal, radial, and axial axes, respectively. The boundary conditions of Equations (1)–(4) are as follows [20,24]:

$$\begin{gathered} V_\theta=r\Omega, V_r=V_z=0, p=p_0, \text{when } z=0 \\ V_r=V_z=0, \text{when } z=+\infty \end{gathered} \tag{5}$$

where the Ω is the constant angular velocity. With the help of the following similarity variables that were introduced by Von Kármán [2,20,24,54]:

$$\begin{gathered} V_r=r\Omega F(\xi) \\ \xi=(\Omega/\nu)^{1/2}z \\ V_\theta=r\Omega G(\xi) \\ V_z=(\nu\Omega)^{1/2}H(\xi) \\ p=p_0+\rho\nu\Omega P(\xi) \end{gathered} \tag{6}$$

where $F(\xi)$ is similarity radial velocity, $G(\xi)$ is similarity azimuthal velocity, $H(\xi)$ is the similarity axial velocity, $P(\xi)$ is the similarity pressure distribution perpendicular to the wall, ξ is the dimensionless wall distance, p_0 is pressure at surface of the disk, and p is the pressure distribution function. Equations (1)–(4) can be transformed into the following ordinary differential equation system [20,24,54]:

$$2F(\xi) + \frac{\mathrm{d}}{\mathrm{d}\xi}H(\xi) = 0 \tag{7}$$

$$F(\xi)^2 + \frac{\mathrm{d}}{\mathrm{d}\xi}F(\xi)H(\xi) - G(\xi)^2 - \frac{\mathrm{d}^2}{\mathrm{d}\xi^2}F(\xi) = 0 \tag{8}$$

$$2F(\xi)G(\xi) + H(\xi)\frac{\mathrm{d}}{\mathrm{d}\xi}G(\xi) - \frac{\mathrm{d}^2}{\mathrm{d}\xi^2}G(\xi) = 0 \tag{9}$$

$$\frac{\mathrm{d}}{\mathrm{d}\xi}P(\xi) + H(\xi)\frac{\mathrm{d}}{\mathrm{d}\xi}H(\xi) - \frac{\mathrm{d}^2}{\mathrm{d}\xi^2}H(\xi) = 0 \tag{10}$$

The boundary conditions of Equation (5) are reduced to the following dimensionless form by using Von Kármán similarity transformation variables [20,24,54]:

$$\begin{gathered} F(0) = 0, G(0) = 1, H(0) = 0, \\ P(0) = 0, F(\infty) = 0, G(\infty) = 0. \end{gathered} \tag{11}$$

According to the Equations (7)–(10), the velocity fields of $F(\xi)$, $H(\xi)$, and $G(\xi)$ are coupled with each other except for the $P(\xi)$ and the pressure distribution perpendicular to the wall can be determined after solving Equations (7)–(9) with their corresponding boundary conditions of Equation (11). First the velocity field is determined from solving the Equations (7)–(10), and then the $P(\xi)$ is calculated. So, the pressure can be found as below [54]:

$$P(\xi) = \int \frac{\mathrm{d}}{\mathrm{d}\xi}P(\xi)\mathrm{d}\xi = \int \left[\frac{\mathrm{d}^2}{\mathrm{d}\xi^2}H(\xi) - H(\xi)\frac{\mathrm{d}}{\mathrm{d}\xi}H(\xi)\right]\mathrm{d}\xi = \frac{\mathrm{d}}{\mathrm{d}\xi}H(\xi) - \frac{1}{2}H(\xi)^2 \tag{12}$$

In addition to obtaining the solution of the pressure distribution after solving Equations (7)–(9), it is possible to obtain the thickness of the layer, the slope of the streamlines at the wall to the circumferential direction, the peripheral component of the shear stress of the wall, the moment of one side of the wetted disk, the dimensionless coefficient for the moment on both sides of the wetted disk, the Reynolds number in terms of the finite radius of the disk, the volume flux, and the mechanical power [54].

By substituting a specific value of $\xi = \xi_{1\%}$ into Equation (13) when the fluid's circumferential velocity of V_r is approximately 1% of the disk velocity, the layer thickness of δ can be calculated as below:

$$\delta = \xi(\nu/\Omega)^{1/2} \tag{13}$$

The slope of the flow lines in the wall in the circumferential direction is denoted by φ_0 and it is formulated as below:

$$\varphi_0 = \tan^{-1}\left(\left(-\frac{\partial V_r/\partial z}{\partial V_\theta/\partial z}\right)_w\right) = \tan^{-1}\left(-\frac{F'(0)}{G'(0)}\right) \tag{14}$$

The parameters of δ and φ_0 are related only to rotating disks with infinite radius. The results now apply to a circular disk of finite radius R. It is certainly allowed if the radius R is large compared to the thickness δ of the disc carrier layer so that the edge effects are limited in the entire circular region. into a small ring-shaped area. The circumferential component of the wall shear stress is denoted by $\tau_{z\varphi}$ and it is as below:

$$\tau_{z\varphi} = \mu(\partial V_\theta/\partial z)_w = \rho r\Omega(\nu\Omega)^{1/2}G'(0) \tag{15}$$

The moment of a disk wetted on one side is denoted by M and it is as follows:

$$M = \int_0^R -2\pi r^2 \tau_{z\phi} \mathrm{d}r = -\frac{\pi}{2}\rho R^4 (\nu\Omega^3)^{\frac{1}{2}} G'(0) \tag{16}$$

where r is variable of radius and R is the finite radius of the disk. It is common to have the following dimensionless coefficient of c_M for the moment introduced for the disc wetted on both sides:

$$c_M = \frac{2M}{\rho\Omega^2(R^5/2)} \tag{17}$$

The Reynolds number of Re is formulated as below:

$$Re = \frac{R^2\Omega}{\nu} \tag{18}$$

Due to considering the laminarity for the flow, the Reynolds number Equation (18) is valid up to 3×10^5 [54]. The parameters of $\tau_{z\phi}$, M, c_M, and Re that are already mentioned in Equations (15)–(18) can be calculated only when the radius of the disk is finite.

The volume flux that is sucked in the axial direction towards the plate and injected radially out by the centrifugal force from around a disk with a finite radius of R, is calculated as follows [54]:

$$Q = 2\pi R \int_0^\infty V_r \mathrm{d}z = -H(\infty)\pi R^2 (\nu\Omega)^{\frac{1}{2}} \tag{19}$$

where ∞ is the maximum value of ξ that is possible to calculate. Considering the proportionality of the pressure difference on the disc with $\rho\nu\Omega$, it can be said that at low viscosities, the pressure difference is very small, and the pressure depends only on the axial distance from the wall and therefore is independent of the radius R [54]. Since the fluid flow through the rotating discs acts as a pump, the fluid flow also experiences an increase in mechanical power P_M due to the increase in total pressure and is calculated as follows [54]:

$$P_M = \int_0^\infty \left[p + \frac{\rho}{2}\left(V_r^2 + V_\theta^2 + V_z^2\right)\right] 2\pi R V_r \mathrm{d}z = \pi\rho R^4 \Omega(\nu/\Omega)^{1/2} \left[\int_0^\infty (F(\xi)^2 + G(\xi)^2)F(\xi)\mathrm{d}\xi - \frac{4}{Re}\int_0^\infty F(\xi)^2 \mathrm{d}\xi\right] \tag{20}$$

Calculation of P_M is possible only when exact solutions of Equations (7)–(9) are obtained.

3. Mathematical description

3.1. Description of the HAN method

A new semi-analytical method called the HAN method [38,44,45,48] is capable of approximating many problems with unsolvable nonlinear equations. In this mathematical method for finding the analytical solution of an equation, the equation must first be solved numerically, and the numerical method in this method is not limited to a specific method, and this flexibility is one of the strengths of this method. Another strength of the HAN method is that it can be a power series with a much more limited number of sentences than other semi-analytical solutions. The explanation of this method is as follows:

The general form of differential equations with order of m will be as follows:

$$\Gamma\left(f(\xi), f'(\xi), f''(\xi), \dots, f^{(m)}(\xi)\right) = 0 \tag{21}$$

Equation (21) represents a nonlinear differential equation where Γ is a function of $f(\xi)$. The function $f(\xi)$ and its derivatives with respect to ξ are displayed as follows:

$$\begin{cases} f(\xi) = f_0, \quad f'(\xi) = f_1, \dots, \quad f^{(m-1)}(\xi) = f_{m-1} \text{ when } \xi = 0 \\ f(\xi) = f_{L_0}, \quad f'(\xi) = f_{L_1}, \dots, \quad f^{(m-1)}(\xi) = f_{L_{m-1}} \text{ when } \xi = L \end{cases} \tag{22}$$

The following n-order polynomial with constant coefficients is considered as the solution of Equation (21):

$$f(\xi) = \sum_{i=0}^{n} a_i \xi^i = a_0 + a_1\xi^1 + a_2\xi^2 + \dots + a_n\xi^n \tag{23}$$

The solution of Equation (21) is Equation (23), which is an nth-order polynomial with $n + 1$ unknown coefficients. Solving a system of $n + 1$ unknowns and $n + 1$ equations can determine unknown coefficients of Equation (23), or in other words, the solution of Equation (21) is calculated. We can achieve some of these equations with boundary conditions of the problem, which is shown in the following Equations (24) and (25):

$$\begin{cases} f(0) = a_0 = f_0, \\ f'(0) = a_1 = f_1, \\ f''(0) = a_2 = f_2, \\ \quad . \quad . \quad . \\ \quad . \quad . \quad . \end{cases} \tag{24}$$

$$\begin{cases} f(L) = a_0 + a_1L + a_2L^2 + \dots + a_nL^n = f_{L_0} \\ f'(L) = a_1 + 2a_2L + 3a_3L^2 + \dots + na_nL^{n-1} = f_{L_1} \\ f''(L) = 2a_2 + 6a_3L + 12a_4L^2 + \dots + n(n-1)a_nL^{n-2} = f_{L_2} \\ \quad . \quad . \quad . \\ \quad . \quad . \quad . \end{cases} \tag{25}$$

According to the numerical solution of Equation (21), the new approximated boundary conditions are as follows:

The constructed equations from boundary conditions of the problem, as they can be seen in Equations (24) and (25), are limited because we assume the value of n is higher than m earlier in this methodology. All the explanations given about HAN from Equations (21)–(25) overlap with the AGM method, but from here on the difference between the HAN and AGM methods will be explained. To increase the number of constructed equations to $n + 1$ equations, more boundary equations are needed, and the numerical methods (no matter which numerical method) can approximate these additional boundary conditions for making the remaining needed equations. So, the new approximated boundary conditions are as follows:

$$\begin{cases} f(\xi) = \alpha_0, f'(\xi) = \alpha_1, \dots, f^{(m-1)}(\xi) = \alpha_{m-1} \; at \; \xi = L_0 \\ f(\xi) = \beta_0, f'(\xi) = \beta_1, \dots, f^{(m-1)}(\xi) = \beta_{m-1} \; at \; \xi = L_1 \\ f(\xi) = \gamma_0, f'(\xi) = \gamma_1, \dots, f^{(m-1)}(\xi) = \gamma_{m-1} \; at \; \xi = L_2 \\ \quad . \quad . \quad . \\ \quad . \quad . \quad . \\ f(\xi) = \varepsilon_0, f'(\xi) = \varepsilon_1, \dots, f^{(m-1)}(\xi) = \varepsilon_{m-1} \; at \; \xi = L_z \end{cases} \tag{26}$$

The new approximated boundary conditions of Equation (26) from the numerical results can be used like Equations (24) and (25) for making new equations, and from Equation (26) it can be derived as many equations as are needed to create a system with $n + 1$ equations and $n + 1$ unknowns. For instance, from the following equations, Equations (27)–(30) shown new equations in addition to equations that were made through the boundary conditions of the problem:

$$\begin{cases} f(L_0) = a_0 + a_1(L_0) + a_2(L_0)^2 + \dots + a_n(L_0)^n = \alpha_0, \\ f'(L_0) = a_1 + 2a_2(L_0) + 3a_3(L_0)^2 + \dots + na_n(L_0)^{n-1} = \alpha_1, \\ f''(L_0) = 2a_2 + 6a_3(L_0) + 12a_4(L_0)^2 + \dots + n(n-1)a_n(L_0)^{n-2} = \alpha_2, \\ \quad . \quad . \quad . \\ \quad . \quad . \quad . \\ \left(f^{(m-1)}(\xi)\right)_{\xi = L_0} = \alpha_{m-1}. \end{cases} \tag{27}$$

$$\begin{cases} f(L_1) = a_0 + a_1(L_1) + a_2(L_1)^2 + \dots + a_n(L_1)^n = \beta_0, \\ f'(L_1) = a_1 + 2a_2(L_1) + 3a_3(L_1)^2 + \dots + na_n(L_1)^{n-1} = \beta_1, \\ f''(L_1) = 2a_2 + 6a_3(L_1) + 12a_4(L_1)^2 + \dots + n(n-1)a_n(L_1)^{n-2} = \beta_2, \\ \quad . \quad . \quad . \\ \quad . \quad . \quad . \\ \left(f^{(m-1)}(\xi)\right)_{\xi = L_1} = \beta_{m-1}. \end{cases} \tag{28}$$

$$\begin{cases} f(L_2) = a_0 + a_1(L_2) + a_2(L_2)^2 + \dots + a_n(L_2)^n = \gamma_0, \\ f'(L_2) = a_1 + 2a_2(L_2) + 3a_3(L_2)^2 + \dots + na_n(L_2)^{n-1} = \gamma_1, \\ f''(L_2) = 2a_2 + 6a_3(L_2) + 12a_4(L_2)^2 + \dots + n(n-1)a_n(L_2)^{n-2} = \gamma_2, \\ \quad . \quad . \quad . \\ \quad . \quad . \quad . \\ \left(f^{(m-1)}(\xi)\right)_{\xi = L_2} = \gamma_{m-1}. \end{cases} \tag{29}$$

$$\begin{cases} f(L_z) = a_0 + a_1(L_z) + a_2(L_z)^2 + \cdots + a_n(L_z)^n = \varepsilon_0, \\ f'(L_z) = a_1 + 2a_2(L_z) + 3a_3(L_z)^2 + \cdots + na_n(L_z)^{n-1} = \varepsilon_1, \\ f''(L_z) = 2a_2 + 6a_3(L_z) + 12a_4(L_z)^2 + \cdots + n(n-1)a_n(L_z)^{n-2} = \varepsilon_2, \\ \quad \cdot \quad \cdot \quad \cdot \\ \quad \cdot \quad \cdot \quad \cdot \\ \left(f^{(m-1)}(\xi)\right)_{\xi = L_z} = \varepsilon_{m-1}. \end{cases} \tag{30}$$

By solving the system of $n + 1$ equations with $n + 1$ unknowns that we already constructed, the constant coefficients of the polynomial solution of Equation (23) can be determined, and then these obtained values can be used as a semi-analytical solution for Equation (21). As mentioned earlier in this section of the article, it should be considered that only a limited part of the AGM method overlaps with the HAN method, and these two methods are completely different.

3.2. Application of the HAN-method

This section is about showing the application of the HAN method in finding the analytical solution of the Von Kármán equations. The governing equations of Von Kármán and their corresponding boundary conditions of Equations (7)–(11) were mentioned in Sec. (2) of the current paper. So, according to explanations given in Sec. (3.1), it is assumed that the following series are the solutions of Equations (7)–(9):

$$F(\xi) = \sum_{i=0}^{10} a_i \xi^i, G(\xi) = \sum_{i=0}^{10} b_i \xi^i, H(\xi) = \sum_{i=0}^{10} c_i \xi^i. \tag{31}$$

There are 33 unknown coefficients in Equation (31), and there have to be 33 equations in order to determine these series solutions of Equations (7)–(9). According to Equation (11), some limited number of equations can be made by the boundary conditions of the problem as below:

$$F(\xi)|_{\xi=0} = \sum_{i=0}^{9} a_i \xi^i \bigg|_{\xi=0} = a_0 = 0 \tag{32}$$

$$G(\xi)|_{\xi=0} = \sum_{i=0}^{9} b_i \xi^i \bigg|_{\xi=0} = b_0 = 1 \tag{33}$$

$$H(\xi)|_{\xi=0} = \sum_{i=0}^{9} c_i \xi^i \bigg|_{\xi=0} = c_0 = 0 \tag{34}$$

$$F(\xi)|_{\xi=+\infty} = \sum_{i=0}^{9} a_i \xi^i \bigg|_{\xi=+\infty} = 0 \tag{35}$$

$$G(\xi)|_{\xi=+\infty} = \sum_{i=0}^{9} b_i \xi^i \bigg|_{\xi=+\infty} = 0 \tag{36}$$

where the Equations (32)–(36) are 5 equations, but due to the semi-infinity of the boundary conditions of the problem, it is not possible to determine what ξ is at infinity. Then, among Equations (32)–(36), only Equations (32)–(34) are applicable. So, it is obvious that 3 equations are not enough because 30 more equations are needed to find all the unknown coefficients. The remaining equations must be made by the new boundary conditions, and it is possible when they are approximated by a numerical method of RK4. So, by solving Equations (7)–(9) with boundary conditions of Equations (11) numerically, the following approximated boundary conditions can be calculated, and they are demonstrated in the following **Table 1**:

Table 1. The numerical results $F(\xi)$, $G(\xi)$, $H(\xi)$, and $P(\xi)$ from RK4 method.

The Runge-Kutta solutions					
ξ	$F(\xi)$	$F'(\xi)$	$G(\xi)$	$G'(\xi)$	$H(\xi)$
0	0	0.5101887308	1	−0.6158937994	0
1	0.1801057123	−0.0157626785	0.4766431672	−0.3911422046	−0.2654256959
2	0.1187359055	−0.0739557439	0.2033285370	−0.1771959836	−0.5729889369
3	0.0579431177	−0.0455178756	0.0844172286	−0.0746402952	−0.7447389737
4	0.0254429777	−0.0216794352	0.0347439986	−0.0309804734	−0.8241490046
5	0.0106359117	−0.0094759338	0.0141547055	−0.0128296650	−0.8582098557
6	0.0042708523	−0.0040080425	0.0056284748	−0.0053135787	−0.8722151508
7	0.0015961207	−0.0016735748	0.0020965052	−0.0022017798	−0.8776977020
8	0.0004820674	−0.0006953943	0.0006326466	−0.0009128045	−0.8796148863
9	0.0000195560	−0.0002884880	0.0000256624	−0.0003785633	−0.8800495476
9.069895	0	−0.0002712777	0		−0.8800509002

The remaining 30 equations can be made from the approximated boundary conditions of **Table 1** just like how Equations (32)–(36) are created from Equation (11). Considering that writing these 30 new equations makes the paper longer and they are like Equations (32)–(36), writing them is omitted. Having 3 equations that were made from the boundary conditions of the problem and 30 other equations that were obtained from the approximated boundary conditions of **Table 1** made a mathematical system of 33 equations and 33 unknowns, and by solving it, all the unknown coefficients of Equation (31) are determined. So, the analytical solutions of Equations (7)–(10) are as follows:

$$\begin{aligned} F(\xi) = {} & -6.07431182 \times 10^{-9}\xi^{10} + 3.90124387 \times 10^{-7}\xi^{9} \\ & - 0.00001118416228\xi^{8} + 0.000188446481\xi^{7} \\ & - 0.00206538565\xi^{6} + 0.01535505061\xi\text{\textasciicircum}5 \\ & - 0.0779872538\xi\text{\textasciicircum}4 + 0.2632321130\xi\text{\textasciicircum}3 \\ & - 0.5413702437\xi\text{\textasciicircum}2 + 0.5227637854\xi, \end{aligned} \tag{37}$$

$$\begin{aligned} G(\xi) = &-1.77745633 \times 10^{-8}\xi^{10} + 9.75590571 \times 10^{-7}\xi^{9} \\ &- 0.00001118416228\xi^{8} + 0.000188446481\xi^{7} \\ &- 0.00206538565\xi^{6} + 0.01535505061\xi^{5} \\ &- 0.0779872538\xi^{4} + 0.2632321130\xi^{3} - 0.5413702437\xi^{2} \\ &+ 0.5227637854\xi, \end{aligned} \tag{38}$$

$$\begin{aligned} H(\xi) = &-1.97842177 \times 10^{-8}\xi^{10} + 1.150613857 \times 10^{-6}\xi^{9} \\ &- 0.0000296999488\xi^{8} + 0.000448000973\xi^{7} \\ &- 0.00436837101\xi^{6} + 0.0286496680\xi^{5} - 0.1263248188\xi^{4} \\ &+ 0.3550648993\xi^{3} - 0.5210507216\xi^{2} + 0.0021842162\xi. \end{aligned} \tag{39}$$

where Equation (37) represents the similarity radial velocity, Equation (38) represents the similarity azimuthal velocity field, and Equation (39) represents the similarity axial velocity field. According to Equation (12) in Sec. (2), the pressure field of $P(\xi)$ can be determined from the analytical solution of the axial velocity field of Equation (39). So, the pressure fields of $P(\xi)$ is as follows:

$$\begin{aligned} P(\xi) = &-1.042101443x + 1.065192313x^{2} - 0.5041611878x^{3} \\ &+ 0.0067258742x^{4} + 0.1590725166x^{5} - 0.1257837496x^{6} \\ &+ 0.05955338116x^{7} - 0.02041823728x^{8} \\ &+ 0.005403517588x^{9} - 0.001136782528x^{10} \\ &- 1.957076350 \times 10^{-16}x^{20} + 2.276399504 \times 10^{-14}x^{19} \\ &- 1.249546377 \times 10^{-12}x^{18} + 4.303652142 \times 10^{-11}x^{17} \\ &- 1.042944410 \times 10^{-9}x^{16} + 1.889872545 \times 10^{-8}x^{15} \\ &- 2.655567739 \times 10^{-7}x^{14} + 2.960303904 \times 10^{-6}x^{13} \\ &- 0.00002654710360x^{12} + 0.0001928910016x^{11} \\ &+ 0.0021842162, \end{aligned} \tag{40}$$

where Equations (37)–(40) are valid when $0 \leq \xi \leq 9$ and Reynolds numbers are up to 3×10^{5}. The graphical representation of Equations (37)–(40) is shown in **Figures 2** and **3** as below:

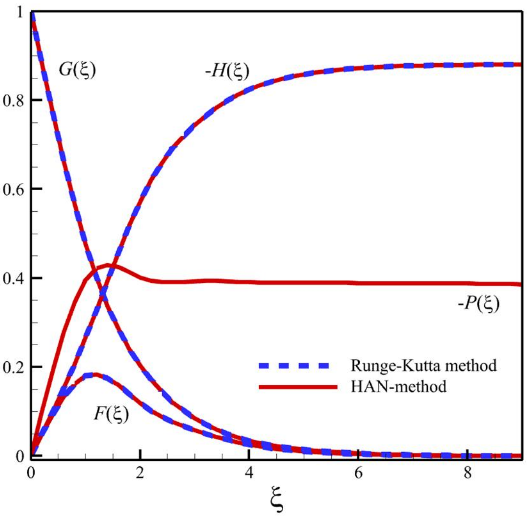

Figure 2. The graphical representation of $F(\xi)$, $G(\xi)$, $-H(\xi)$, and $-P(\xi)$ from the HAN method when they were compared with the RK4 solution.

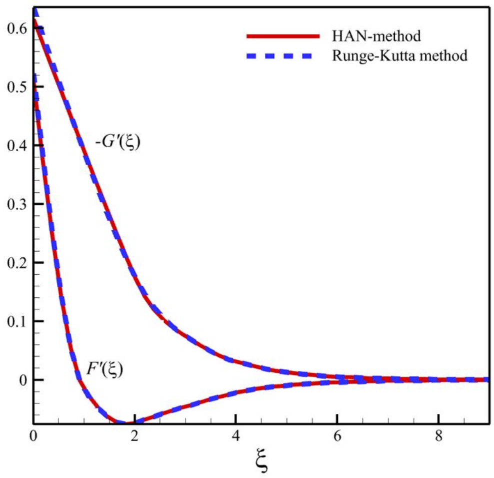

Figure 3. The graphical representation of $F'(\xi)$ and $-G'(\xi)$ from the HAN method when they were compared with the RK4 solution.

Considering the results of the analytical solutions of Equations (37)–(40) were made with the help of Equation (11) and the approximated boundary conditions of **Table 1**, it should be proved that they are the solutions of Equations (7)–(10). So, by substituting $F(\xi)$, $G(\xi)$, and $H(\xi)$ in Equations (7)–(9), the following functions Eq_1, Eq_2, and Eq_3 are concluded as below:

$$\begin{aligned} Eq_1(\xi) &:= 2F(\xi) + \frac{d}{d\xi}H(\xi) \\ &= -0.00001201279985\xi^8 + 0.0001392933716\xi^7 \\ &- 0.000994764489\xi^6 + 0.00449987516\xi^5 \\ &- 0.017545789\,\xi^2 - 0.0127261676\xi^4 + 0.0211649508\xi^3 \\ &+ 0.003426128\xi + 0.0021842162, \end{aligned} \tag{41}$$

$$\begin{aligned} Eq_2(\xi) &:= F(\xi)^2 + \frac{d}{d\xi}F(\xi)H(\xi) - G(\xi)^2 - \frac{d^2}{d\xi^2}F(\xi) \\ &= -0.307402949\xi + 0.4107046877\xi^2 - 0.2321553404\xi^3 \\ &- 0.00843845310\xi^4 + 0.1086421640\xi^5 \\ &- 0.09009491674\xi^6 + 0.04492264842\xi^7 \\ &- 0.01617323018\xi^8 + 0.004491785456\xi^9 \\ &- 0.0009928055786\xi^{10} - 2.790378364 \times 10^{-16}\xi^{20} \\ &+ 3.114367344 \times 10^{-14}\xi^{19} - 1.636267524 \times 10^{-12}\xi^{18} \\ &+ 5.381185038 \times 10^{-11}\xi^{17} - 1.242466579 \times 10^{-9}\xi^{16} \\ &+ 2.141012685 \times 10^{-8}\xi^{15} - 2.856808912 \times 10^{-7}\xi^{14} \\ &+ 3.021499866 \times 10^{-6}\xi^{13} - 0.00002570345111\xi^{12} \\ &+ 0.0001772650607\xi^{11} + 0.082740487, \end{aligned} \tag{42}$$

$$
\begin{aligned}
Eq_3(\xi) \coloneqq 2F(\xi)G(\xi) + H(\xi)\frac{d}{d\xi}G(\xi) - \frac{d^2}{d\xi^2}G(\xi) \\
= 0.4839414608\xi - 0.7624858733\xi^2 + 0.6759490582\xi^3 \\
- 0.3973164381\xi^4 + 0.1695434802\xi^5 - 0.05457796061\xi^6 \\
+ 0.01297296166\xi^7 - 0.001964958929\xi^8 \\
+ 0.000027790893\xi^9 + 0.000086658628\xi^{10} \\
+ 2.159364798 \times 10^{-16}\xi^{20} - 2.220410560 \times 10^{-14}\xi^{19} \\
+ 1.065302664 \times 10^{-12}\xi^{18} - 3.164126757 \times 10^{-11}\xi^{17} \\
+ 6.505497573 \times 10^{-10}\xi^{16} - 9.79783102 \times 10^{-9}\xi^{15} \\
+ 1.113614153 \times 10^{-7}\xi^{14} - 9.66164830 \times 10^{-7}\xi^{13} \\
+ 6.34572864 \times 10^{-6}\xi^{12} - 0.0000301523536\xi^{11} \\
- 0.1199093502.
\end{aligned}
\tag{43}
$$

By plotting the functions $Eq_1(\xi)$, $Eq_2(\xi)$, and $Eq_3(\xi)$ in the following figure, when $0 \leq \xi \leq 9$, the local error value of the obtained analytical solutions can be calculated as follows:

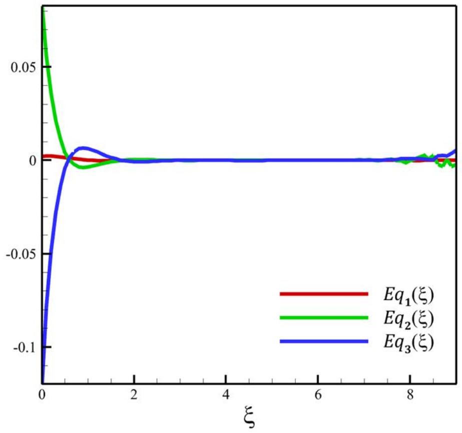

Figure 4. The graphical representation of $Eq_1(\xi)$, $Eq_2(\xi)$, and $Eq_3(\xi)$, when the HAN solutions were substituted in the governing equations.

As the error rate of the HAN solution can be seen in **Figure 4**, the maximum positive error of the semi-analytical solutions of Equations (7)–(9) is equal to 0.082740487, and the maximum negative error is equal to −0.1199093502.

4. Validation

Considering that the Von Kármán equations are not solved for the first time, it is necessary to compare them with previously published solutions. In **Figures 5–10**, the analytical results of HAN are compared with the numerical results of Von Kármán [2] and Cochran [3] as follows:

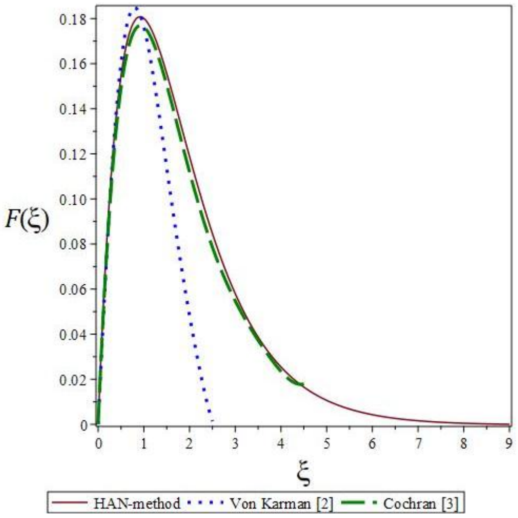

Figure 5. The graphical representation of $F(\xi)$ from the HAN method when they were compared with Von Kármán and Cochran results.

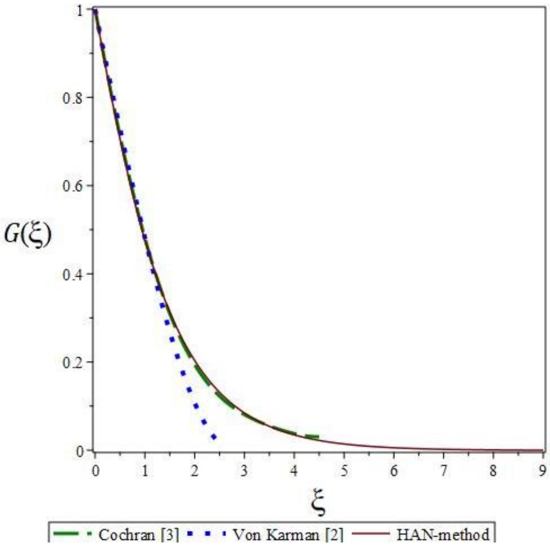

Figure 6. The graphical representation of $G(\xi)$ from the HAN method when they were compared with Von Kármán and Cochran results.

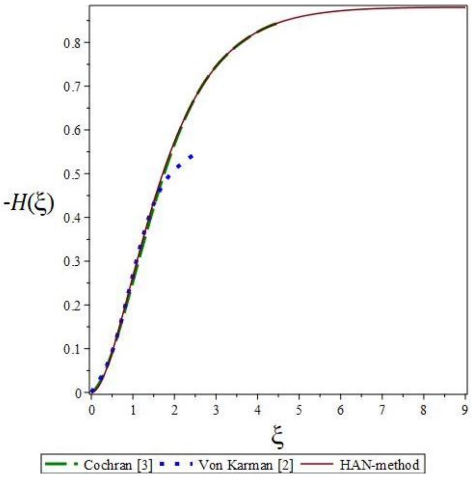

Figure 7. The graphical representation of $-H(\xi)$ from the HAN method when they were compared with Von Kármán and Cochran results.

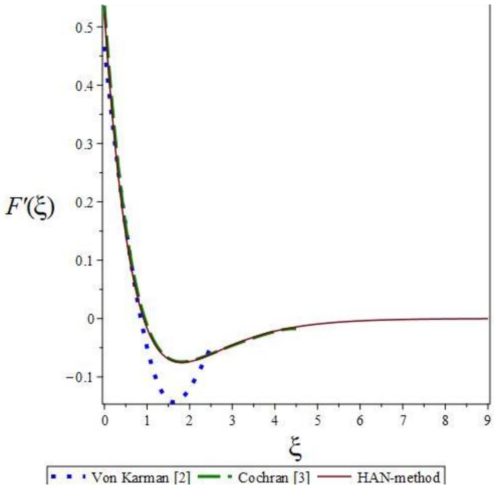

Figure 8. The graphical representation of $F^{'}(\xi)$ from the HAN method when they were compared with Von Kármán and Cochran results.

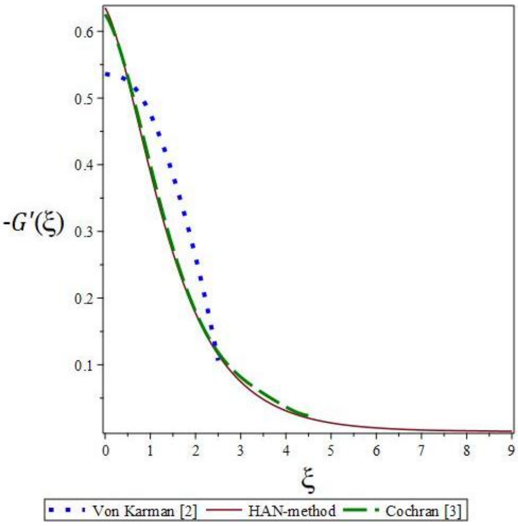

Figure 9. The graphical representation of $-G^{'}(\xi)$ from the HAN method when they were compared with Von Kármán and Cochran results.

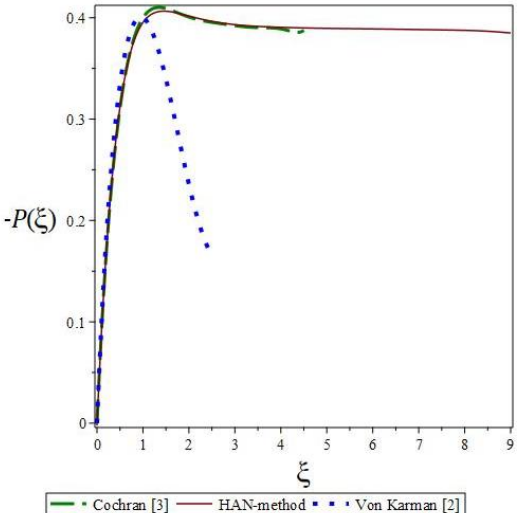

Figure 10. The graphical representation of $-P(\xi)$ from the HAN method when they were compared with Von Kármán and Cochran results.

The reason for the superiority of HAN solutions over previous numerical solutions can be seen in **Figures 5–10**. According to **Figures 2** and **3**, the analytical solutions (37–39) are very close to the Runge-Kutta numerical solution because the analytical solutions of HAN are constructed from the numerical solution. The validity of the results obtained from the numerical methods and especially the Runge-Kutta method in this research can be expressed in this way: The analytical solution of HAN can be placed in the differential equations, and its accuracy can be seen in **Figure 4**. According to **Figure 4**, the accuracy of solving the rotating Von Kármán fluid problem exceeds the minimum engineering value, which means that these solutions can be used for other applications that have an accuracy beyond engineering problems.

5. Results and discussion

According to the second part of the article, which is related to the research methodology, it is possible to obtain many practical outputs from the analytical solutions of Equations (7)–(9) by using the HAN method. Despite this classic Von Kármán problem about the rotation of a disk, which is one of the basic problems in fluid mechanics and boundary layer theory, it has solutions that are not very acceptable in the diagnosis and results of the previous solutions. Considering that the obtained analytical solutions have sufficient accuracy, these solutions can be used to obtain more accurate physical results. Considering that the Equations (37)–(39) are the analytical solution of the system of differential Equations (7) and (8), in addition to **Table 2**, the thickness of the layer of δ, the slope of the streamlines at the wall to the circumferential direction of φ_0, the peripheral component of the shear stress of the wall $\tau_{z\varphi}$, the moment of one side of the wetted disk M, the dimensionless coefficient for the moment on both sides of the wetted disk c_M, the volume flux of Q, and the mechanical power of P_M can be calculated. **Table 2** is as follows:

Table 2. The analytical results $F(\xi)$, $G(\xi)$, $H(\xi)$, and $P(\xi)$ from HAN-method.

The HAN solutions					
ξ	$F(\xi)$	$F'(\xi)$	$G(\xi)$	$G'(\xi)$	$H(\xi)$
0	0	0.5227637854	1	−0.6354239499	0
1	0.1801057122	−0.0166133362	0.4766431674	−0.3894695277	−0.2654256961
2	0.118735904	−0.0738347626	0.2033285374	−0.1775066595	−0.5729889366
3	0.057943116	−0.0455456786	0.0844172287	−0.0745436673	−0.7447389684
4	0.025442973	−0.0216700926	0.034744002	−0.0310263911	−0.8241490012
5	0.010635897	−0.0094802696	0.014154687	−0.0127978089	−0.8582098690
6	0.004270832	−0.0040054766	0.005628444	−0.0053453487	−0.8722151328
7	0.001596018	−0.0016753136	0.002096310	−0.0021575985	−0.8776977466
8	0.000481883	−0.0006952106	0.000632846	−0.0009940183	−0.8796148504
9	0.000019629	−0.0002928376	0.000025802	−0.0003436079	−0.8800500042

The thickness of the boundary layer that was formed on the infinite radius disk ends when the circumferential velocity of the fluid reaches 1% of the disk's velocity. Since the circumferential velocity of fluid is V_r and is proportional with $F(\xi)$, a specific value of $\xi = \xi_{1\%}$ must be found when $F(\xi) = 0.01$. So, the value of $\xi_{1\%}$ can be determined by interpolating in **Table 1**, and according to Equation (13), the thickness of the boundary layer of δ, that was formed on the disk can be calculated as below:

$$\delta = \xi_{1\%}(\nu/\Omega)^{1/2} = 5.099904243(\nu/\Omega)^{1/2} \tag{44}$$

According to Schlichting and Gersten [54], the value of $\xi_{1\%}$ was calculated as 5.5 before, but Equation (44) was stated more accurately. According to Equation (14), the slope of the flow lines in the wall in the circumferential direction can be calculated as below:

$$\varphi_0 = tan^{-1}\left(-\frac{F'(0)}{G'(0)}\right) = tan^{-1}\left(-\frac{0.5227637854}{-0.6354239499}\right) \approx 39.444° \tag{45}$$

where φ_0 was calculated 39.6° before [54], but Equation (45) gives a more accurate result. So, in **Figure 1**, the value of φ_0 is 39.444°. According to Equation (15), the circumferential component of the wall shear stress can be calculated as follows:

$$\tau_{z\varphi} = \rho r\Omega(\nu\Omega)^{1/2}G'(0) = -0.6354239499\rho r\Omega(\nu\Omega)^{\frac{1}{2}} \tag{46}$$

The moment of a disk wetted on one side, according to Equation (16), can be determined as follows:

$$M = -\frac{\pi}{2}\rho R^4(\nu\Omega^3)^{\frac{1}{2}}G'(0) = 0.9981216066\rho R^4(\nu\Omega^3)^{\frac{1}{2}} \tag{47}$$

The moment for disc wetting on both sides, according to Equation (17), can be found as below:

$$c_M = \frac{2M}{\rho\Omega^2(R^5/2)} = 1.996243213\frac{R^4(\nu\Omega^3)^{\frac{1}{2}}}{\Omega^2(R^5/2)} \tag{48}$$

The value of $G^{'}(0)$ was calculated as −0.61592 before [54], but Equations (46)–(48) give more accurate results. According to Equation (19), the volume flux can be calculated as below:

$$Q = -H(\infty)\pi R^2(\nu\Omega)^{\frac{1}{2}} = 0.8800500042\pi R^2(\nu\Omega)^{\frac{1}{2}} \tag{49}$$

where $H(\infty)$ was equals to 0.88446 according to Schlichting and Gersten [54], but Equation (49) calculates the volume flux more accurately. According to Equation (20), the mechanical power of P_M calculated as follows:

$$P_M = \pi\rho R^4\Omega(\nu/\Omega)^{1/2}\left[\int_0^\infty (F(\xi)^2 + G(\xi)^2)F(\xi)d\xi - \frac{4}{Re}\int_0^\infty F(\xi)^2 d\xi\right] \tag{50}$$

With considering $\xi = 9$ instead of ∞ and by substituting Equations (37) and (38) in Equation (50), the mechanical power can be determined as follows:

$$P_M = \left(0.08823081036 - \frac{0.2166429892}{Re}\right)\pi\rho R^4\Omega(\nu/\Omega)^{1/2} \tag{51}$$

Considering large Reynolds numbers, Equation (51) reduces to the following form:

$$P_M = (0.08823081036)\pi\rho R^4\Omega(\nu/\Omega)^{1/2} \tag{52}$$

where Equation (52) is approximately like the previous calculations and states the accuracy of Equations (37)–(39).

6. Conclusion

6.1. Summary of mathematical achievements

This study introduced the Hybrid Analytical and Numerical (HAN) method as a novel approach for solving nonlinear fluid flow problems, emphasizing its accuracy and flexibility. The method's analytical solutions were derived from numerical results obtained using the Runge-Kutta method, as depicted in **Figures 2** and **3**. The numerical solution, shown as a blue dashed line, served as the foundation for constructing the analytical solution, illustrated by the solid red line in the same figures. Importantly, **Figure 4** does not represent numerical errors but rather demonstrates the correctness of the semi-analytical solution derived through the HAN method, based on the substitution of Equations (37)–(39) into the original differential equations such as Equations (7)–(9). Comparisons with [2,3] validate the higher accuracy of the HAN method. The claim that the HAN method offers improved accuracy is further substantiated by **Figures 5–10**. While the method theoretically allows for an unlimited number of polynomial coefficients, practical considerations impose constraints. Increasing the number of terms in the polynomial solution can lead to significant errors rather than improving the results. In this study, 11 terms were selected as the optimal number to ensure accuracy, as outlined in Equation (31). This choice is supported by the high-quality results presented in the study, which demonstrate significant improvements over previous research. Increasing the number of terms beyond this limit would reduce the range of functions such as Equations (41)–(43) and diminish the solution's reliability, as reflected in **Figure 4**. The comparison between **Tables 1** and **2** underscores the validity of the HAN method. **Table 1** presents the numerical solution of Equations (7)–(9) derived via the Runge-Kutta method with the help of Maple mathematical software, renowned for its precision in solving nonlinear coupled differential equations. **Table 2** represents the analytical solution obtained using the HAN method, constructed from the numerical data in **Table 1**. The consistency between the two tables reaffirms the reliability and robustness of the HAN method's semi-analytical solutions, confirming their validity in addressing complex problems. The analysis of **Figure 4**, along with comparisons to the numerical solutions and prior research, highlights the advantages of the HAN method in capturing intricate details of nonlinear fluid flow phenomena. While some regions, such as those close to the disk surface or the edge of the boundary layer, exhibit noticeable discrepancies, these do not undermine the overall accuracy and reliability of the method. Instead, they showcase the method's potential for refining and extending analytical solutions for nonlinear problems. In conclusion, the HAN method offers a robust framework for solving nonlinear differential equations, combining the strengths of numerical and analytical approaches. Its effectiveness is demonstrated through comparisons with prior studies, as well as the high accuracy of its results in addressing classical fluid flow problems. This research contributes significantly to both the theoretical and practical aspects of fluid mechanics, paving the way for further exploration and applications of hybrid methodologies in solving complex problems.

6.2. Summary of physical achievements

In this section, a summary of the achievements and novelty of this article is presented. The equations of this article were solved by the HAN mathematical method, not because they had not been solved yet, but because after all these years after the introduction of this problem, much more powerful calculation tools have been provided than before. At the same time, the equations of this article are simple, but they are very fundamental and practical, and any solution that is more accurate than the previous solutions can give more reliable results. The practicality of this classic problem is that the physics of this problem is like a three-dimensional pump, and, for example, if our solutions are accurate enough, they can be used even beyond engineering problems, such as medical problems. But another reason for writing the article is to show the application of the HAN method in non-linear problems, and even though the analytical solutions obtained from HAN are proven to be accurate, it is still possible to get much more accurate solutions from this method. Therefore, to finish the article, all the achievements of the article can be concluded as follows:

- The Hybrid Analytical and Numerical method (HAN method) is a powerful and flexible mathematical tool for solving nonlinear problems semi-analytically.
- The solutions of the Von Kármán equations for the rotation of a disk were approximated more accurately than before.
- Despite the application of the current solutions to a wide range of problems due to sufficient accuracy, it is still possible to obtain much more accurate solutions.
- The thickness of the boundary layer can be calculated more accurately with the help of the HAN method.
- If the slope of the flow lines in the wall in the circumferential direction is considered 39.444° instead of 39.6°, the results will be more accurate.
- More accurate results will be achieved by using current calculated parameters such as the circumferential component of the wall shear stress, the moment of a disk wetted on one side, and the moment for a disc wetted on both sides.
- The volume flux that is calculated in this study is more accurate than the previous ones.
- Unlike previous studies, the calculations of the mechanical power in this paper belong to different Reynolds numbers, and just for a special case when the Reynolds number is large, the calculations of the mechanical power are approximately the same as the previous ones.

While this study validates the accuracy of the HAN method through comparisons with [2,3], it is acknowledged that these references are somewhat dated. The selection of these comparisons aligns with the study's focus on solving the classical Von Kármán equations, ensuring consistency with the original formulation of the problem. Many recent studies utilize modified or extended versions of the Von Kármán equations, but the aim here has been to revisit the classical equations and improve the accuracy of their solutions using the HAN method. As illustrated in **Figures 5–10**, the solutions derived in this study successfully demonstrate the precision of the HAN method. These comparisons with prior approximation methods highlight the validity and robustness of the presented approach in addressing this classical problem. By refining and extending existing results, this research underscores the novelty and significance of applying the HAN method to classical equations. Future studies could broaden the scope of comparisons to include newer approximation methods, particularly for modified versions of the equations, to further validate and enhance the persuasiveness of the HAN method's applications.

Conflict of interest: The author declares no conflict of interest.

References

1. Kataoka H, Tomiyama A, Hosokawa S, et al. Two-Phase Swirling Flow in a Gas-Liquid Separator. Journal of Power and Energy Systems. 2008; 2(4): 1120-1131. doi: 10.1299/jpes.2.1120
2. Kármán TV. About laminar and turbulent friction (German). ZAMM—Journal of Applied Mathematics and Mechanics. 1921; 1(4): 233-252. doi: 10.1002/zamm.19210010401
3. Cochran WG. The flow due to a rotating disc. Mathematical Proceedings of the Cambridge Philosophical Society. 1934; 30(3): 365-375. doi: 10.1017/s0305004100012561
4. Bödewadt UT. The rotary flow over solid ground (German). ZAMM—Journal of Applied Mathematics and Mechanics. 1940; 20(5): 241-253. doi: 10.1002/zamm.19400200502
5. Fettis HE. On the integration of a class of differential equations occurring in boundary layer and other hydrodynamic problems. In: Proceedings of the 4th Midwest Fluid Mechanics Conference; 1955.
6. Rogers MH, Lance GN. The rotationally symmetric flow of a viscous fluid in the presence of an infinite rotating disk. Journal of Fluid Mechanics. 1960; 7(4): 617-631. doi: 10.1017/s0022112060000335
7. Batchelor GK. Note on a class of solutions of the Navier-stokes equations representing steady rotationally-symmetric flow. The Quarterly Journal of Mechanics and Applied Mathematics. 1951; 4(1): 29-41. doi: 10.1093/qjmam/4.1.29
8. Benton ER. On the flow due to a rotating disk. Journal of Fluid Mechanics. 1966; 24(04): 781. doi: 10.1017/s0022112066001009
9. Zandbergen PJ, Dijkstra D. Von Karman Swirling Flows. Annual Review of Fluid Mechanics. 1987; 19(1): 465-491. doi: 10.1146/annurev.fl.19.010187.002341
10. Tien CL, Tsuji J. Heat transfer by laminar forced flow against a non-isothermal rotating disk. International Journal of Heat and Mass Transfer. 1964; 7(2): 247-252. doi: 10.1016/0017-9310(64)90089-4
11. Evans GH, Greif R. Forced flow near a heated rotating disk: a similarity solution. Numerical Heat Transfer. 1988; 14(3): 373-387. doi: 10.1080/10407788808913650
12. Sharma H. Flow of a second-order fluid between two infinite rotating discs with injection. International Journal of Mathematics Trends and Technology. 1975.
13. Kumari M, Takhar HS, Nath G. Nonaxisymmetric unsteady motion over a rotating disk in the presence of free convection and magnetic field. International journal of engineering science. 1993; 31(12): 1659-1668. doi: 10.1016/0020-7225(93)90081-5
14. Öztekin A, Brown RA. Instability of a viscoelastic fluid between rotating parallel disks: analysis for the Oldroyd-B fluid. Journal of Fluid Mechanics. 1993; 255(1): 473. doi: 10.1017/s0022112093002563
15. Deshpande AG, Ghosh SG. Numerical study of the unsteady flow in fluid-particle suspension from an infinite rotating disk. Indian Journal of Pure and Applied Mathematics. 1996.
16. Choudhury R, Das ALOK. Elastico-viscous flow and heat transfer between two rotating discs of different transpiration. Indian Journal of Pure and Applied Mathematics. 1997.
17. Shevchuk IV, Buschmann MH. Rotating disk heat transfer in a fluid swirling as a forced vortex. Heat and Mass Transfer. 2005; 41(12): 1112-1121. doi: 10.1007/s00231-005-0635-8

18. aus der Wiesche S. Heat transfer from a rotating disk in a parallel air crossflow. International Journal of Thermal Sciences. 2007; 46(8): 745-754. doi: 10.1016/j.ijthermalsci.2006.10.013
19. Hayat T, Khan SB, Sajid M, et al. Rotating flow of a third grade fluid in a porous space with Hall current. Nonlinear Dynamics. 2006; 49(1-2): 83-91. doi: 10.1007/s11071-006-9105-1
20. Yang C, Liao S. On the explicit, purely analytic solution of Von Kármán swirling viscous flow. Communications in Nonlinear Science and Numerical Simulation. 2006; 11(1): 83-93. doi: 10.1016/j.cnsns.2004.05.006
21. Attia HA. Rotating disk flow and heat transfer through a porous medium of a non-Newtonian fluid with suction and injection. Communications in Nonlinear Science and Numerical Simulation. 2008; 13(8): 1571-1580. doi: 10.1016/j.cnsns.2006.05.009
22. Bessaïh R, Boukhari A, Marty P. Magnetohydrodynamics stability of a rotating flow with heat transfer. International Communications in Heat and Mass Transfer. 2009; 36(9): 893-901. doi: 10.1016/j.icheatmasstransfer.2009.06.009
23. Rahman MM, Postelnicu A. Effects of thermophoresis on the forced convective laminar flow of a viscous incompressible fluid over a rotating disk. Mechanics Research Communications. 2010; 37(6): 598-603. doi: 10.1016/j.mechrescom.2010.07.002
24. Abdou MA. New Analytic Solution of Von Karman Swirling Viscous Flow. Acta Applicandae Mathematicae. 2009; 111(1): 7-13. doi: 10.1007/s10440-009-9526-1
25. Turkyilmazoglu M. Analytic approximate solutions of rotating disk boundary layer flow subject to a uniform suction or injection. International Journal of Mechanical Sciences. 2010; 52(12): 1735-1744. doi: 10.1016/j.ijmecsci.2010.09.007
26. Turkyilmazoglu M. Analytic approximate solutions of rotating disk boundary layer flow subject to a uniform vertical magnetic field. Acta Mechanica. 2010; 218(3-4): 237-245. doi: 10.1007/s00707-010-0416-4
27. Rashidi MM, Abelman S, Freidooni Mehr N. Entropy generation in steady MHD flow due to a rotating porous disk in a nanofluid. International Journal of Heat and Mass Transfer. 2013; 62: 515-525. doi: 10.1016/j.ijheatmasstransfer.2013.03.004
28. Alam MS, Chapal Hossain SM, Rahman MM. Transient thermophoretic particle deposition on forced convective heat and mass transfer flow due to a rotating disk. Ain Shams Engineering Journal. 2016; 7(1): 441-452. doi: 10.1016/j.asej.2015.04.005
29. Hayat T, Qayyum S, Imtiaz M, et al. Partial slip effect in flow of magnetite-Fe3O4 nanoparticles between rotating stretchable disks. Journal of Magnetism and Magnetic Materials. 2016; 413: 39-48. doi: 10.1016/j.jmmm.2016.04.025
30. Doh DH, Muthtamilselvan M. Thermophoretic particle deposition on magnetohydrodynamic flow of micropolar fluid due to a rotating disk. International Journal of Mechanical Sciences. 2017; 130: 350-359. doi: 10.1016/j.ijmecsci.2017.06.029
31. Das A, Sahoo B. Flow of a Reiner-Rivlin fluid between two infinite coaxial rotating disks. Mathematical Methods in the Applied Sciences. 2018; 41(14): 5602-5618. doi: 10.1002/mma.5103
32. Kumar A, Tripathi R, Singh R. Von Kármán swirling flow and heat transfer analysis on MHD fluid subject to partial slip and temperature jump conditions. Waves in Random and Complex Media; 2022. doi: 10.1080/17455030.2022.2075044
33. Visuvasam J, Alotaibi H. Analysis of Von Kármán Swirling Flows Due to a Porous Rotating Disk Electrode. Micromachines. 2023; 14(3): 582. doi: 10.3390/mi14030582
34. Ali F, Zaib A, Loganathan K, et al. Scrutinization of second law analysis and viscous dissipation on Reiner-RivlinNanofluid with the effect of bioconvection over a rotating disk. Heliyon. 2023; 9(2): e13091. doi: 10.1016/j.heliyon.2023.e13091
35. Jalili P, Azar AA, Jalili B, et al. Heat transfer analysis in cylindrical polar system with magnetic field: A novel Hybrid Analytical and Numerical Technique. Case Studies in Thermal Engineering. 2022; 40: 102524. doi: 10.1016/j.csite.2022.102524
36. Jalili P, Azar AA, Jalili B, et al. The HAN method for a thermal analysis of forced non-Newtonian MHD Reiner-Rivlin viscoelastic fluid motion between two disks. Heliyon. 2023; 9(6): e17535. doi: 10.1016/j.heliyon.2023.e17535
37. Jalili B, Azar AA, Esmaeili K, et al. A novel approach to micropolar fluid flow between a non-porous disk and a porous disk with slip. Chinese Journal of Physics. 2024; 87: 118-137. doi: 10.1016/j.cjph.2023.11.023
38. Ahmadi Azar A, Jalili B, Jalili P, et al. Investigating the effect of structural changes of two stretching disks on the dynamics of the MHD model. Scientific Reports. 2023; 13(1). doi: 10.1038/s41598-023-48988-4
39. Jalili P, Azar AA, Jalili B, et al. A Novel Analytical Investigation of a Swirling Fluid Flow and a Rotating Disk in the Presence of Uniform Suction. Arabian Journal for Science and Engineering. 2023; 49(8): 10453-10469. doi: 10.1007/s13369-023-08391-7

40. Jalili P, Azar AA, Jalili B, et al. Study of nonlinear radiative heat transfer with magnetic field for non-Newtonian Casson fluid flow in a porous medium. Results in Physics. 2023; 48: 106371. doi: 10.1016/j.rinp.2023.106371
41. Jalili B, Azar AA, Jalili P, et al. Analytical approach for micropolar fluid flow in a channel with porous walls. Alexandria Engineering Journal. 2023; 79: 196-226. doi: 10.1016/j.aej.2023.08.015
42. Jalili B, Azar AA, Jalili P, et al. Investigation of the unsteady MHD fluid flow and heat transfer through the porous medium asymmetric wavy channel. Case Studies in Thermal Engineering. 2024; 61: 104859. doi: 10.1016/j.csite.2024.104859
43. Jalili P, Ahmadi Azar A, Jalili B, et al. A novel technique for solving unsteady three-dimensional brownian motion of a thin film nanofluid flow over a rotating surface. Scientific Reports. 2023; 13(1). doi: 10.1038/s41598-023-40410-3
44. Azar EA, Jalili B, Azar AA, et al. An exact analytical solution of the Emden–Chandrasekhar equation for self-gravitating isothermal gas spheres in the theory of stellar structures. Physics of the Dark Universe. 2023; 42: 101309. doi: 10.1016/j.dark.2023.101309
45. Azar AA, Jalili P, Moziraji ZP, et al. Analytical solution for MHD nanofluid flow over a porous wedge with melting heat transfer. Heliyon. 2024; 10(15): e34888. doi: 10.1016/j.heliyon.2024.e34888
46. Jalili B, Azar AA, Jalili P, et al. Impact of variable viscosity on asymmetric fluid flow through the expanding/contracting porous channel: A thermal analysis. Case Studies in Thermal Engineering. 2023; 52: 103672. doi: 10.1016/j.csite.2023.103672
47. Jalili B, Azar AA, Liu D, et al. Analytical formulation of the steady-state planar Taylor–Couette flow constitutive equations with entropy considerations. Physics of Fluids. 2024; 36(11). doi: 10.1063/5.0239765
48. Ahmadi Azar A, Jalili P, Jalili B, et al. The comprehensive analysis of magnetohydrodynamic Casson fluid flow with rectangular porous medium through expanding/contracting channel. Multidiscipline Modeling in Materials and Structures. 2024; 21(1): 68-97. doi: 10.1108/mmms-07-2024-0179
49. Heidari N, de Montigny M, Azar AA, et al. Solutions of the nonlinear Klein-Gordon equation and the generalized uncertainty principle with the hybrid analytical and numerical method. Nuclear Physics B. 2024; 1009: 116750. doi: 10.1016/j.nuclphysb.2024.116750
50. Xu H, Liao SJ. Series solutions of unsteady MHD flows above a rotating disk. Meccanica. 2006; 41(6): 599-609. doi: 10.1007/s11012-006-9006-x
51. Mehmood A, Ali A, Takhar HS, et al. Unsteady Von Kármán swirling flow: analytical study using the Homotopy Method. International Journal of Applied Mathematics and Mechanics. 2010.
52. Sadiq MA. Serious Solutions for Unsteady Axisymmetric Flow over a Rotating Stretchable Disk with Deceleration. Symmetry. 2020; 12(1): 96. doi: 10.3390/sym12010096
53. Bég OA, Mabood F, Nazrul Islam M. Homotopy Simulation of Nonlinear Unsteady Rotating Nanofluid Flow from a Spinning Body. International Journal of Engineering Mathematics. 2015; 2015: 1-15. doi: 10.1155/2015/272079
54. Schlichting H, Gersten K. Boundary-Layer Theory. Springer Berlin Heidelberg; 2017. doi: 10.1007/978-3-662-52919-5

Mechanical Engineering Advances 2025, 3(2), 2052.
https://doi.org/10.59400/mea2052

Article

Two-phase heat conductors for passive thermal regulation systems of electric vehicles

Leonard Vasiliev[*], **Alexander Zhuravlyov, Dmitry Sadchenko**

Porous Media Laboratory, A.V. Luikov Heat and Mass Transfer Institute of the National Academy of Science of Belarus, Minsk 220072, Republic of Belarus

* **Corresponding author:** Leonard Vasiliev, leonard_vasiliev@rambler.ru

CITATION

Vasiliev L, Zhuravlyov A, Sadchenko D. Two-phase heat conductors for passive thermal regulation systems of electric vehicles. Mechanical Engineering Advances. 2025; 3(2): 2052. https://doi.org/10.59400/mea2052

ARTICLE INFO

Received: 7 February 2025
Accepted: 27 February 2025
Available online: 9 April 2025

COPYRIGHT

Copyright © 2025 by author(s). *Mechanical Engineering Advances* is published by Academic Publishing Pte. Ltd. This work is licensed under the Creative Commons Attribution (CC BY) license. https://creativecommons.org/licenses/by/4.0/

Abstract: Due to the growing demands for a better environment, great efforts are currently being made in the world to create and improve electric and hybrid vehicles. Heat-loaded equipment of electric transport requires efficient cooling systems. A loop thermosyphon made of aluminum, having two flat multi-channel evaporators and one condenser for cooling electronic components, is developed and tested with acetone as the working fluid. The procedure and results of an experimental study of the characteristics of a thermosyphon are described. The evaporators are supplied with a heat load of varying power; the absorbed heat is dissipated by the condenser. The working fluid is acetone. The influence of thermal load and volume of working fluid on the thermal resistance of a thermosyphon and its components was determined and investigated. The lowest evaporator thermal resistance is 0.15 K/W for the heat load range 30–60 W. The thermosyphon operates stably in a wide range of thermal loads and quickly responds to their changes.

Keywords: electric and hybrid vehicles; thermosyphon; double evaporator loop thermosyphon; passive thermal regulation; multi-channel evaporators; green technologies in transport

1. Introduction

Reducing the consumption of hydrocarbon fuels and improving the environmental situation are urgent tasks. Vehicle emissions are a very serious problem. Internal combustion engines (ICE) emit carbon dioxide CO_2, carbon monoxide CO, nitrogen oxides NO_x and other harmful substances into the atmosphere. While industry, the electricity grid and other polluters have cut fossil CO_2 over the past 30 years, fossil CO_2 from transport continues to increase. For example, in the UK alone, the number of cars has increased to 40.7 million units in 2023, while their weight has doubled and they require twice as much fuel since 1980 [1]. According to a study [2], global aviation accounts for approximately 2.1% of anthropogenic CO_2 emissions. If no effective measures are taken, then by 2050 CO_2 emissions from air transport will reach 23% of all transport emissions and 5% (15% in the worst-case scenario) of total greenhouse gas emissions. In this regard, great importance is attached to the creation and improvement of hybrid and electric technologies in transport [3,4].

According to some estimates, replacing internal combustion engine vehicles with electric vehicles could reduce greenhouse gas emissions by 20% and by 40% when generating electricity from renewable sources [5,6]. The importance of the above-mentioned problems and the prospects of the chosen strategy are evidenced by the fact that work on the creation of electric and hybrid power plants is actively carried out not only in the automobile industry but also in the aircraft industry, where the requirements for reliability, safety, and efficiency (including weight) are extremely strict. In aviation, one of the promising solutions to this global problem is electric aircraft. Replacing aircraft with internal combustion engines with electric ones will ensure a significant reduction in greenhouse gas emissions [7–9].

Modern means of transport (electric cars, electric aircraft, hybrid vehicles, etc.) are characterized by designs that operate under conditions of intense, often extreme, thermal effects. Electric and hybrid vehicles require efficient cooling due to the presence of a significant number of heat-generating components, including the powertrain, navigation electronics, battery, headlights, etc. (**Figures 1** and **2**).

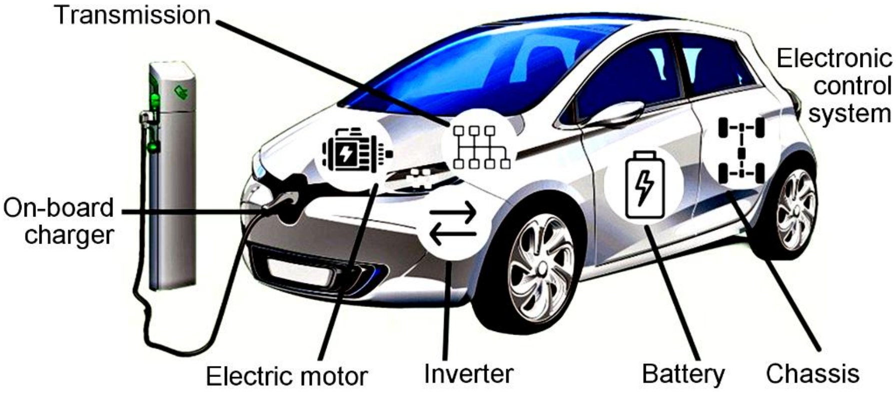

Figure 1. Heat-loaded elements of an electric vehicle.

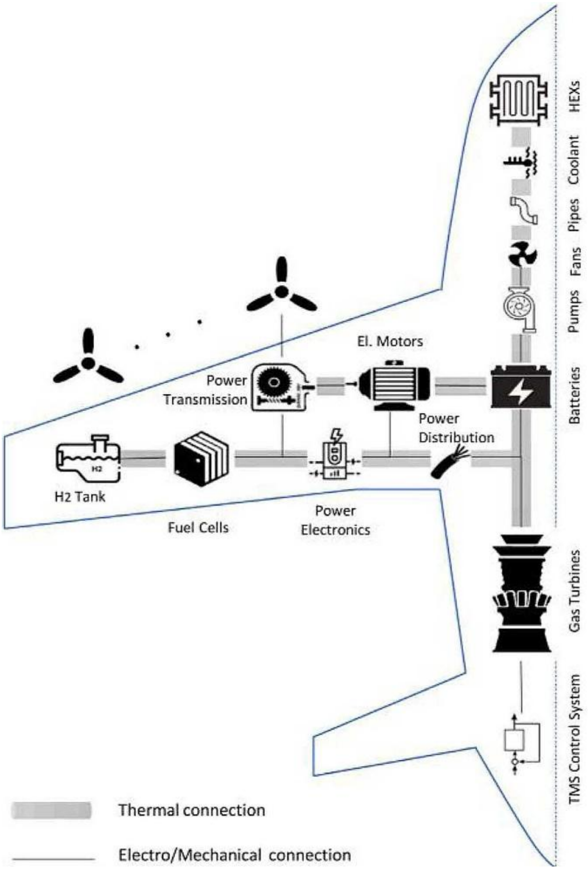

Figure 2. Main subsystems and components of the thermal control system in a general-purpose hybrid electric propulsion aircraft [10].

For thermal regulation of heat-generating objects of electric transport, various systems can be used: air, liquid, with the use of phase-changing materials, thermoelectric, immersion in boiling liquid. The air free-convection system is simple, relatively cheap, and electrically safe, but due to the low heat capacity and thermal conductivity of air, it is effective when intensive blowing of radiators is possible. Liquid cooling is more effective but requires a coolant reservoir and an energy-consuming pumping system. Phase-changing materials maintain a constant temperature of the object, are not energy-consuming, allow for the possibility of leakage of molten material, and are limited by the available amount of latent heat. energy-consuming pumping system. Thermoelectric coolers based on the Peltier effect are capable of precisely controlling the temperature of an object, are reliable, silent, compact, lightweight, and easy to operate, but are less efficient than other systems.

The problem of removing excess heat from heat-generating electronic equipment can be successfully solved using heat pipes and thermosyphons—highly heat-conducting two-phase heat conductors with an evaporation-condensation cycle, in which heat is transferred by transferring the latent heat of evaporation. These devices are autonomous and silent, and their operation does not require energy consumption, which is very important for wireless electric transport. They can absorb heat from the object being cooled, transfer it outside the volume filled with equipment, and then transfer it to the cooling liquid or air. Heat pipes and thermosyphons are easy to operate, have no mechanical moving parts, do not require energy consumption or maintenance, and can provide heat exchange between the surface of the cooled object and the external environment with virtually no heat loss. They can be used to ensure efficient heat removal from a heat-loaded component.

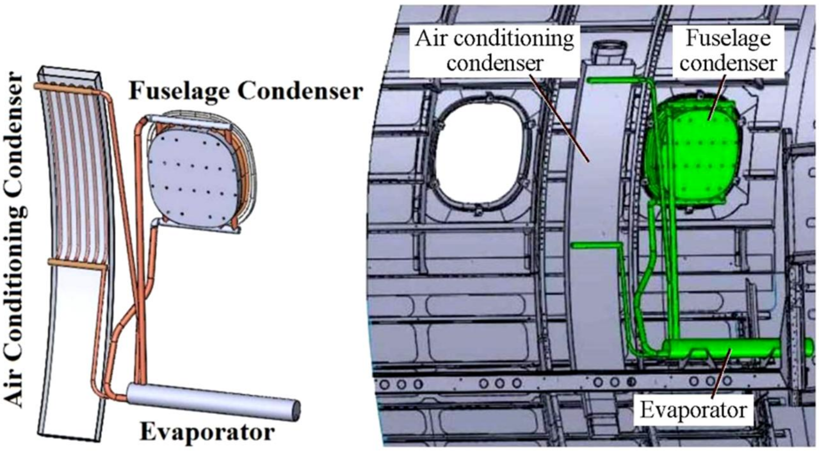

Figure 3. Thermal control system based on a loop thermosiphon with heat removal to the fuselage and dissipation into the surrounding air [11].

In aircraft with electric traction, the choice of passive thermal control systems is more relevant than in aircraft with internal combustion engines, due to the need to save electricity by eliminating coolant pumping systems and blower fans. No less important is the absence of a traditional fuel system in an electric aircraft, since fuel is the main, and sometimes the only, heat sink for heat-loaded equipment. Heat receivers in aircraft with an electric drive are the aircraft structure or the surrounding air. **Figure 3** shows a loop thermosyphon-based thermal control system, flight tested on an Embraer aircraft [11]. The thermosyphon condensers are connected to the same evaporator by independent vapor and liquid lines. One part of the heat from the cooled object is transferred to the fuselage; the other is used for air conditioning, which must be heated to a comfortable temperature.

The A.V. Luikov Heat and Mass Transfer Institute of the National Academy of Sciences of Belarus developed heat pipes and thermosyphons for various purposes [12–14], including for cooling objects that are sources of powerful heat generation [12]. One of the latest developments is a loop thermosyphon made of aluminum, having two flat multi-channel evaporators and one condenser for cooling electronic components, developed and tested with acetone as the working fluid. In loop thermosyphons, the vapor and liquid flows are separated from each other. The coolant, as in a conventional thermosyphon, flows down from the condenser to evaporators under the action of gravity, but the absence of friction between the vapor and the liquid allows increasing the heat transfer capacity of this heat conductor. Therefore, they can be successfully used in cooling systems of electric transport power electronics. The use of aluminum as a structural material provides a significant gain in weight, which is extremely important for transport, especially aviation. A two-phase loop thermosyphon (TPLT) is a type of passive heat transfer device that has the ability to efficiently transfer heat over a long distance without any external power supply.

2. Materials and methods

2.1. Thermosyphon design

To solve the problem of increasing the efficiency of heat exchange equipment, a prototype of a loop thermosyphon was designed and manufactured, the general appearance of which is shown in **Figure 4**. The evaporator is made flat for the convenience of placing chips or other cooled elements on it. All parts of the thermosyphon are made of aluminum.

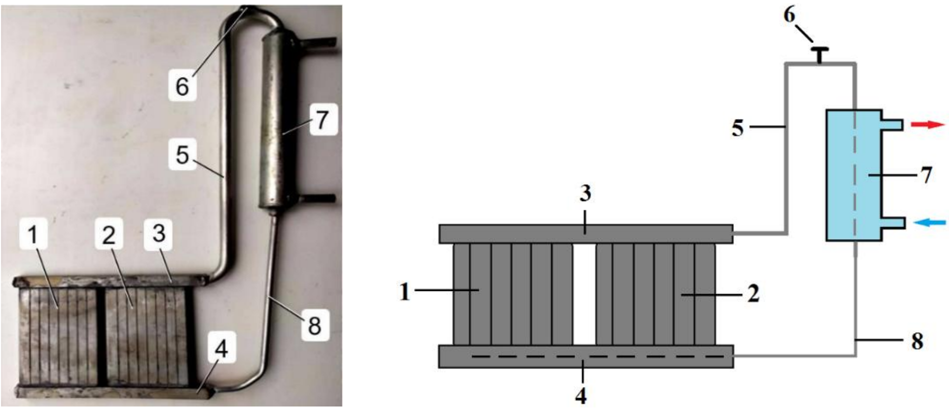

(a) **(b)**

Figure 4. Investigated double evaporator loop thermosyphon, photograph **(a)** and schematic diagram **(b)**: 1) evaporator 1; 2) evaporator 2; 3) vapor collector; 4) liquid collector; 5) vapor tube; 6) filling connection; 7) condenser; 8) liquid tube.

Table 1. Specifications of the thermosyphon (dimensions in mm).

Specifications	**Size**
Evaporator	
Number of evaporators	2
Number of mini-channels in one evaporator	8
Dimensions of one mini-channel (length × width × height)	7 × 3 × 110
Hydraulic diameter	4.2
Condenser	
Type	Tube in tube
External dimensions (length × external diameter)	200 × 24
Wall thickness	2
Vapor and liquid collectors	
Length × width × height	160 × 9 × 9
Vapor tube: $d_{in} \times L$	8 × 400
Liquid tube: $d_{in} \times L$	4 × 200

The peculiarity of the thermosyphon is the availability of two equal vertically oriented multi-channel evaporators 1 and 2, which are connected to the condenser through vapor 3 and liquid 4 collectors. The evaporators are heat receivers, each of them can have heat sources of different power (for example, chips). The heat absorbed during evaporation is transferred with the mass of vapor through the vapor outlet tube 5 to the condenser 7, which is cooled by a flow-through liquid heat exchanger. The condensate flows down to the evaporators through liquid transport tube 8. The liquid tube connects the condenser to the evaporator through the liquid collector, continues inside the liquid collector along its entire length, and evenly supplies the evaporators with working fluid. The thermosyphon condenser is equipped with a flow-through liquid heat exchanger, but heat can also be removed from the condenser of devices of this type by air convection. In this case, it is advisable to make the condenser in the form of a radiator with a developed finned heat exchange surface. All components of the thermosiphon are made of aluminum. The geometric characteristics of the thermosyphon are presented in **Table 1**.

The mini-channels in each evaporator are separated by 1 mm thick walls. The walls of the mini-channels act as internal ribs, increasing the heat exchange surface area and the evaporation rate of the working fluid. Multi-channel flat evaporator is made of extruded aluminum profile ALS-7PK70_011.1 (**Figure 5**). Wall thickness is 2 mm. The inner and outer walls of the evaporator have a smooth surface.

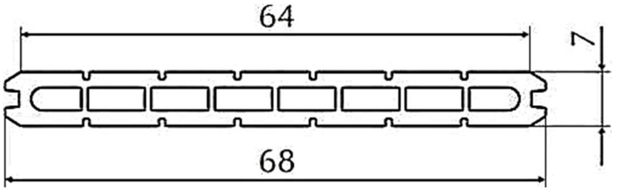

Figure 5. Cross-section of the evaporator panel.

The evaporator is made flat for the convenience of mounting the cooled elements on its surface. Tight fit of the objects of thermal regulation to the evaporator allows minimizing the contact thermal resistance. Since wetting a large area of a vertically located surface is difficult, the internal volume of the evaporator is divided into parallel channels, which improves the conditions for supplying the evaporation centers with liquid. The presence of curvilinear meniscuses formed on the walls of the channels ensures the occurrence of capillary pressure necessary for the spread of the liquid phase along the height of the channel. The division of the internal space of the evaporator into channels also helps to organize the flow and laminarize the flow of the resulting vapor, which is discharged through the vapor collector and the vapor tube into the condenser. The contribution of capillary pressure, caused by the presence of a curvilinear meniscus, to the organization of wetting of the heat exchange surface is of significant importance, since the evaporator channels have a smooth surface.

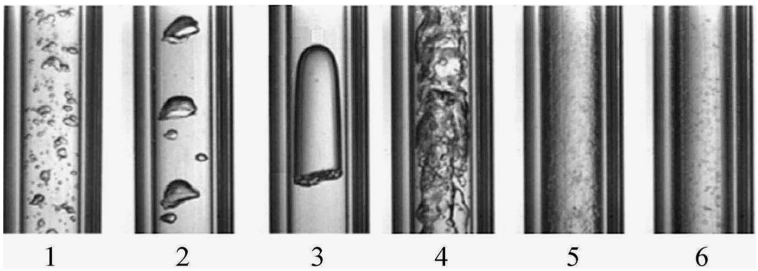

Figure 6. Changes in the two-phase flow modes in vertical mini-channels of the evaporator (d_{ch} = 4 mm) with an increase in the heat load [15]: 1) formation of mini-bubbles on the heat exchange surface; 2) merging of mini-bubbles into large clusters; 3) separation of a liquid flow into vapor plugs and liquid cuffs; 4) turbulent vapor-liquid flow; 5) stratification of a two-phase flow and formation of a thin liquid film on the wall with an accompanying increase in the vapor content in the flow; 6) flow of wet vapor.

Two-phase heat exchange during the movement of vapor-liquid mixtures through small-section channels has been considered in a number of works. Karayiannis and Mahmoud [13] conducted a study of the flow of boiling liquid in rectangular microchannels using high-speed video filming, which made it possible to examine the dependence of flow regimes on the magnitude of the heat flux supplied to the system and the relationship of the regimes with the intensity of heat transfer. In mini-channels of the heat-loaded thermosyphon evaporator, as a result of the phase transition, vapor bubbles are generated, which, with an increase in the heat flow supplied to the evaporator, grow, merge into clusters, and affect the nature of the two-phase flow. Each flow regime, from the generation of mini-bubbles on the channel wall to the flow of wet vapor, is characterized by different vapor content (**Figure 6**) [15].

The driving forces that ensure the circulation of the working fluid along the circuit of the thermosyphon are the gravitational pressure ΔP_{g} and the pressure ΔP_{vg}, arising as a result of the vapor generation in the annular channel of the evaporator. The operability of the thermosyphon is maintained under the condition that the combination of these driving forces exceeds or is equal to the pressure losses in the circuit:

$$\Delta P_g+\Delta P_{vg} \geq \Delta P_l +\Delta P_v +\Delta P_e +\Delta P_c \; a = 1 \tag{1}$$

where ΔP_l, ΔP_v—pressure losses in liquid and vapor tubes; ΔP_e, ΔP_c—pressure drop due to vapor generation or condensation at the liquid–vapor interface.

The internal diameter of the liquid tube is smaller than the internal diameter of the vapor tube (ratio 1:2) in order to avoid reverse vapor flow and blocking of the liquid tube.

To remove air from the thermosyphon circuit and fill it with working fluid, the device design has a filling nipple. To ensure the ability to change the filling level for research purposes, the ability to repeatedly depressurize, perform a refilling procedure, and subsequently seal the thermosyphon is provided.

2.2. Experimental equipment and experimental procedure

Heat transfer properties of the thermosyphon were determined on an experimental stand, the diagram of which is shown in **Figure 7**. The heat flow to the evaporator was supplied by means of an electric heater, which was powered by a stabilized direct current source HY10010E with a voltage setting accuracy of 1 V and a current of 0.1 A. T-type thermocouples (copper-constantan) were installed at the points of measuring the temperature of the thermosyphon components. (**Figure 8**). Thermocouple signals were recorded and analyzed by an Agilent 34980A multifunction switching and measurement unit connected to a computer. The evaporator, condenser, vapor and liquid tubes were reliably insulated to prevent heat leakage. The thermosyphon condenser is a “tube in tube” type heat exchanger and is cooled by running water coming from the LOIP FT-316-40 thermostat with a temperature maintenance accuracy of ± 0.1 ℃. The temperature of the cooling water during the experiments was 20 ℃.

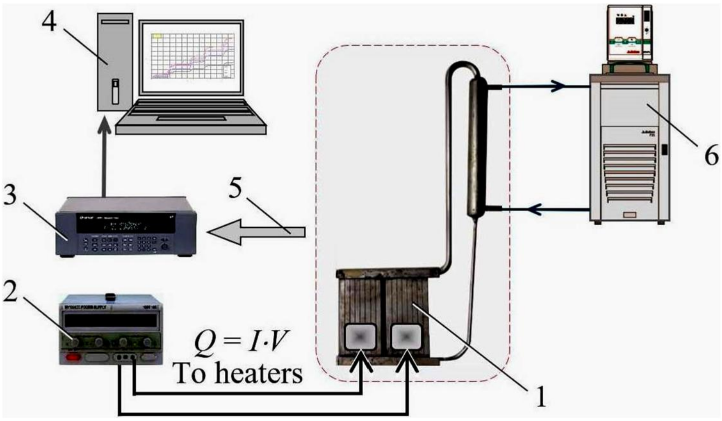

Figure 7. Schematic diagram of the experimental setup for studying the thermosyphon: 1) thermosyphon, 2) DC source, 3) Agilent, 4) computer, 5) signals from thermocouples installed on the thermosyphon, 6) thermostat.

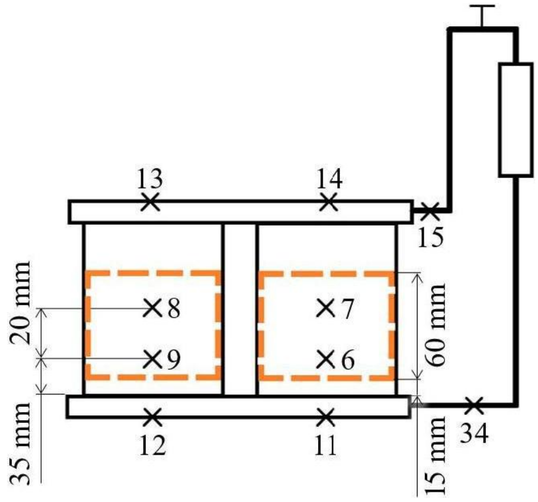

Figure 8. Arrangement of the thermocouples (×) on the evaporator panels with two heaters, condenser, vapor and liquid collectors, vapor, and liquid tubes.

Acetone, a substance of organic origin, which is a volatile liquid (dimethyl ketone, chemical formula—C_3H_6O), was used as the working fluid, the filling ratio in different experiments ranged from 15% to 63% of the evaporator volume. Acetone easily mixes with water and is characterized by low toxicity. The main properties of acetone are given in **Table 2** [16].

Table 2. Basic physical properties of acetone [16].

T_{melt}, °C	q_{melt}, kJ/kg	T_{boil}, °C	r, kJ/kg at T_{boil}	T_{cr}, °C	P_{cr}, bar	ρ_{cr}, kg/m^3
–93.2	96	56.1	524	235.0	47.6	273

The temperature distribution in the thermosyphon is determined. The thermal resistances of the evaporator (R_e), the condenser (R_c), and the entire thermosyphon (R_{TS}) at different heat powers and temperatures of the cooling medium are calculated using Equations (2)–(4):

$$R_e = \frac{\bar{T}_e - \bar{T}_v}{Q} = \frac{\frac{1}{m}\sum_{i=1}^{m} T_{e,i} - \frac{1}{n}\sum_{i=1}^{n} T_{v,i}}{Q} \tag{2}$$

$$R_c = \frac{\bar{T}_v - \bar{T}_c}{Q} = \frac{\frac{1}{n}\sum_{i=1}^{n} T_{v,i} - \frac{1}{k}\sum_{i=1}^{k} T_{c,i}}{Q} \tag{3}$$

$$R_{\mathrm{TS}} = R_e + R_c = \frac{\bar{T}_e - \bar{T}_c}{Q} = \frac{\frac{1}{m}\sum_{i=1}^{m} T_{e,i} - \frac{1}{k}\sum_{i=1}^{k} T_{c,i}}{Q} \tag{4}$$

where $\bar{T}_e$, $\bar{T}_v$, and $\bar{T}_c$ are average values of the evaporator, vapor, and condenser temperatures, Q is the heat load.

The heat load was determined by the supplied electric power $I \times U$. Heat leakage in the wires and thermal conductivity through the thermal insulation were taken into account. Heat losses to the environment due to radiant heat exchange were estimated using Equation (5):

$$Q = \varepsilon \sigma A (T_1^4 - T_2^4) \tag{5}$$

Here $\varepsilon = 0.77$ is the coefficient of surface radiation; $\sigma = 5.67\times10^{-8}$ W m^{-2} K^{-4} is the Stefan-Boltzmann constant; A is the area of the radiating surface, m^2; T_1 is the average temperature of the outer surface of the thermal insulation of the thermosyphon; T_2 is the ambient temperature (room temperature).

2.3. Experiments

2.3.1. Heat loaded evaporator 1

Figure 9 illustrates the change in the temperature field in different zones of the loop thermosyphon during the experiment at a filling rate of 33% with the working fluid (acetone). Only evaporator 1 ($Q = 40$ W) is heat loaded; evaporator 2 at this stage acts as an auxiliary condenser and facilitates the rapid start of the thermosyphon. During the transition period of time 1, non-stationary heating of thermosyphon 1 occurs. The vapor is not directed into the steam tube until the saturation temperature in the steam collector reaches 60 °C.

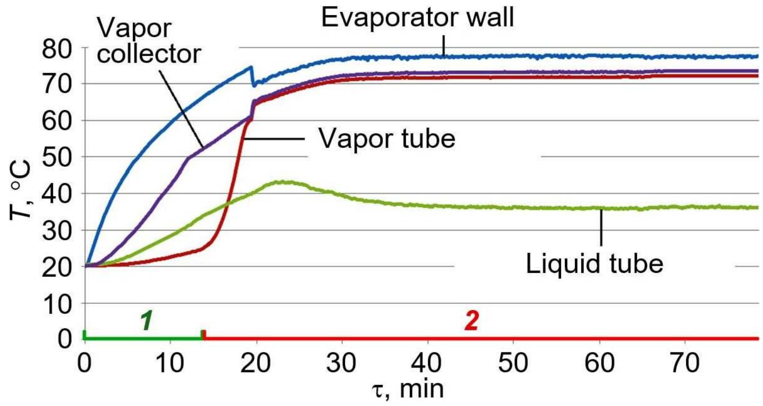

Figure 9. Temperature distribution graph during the experiment at an acetone filling rate of 33%, heat power of 40 W: 1) non-stationary process, 2) steady-state process.

After heat is supplied to evaporator 1 in the initial stage of the process (stage 1), the vapor tube heats up weakly. This indicates that this line is not filled with vapor and, therefore, the condenser is passive. It starts working after evaporator 2 is heated by the vapor condensing in its channels, which came from evaporator 1, to the saturation temperature. The steady-state operating mode of the thermosyphon is established (stage 2). A sign of completion of the transition period of the thermosyphon operation and the beginning of the stationary period is a cessation of growth and then stabilization of the temperature of the liquid phase flowing out of the condenser (**Figure 8**).

The transition from a non-stationary operating mode to a stationary one is shown in **Figure 10**. The small contour (dashed line) corresponds to the transient mode of operation of the thermosyphon (start-up mode, panel 2 acts as a condenser), the large contour (solid line) corresponds to the stationary mode of operation.

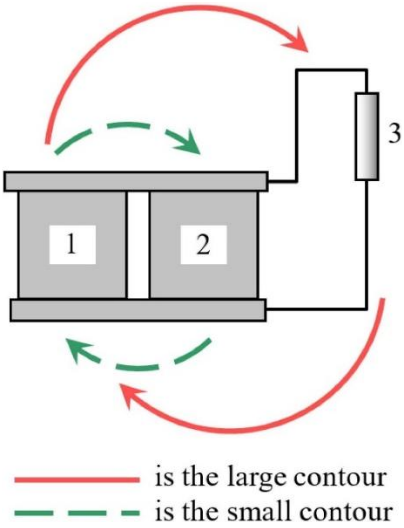

Figure 10. Two modes of operation of a thermosyphon with two evaporators: 1) evaporator 1; 2) evaporator 2; 3) condenser. The small circuit corresponds to the transient mode; the large circuit corresponds to the steady-state mode.

A Graph of temperature values of the thermosyphon components in steady-state mode (heat load supplied to panel 1) is shown in **Figure 11**.

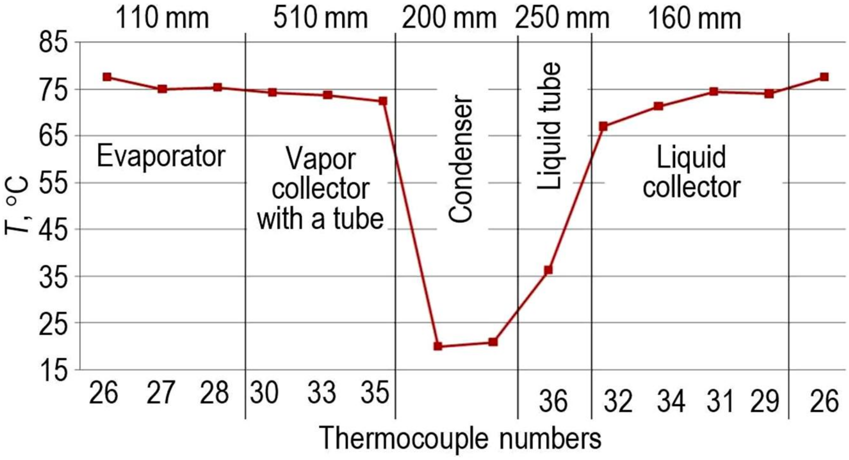

Figure 11. Temperatures of the thermosyphon components in steady-state mode.

The average value of the heat transfer coefficient in the evaporator over the phase transition surface is calculated using the Newton-Richmann equation:

$$h = \frac{Q}{A(\bar{T}_e - \bar{T}_v)} = \frac{q}{\Delta T} \tag{6}$$

Heat transfer coefficients of the evaporator 1 surface at a heat load of 40 W for different rates of filling the thermosyphon with working liquid (as a percentage in relation to the internal volume of the evaporator), is shown in **Figure 12**.

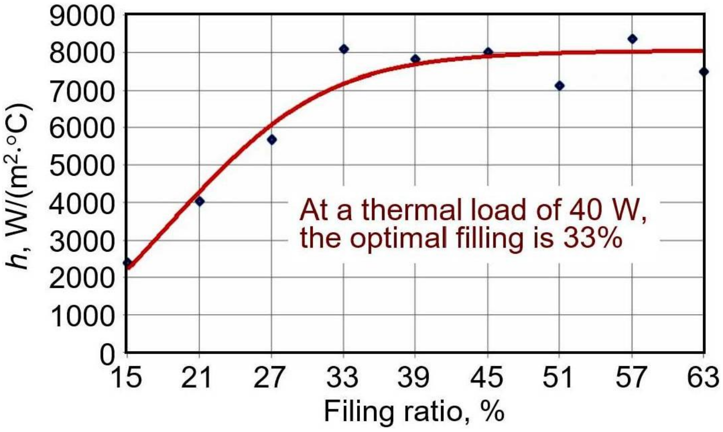

Figure 12. Effect of the degree of filling ratio with acetone on the heat transfer intensity in the evaporator, Q = 40 W.

It is evident from the graph in **Figure 12** that when the thermosyphon transfers a heat load of 40 W, significant changes in the heat transfer coefficient occur at a filling level of the evaporator with acetone up to 33%. Further increase in the rate of filling the thermosyphon with working fluid does not lead to a change in the heat transfer coefficient. Therefore, for this heat load, the optimal filling is 33%.

Important characteristics of closed two-phase thermosyphons are the total thermal resistance of the device and the thermal resistances of individual components. The graphs of the dependence of thermal resistances of the evaporator, condenser, and the entire thermosyphon (R_e, R_c, and R_{TS}), calculated using Equations (1)–(3), are shown in **Figure 13**.

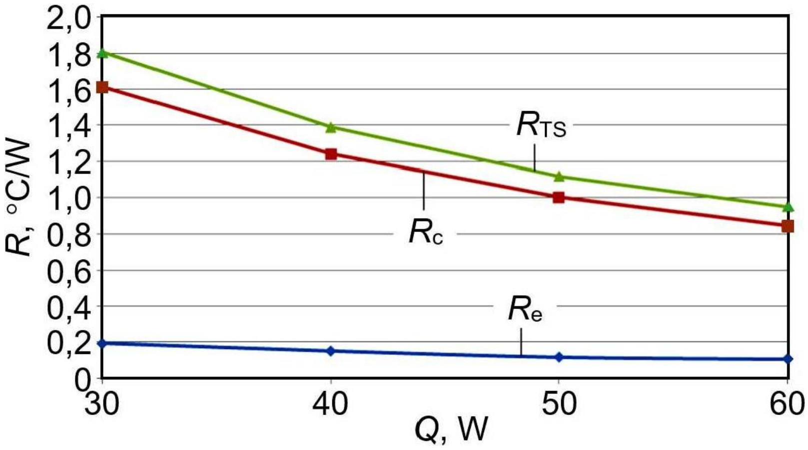

Figure 13. Dependence of thermal resistances of the evaporator (R_e), condenser (R_c), and total thermal resistance (R_{TS}) on the thermal load Q.

2.3.2. Evaporators 1 and 2 are heat loaded

A loop thermosyphon with two evaporators has the ability to receive heat from two heat sources of equal or different thermal power. To determine the behavior of the thermosiphon when a load is applied to both evaporators, the main evaporator (1) was started with a heat flow of 40 W, after reaching the steady state, a heater with a power of 20 W was connected to the additional evaporator (2). Temperature distribution data are shown in **Figure 14**. The curves in the figure indicate three stages of the process.

First, the thermosyphon is started with a heat load of 40 W on evaporator 1 (stage 1). At stage 2, the thermosyphon with the heat-loaded evaporator 1 reaches a steady-state operating mode. The third stage corresponds to the inclusion of the previously inactive evaporator 2 into operation with a heat load of 20 W and the thermosyphon reaching a steady-state mode with two heat-loaded evaporators.

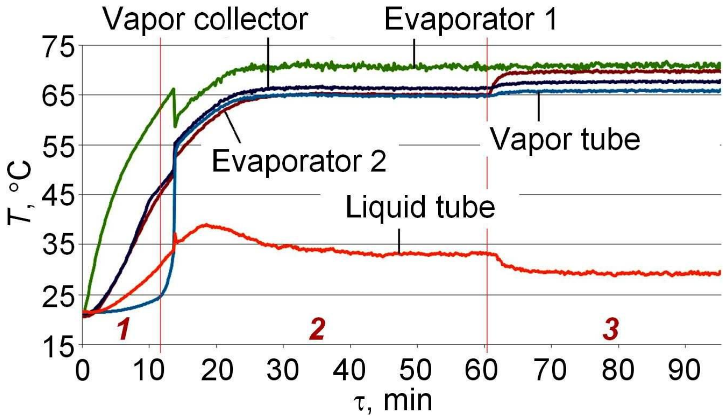

Figure 14. Temperatures of thermosyphon components with sequential switching on of evaporator 1 (40 W) and evaporator 2 (20 W).

When the heat load was applied to evaporator 2, the temperature of the main evaporator 1 remained virtually unchanged. A slight increase in the vapor temperature was observed with a noticeable cooling of the liquid phase, which is explained by the increased heat exchange in the condenser. **Figure 15** shows the temperature values on the thermosyphon body in steady-state mode with a load of 40 W on evaporator 1 and 20 W on evaporator 2. The layout of the temperature sensors on the thermosyphon is shown in **Figure 8**.

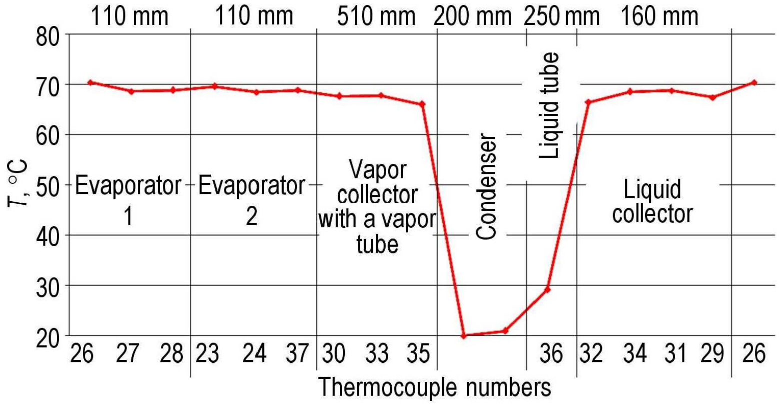

Figure 15. Temperature field along the thermosyphon in steady state with both thermosyphon evaporators active.

3. Discussion

Electric and hybrid transport allows for the reduction of the consumption of hydrocarbon fuels and improves the ecology of the planet, which is the reason for its increasing prevalence. The design of both cars and aircraft with electric power plants includes components that generate a large amount of heat during operation. This heat-loaded equipment requires efficient and energy-saving thermal control systems. Cooling systems based on heat pipes and thermosyphons, possessing the above-mentioned qualities, have proven themselves well and require further development in connection with the growing energy intensity of electric and hybrid vehicles. A new loop thermosyphon with two evaporators and one condenser for cooling electronic components is developed and tested with acetone as the working fluid.

The results of the experimental study of the thermosyphon with two parallel panels showed that its operation is related to the difference in heating power between the two panels. The hydraulic resistance of the high-load panel is higher than the low-load panel. When there is a significant difference in the loads of the two evaporators, the high-load evaporator experiences overheating due to the insufficient fluid flow, while the low-load evaporator incurs some flow wastage. The tested thermosyphon is characterized by dynamic entry into the operating mode. Considering the importance of weight characteristics for equipment used in transport, the advantage of the thermosyphon is also its lightness, due to the choice of aluminum as a construction material.

4. Conclusions

Among the various means of temperature control of heat-loaded equipment of electric and hybrid vehicles, systems on heat pipes and thermosyphons stand out due to a number of advantages, including efficiency, simplicity, no need for energy consumption for their operation, and automatic start-up. To solve problems of optimizing the temperature conditions of operation of electronic systems, including on-board equipment of electric and hybrid transport, an aluminum loop thermosyphon was created and tested. Based on the results of the study, the following conclusions can be drawn:

1) As the transferred heat flow increases, the thermal resistance of the thermosyphon decreases, since the circulation of the working fluid along the circuit accelerates and heat exchange processes intensify. The stability of heat transfer by the thermosyphon is maintained even with non-stationary and asymmetrical heat load supplies to the evaporators.
2) An additional evaporator (2) helps to start the thermosyphon with the filling ratio 30%, acting as an auxiliary condenser during the transition mode.
3) Thermosyphons of this type can be used to create heat exchangers for passive thermal control systems for electronics, space equipment, avionics, traction drives for electric transport, etc.

Experience with aluminum shows that there are difficulties in creating effective porous structures with the required porosity, permeability and capillary potential for evaporators, since the method of their production by sintering powder particles is not applicable in this case. Modification of heat exchange surfaces can be carried out by structuring, coating with aluminum dioxide particles and other methods.

Author contributions: Conceptualization, LV and AZ; methodology, DS; software, DS; validation, LV, AZ and DS; formal analysis, AZ; investigation, DS; resources, LV; data curation, DS; writing—original draft preparation, AZ; writing—review and

editing, AZ; supervision, LV; project administration, LV. All authors have read and agreed to the published version of the manuscript.

Funding: This research was funded by the Belarusian Republican Foundation for Fundamental Research, grant No. T23RNF-227.

Conflict of interest: The authors declare no conflict of interest.

References

1. Kendall K. Low carbon integrated vehicles and buildings. Mechanical Engineering Advances. 2024; 2(1). doi: 10.59400/mea.v2i1.282
2. Ekici F, Orhan G, Gümüş Ö, et al. A policy on the externality problem and solution suggestions in air transportation: The environment and sustainability. Energy. 2022; 258: 124827. doi: 10.1016/j.energy.2022.124827
3. Gan Y, Wang M, Lu Z, et al. Taking into account greenhouse gas emissions of electric vehicles for transportation de-carbonization. Energy Policy. 2021; 155: 112353. doi: 10.1016/j.enpol.2021.112353
4. Sanguesa JA, Torres-Sanz V, Garrido P, et al. A Review on Electric Vehicles: Technologies and Challenges. Smart Cities. 2021; 4(1): 372-404. doi: 10.3390/smartcities4010022
5. Andersen PH, Mathews JA, Rask M. Integrating private transport into renewable energy policy: The strategy of creating intelligent recharging grids for electric vehicles. Energy Policy. 2009; 37(7): 2481-2486. doi: 10.1016/j.enpol.2009.03.032
6. Coutinho M, Afonso F, Souza A, et al. A Study on Thermal Management Systems for Hybrid–Electric Aircraft. Aerospace. 2023; 10(9): 745. doi: 10.3390/aerospace10090745
7. Xie Y, Savvarisal A, Tsourdos A, et al. Review of hybrid electric powered aircraft, its conceptual design and energy management methodologies. Chinese Journal of Aeronautics. 2021; 34(4): 432-450. doi: 10.1016/j.cja.2020.07.017
8. Justin CY, Payan AP, Briceno SI, et al. Power optimized battery swap and recharge strategies for electric aircraft operations. Transportation Research Part C: Emerging Technologies. 2020; 115: 102605. doi: 10.1016/j.trc.2020.02.027
9. Tom L, Khowja M, Vakil G, et al. Commercial Aircraft Electrification—Current State and Future Scope. Energies. 2021; 14(24): 8381. doi: 10.3390/en14248381
10. Asli M, König P, Sharma D, et al. Thermal management challenges in hybrid-electric propulsion aircraft. Progress in Aerospace Sciences. 2024; 144: 100967. doi: 10.1016/j.paerosci.2023.100967
11. Oliveira JLG, Tecchio C, Paiva KV, et al. In-flight testing of loop thermosyphons for aircraft cooling. Applied Thermal Engineering. 2016; 98: 144-156. doi: 10.1016/j.applthermaleng.2015.12.008
12. Vasiliev L, Zhuravlyov A, Kuzmich M, et al. Development and testing of a novel horizontal loop thermosyphon as a kW-class heat transfer device. Applied Thermal Engineering. 2022; 200: 117682. doi: 10.1016/j.applthermaleng.2021.117682
13. Vasiliev LL, Zhuravlyov AS. Two-phase heat transfer devices for passive cooling of electric and hybrid aircraft onboard equipment. International Journal of Sustainable Aviation. 2023; 9(2): 89. doi: 10.1504/ijsa.2023.129938
14. Vasiliev LL, Zhuravlyov AS, Kuz′mich MA, et al. Loop Thermosyphon for Cooling Heat-Loaded Electronics Components. Journal of Engineering Physics and Thermophysics. 2023; 96(7): 1708-1715. doi: 10.1007/s10891-023-02840-8
15. Karayiannis TG, Mahmoud MM. Flow boiling in microchannels: Fundamentals and applications. Applied Thermal Engineering. 2017; 115: 1372-1397. doi: 10.1016/j.applthermaleng.2016.08.063
16. Vargaftik NB, Vinogradov YK, Yargin VS. Handbook of physical Properties of Liquids and Gases. Pure Substances and Mixures, 3rd ed. Begel House, Inc., New York, Wallingford (UK); 1996.

Mechanical Engineering Advances 2025, 3(2), 2512.
https://doi.org/10.59400/mea2512

Article

On the analytical mechanics methods in mathematical modeling the dynamics systems with geometric constraints

Aleksandr Ya Krasinskiy

[1] Department of Computer Modeling and Probability Theory, Moscow Aviation Institute, National Research University, 125993 Moscow, Russia; krasinsk@mail.ru
[2] Information and Computing Center, Rosbiotech, 125080 Moscow, Russia

CITATION

Krasinskiy AY. On the analytical mechanics methods in mathematical modeling the dynamics systems with geometric constraints. Mechanical Engineering Advances. 2025; 3(2): 2512.
https://doi.org/10.59400/mea2512

ARTICLE INFO

Received: 6 January 2025
Accepted: 20 March 2025
Available online: 8 May 2025

COPYRIGHT

Copyright © 2025 by author(s). *Mechanical Engineering Advances* is published by Academic Publishing Pte. Ltd. This work is licensed under the Creative Commons Attribution (CC BY) license.
https://creativecommons.org/licenses/by/4.0/

Abstract: A necessary condition for the most effective application of the mathematical control theory results to the modern automatic devices dynamics consideration is the presence of an adequate nonlinear mathematical model obtained by strict general methods. Methods for reducing the dimensions of dynamic models of systems with geometric constraints by analytical mechanics methods for non-free systems are considered due to the transition to equations in redundant coordinates free of constraint multipliers. A detailed algorithm for this procedure and its justification is given. Using the theory of critical cases, a complete solution is given to the stabilizing problem of a given configuration of systems with geometric constraints.

Keywords: mathematical dynamics model; geometric constraints; stabilization

1. Introduction

The trouble-free operation of modern automatic technical devices is determined by the reliability of their control systems. The mathematical control theory with incomplete state information [1] has developed methods for increasing this reliability by not only reducing the control vector dimension (the number of actuators) [2,3], but also by reducing the volume of current measurement information (the number of measuring sensors) that ensure the formation and implementation of the necessary control actions in real time.

A necessary condition for the these results effective application is the adequate nonlinear mathematical model of the dynamics device under study, obtained by strict abstract-theoretical methods. Despite intensive research, the methods development for the strict nonlinear controlled dynamics modeling of modern automatic devices requires further development. All of the above fully applies to such a widespread and rapidly developing class of automatic systems as manipulators with parallel kinematics [4].

At the initial stage, completely incorrect attempts were made to describe the such systems dynamics using classical Lagrange equations of the second kind. The such equations use is based on the generalized coordinate introduction, i.e. independent parameters in the smallest number, uniquely determining the system state. This procedure is not feasible in the presence of relationships describing geometric connections.

Later, traditionally, studies began on modeling the dynamics of manipulators with parallel kinematics using the Lagrange equations with constraint multipliers. The need for a general solution to the inverse kinematics problem that arises with this approach makes it impossible to obtain an analytical form of a nonlinear model. Since in the absence of such a model, the effective application for the mathematical control theory results is impossible, published studies are limited to considering specific technical devices.

2. Methods

Until now, to construct mathematical models of these devices as systems with geometric constraints, a method [5–9] has been used that is far from being the most effective, based on the use of equations with constraint multipliers [10–14]. As is known, such an approach increases the dimensionality of the model: the variables of the model are, in addition to all coordinates, all (including dependent) velocities, and additionally constraint multipliers. Attempts are being made to simplify the study (reduce the dimensionality of the model) of specific devices by excluding constraint multipliers using an extremely labor-intensive method associated with double differentiation with respect to time of the geometric constraint equations and substitution into the obtained acceleration ratios of all coordinates expressed from equations with constraint multipliers.

The algorithm of such a study method was proposed and substantiated by Lyapunov [15] in 1885: the unique nontrivial solvability of the obtained ratios as linear inhomogeneous algebraic equations with respect to constraint multipliers was proven. The dimensionality of the mathematical model is reduced by this method by excluding the constraint multipliers from consideration. The applicability of this cumbersome method is obvious only to the study of the specific device dynamics; it cannot have general theoretical significance.

But even with the use of modern software for processing symbolic information, it is not possible to obtain the dynamics mathematical model for a specific technical device in analytical form due to the already noted extreme labor intensity by the practical implementation of the Lyapunov algorithm. Consideration using this method, in particular, of the Delta robot dynamics was limited [6,8,9] only to the device behavior computer simulation with an arbitrarily specified vector of control actions.

Analytical mechanics of non-free systems with geometric constraints (which include manipulators with parallel kinematics) has effective general theoretical methods for reducing the dimensions of mathematical models [10,11,13,14] of their dynamics by excluding from consideration not only the constraint multipliers, but also the velocities of coordinates dependent on the constraints [12].

However, as the analysis of publications shows, despite the numerous articles [16–19], these results have not yet found application in technical practice. In stabilizing problems for the given configuration manipulators with parallel kinematics, a further reduction of the mathematical model dimension for determining the stabilizing controls can be achieved by applying the theory of critical cases of nonlinear stability theory [20–22]. But for a justified conclusion, due to this theory, not only a strict selection of the first approximation is necessary, but also a complete analysis of the nonlinear terms of the equations of perturbed motion in analytical form. In such situations, no computer modeling can solve the problem. A complete nonlinear model obtained by strict abstract-theoretical methods with the necessary reduction of the equations to a special form using the replacement [23] is required. The use of general methods makes it possible to further reduce the control problems dimensions by moving, in particular, to Routh variables [24,25].

3. Traditional method for modeling the non-free systems dynamics

Let us consider the algorithm for compiling Lagrange equations with constraint multipliers for a system with coordinates $q_1, \dots, q_{n+m}$ and geometrical constraints,

$$F(q) = 0;\ F'(q) = \left(F_1(q), \dots, F_m(q)\right) \tag{1}$$

$$\det \left\| \frac{\partial\left(F_1(q), \dots, F_m(q)\right)}{\partial\left(q_{n+1}, \dots, q_{n+m}\right)} \right\| \neq 0; \tag{2}$$

with kinetic energy of the most general form (here and below, summation is performed over repeating indices)

$$T(q, \dot{q}) = {}^1\!/_2\, a_{ik}(q)\dot{q}_i\dot{q}_k + a_i(q)\dot{q}_i + T_0;\ i,k = \overline{1,n+m}; \tag{3}$$

Due to the presence of relations (1), the following conditions are imposed on the variations of the coordinates:

$$b_{\sigma i}(q)\delta q_i = 0;\ b_{\sigma i} = \frac{\partial F_\sigma}{\partial q_i}\ ;\ \sigma = \overline{1,m};\ i = \overline{1,n+m}; \tag{4}$$

imposed on the variations of coordinates due to the presence of constraints (1) on which the forces Q_i, related to the coordinates (potential and non-potential) act.

The equations of motion with constraint multipliers

$$\frac{d}{dt}\frac{\partial T}{\partial \dot{q}_i} - \frac{\partial T}{\partial q_i} = Q_i + \lambda_\sigma b_{\sigma i};\ \sigma = \overline{1,m};\ i = \overline{1,n+m}; \tag{5}$$

can be obtained [10–14] from the d'Alembert-Lagrange principle. The variables of the model are

$$q_i,\ \dot{q}_i,\ \lambda_\sigma i = \overline{1,n+m};\ \sigma = \overline{1,m};$$

In general, to obtain a complete nonlinear dynamics mathematical model of a system with geometric constraints, m nonlinear algebraic geometric constraints in Equation (1) should be added to $n + m$ second-order differential Equation (5). The model includes all coordinates and all velocities (including those dependent on constraints). To determine the Lagrange multipliers, it is necessary to take into account relations (1) for determining the constraint multipliers. When passing to the normal form, we obtain $2(n + m)$ first-order differential equations and m algebraic constraint equations. The variables of such a high-dimensional model are all $n + m$ coordinates, all $n + m$ velocities and m constraint multipliers. The total dimension of the model is $2(n + m) + m = 2n + 3m$.

This approach leads to an unjustified increase in the dimensions of the models, which greatly exceeds the number of degrees of freedom of the system. Therefore, for controlled systems with geometric constraints, there is still practically no analytical form of mathematical dynamics models, including the actuator models.

The situation persists [5–9], despite the fact that in the analytical mechanics of non-free systems, methods have been developed [12,16–19] for reducing the dimensions of models by switching to equations in redundant coordinates by excluding dependent velocities from consideration using differentiated equations of geometric constraints and the expression for the Lagrange multipliers found in the general case.

Remark 1. *It should be noted that attempts have been made to model the system's dynamics with geometric constraints using Lagrange equations of the second kind. In particular, such an approach was used to study the dynamics of the well-known Ball and Beam (**Figure 1**).*

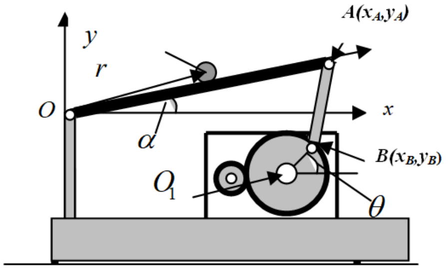

Figure 1. Scheme of the "Ball and Beam" stand.

In this system, the electric drive, due to the inclination of the chute OA, can roll the ball C to any predetermined position on the chute and stabilize this equilibrium. The chute is connected on one side at point O to a fixed supporting post, and on the other to a movable lever AB. The motion of the lever is controlled by a DC motor. A nonlinear geometric relationship is imposed on the system: the distance between points $A(x_A, x_B)$ *and* $B(x_B, y_B)$ *is constant:*

$$\left(L(cos\alpha-1)+d(1-cos\theta)\right)^2+(Lsin\alpha+l-dsin\theta)^2=l^2; \qquad (6)$$

(L = OA − length of the trough, l = AB − length of the lever, d − radius of the output drive wheel).

Starting with [26], in all studies of the dynamics of the Ball and Beam stand with a geometric constraint [26–31], when constructing a mathematical model, immediately, starting with [26] and up to now [30,31], they completely unjustifiably move from a nonlinear Equation (6) to a linear dependence $\alpha \approx \frac{d}{L}\theta$ and exclude the dependent coordinate from consideration. Despite the fact that the incorrectness of such an approach has already been discussed in detail earlier [16–18], such a model is still used [30,31], and even referring to the article [17] (compare with [32]). Therefore, the author considered it appropriate to once again present in detail an alternative algorithm for obtaining, using strict methods of analytical mechanics, non-free systems of complete nonlinear models, the dimensions of which are significantly smaller than those traditionally used.

4. Method of excluding constraint multipliers in dynamics models for specific systems with geometric constraints.

The labor intensity by the dynamics research of specific technical devices with geometric constraints is determined by the dimensionality of the model used. Most often, information on constraint reactions is not required in technical practice. Therefore, it is possible to simplify the study by defining an explicit form of constraint multipliers to exclude them from consideration.

The general procedure for this operation was developed by Lyapunov [15]. With this modeling method, the dynamics of a specific system, it is necessary to consistently perform extremely labor-intensive and cumbersome operations:

1) Express all accelerations $\ddot{q}_i$ from the equations of motion with constraint multipliers (6).

2) Obtain a system of linear algebraic relations with respect to accelerations by differentiating the expressions of geometric constraints twice with respect to time.

3) By substituting the expressions for accelerations from the motion equations into these relations, obtain a linear inhomogeneous algebraic equations system with respect to the constraint multipliers λ_σ.

4) Express the constraint multipliers from these equations as $\lambda_{\sigma(}(q,\dot{q})$.

5) Substitute the expressions $\lambda_{\sigma(}(q,\dot{q})$ into Equation (6) to obtain a mathematical model of the system dynamics without constraint multipliers.

Despite the extreme labor intensity of this method of obtaining a model, proposed back in the 19th century, it is this method that is still used in the study of the Delta robot [5]. The complexity of the resulting mathematical model (only the mechanical component of the robot without taking transient processes into account for the actuators is considered) leads to the possibility of considering only a computer simulation.

It should be noted that (using modern information technologies) the method [15] was used [5] without references. It is obvious that it is fundamentally impossible to obtain an explicit analytical form of a nonlinear mathematical model of the device under study dynamics in this way. In our opinion, that leads to the fact that in modern dynamics studies for robotic devices with parallel kinematics, the mechanical robot component behavior analysis from the analytical mechanics standpoint is not at all carried out, and immediately a transition to computer modeling is carried out.

Moreover, a completely unfounded conclusion about the model adequacy constructed using modern information technologies with selected specific numerical values of the device parameters is made on the basis of the model's behavior proximity (obtained as a numerical experiment result) to the real object dynamics. Analysis of the particular solution behavior for a nonlinear differential equations system, especially one obtained using one or another approximate calculation method, in principle cannot serve as the basis for any conclusions about the nature of this system's general solution.

5. Some general methods for reducing the dimension of the mathematical model in modeling the non-free systems dynamics

General methods for such an exclusion, associated with a single or double differentiation with respect to time of the equation of geometric constraints (1) Lurye [10], Suslov [11] developed.

Separating in Equation (4) the variations of independent and dependent coordinates we obtain

$$b_{\sigma\rho}(q)\delta q_\rho + b_{\sigma\mu}(q)\delta q_\mu = 0;\ \mu = \overline{n-m+1, n+m};\ \sigma = \overline{1,m};\ \rho = \overline{1,n}; \quad (7)$$

According to Equation (2) we can express from Equation (7) the dependent variations.

$$\delta q_\mu = B_{\mu\rho}(q)\delta q_\rho;\ \left\|B_{\sigma\rho}(q)\right\| = -\left\|\frac{\partial(F_1,\dots,F_m)}{\partial(q_{n+1},\dots,q_{n+m})}\right\|^{-1}\left\|\frac{\partial(F_1,\dots,F_m)}{\partial(q_1,\dots,q_n)}\right\|; \quad (8)$$

The conditions imposed by the constraints Equation (1) on the variations take the form

$$\delta q_\mu - B_{\mu\rho}(q)\delta q_\rho = 0 \quad (9)$$

Using Equation (9) we can separate Equation (5) for dependent and independent coordinates.

$$\frac{d}{dt}\frac{\partial T}{\partial \dot{q}_\rho} - \frac{\partial T}{\partial q_\rho} = Q_\rho - B_{\sigma\rho}\lambda_\sigma;\ \frac{d}{dt}\frac{\partial T}{\partial \dot{q}_\sigma} - \frac{\partial T}{\partial q_\sigma} = Q_\sigma + \lambda_\sigma;\ \sigma = \overline{1,m};\ \rho = \overline{1,n}; \quad (10)$$

Expressing the multipliers from the second Equation (10)

$$\lambda_\sigma = \frac{d}{dt}\frac{\partial T}{\partial \dot{q}_\sigma} - \frac{\partial T}{\partial q_\sigma} - Q_\sigma; \sigma = \overline{n+1, n+m}; \quad (11)$$

After substituting Equation (11) for the first equation of system Equation (10), we obtain

$$\frac{d}{dt}\frac{\partial T}{\partial \dot{q}_\rho} - \frac{\partial T}{\partial q_\rho} = Q_\rho - B_{\sigma\rho}\left(\frac{d}{dt}\frac{\partial T}{\partial \dot{q}_\sigma} - \frac{\partial T}{\partial q_\sigma} - Q_\sigma\right);$$

From the equations of the constraints (1), differentiated once with respect to time, it is possible to express the dependent velocities.

$$\dot{q}_\sigma = B_\mu(q)\dot{q}_j;\ \sigma = \overline{1,m}; j = \overline{1,n}; \quad (12)$$

In our opinion, a much more effective way to reduce the dimensionality of the model is the alternative method of Shulgin [12] of transition to decreases in redundant coordinates by excluding from consideration the multipliers and dependent velocities.

Denoting the result of eliminating dependent velocities using Equation (12) from the kinetic energy Equation (3) through $T^*(q_1, \dots, q_{n+m}, \dot{q}_1, \dots, \dot{q}_n)$, and from the acting forces through Q_i^*.

$$T^* = {}^1\!/_2\, a^*_{\gamma\rho}(q)\dot{q}_\rho\dot{q}_\gamma + a^*_\rho(q)\dot{q}_\rho + T_0;\ \rho, \gamma = \overline{1,n}; \quad (13)$$

$$a^*_{\gamma\rho}(q) = a_{\gamma\rho} + a_{\mu\gamma}B_{\mu\gamma}B_{\mu\rho} + a_{\mu\rho}B_{\mu\gamma} + a_{\mu\sigma}B_{\mu\rho}B_{\sigma\gamma};\ a^*_\rho(q) = a_\rho + a_\mu B_{\mu\rho}.$$

Comparing the corresponding derivatives $T^*(q_1, \dots, q_{n+m}, \dot{q}_1, \dots, \dot{q}_n)$ and $T(q_1, \dots, q_{n+m}, \dot{q}_1, \dots, \dot{q}_{n+m})$ and taking into account the integrability of the constraints (12), we will have as a result, in the general case, a nonlinear mathematical model of the system dynamics is obtained in the form of M.F. Shulgin's equations free of multipliers [12] in redundant coordinates (cf. the equations of Voronets [33–35] into account the integrability of the kinematic constraints (12):

$$\frac{d}{dt}\frac{\partial T^*}{\partial \dot{q}_\rho} - \frac{\partial T^*}{\partial q_\rho} = Q_\rho^* + B_{\sigma\rho}(q)\left(\frac{\partial T^*}{\partial q_\sigma} + Q_\sigma^*\right);\ \dot{q}_\sigma = B_{\sigma\rho}(q)\dot{q}_\rho; \tag{14}$$

$$\sigma = \overline{n+1, n+m};\ \ \rho = \overline{1, n};$$

It should be noted that, unlike the approach of Lyapunov [15], this is a general theoretical method. In the general case, the dimension of the mathematical model of the dynamics of systems with geometric constraints in the form (14) is reduced in comparison with Equation (5) by a double number of constraints (1). In addition to the multipliers, the model does not contain the velocity coordinates that depend on the presence constraints (1). Moreover, it should be especially noted that the application of this modeling method to the study of the dynamics of specific technical devices generally eliminates the need to solve the inverse kinematics problem (cf. [5]). The strict nonlinear model is obtained in analytical form and includes in normal form only $2n + m$ differential equations of the first order, i.e., it is reduced by $2m$ in comparison with the dimension $2n + 3m$ of model (1), (5).

Let us once again present a step-by-step algorithm for obtaining a generally nonlinear mathematical model (14) of the dynamics of a system with geometric constraints (1):

1) Differentiate the equations of geometric relationships (1) once with respect to time.

2) Express the velocities of dependent coordinates (12) from this linear algebraic system.

3) After substituting (12) into the acting forces, kinetic energy (3) is obtained as kinetic energy (13) with the dependent velocities excluded.

4) Obtain a mathematical model (14) of the dynamics of systems in redundant coordinates.

It is extremely important to note that, for the practical application of this mathematical modeling method for the systems dynamics with geometric constraints, mathematical training in the amount of standard engineering education is quite sufficient. No additional competencies in the field of analytical mechanics of non-free systems are required.

The obtained general analytical form of the mathematical model of nonlinear dynamics allows, in the general case, to present the mathematical dynamics model for any system with geometric constraints (under the action of arbitrary potential and non-potential forces that do not violate the conditions for the existence and uniqueness of the differential equations solutions) in the form of the Shulgin Equation (14) in explicit scalar form [16,17,36] without resolving the inverse problem of kinematics (cf. [5,7,8,37,38]):

$$\begin{aligned} a_{lr}^*\ddot{q}_r + \frac{\partial a_{lr}^*}{\partial q_j}\dot{q}_r\dot{q}_j + \frac{\partial a_{lr}^*}{\partial q_\mu}B_{\mu j}\dot{q}_l\dot{q}_j - \frac{1}{2}\frac{\partial a_{lj}^*}{\partial q_l}\dot{q}_r\dot{q}_j - \frac{1}{2}\frac{\partial a_{lj}^*}{\partial q_\mu}B_{\mu l}\dot{q}_r\dot{q}_j + \left(\frac{\partial a_l^*}{\partial q_r} - \frac{\partial a_r^*}{\partial q_l} + B_{\mu l}\frac{\partial a_l^*}{\partial q_r} - B_{\mu l}\frac{\partial a_r^*}{\partial q_\mu}\right)\dot{q}_r \\ + \frac{\partial W}{\partial q_l} + B_{\mu l}\frac{\partial W}{\partial q_\mu} = Q_l^* + B_{\mu l}Q_\mu^*; \dot{q}_\sigma = B_{\sigma j}(q)\dot{q}_j; \end{aligned} \tag{15}$$

$$\mu, \sigma = \overline{n+1, n+m}; \;\; l, j, r = \overline{1, n};$$

here $W(q) = \Pi(q) - T_0(q)$ is the changed (reduced) potential energy, $\Pi(q)$ - potential energy, and Q_l^*, Q_μ^* now denotes the non-potential forces corresponding to the coordinates q_l, q_μ when they are introduced in excess.

One of the most important problems in technical practice of the technical objects control is ensuring stable implementation of the object specified behavior. The analytical form of the obtained mathematical model created the possibility for the Krasovskii's method using by determining the stabilizing control that solves this problem. The developed complex application of analytical mechanics strict methods for non-free systems [10–14] and nonlinear stability theory [20–22] to real modern technical devices due to the reduction of the model dimension allows including the actuators dynamics in the consideration. In particular, in detailed studies of the Ball and Beam stand, additional voltage on the armature winding of the actuator drive commutator motor was considered as a stabilizing control. The control coefficients were determined [16–19] from the linear-quadratic stabilization problem solution by the Krasovskii method [39]. To conclude about the asymptotic (despite the presence of the zero root of the characteristic equation) stability [20–24] in the complete nonlinear system closed by the found control, a proof of the general theorem [16,17] was required.

The results obtained in the complete study of the Ball and Beam stand dynamics created [16–18,34] the basis for the development of such a general modeling method for the controlled dynamics of non-free mechanical systems with geometrical constraints in general [19], which turned out to be an effective tool for the nonlinear dynamics modeling of manipulators with parallel kinematics [36]. The rigorous nonlinear mathematical models obtained with its use made it possible to apply general methods of nonlinear stability theory [20–24] for a complete solution, in particular, in stabilization problems of given parallel manipulator configurations.

6. Application of the developed mathematical model to the general stabilization problem for non-free systems

Let the system admit an equilibrium position.

$$q_i = q_{i0}, \quad q_\mu = q_{\mu 0} \tag{16}$$

Equilibrium equations can be obtained in the general case from the Equation (15).

$$\frac{\partial W}{\partial q_i} + B_{\mu i}\frac{\partial W}{\partial q_\mu} = Q_{i(\dot{q}=0)} + \left(B_{\mu i} Q_\mu\right)_{(\dot{q}=0)} \tag{17}$$

When $T_0(q) = 0$ and there are no non-potential forces, we obtain

$$\frac{\partial \Pi}{\partial q_i} + B_{\mu i}\frac{\partial \Pi}{\partial q_\mu} = 0.$$

Remark 2. *It follows that the equilibrium position when using redundant coordinates may not be a stationary point of potential energy. However, if the* *potential energy can be expressed through independent generalized coordinates* $\Pi(q_1, \dots, q_n)$*, then for it, in the absence of non-potential positional forces, all*

$$\frac{\partial \Pi}{\partial q_i} = 0, i = \overline{1, n}.$$

Remark 3. *From the equilibrium Equation (17) it follows that potential and non-potential positional forces may contain constant non-zero terms*

$$\left(\frac{\partial W}{\partial q_i}\right)_0 \neq 0, \left(\frac{\partial W}{\partial q_\mu}\right)_0 \neq 0,\ Q_i(q_0) \neq 0, Q_\mu(q_0) \neq 0: \tag{18}$$

In order to formulate the equations of disturbed motion necessary for solving the stabilization problem, we introduce disturbances.

$$q_{i0} = q_{i0} + x_i, q_\mu = q_{\mu o} + y_\mu.$$

To solve the stabilization problem, equations of perturbed motion should be drawn up. Let us introduce disturbances, compose equations of perturbed motion and select the first approximation in them. Let us formulate the equations of the perturbed motion and select the first approximation in them.

Here, for ease of understanding the taking-into-account problem of the required order in the constraint equations with a strict selection of the first approximation, the equations are written without taking into account non-potential forces (among which there may be control ones):

$$\begin{aligned} a_{is}^*(0)\ddot{x}_s &+ \left[\left(\frac{\partial a_i^*}{\partial q_s}\right)_0 - \left(\frac{\partial a_s^*}{\partial q_i}\right)_0 + B_{\mu s}(0)\left(\frac{\partial a_i^*}{\partial q_\mu}\right)_0 - \left(\frac{\partial a_s^*}{\partial q_\mu}\right)_0 B_{\mu i}(0)\right]\dot{x}_s \\ &+ \left[\left(\frac{\partial^2 W}{\partial q_i \partial q_s}\right)_0 + B_{\mu i}(0)\left(\frac{\partial^2 W}{\partial q_\mu \partial q_s}\right)_0 + \left(\frac{\partial W}{\partial q_\mu}\right)_0 \left(\frac{\partial B_{\mu i}}{\partial q_s}\right)_0\right] x_s \\ &+ \left[\left(\frac{\partial^2 W}{\partial q_i \partial q_k}\right)_0 + B_{\mu i}(0)\left(\frac{\partial^2 W}{\partial q_k \partial q_\mu}\right)_0 + \left(\frac{\partial B_{\mu i}}{\partial q_k}\right)_0 \left(\frac{\partial W}{\partial q_\mu}\right)_0\right] y_k = X_i^{(2)}(\dot{x}, x, y); \end{aligned} \tag{19}$$

here $(\cdots)_0$ means the value of the expression in brackets in equilibrium (16), and the number in the brackets in the upper index is the order of the lowest terms in the corresponding expression expansion.

Let us add to these equations the equations of differential constraints with the selected first approximation

$$\dot{y}_k = B_{jk}(0)\dot{x}_k + B_{jk}^{(1)}(x, y)\dot{x}_k \tag{20}$$

$$B_{jk}^{(1)}(x, y) = B_{jk}\left(q_{i0} + x, q_{\mu 0} + y\right) - B_{jk}\left(q_{i0}, q_{\mu 0}\right);\ B_{jk}\left(q_{i0}, q_{\mu 0}\right) = B_{jk}(0).$$

If a linear replacement is carried out in system (18), (19) [23]

$$z_k = y_k - B_{kj}(0)x_j \tag{21}$$

then the constraint equations will take the form

$$\dot{z}_k = B_{kj}^{(1)}(x, z + B(0)x)\dot{x}_j; \tag{22}$$

After replacement (21), there are no linear terms on the right in Equation (22). Obviously, the variables z_k correspond to the zero roots of the characteristic equation of the system.

$$
\begin{aligned}
a_{is}^{*}(0)\ddot{x}_s &+ \left[\left(\frac{\partial a_i^{*}}{\partial q_s}\right)_0 - \left(\frac{\partial a_s^{*}}{\partial q_i}\right)_0 + B_{\mu s}(0)\left(\frac{\partial a_i^{*}}{\partial q_\mu}\right)_0 - \left(\frac{\partial a_s^{*}}{\partial q_\mu}\right)_0 B_{\mu i}(0)\right]\dot{x}_s \\
&+ \left[\left(\frac{\partial^2 W}{\partial q_i \partial q_s}\right)_0 + B_{\mu i}(0)\left(\frac{\partial^2 W}{\partial q_\mu \partial q_s}\right)_0 + \left(\frac{\partial W}{\partial q_\mu}\right)_0\left(\frac{\partial B_{\mu i}}{\partial q_s}\right)_0\right]x_s \\
&+ \left[\left(\frac{\partial^2 W}{\partial q_i \partial q_k}\right)_0 + B_{\mu i}(0)\left(\frac{\partial^2 W}{\partial q_k \partial q_\mu}\right)_0 + \left(\frac{\partial B_{\mu i}}{\partial q_k}\right)_0\left(\frac{\partial W}{\partial q_\mu}\right)_0\right]\left(z_k + B_{kj}(0)x_j\right) \\
&= X_i^{(2)}(\dot{x}, x, z + B(0)x)
\end{aligned}
\tag{23}
$$

$$\dot{z}_k = B_{kj}^{(1)}(x, z + B(0)x)\dot{x}_j.$$

The system of Equation (23) represents a mathematical model of the dynamics of an arbitrary system with geometric constraints with a strictly selected first approximation. It should be noted that in the equations of the first approximation, in the general case, due to conditions (18), there may be terms

$$\left(\frac{\partial B_{\mu i}}{\partial q_k}\right)_0, \left(\frac{\partial B_{\mu i}}{\partial q_s}\right)_0,$$

determined by the coefficients of quadratic terms in the geometric constraint expansion in the neighborhood equilibrium (16), since the matrix

$$\left\|B_{\sigma\rho}(q)\right\| = -\left\|\frac{\partial(F_1,\ldots,F_m)}{\partial(q_{n+1},\ldots,q_{n+m})}\right\|^{-1}\left\|\frac{\partial(F_1,\ldots,F_m)}{\partial(q_1,\ldots,q_n)}\right\|,$$

through the first-order terms in this expansion. The need to take into account quadratic terms in the constraint equations expansion when studying the stability of systems with geometric constraints was pointed out by Rouse [13].

Now let us assume that in addition to potential forces with energy *Π(q)*, non-potential positional forces and forces depending on velocities act on the system. Having singled out the first approximation in the motion equations for such systems and using the vector-matrix form of recording, we will have

$$Q_i = f_{ij}\dot{q}_j + f_{i\mu}\dot{q}_\mu + p_{ij}q_j + iq_\mu + \cdots.$$

After eliminating dependent velocities and replacing (21) for dependent coordinates, we obtain the characteristic equation of the first approximation system in the general case by the action of potential and non-potential forces.

$$\lambda^m\, det\left[A\lambda^2 + (G + D)\lambda + C_1 + C_2B + B'C_3 + B'C_4B + C^B + P\right] = 0 \tag{24}$$

$$\mathrm{D} = \left\|f_{ij} + f_{i\mu}B_{\mu i} + f_{\mu i}b_{\mu j} + f_{\mu i}b_{\mu k}B_{kj}\right\|;\ G = \{g_{is}(0)\};$$

$$\mathrm{P} = \left\|p_{ij} + p_{i\mu}B_{\mu i} + B_{\mu j}p_{\mu j} + B_{\mu i}p_{\mu k}B_{kj}\right\|;$$

$$\mathrm{A} = \|a^{*}(0)\|;\ G = \|g_{is}(0)\|; C_1 = \left\|\left(\frac{\partial^2 W}{\partial q_i \partial q_s}\right)_0\right\|; C_2 = \left\|\left(\frac{\partial^2 W}{\partial q_i \partial q_\mu}\right)_0\right\|:$$

$$C_4 = \left\| \left(\frac{\partial^2 W}{\partial q_\mu \partial q_\sigma} \right)_0 \right\|;\ C^B = \left\| \left(\frac{\partial W}{\partial q_\mu} \right)_0 \left(\frac{\partial B_{\mu i}}{\partial q_s} \right)_0 + \left(\frac{\partial W}{\partial q_\mu} \right)_0 \left(\frac{\partial B_{\mu i}}{\partial q_k} \right)_0 B_{ks}(0) \right\|;$$

$$\mathrm{B} = \|B_{\mu i}(0)\|;\ g_{is}(0) = \left[\left(\frac{\partial a_i^*}{\partial q_s} \right)_0 - \left(\frac{\partial a_s^*}{\partial q_i} \right)_0 + B_{\mu s}(0) \left(\frac{\partial a_i^*}{\partial q_\mu} \right)_0 - \left(\frac{\partial a_s^*}{\partial q_\mu} \right)_0 B_{\mu i}(0) \right].$$

Let us note once again that in the equations of the perturbed motion after the replacement (21), in the general case, linear terms appear with the matrix C^B, which depends on the linear terms of the expansion of the coefficients of the kinematic constraints $\left(\frac{\partial B_{\mu i}}{\partial q_s} \right)_0, \left(\frac{\partial B_{\mu i}}{\partial q_k} \right)_0$. Hence, the conclusion follows: in the general case, to obtain a linear approximation of the equations of perturbed motion, one cannot limit oneself to considering only the linear term of the expansion of the kinematic constraint Equation (1) (cf. [26–28,30–32]).

Obviously, the characteristic equation (24) in the general case always, under the action of any forces, including control forces, has m zero roots. Consequently, the stability of the equilibrium states of systems with geometric connections is possible only in critical cases [20–22]. Using Kamenkov's [22] theorem, the following is proved:

Theorem [16,17]: If the real parts of all other, except m zero, roots of the characteristic equation are negative, then the equilibrium position [16] is asymptotically stable.

Remark 4. *The developed method basis is the reduction principle results of the nonlinear variables stability theory, when in addition to roots with zero real parts, there necessarily exist roots with negative real parts. The rigorous results of the general reduction principle are formulated after two variable changes. The first of them, linear, should reduce the equations to the so-called special form. With the indicated arrangement of roots, this change always exists. The second nonlinear change existence over all noncritical variables is a difficult problem to solve, since these functions are defined as the series in the variable powers, which convergence conditions in the theorem in the general case cannot be formally verified.*

However, in the mechanical systems special case with differential constraints, due to the nonlinear equations structure, it turned out to be possible to carry out the change only over the part of noncritical variables. And for such systems, the nonlinear change solves the problem of stability (non-asymptotic) in a special case. When passing from geometric constraints in the form of finite equations (1) to the differential constraints in the form (12), taking into account the structure of the arising perturbed motion equations, in contrast to the general case, it is the asymptotic stability of the unperturbed motion that is proven.

Therefore, to solve the problem of stabilizing equilibrium (16) it is necessary to ensure the negativity of the real roots of the equation.

$$det[A\lambda^2 + (G + D)\lambda + C_1 + C_2 B + B'C_3 + B'C_4 B + C^B + P] = 0 \tag{25}$$

The location of the roots of Equation (25) is determined by the linear subsystem.

$$\begin{aligned} a^*_{is}(0)\ddot{x}_s &+ \left[\left(\frac{\partial a^*_i}{\partial q_s}\right)_0 - \left(\frac{\partial a^*_s}{\partial q_i}\right)_0 + B_{\mu s}(0)\left(\frac{\partial a^*_i}{\partial q_\mu}\right)_0 - \left(\frac{\partial a^*_s}{\partial q_\mu}\right)_0 B_{\mu i}(0)\right]\dot{x}_s \\ &+ \left[\left(\frac{\partial^2 W}{\partial q_i \partial q_s}\right)_0 + B_{\mu i}(0)\left(\frac{\partial^2 W}{\partial q_\mu \partial q_s}\right)_0 + \left(\frac{\partial W}{\partial q_\mu}\right)_0 \left(\frac{\partial B_{\mu i}}{\partial q_s}\right)_0\right] x_s \\ &+ \left[\left(\frac{\partial^2 W}{\partial q_i \partial q_k}\right)_0 + B_{\mu i}(0)\left(\frac{\partial^2 W}{\partial q_k \partial q_\mu}\right)_0 + \left(\frac{\partial B_{\mu i}}{\partial q_k}\right)_0 \left(\frac{\partial W}{\partial q_\mu}\right)_0\right] B_{kj}(0)x_j = 0 \end{aligned} \tag{26}$$

The dimension of this subsystem in normal form is 2*n*, i.e., it is further reduced by the number of constraints. Thus, using the analytical mechanics of non-free systems, strict methods, and nonlinear stability theory, a mathematical model is obtained for the general stabilizing problem of given configurations for systems with geometric constraints (in particular, manipulators with parallel kinematics), which dimension is equal to the number of freedom degrees of the system.

The mathematical model (26) includes any possible (not violating the theorem's conditions about the existence and uniqueness of solutions for the corresponding differential equations) potential and non-potential forces. Among these forces, there may also be control mechanical actions (forces and moments) that ensure the specified behavior of the system.

The achieved significant reduction in the model dimensionality and the methods rigor used to obtain it make it possible to include in the controlled dynamics model for a controlled subsystem a mathematical actuators model that creates these control actions. By virtue of the proven theorem on asymptotic stability (taking into account the nonlinear terms) for the model (26) in additional equations modeling the dynamics of actuators, it is sufficient to limit ourselves to only linear terms: with respect to these variables, under the controllability condition, it is always possible to achieve asymptotic stability by the first approximation.

To simplify the further presentation, in accordance with the different nature of the dependence of kinetic and potential energies, geometric constraints and non-potential forces, we introduce vectors.

$$q = \begin{pmatrix} q_1 \\ \vdots \\ q_{n+m} \end{pmatrix}; r = \begin{pmatrix} q_1 \\ \vdots \\ q_n \end{pmatrix}; s = \begin{pmatrix} q_{n+1} \\ \vdots \\ q_{n+m} \end{pmatrix}; F(q) = \begin{pmatrix} F_1 \\ \vdots \\ F_m \end{pmatrix}; Q(q, \dot{q}) = \begin{pmatrix} Q_1 \\ \vdots \\ Q_{n+m} \end{pmatrix}$$

$$Q_r(q, \dot{q}) = \begin{pmatrix} Q_1 \\ \vdots \\ Q_n \end{pmatrix}; Q_s(q, \dot{q}) = \begin{pmatrix} Q_{n+1} \\ \vdots \\ Q_{n+m} \end{pmatrix},$$

and we will move on to the vector form of the dynamics model

$$\frac{d}{dt}\frac{\partial T^*}{\partial \dot{r}} - \frac{\partial T^*}{\partial r} = Q^*_r - B'(q)\left(\frac{\partial T^*}{\partial s} - Q^*_s\right); \dot{s} = B(q)\dot{r}; \tag{27}$$

Equilibrium position (16) in vector form

$$r = r_0; s = s_0: \tag{28}$$

Let us introduce disturbances and write down the equations of the disturbed motion with the selected first approximation.

$$\mathrm{r} = r_0 + x; \dot{r} = x_1; s = s_0 + y:$$

$$\dot{x} = x_1;$$

$$\dot{x}_1 = ax + bx_1 + hy + X_1^{(2)}(x, x_1, y); \tag{29}$$

$$\dot{y} = B(x, y)x_1.$$

The matrices in system (29) are expressed in a known [16–19,32,36] manner through the parameters of the system.

After replacement (21) in vector form

$$z = y - B(0)x; \tag{30}$$

the system (29) will go into

$$\dot{x} = x_1.$$

$$\dot{x}_1 = (a + hB(0))x + bx_1 + hz + X_1^{(2)}(x, x_1, z + B(0)x); \tag{31}$$

$$\dot{z} = B^{(1)}(x, z + B(0)x)x_1.$$

The characteristic equation of this system is

$$\begin{vmatrix} E_n\lambda & -E_n & 0 \\ -a - hB(0) & E_n\lambda - b & 0 \\ 0 & 0 & E_m\lambda \end{vmatrix} = 0: \tag{32}$$

According to the Theorem [16,17] asymptotic stability sufficient condition for the zero solution in the complete nonlinear system (29), the real parts of the roots equation must be negative.

$$\begin{vmatrix} E_n\lambda & E_n\lambda \\ -a - hB(0) & E_n\lambda - b \end{vmatrix} = 0 \tag{33}$$

If this condition is not met, a stabilization problem arises: it is necessary to introduce control that ensures the desired location of the characteristic equation roots for the closed system. If we do not consider the actuators dynamics, to determine the stabilizing mechanical action we obtain the following model for linear system of dimension 2*n*.

$$\dot{x} = x_1;$$

$$\dot{x}_1 = \left(a + hB(0)\right)x + bx_1 + Vu; \tag{34}$$

Here the matrix *V* models the way the control *u* is applied. To formulate sufficient conditions for the solvability of the stabilization problem, we will reduce system (34) to the standard form of mathematical control theory.

$$\dot{\eta} = P\eta + Qu;\ \eta' = (x', x'_1);\ P = \begin{pmatrix} 0 & E_n \\ a + hB(0) & b \end{pmatrix};\ Q = \begin{pmatrix} 0 \\ V; \end{pmatrix} \tag{35}$$

When the controllability condition for the system is met Equation (35)

$$rank[Q\ PQ\ P^2\ Q\ \cdots\ P^{2n-1}\ Q] = 2n; \tag{36}$$

control

$$u = K_1 x + K_2 x_1; \tag{37}$$

can be determined by solving the linear-quadratic problem for system Equation (35) using Krasovskii's method [39]. The minimum dimension r of the control vector sufficient to satisfy condition Equation (36) is determined [2] by the number of the non-trivial invariant polynomials matrix *P*.

The simplification study due to the model dimension reduction creates the possibility for including the actuators dynamics in the consideration. For example, if the implementation of mechanical control actions is ensured by electric drives with collector motors with independent excitation, a linear approximation of transient processes in the motors anchor windings should be added to the model [40].

$$I_\rho \frac{di_\rho}{dt} + R_\rho i_\rho + k_{1(\rho)} \dot{x}_{1(\rho)} = e_\rho;\ \rho = \overline{1, r}; \tag{38}$$

The meaning of the designations in Equation (38): I_ρ is the inductance of the armature winding, $R_\rho$is its ohmic resistance, $k_{1(\rho)}$ is the coefficient of back-EMF, and e_ρ is voltage on the armature winding, additional to the voltage $e_{\rho 0}$, that ensures the flow $i_{\rho 0}$ of current in the armature winding, creating a moment that realizes equilibrium (28). The most detailed presentation of the complete solution to the stabilization problems by moments created by DC electric drives with collector motors is given in [16–18,36].

7. Result

The abstract theoretical results on analytical mechanics of non-free systems obtained in the Soviet Union and Russia apparently remain unknown to specialists in technical practice. Despite the fact that the main works have been translated and the author has published numerous publications on their application, they remain unclaimed. This article once again describes in detail how effective the application of analytical mechanics methods of non-free systems is to modeling the behavior of manipulators with parallel kinematics.

The abstract theoretical results of the application of the non-free systems analytical mechanics to modeling the behavior of manipulators with parallel kinematics as systems with geometric constraints in the general case frees one from considering the inverse problem of kinematics.

Due to the exclusion of constraint multipliers and velocities of coordinates dependent on constraints from consideration, the dimensionality of the model, compared to traditional models in the form of equations with constraint multipliers (expressions of which in the coordinates and velocities functions form require additional definition), is reduced by the number of constraints. The developed transition to constraint multipliers-free equations in redundant coordinates allows, in contrast to all known results, in the general case to include the dynamics of actuators in consideration.

8. Discussion

Numerous articles on modeling the dynamics of systems with geometric constraints develop a method whose mandatory stage is the consideration of the inverse kinematics problem. It is obvious that it is impossible to obtain a general solution to the inverse kinematics problem in an analytical form. Therefore, all publications model the dynamics of only a specific device. Moreover, the inverse problem is solved using software environments for processing symbolic information.

Our approach is based on the transition to equations in redundant coordinates free of constraint multipliers. Such a procedure not only reduces the model dimensionality by excluding dependent velocities from consideration, but, most importantly, does not require solving the inverse kinematics problem in principle. Equations (14) and (15) generally represent the analytical form for a complete nonlinear dynamics model of an arbitrary system with geometric constraints (1).

The explicit analytical form of the model (cf. the simulation methods [41–46] created the possibility for a complete solution to the general problem of stabilizing a given configuration of a non-free system with constraints (1) by applying the mathematical control theory results with the involvement of the critical cases theory. The proposed method's effectiveness is demonstrated by a complete solution to the stabilization problem at the specified grip position of the Delta robot. Unfortunately, our highly effective, strictly substantiated approach is not only not used by technical practitioners, but is not reflected in any way even in such review articles as [41,46] with a list of references of many dozens of articles.

The analytical model form creates the possibility not only for the rigorous selection of the first approximation in the perturbed motion equations, but also for conducting an analysis of the nonlinear term structure from the point of the critical cases theory view. On this basis, in the general stabilizing problem, a given manipulator configuration, the control problem dimension is additionally reduced by the number of dependent coordinates. At the same time, it is strictly proven that the control that solves the problem of stabilization to asymptotic stability for the unperturbed configuration in the complete nonlinear system is a linear function of only independent velocities and perturbations of the corresponding coordinates.

In the presence of cyclic coordinates, it is possible to further simplify the study by switching to Routh variables. The reduction in the dimensionality of the problem for determining the stabilizing control is achieved by excluding uncontrolled impulses from consideration [24,25].

9. Conclusion

The developed simplification of the mathematical model makes it possible to include a description of the dynamics of the actuators. If we take an electric drive with collector motors with independent excitation, mechanical moments proportional to the currents in the anchor windings of the motors should be added to the model [16–18,36]. In this case, additional voltages on the anchor windings of the drive motors should be considered as stabilizing controls.

This approach has shown high efficiency in solving current stabilization problems for complex modern automatic devices with parallel kinematics. A full description of its application is presented in detail in several studies. The very first object with one geometric constraint was the stand Ball and Beam [16–18,32].

The solution algorithm developed there was then applied to the complete solution of the stabilization problem for the given position of the Delta robot gripper. This device was considered as a system with three geometric constraints [36] (without the need to consider the inverse problem of kinematics, cf. [5–9,37,38]). The rigor of the applied abstract-theoretical methods created not only the possibility of taking into account the dynamics of actuators in the nonlinear model, but also the possibility of obtaining a complete solution to the stabilization problem with the determination of the stabilizing control coefficients controlled by the method of Krasovskii [39].

Conflict of interest: The author declares no conflict of interest.

References

1. Kalman RE, Falb PL, Arbib MA. Topics in Mathematical System Theory. New York, McGraw-Hill; 1969.
2. Gabasov R, Kirillova F, Casti J. The qualitative theory of optimal processes. Available online: https://api.semanticscholar.org/CorpusID:120242129 (accessed on 2 January 2025).
3. Kuntsevich VM, Lychak MM. Synthesis of an automatic control system using Lyapunov functions (Russian). Moscow: Nauka; 1977.
4. Deabs A, Gomaa FR, Khader K. Parallel Robot. Journal of Engineering Science and Technology Review. 2021; 14(6): 10-27. doi: 10.25103/jestr.146.02
5. Brinker J, Corves B, Wahle M. Comparative study of inverse dynamics based on Clavel's Delta robot. In: Proceedings of the 14th IFToMM World Congress; 25-30 October 2015; Taipei, Taiwan.
6. Brinker J, Funk N, Ingenlath P, et al. Comparative Study of Serial-Parallel Delta Robots With Full Orientation Capabilities. IEEE Robotics and Automation Letters. 2017; 2(2): 920-926. doi: 10.1109/lra.2017.2654551
7. Brinker J, Corves B, Takeda Y. Kinematic and Dynamic Dimensional Synthesis of Extended Delta Parallel Robots. In: Robotics and Mechatronics. Springer International Publishing: Cham, Switzerland; 2019.
8. Kim TH, Kim Y, Kwak T, et al. Metaheuristic Identification for an Analytic Dynamic Model of a Delta Robot with Experimental Verification. Actuators. 2022; 11(12): 352. doi: 10.3390/act11120352
9. Makwana MA, Patolia HP. Model-based motion simulation of delta parallel robot. Journal of Physics: Conference Series. 2021; 2115(1): 012002. doi: 10.1088/1742-6596/2115/1/012002
10. Lurie AI. Analytical mechanics (Foundations of Engineering Mechanics). Springer- Verlag, Berlin; 2002.
11. Suslov GK. Teoreticheskaya mekhanika. In: Russian/Theoretical Mechanics. Moscow-Leningrad: OGIZ; 1946.
12. Shulgin MF. On some differential equations of analytical dynamics and their integration (Russian). In: Proceedings of the Lenin Central Asian state University 1958; 144.
13. Routh EJ. Dynamics of a System of Rigid Bodies. MacMillan, London; 1905.
14. Pars LA. A Treatise on Analytical Dynamics. Heinemann; 1965.
15. Lyapunov AM. Lectures on Theoretical Mechanics (Russian). Available online: https://www.studmed.ru/lyapunov-am-lekcii-po-teoreticheskoy-mehanike_75448b2cab8.html (accessed on 2 January 2025).
16. Krasinskaya E, Krasinskiy A. Modeling of the dynamics of GBB1005 Ball & Beam Educational Control System as a controlled mechanical system with a redundant coordinate. Science and Education of the Bauman MSTU. 2014; 14(01). doi: 10.7463/0114.0646446
17. Krasinskiy AYa, Ilyina AN, Krasinskaya EM. Modeling of the Ball and Beam system dynamics as a nonlinear mechatronic system with geometric constraint. Vestnik Udmurtskogo Universiteta Matematika Mekhanika Komp'yuternye Nauki. 2017; 27(3): 414-430. doi: 10.20537/vm170310
18. Krasinskiy AY, Krasinskaya EM. Complex Application of the Methods of Analytical Mechanics and Nonlinear Stability Theory in Stabilization Problems of Motions of Mechatronic Systems. In: Radionov A, Karandaev A. (editors). Advances in Automation. Springer, Cham; 2019.

19. Krasinskiy AY. On a General Method for Modeling the Controlled Dynamics of Manipulators with Parallel Kinematics as Systems with Geometrical Constraints. In: Proceedings of the 10th International Conference (MMSE 2024); 27–28 July 2024; Paris, France.
20. Lyapunov AM. General problem of motion stability (Russian). Available online: https://www.directmedia.ru/book-113347-obschaya-zadacha-ob-ustoichivosti-dvizheniya/?srsltid=AfmBOop9lIYbutiAZUkty2Y8Td4emYKaydEx8rSHKJPmlJ5wJ2oYTOBC (accessed on 2 January 2025).
21. Malkin IG. Theory of stability of motion. U.S. Atomic Energy Commission; 1952.
22. Kamenkov GV. Izbrannyye trudi. T.2. Selected works. V.2. 1972; M: Nauka (Russian). Available online: https://biblioclub.ru/index.php?page=book&id=468139 (accessed on 2 January 2025).
23. Aiserman MA, Gantmacher FR. Stability of the equilibrium position in a non-holonomic system (German). ZAMM - Journal of Applied Mathematics and Mechanics/Zeitschrift für Angewandte Mathematik und Mechanik. 1957; 37(1-2): 74-75. doi: 10.1002/zamm.19570370112
24. Krasinskiy AYa. On Stability and Stabilization with Permanently Acting Perturbations in Some Critical Cases. In: Tarasyev A, Maksimov V, Filippova T. (editors). Stability, Control and Differential Games. Springer; 2020.
25. Krasinskiy A, Ilyina A. Stabilization of steady motions of systems with geometric constraints and cyclic coordinates. In: Proceedings of the 2020 15th International Conference on Stability and Oscillations of Nonlinear Control Systems (Pyatnitskiy's Conference) (STAB); 2020.
26. Yu W. Nonlinear PD Regulation for Ball and Beam System. International Journal of Electrical Engineering & Education. 2009; 46(1): 59-73. doi: 10.7227/ijeee.46.1.5
27. Koo MS, Choi HL, Lim JT. Adaptive nonlinear control of a ball and beam system using centrifugal force term. International Journal of Innovative Computing, Information and Control. 2012; 8(9): 5999-6009.
28. Keshmiri M, Jahromi AF, Mohebbi A, et al. Modeling and Control of Ball and Beam System using Model Based and Non-Model Based Control Approaches. International Journal on Smart Sensing and Intelligent Systems. 2012; 5(1): 14-35. doi: 10.21307/ijssis-2017-468
29. Andreev F, Auckly D, Gosavi S, et al. Matching, linear systems, and the ball and beam. Automatica. 2002; 38(12): 2147-2152. doi: 10.1016/S0005-1098(02)00145-0
30. Ding M, Liu B, Wang L. Position control for ball and beam system based on active disturbance rejection control. Systems Science & Control Engineering. 2019; 7(1): 97-108. doi: 10.1080/21642583.2019.1575297
31. Ahmad NS. Modeling and Hybrid PSO-WOA-Based Intelligent PID and State-Feedback Control for Ball and Beam Systems. IEEE Access. 2023; 11: 137866-137880. doi: 10.1109/access.2023.3339879
32. Krasinskiy AYa, Ilyina AN. Nonlinear Mathematical Model of the Systems Dynamics with Geometric Constraints and its Simplification Due to the Justified Linearization of Constraints. In: Proceedings of the 2024 6th International Conference on Control Systems, Mathematical Modeling, Automation and Energy Efficiency (SUMMA); 2024.
33. Neimark JI, Fufaev NA. Dynamics of nonholonomic systems. Translations of Mathematical Monographs. 1970; 33.
34. Voronets PV. On the equations of motion for nonholonomic systems (Russian). Matematicheskiy sbornik. 1901; 22(4): 659-686.
35. Karapetyan AV, Rumyantsev VV. Stability of conservative and dissipative systems (Russian). General mechanics. 1983; 6.
36. Krasinskiy A, Yuldashev A. Nonlinear Model of Delta Robot Dynamics as a Manipulator with Geometric Constraints. In: Proceedings of the 2021 3rd International Conference on Control Systems, Mathematical Modeling, Automation and Energy Efficiency (SUMMA); 2021.
37. Sun M. Modeling and Regulation of a Delta Planar Robot. In: Proceedings of the 2022 4th International Conference on Electrical Engineering and Control Technologies (CEECT); 2022.
38. Zhang S, Liu X, Yan B, et al. Dynamics Modeling of a Delta Robot with Telescopic Rod for Torque Feedforward Control. Robotics. 2022; 11(2): 36. doi: 10.3390/robotics11020036
39. Krasovskii NN. Problems of stabilization of controlled motions. In: Malkin IG (editor). Theory of motion stability. Наука; 1966.
40. Zenkevich SL, Yushchenko AS. Fundamentals of Control of Manipulation Robots, 2nd ed. Moscow: Bauman Moscow State Technical University; 2004.

41. Müller A. A constraint embedding approach for dynamics modeling of parallel kinematic manipulators with hybrid limbs. Robotics and Autonomous Systems. 2022; 155: 104187. doi: 10.1016/j.robot.2022.104187
42. Müller A, Kumar S, Kordik T. A Recursive Lie-Group Formulation for the Second-Order Time Derivatives of the Inverse Dynamics of Parallel Kinematic Manipulators. IEEE Robotics and Automation Letters. 2023; 8(6): 3804-3811. doi: 10.1109/lra.2023.3267005
43. Gamper H, Rodrigo Pérez L, Mueller A, et al. An Inverse Kinematics Algorithm With Smooth Task Switching for Redundant Robots. IEEE Robotics and Automation Letters. 2024; 9(5): 4527-4534. doi: 10.1109/lra.2024.3379860
44. Gnad D, Gattringer H, Müller A, et al. Dedicated Dynamic Parameter Identification for Delta-Like Robots. IEEE Robotics and Automation Letters. 2024; 9(5): 4393-4400. doi: 10.1109/lra.2024.3380924
45. Muller A. AnO(n)-Algorithm for the Higher-Order Kinematics and Inverse Dynamics of Serial Manipulators Using Spatial Representation of Twists. IEEE Robotics and Automation Letters. 2021; 6(2): 397-404. doi: 10.1109/lra.2020.3044028
46. Müller A. Review of the exponential and Cayley map on SE(3) as relevant for Lie group integration of the generalized Poisson equation and flexible multibody systems. Proceedings of the Royal Society A: Mathematical, Physical and Engineering Sciences. 2021; 477(2253): 20210303. doi: 10.1098/rspa.2021.0303

Mechanical Engineering Advances 2025, 3(2), 2838.
https://doi.org/10.59400/mea2838

Article

Innovative semi-analytical approaches to micropolar MHD fluid flow between stretching disks under radiant heat flux

Ali Ahmadi Azar

Department of Mechanical Engineering, NT.C., Islamic Azad University, Tehran, Iran; aliahmadiazar.mech@gmail.com, a.ahmadi.azar@iau-tnb.ac.ir

CITATION

Ahmadi Azar A. Innovative semi-analytical approaches to micropolar MHD fluid flow between stretching disks under radiant heat flux. Mechanical Engineering Advances. 2025; 3(2): 2838. https://doi.org/10.59400/mea2838

ARTICLE INFO

Received: 24 February 2025
Accepted: 11 April 2025
Available online: 26 June 2025

COPYRIGHT

Copyright © 2025 by author(s). *Mechanical Engineering Advances* is published by Academic Publishing Pte. Ltd. This work is licensed under the Creative Commons Attribution (CC BY) license. https://creativecommons.org/licenses/by/4.0/

Abstract: This study investigates the viscous, incompressible, laminar, time-independent micropolar MHD fluid flow between two stretching disks under radiant heat flux, with applications in industrial systems like turbines and nuclear reactors. Using suitable similarity transformations, the nonlinear constitutive equations are reduced to coupled ODEs and solved through two novel semi-analytical approaches: the Hybrid Analytical-Numerical method (HAN method), which constructs analytical solutions from numerical data, and the modified Akbari-Ganji Method (modified AGM) that operates independently of numerical solutions. Results demonstrate that stretching Reynolds number, magnetic parameter, and three micropolar parameters significantly affect all five dimensionless quantities (axial/radial velocity, microrotation, temperature, and concentration), while Eckert number variations cause a 16.5% maximum temperature increase when doubled from 1 to 2. A 429% temperature surge occurs as the Prandtl number rises from 3 to 22, whereas the Schmidt number (0.1–1.5) only modifies the concentration profile shape without changing extrema. The radiation parameter (0–8) alters temperature distribution between disks without affecting maxima/minima. Three validation methods confirm solution accuracy: graphical verification, comparison with existing analytical results, and cross-method consistency between HAN and modified AGM outputs. The study's innovative dual-method approach coupled with 3D contour visualizations provides unprecedented semi-analytical solutions for this classical problem, offering both theoretical advancement and practical industrial insights.

Keywords: MHD flow; semi-analytical methods; stretchable disks; modified AGM; HAN-method

1. Introduction

Integrating heat and mass transfer with fluid flow analysis is essential in many engineering and scientific processes, prompting extensive research into stretching disk models. Magnetohydrodynamics (MHD) is a practical fluid model for understanding the flow of electrically conductive fluids in magnetic fields [1]. It is fundamental in physics, particularly in studying low-frequency, large-scale magnetic behavior in plasma and liquid metals, with applications in geophysics, astrophysics, and engineering. Non-Newtonian fluids, such as micropolar fluids that include two velocity variables not found in the Navier-Stokes equations, are also widely researched for their industrial applications [2]. While mathematical models can describe natural phenomena, their nonlinear equations lack exact analytical solutions, necessitating numerical and semi-analytical methods for approximate solutions. This study is significant mathematically as it introduces two new methods for the semi-analytical solution of nonlinear ODEs, demonstrating their application. Eringen's micropolar fluid theory, proposed and later refined in the 1960s, has been extensively studied [3–

6]. Turkyilmazoglu investigated the time-independent, incompressible, and viscous fluid flow due to the rotation of a permeable disk with uniform suction/injection capability [7–9]. Other researchers, including Sahoo, Srivastava, and Iqbal, have examined the fluid dynamics and heat transfer in non-Newtonian and MHD fluids in various configurations, often using similarity transformations to convert the constitutive equations into ordinary differential equations (ODEs) for numerical or analytical solutions [10–18]. This body of work highlights the complicated nature of fluid dynamics and the ongoing efforts to develop robust mathematical models for practical applications. Tabassum and Mustafa [19] explored the flow of non-Newtonian Reiner-Rivlin fluid caused by the rotation of an impermeable swirling disk. They simplified the governing PDEs and analyzed them numerically. Yao and Lian [20] studied the Von Kármán rotational flow problem arising from the rotation of an infinitely large disc, converting the constitutive equations into a set of ODEs using similarity transformations. Sahoo and Shevchuk [21] examined the flow and heat transfer in a rotating non-Newtonian Reiner-Rivlin fluid caused by a constantly stretching disk. Yao and Lian [22] also investigated Von Kármán rotational viscous flow due to disk rotation in a porous medium, solving the equations using the HAM method after converting them to ODEs and validating their results against similar studies. Zangooee et al. [23] focused on heat and mass transfer in nanofluid MHD flow due to the stretching and rotation of two disks, using AGM to solve the simplified equations. Das and Sarkar [24] analyzed non-Newtonian Reiner-Rivlin fluid flow between two swirling stretchable circular sheets and solved the equations analytically after converting them to ODEs. Naqvi et al. [25] investigated time-independent, incompressible nanofluid flow due to the rotation of an impermeable disk at a constant angular velocity. Usman et al. [26] studied heat transfer and fluid dynamics of a wavy surface plate with temperature variations, rotating in a uniform flow. Various similar analytical studies have been conducted [27–37]. Khan [38] examined a two-dimensional MHD problem through a porous channel, simplifying the governing PDEs with similarity variables and solving them analytically. Ahmad et al. [39] investigated polymer fluid effects on a stretchable disk in a magnetic field using the FENEP model. Khan et al. [40] studied non-Newtonian micropolar fluid flow, simplifying the equations with dimensionless variables and analyzing them numerically. Khan [41] examined linear viscoelastic fluid flow on a shrinking/stretching plane, simplifying the PDEs with dimensionless variables and analyzing them using HPM. Anusha et al. [42] analyzed heat and mass transfer in a time-independent, slow, viscoelastic 2D flow caused by a porous widening/shrinking slip, simplifying the PDEs and analyzing them analytically. Ghadikolaei et al. [43] studied 3D nanofluid flow through a swirling channel with thermal radiation, simplifying the PDEs and solving them numerically. Ghasemi et al. [44] examined non-Newtonian MHD third-grade blood flow in porous arteries, simplifying the equations and analyzing them using both analytical and numerical methods. Fakour et al. [45] investigated non-turbulent micropolar fluid flow in a 2D permeable channel, converting the equations into ODEs using similarity transformations and solving them analytically and numerically. Rashad et al. [46] studied the magnetohydrodynamic (MHD) flow and heat transfer of a Casson-Carreau hybrid nanofluid (Al_2O_3-Cu/water) in a Darcy-Forchheimer porous medium under thermal radiation, magnetic field, heat sink/source, and slip conditions. Using non-similar transformations, they converted the governing equations into a solvable form and obtained numerical solutions. Their results showed that thermal radiation and blowing/suction parameters enhanced heat transfer, while the skin friction coefficient responded similarly to radiation but oppositely to suction/injection effects. In another study, Rashad et al. [47] investigated the flow of a Jeffrey hybrid nanofluid over a moving porous surface under the influence of a magnetic field, heat sink/source, yield stress, and chemical reaction. Using similarity transformations, they converted the governing partial differential equations into nonlinear ordinary differential equations, which were then solved numerically using the RKF45 method with shooting technique. Their analysis focused on key physical parameters affecting heat flux, temperature distribution, flow velocity, and surface friction. The results demonstrated that increased permeability, yield stress, heat generation, and magnetic field strength enhanced temperature distribution while reducing heat transfer efficiency. Conversely, chemical reaction and heat source parameters improved mass transport. This study provides valuable insights for thermal engineering applications. Abdelhafez et al. [48] investigated the enhancement of convective heat transfer in industrial applications using magnetohydrodynamic Maxwell nanofluid flow through a porous medium over a convectively heated stretching cylinder. The study incorporated higher-order chemical reactions and employed the optimal homotopy analysis method to solve the governing ordinary differential equations. Through graphical analysis, the authors examined the effects of key parameters on velocity, temperature, and concentration profiles. Their results demonstrated that heat transfer rates improved with increasing Biot number and chemical reaction order, while higher values of reaction parameter, magnetic field strength, permeability, and Eckert number reduced heat transfer efficiency. Mass transfer increased with Joule heating, chemical reaction rate, and Biot number but decreased with stronger magnetic fields, greater permeability, and higher-order chemical reactions. The findings were validated against previous studies and provide valuable insights for applications involving fluid transport in cylindrical tanks, particularly in water, oil, and gas systems. Turkyilmazoglu [49] conducted a two-fold study to (1) compare the behavior of a stretching jet under quadratic air resistance with classical frictionless jet formation, and (2) validate similarity flows for stretching thin bodies under boundary layer approximations. The research extended electrohydrodynamic jet theory—typically applied to electrospinning and jet printing—by incorporating air resistance effects in both the cone and final regimes before substrate deposition. Analysis of the nonlinear governing equations revealed that near the nozzle, viscous and electrical forces rapidly thin the jet, with air resistance enhancing this effect and improving alignment with experimental observations. The jet exhibited exponential thinning, accelerated by inversely quadratic liquid particle speeds, confirming similarity flow over exponentially stretching sheets. In the final regime, frictionless jets decayed algebraically, while air resistance caused exponential decay to a limiting speed—yielding square-root-dependent similarity flow for free jets and Sakiadis-type flow for resisted cases. The study uniquely integrated electrostatic forces (Coulombic effects) with quadratic drag, supported by experimental glycerol jet data. Numerical simulations further validated the asymptotic jet behavior under combined electrostatic pull and electric currents from bulk/surface charge transport, offering insights beyond conventional jet hydrodynamics. In another study, Turkyilmazoglu [50] investigated unsteady heat and fluid flow phenomena over stretching/shrinking surfaces through rigorous mathematical modeling. The study developed two distinct approaches: (1) a conventional model yielding trivial steady-state solutions, and (2) a novel formulation that successfully captured physically meaningful steady-state solutions documented in existing literature. Key contributions include deriving new similarity solutions for temperature fields in the conventional model and establishing that uniform wall temperature conditions optimize heat transfer rates. While the proposed model permits similarity solutions for specific cases, they noted that general conditions may require non-similar solution approaches. The analysis provides valuable insights for stagnation-point flows and non-Newtonian viscoelastic fluids, while identifying important directions for future research in this domain. Enamul and Ontela [51] investigated heat transfer and entropy generation in a hybrid nanofluid flow between rotating porous disks, focusing on applications like cooling systems and energy storage. They analyzed a $TiO_2/CoFe_2O_4$-engine oil nanofluid, incorporating Hall currents, viscous dissipation, and convective effects. Using similarity transformations and homotopy analysis, they solved the governing equations and found that temperature profiles improved with higher Brinkman numbers and Biot numbers, while skin friction decreased with increased TiO_2 concentration, porosity, and magnetic fields. Their results demonstrated enhanced heat transfer rates with larger nanoparticle shape factors and magnetic parameters, providing valuable insights for optimizing thermal management in MHD systems and nanofluid-cooled devices. Hussain et al. [52] developed a novel numerical model to analyze heat, mass, and microorganism transfer in nanofluid flow over a rotating stretched disk. They combined bioconvection of motile microorganisms with thermal transport equations to enhance system efficiency in cooling applications. The researchers incorporated internal heat generation and nanoparticle diffusion effects into modified momentum equations and solved them using shooting method with Runge-Kutta technique. Their analysis revealed that increasing unsteadiness (S) accelerated thermal energy dissipation, while bioconvection significantly altered velocity and temperature profiles by thinning microorganism layers. The study demonstrated how these mechanisms could optimize thermal management in aerospace systems experiencing extreme frictional heating. Key achievements included establishing the first bioconvection-nanofluid model for rotating disks and quantifying microorganism-enhanced heat transfer efficiency for practical engineering applications. Lone et al. [53] investigated MHD Casson hybrid nanofluid flow between two rotating stretchable circular plates with variable porous spacing, employing the Cattaneo-Christov heat flux model to analyze thermal performance. They computationally solved the governing equations using the bvp4c method, examining magnetic field, thermal radiation, and non-uniform heat source/sink effects. Their results showed that axial velocity decreased near the lower disk ($0 \leq \xi < 0.4$) but increased near the upper disk ($0.4 < \xi \leq 1.0$) with higher magnetic factors, while radial velocity exhibited interval-specific variations. They demonstrated that increased porous spacing enhanced axial/tangential velocities and that thermal distribution improved with radial/magnetic factors and Biot number but declined with thermal relaxation time. The study provided validated insights for optimizing heat transfer in rotating plate systems through comparative analysis. Mandal et al. [54] examined entropy generation in MHD hybrid nanofluid (Ag-MgO) flow over a permeable rotating disk with variable fluid properties, incorporating time-dependent stretching, velocity/temperature slip effects, and nonlinear thermal radiation. They transformed the governing equations using similarity variables and solved them numerically via shooting technique with 4th-order Runge-Kutta-Fehlberg method. The team discovered that disk rotation accelerated fluid motion while magnetic fields, thermal radiation, and temperature-dependent viscosity significantly influenced heat transfer rates, skin friction, and entropy production (quantified by Bejan number). Their analysis revealed optimal parameter combinations for minimizing entropy generation and enhancing system efficiency. Key achievements included: (1) developing a comprehensive model for entropy-optimized nanofluid flows, (2) quantifying rotational and magnetic effects on thermal performance, and (3) providing design insights for energy-efficient thermal systems in sustainable engineering applications. Naveed Khan et al. [55] studied the boundary layer flow of a hybrid Ag-MgO/water nanofluid containing gyrotactic microorganisms over a rotating porous disk, incorporating double diffusion theory, Joule heating, and chemical reactions. They modeled multiple slip boundary conditions and transformed the governing equations into nonlinear ODEs using similarity transformations, which were solved numerically via the BVP4C MATLAB solver. Their results demonstrated that increasing nanoparticle volume fraction enhanced both velocity and temperature fields, while higher porosity parameters and inertia coefficients reduced velocity distribution. The team validated their findings through comparative analysis with previous studies. Key achievements included: (1) developing a comprehensive bio-nanofluid model with slip effects, (2) quantifying how nanoparticle concentration and porous media interactively affect flow dynamics, and (3) providing optimized parameters for microbial-enhanced thermal systems in rotating machinery applications. Rauf et al. [56] investigated the steady-state flow of a viscous fluid over a variable-thickness rotating disk with stretching effects, incorporating a horizontal magnetic field to regulate flow dynamics and thermal energy in high-temperature applications. They analyzed thermal radiation and melting heat transfer, employing similarity transformations to convert governing equations into dimensionless form, which were solved numerically using the RKF-45 method. Their results demonstrated that melting reduced fluid resistance near the surface, increasing flow velocity while decreasing temperature gradients due to latent heat absorption. The study revealed that the horizontal magnetic field stabilized radial flow at angles (α_1) between 0-30°, and the dimensionless radius enhanced thermal transport from the disk surface. Key achievements included: (1) developing a magnetohydrodynamic model for variable-thickness rotating surfaces, (2) quantifying how melting and magnetic fields synergistically affect flow/thermal profiles, and (3) providing design insights for thermal management in turbines and phase-change material systems. Senbagaraja and De [57] analyzed the three-dimensional electro-osmotic flow of EMHD tangent hyperbolic nanofluid over a stretching rotating porous disk, incorporating thermal radiation, variable thermal conductivity, chemical reactions, and Stefan blowing effects. They transformed the governing partial differential equations into ordinary differential equations using similarity variables and solved them numerically via fifth-order Runge-Kutta-Fehlberg with shooting method. Through response surface methodology, they identified an optimal heat transfer rate of 6.46 for high magnetic/thermal radiation parameters with low electric field, while sensitivity analysis showed thermal radiation had 91.44% relative sensitivity at medium levels. Their study uniquely addressed previously unexplored assumptions with advanced boundary conditions. Key achievements included: (1) developing the first comprehensive EMHD nanofluid model with Stefan blowing, (2) optimizing heat transfer parameters through statistical analysis, and (3) demonstrating applications in biomedical, industrial, and microfluidic systems like drug delivery and electronics cooling. Sultana et al. [58] investigated the magnetohydrodynamic (MHD) forced convective flow of copper-, alumina-, and titania-based nanofluids induced by eccentric rotations of an unsteady stretching porous disk and surrounding fluid. They considered incompressible, viscous, electrically conductive fluid with Joule heating and viscous dissipation effects. The team obtained exact solutions for velocity fields and numerical solutions for temperature profiles using the Crank-Nicolson method. Their analysis revealed that increasing nanoparticle volume fraction reduced velocity while thickening the boundary layer, and higher unsteady parameters enhanced velocity but weakened temperature profiles. Key achievements included: (1) developing exact/numerical solutions for eccentric rotating nanofluid systems, (2) quantifying how porosity (S), magnetic (M^2), and unsteady parameters (C) govern flow-thermal behavior, and (3) demonstrating suction's cooling effect for thermal management in rotating machinery applications. Turkyilmazoglu and Pop [59] examined the flow and heat transfer characteristics of a Bingham viscoplastic fluid subjected to combined axial rotation and radial stretching of a circular disk. They extended existing Bingham fluid models using von Kármán similarity transformations, solving the resulting nonlinear ODE system to analyze momentum and thermal fields. The study identified three key dimensionless parameters (swirling number, Bingham number, modified Reynolds number) governing the flow, revealing that radial stretching required significantly higher yield stresses than rotation alone to exhibit non-Newtonian effects. At high Bingham numbers, they observed a two-layer structure with an unyielded plug region and yielded shear layer near the wall. Key achievements included: (1) developing the first comprehensive model for Bingham fluids under combined stretching-rotation, (2) quantifying how wall movement enhances non-Newtonian behavior, and (3) characterizing the von Kármán pump mechanism in viscoplastic flows with practical implications for industrial processing systems. Usman et al. [60] investigated the flow and heat transfer characteristics of a ternary hybrid nanofluid (THNF) containing Cu, Al_2O_3, and MWCNTs over a rotating stretching disk under magnetic field effects. They transformed the governing equations into nonlinear ODEs and solved them numerically using MAPLE 2022, analyzing dimensionless velocity, temperature, concentration profiles, and performance metrics. Their results demonstrated that THNFs outperformed single and binary nanofluids, achieving a 10–15% enhancement in Nusselt number and an 8–12% reduction in skin friction under moderate magnetic fields. The study revealed that transitioning from pseudoplastic to dilatant behavior decreased tangential/radial velocities and surface temperature. Key achievements included: (1) developing the first THNF model for rotating stretching disks, (2) quantifying synergistic nanoparticle effects on thermal performance, and (3) proving THNF superiority for applications like electronics cooling and lubrication systems. Zada et al. [61] explored entropy generation and heat transfer in an unsteady flow of variable magnetic hybrid nanofluid (SWCNT/MWCNT in water-ethylene glycol) between parallel rotating disks. They developed innovative hybrid nanofluid models and employed the Buongiorno two-phase approach to analyze Brownian motion and thermophoresis effects. The team solved the governing equations using both Homotopy Analysis Method (HAM) and bvp4c numerical techniques, achieving novel results never before compared with other methods. Their analysis revealed how disk rotation and nanoparticle characteristics influenced temperature/concentration distributions in the heat transfer system. Key achievements included: (1) creating the first comprehensive model for magnetic hybrid nanofluids in rotating disk systems, (2) quantifying entropy generation mechanisms in SWCNT/MWCNT suspensions, and (3) establishing benchmark data for thermal optimization in glycol-based nanofluid applications. Ahmadi Azar [62] conducted a rigorous investigation of Von Kármán's viscous swirling flow problem generated by a rotating disk, employing an innovative Hybrid Analytical and Numerical method (HAN method) methodology. The research addressed this classical nonlinear problem through a novel semi-analytical approach that synergistically combines numerical computation with analytical formulation. The HAN method demonstrated exceptional capability in solving complex nonlinear differential equations by utilizing numerical solutions to determine unknown coefficients in analytical polynomial expressions, thereby overcoming the limitations of traditional boundary condition constraints. The study achieved breakthrough precision in quantifying critical hydrodynamic parameters, including boundary layer characteristics, wall shear stress distributions, torque requirements, and mechanical power consumption. Key scientific contributions encompass: (1) development of a robust computational-analytical framework for nonlinear fluid dynamics problems, (2) establishment of new benchmark solutions for rotating disk flows with unprecedented accuracy, and (3) demonstration of advanced mathematical techniques to extract novel physical insights from fundamental fluid mechanics systems. This work significantly advances both theoretical and applied aspects of rotating flow analysis while providing a transformative methodology for complex nonlinear problems in continuum mechanics.

Due to the inherent complexity of natural phenomena, which frequently lack exact analytical solutions because of nonlinearities, numerical and semi-analytical approaches play a pivotal role. The Hybrid Analytical and Numerical Method (HAN method), bridges analytical and numerical techniques by deriving analytical expressions from numerical solutions, offering greater flexibility than traditional semi-analytical methods. This approach was first applied to model heat and mass transfer in a viscous, incompressible, laminar axisymmetric flow of a micropolar fluid subjected to a magnetic field between two stretchable disks. To further validate the HAN method's reliability, the article cites subsequent studies [63–66] where it has been successfully utilized to solve analogous governing equations. In a recent application [63], the HAN method was employed as a semi-analytical tool to examine the steady forced motion of a non-Newtonian MHD Reiner-Rivlin viscoelastic fluid confined between two plates under a magnetic field. The governing partial differential equations (PDEs) were converted into ordinary differential equations (ODEs) via Von

Kármán similarity transformations, which the HAN method then solved analytically alongside their boundary conditions. The results were cross-verified against solutions from the Homotopy Perturbation Method (HPM) and the numerical Runge-Kutta approach, with additional quantitative insights derived from the HAN solutions. Another investigation [64] explored the steady, laminar, incompressible, two-dimensional flow of a micropolar fluid between two disks—one porous and the other non-porous—neglecting body forces and couples. Using Von-Kármán similarity variables, the governing PDEs were reduced to ODEs, which were then solved semi-analytically via the Modified Akbari-Ganji Method (Modified AGM) and the HAN method, marking a novel application of these techniques. The study analyzed the influence of slip coefficients, Reynolds numbers, and micropolar parameters (e.g., vortex viscosity, spin gradient viscosity, and microinertia density) on velocity and microrotation profiles. The solutions were validated against existing literature, with both methods yielding nearly identical results, reinforcing their accuracy. Further research [65] applied the HAN method to nonlinear coupled ODEs to assess how structural variations—such as stretching rate and disk spacing—affected key physical parameters. Findings indicated that higher stretching rates increased temperature and Nusselt number, while greater disk separation reduced microrotation and wall couple stress. By redefining parameters like the magnetic field strength, Eckert number, stretching Reynolds number, and micropolar coefficients, the study quantified their impact, with results corroborated by prior research. In another study [66], the HAN method provided exact solutions for Von Kármán swirling flow induced by a rotating disk with uniform suction. Three scenarios were examined: opposing and aligned swirling flow at infinity, suction without swirling, and combined swirling and suction. Key observations included a peak skin friction coefficient when the fluid's angular velocity at infinity decreased relative to the disk's rotation, while increased fluid rotation reduced it. Higher suction enhanced the skin friction coefficient, particularly on porous disks, and in the absence of both swirling and suction, pressure distribution depended solely on axial distance. These results underscored the HAN method's efficacy in resolving intricate fluid dynamics problems. Beyond swirling flow analyses [67–72], the HAN method's applicability extends to a broader range of fluid mechanics challenges, demonstrating its versatility and robustness. The modified Akbari-Ganji method (AGM) is also valuable for solving nonlinear differential equations. Using these two methods, it is possible to obtain analytical solutions for nonlinear problems where exact solutions are challenging. Approximate analytical solutions of nonlinear differential equations can be effective. Numerous studies [73–78] have employed various methods to solve differential equations, examine parameter effects on dimensionless variables, and present results through graphs and 3D contours.

This article investigates heat and mass transfer in a viscous, incompressible, axially symmetric, and time-independent micropolar fluid confined between two stretchable disks, assuming a negligible magnetic Reynolds number and no polarization voltage. By employing similarity transformations, the governing partial differential equations (PDEs) are converted into a set of nonlinear ordinary differential equations (ODEs). Two innovative semi-analytical methods, the Hybrid Analytical and Numerical (HAN) method and the modified Akbari-Ganji method (modified

AGM), are utilized to solve these equations. The HAN method is a flexible approach that integrates numerical solutions to construct analytical methods, making it highly adaptable as it is not limited to specific numerical techniques, while the modified AGM operates independently of numerical solutions, proving useful when numerical solutions are unavailable or when validating the HAN method. Both methods, first introduced by A. Ahmadi Azar, have demonstrated significant success in addressing nonlinear differential equations, adding innovation and novelty to this study. Moreover, similarity solutions, where PDEs are transformed into ODEs using similarity variables such as von Karman transformations, simplify the complexity of three-dimensional and time-independent fluid flow and heat transfer equations, making them easier to solve. The study addresses key questions that motivated this research, such as (1) how to achieve analytical solutions using numerical solutions without semi-analytical methods (answered by the HAN method explained in Sections 3.1 and 3.2); (2) how to construct analytical solutions independent of numerical solutions (addressed by the modified AGM discussed in Sections 3.3 and 3.4); (3) how to simplify complicated three-dimensional equations governing fluid flow and heat transfer (accomplished using von Karman similarity variables detailed in Section 2); and (4) whether the methods are applicable to specific parameter ranges or limited to particular cases (confirmed through diagrams shown in Section 3.5 and elaborated on in Section 4). These aspects, combined with the study's exploration of key parameters such as radiation, magnetic field, Eckert number, Reynolds number, Schmidt number, and Prandtl number on micro-rotation profiles, velocity, concentration, and temperature profiles, highlight the significance of this research and its differentiation from other similarity solution studies.

2. Governing equations

This article investigates the nonlinear problem of heat and mass transfer of a viscous, time-independent, non-compressible, and axisymmetric micropolar fluid flow among stretchy disks. As demonstrated in **Figure 1**, the disks are placed in $z = l$ and $z = -l$ (l is a positive real number: $l \in \mathbb{R}^+ = [0, +\infty)$) in a circular cylindrical coordinate system (r, θ, z), where $0 \leq r < \infty$, $0 \leq r \leq 2\pi$, $-\infty \leq z < +\infty$. The model examines an electrically conductive micropolar fluid, with a crosswise magnetic field applied at a right angle to the boundaries. The governing equations (GEs) in this work are represented using the cylindrical coordinate system. The magnetic Reynolds number was considered to be insignificant, according to McChesney [79]. Consequently, it was demonstrated that the difference between the imposed and induced magnetic fields is negligible. Furthermore, the fact that no polarization voltage is applied should be taken into account. The following vectorial forms of the continuity, momentum, and microrotation are as follows [4]:

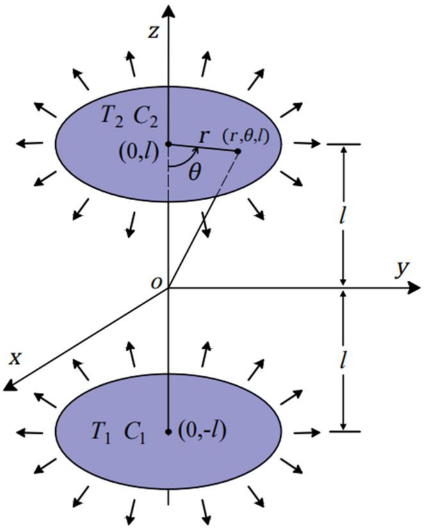

Figure 1. Geometry of the problem.

Continuity equation:

$$\boldsymbol{\nabla}(\mathbf{V}) = \mathbf{0}\,. \tag{1}$$

Momentum equation:

$$(\mu + \kappa)\nabla^2\mathbf{V} + \kappa\boldsymbol{\nabla} \times \mathbf{N} - \boldsymbol{\nabla} p + \mathbf{J} \times \mathbf{B} = \rho\dot{\mathbf{V}}\,. \tag{2}$$

Microrotation equation:

$$(\alpha_1 + \alpha_2 + \alpha_3)\boldsymbol{\nabla}(\boldsymbol{\nabla}\mathbf{N}) - \alpha_3(\boldsymbol{\nabla} \times \boldsymbol{\nabla} \times \mathbf{N}) + \kappa\boldsymbol{\nabla} \times \mathbf{V} - 2\kappa\mathbf{N} = \rho j\dot{\mathbf{N}}\,. \tag{3}$$

The fluid velocity vector is denoted by $\mathbf{V}$, the fluid dynamic viscosity is denoted by μ, the fluid microrotation is denoted by $\mathbf{N}$, the fluid vortex viscosity is denoted by κ, the fluid pressure distribution is denoted by p, the fluid density is denoted by ρ, the density vector of the fluid is denoted by $\mathbf{J}$, the micro inertia per unit mass is denoted by j, the sum of induced and imposed magnetic field is denoted by $\mathbf{B}$, and the gyro-viscosity coefficients are denoted by α_1, α_2, and α_3, respectively. In Equations (1)–(3), $\boldsymbol{\nabla}$ is the gradient operator, $\boldsymbol{\nabla} \times$ is the curl operator and $\dot{} = \mathrm{d}/\mathrm{d}t$ is the operator of the total derivative with respect to the time t.

According to the studies of Agarwal [1] and Jalili et al. [2], the equations of density, energy, and concentration are represented in vector form and for a general state as follows:

Density equation:

$$\mathbf{J} = \sigma_{el}(\mathbf{V} \times \mathbf{B})\,. \tag{4}$$

Energy equation:

$$\rho c_{\mathrm{p}}\frac{\mathrm{D}T}{\mathrm{D}t} = k\nabla^2 T + q_{\mathrm{rh}} + \mu\Phi\,. \tag{5}$$

Concentration equation:

$$\frac{\mathrm{D}C}{\mathrm{D}t} = D_{\mathrm{e}}\nabla^2(C) + \dot{m}'''\,. \tag{6}$$

The electrical conductivity of the fluid is denoted by σ_{el}, the viscous dissipation function is denoted by Φ, the fluid temperature distribution is denoted by T, the fluid specific heat capacity at constant pressure is denoted by c_{p}, the fluid thermal conductivity is denoted by k, the radiant heat flux is denoted by q_{rh}, the concentration of the fluid is denoted by C, the diffusion coefficient of the fluid is denoted by D_{e}, the operator of the total derivative with respect to the time is denoted by $\mathrm{D}/\mathrm{D}t := \mathrm{d}/\mathrm{d}t$ and $\dot{m}'''$ is related to reactive flows. In addition, Agarwal [1] and Jalili et al. [2] considered the relationship between α_1, α_2, α_3, μ, and κ parameters in Equation (7) as follows:

$$2\mu + \kappa \geq 0, \quad \kappa \geq 0, \quad 3\alpha_1 + \alpha_2 + \alpha_3 \geq 0, \quad \alpha_3 \geq |\alpha_2|\,. \tag{7}$$

According to Agarwal [1] and Jalili et al. [2], the velocity and microrotation vector fields in the component's forms are assumed in Equation (8) as follows:

$$\mathbf{V} = u\hat{\mathbf{e}}_1 + w\hat{\mathbf{e}}_3, \quad \mathbf{N} = N_2\hat{\mathbf{e}}_2\,, \tag{8}$$

where the components u, w and N_2 are functions of the variables r, z of the circular cylindrical coordinate system (r, θ, z) and $\hat{\mathbf{e}}_1$, $\hat{\mathbf{e}}_2$, $\hat{\mathbf{e}}_3$ are respectively the unit vectors along the r, θ, z axes.

According to Devi and Devi [80], the radioactive heat flux q_{rh} is show in Equation (5) like this:

$$q_{\mathrm{rh}} = -\frac{4\sigma}{3k_a}\frac{\partial(T^4)}{\partial z}\,, \tag{9}$$

where the constant of Stefan-Boltzmann is denoted by σ, and also the average absorption coefficient is denoted by k_a. The following are the boundary conditions associated with the physical principles underlying the problem as described in Equations (1)–(6) [1,2]:

$$\begin{cases} u = rS, \;\; w = 0, \;\; N_2 = 0, \;\; T = T_1, \;\; C = C_1, \;\; \text{when}\, z = -l, \\ u = rS, \;\; w = 0, \;\; N_2 = 0, \;\; T = T_2, \;\; C = C_2, \;\; \text{when}\, z = l\,. \end{cases} \tag{10}$$

The parameter related to the stretching of the two disks is denoted by S, the temperature of the lower disk is shown by T_1 and the temperature of the top disk is denoted by T_2. The concentration of the lower disk is denoted via C_1 and the top disk is denoted by the C_2. The Equations (1)–(6) will be reduced into a simpler form by the following dimensionless variable [1,2]:

$$\begin{gathered} u = -\frac{rS}{2}f'(\xi), \quad w = Slf(\xi), \quad N_2 = -\frac{rS}{2l^2}g(\xi), \\ \theta(\xi) = \frac{T - T_2}{T_1 - T_2}, \quad \phi(\xi) = \frac{C - C_2}{C_1 - C_2}, \quad \xi = \frac{z}{l}. \end{gathered} \tag{11}$$

where $\theta(\xi)$ is the dimensionless temperature of the fluid, $\phi(\xi)$ is the dimensionless concentration of the fluid, $f(\xi)$ is the dimensionless axial velocity of the fluid, $f'(\xi)$ is the dimensionless radial velocity of the fluid, $g(\xi)$ is the dimensionless microrotation distribution of the fluid. By applying the dimensionless variables given in Equation (11), the partial differential equations listed in Equations (1)–(6) can be transformed into the following system of nonlinear ordinary differential equations [1,2]:

$$F \coloneqq (1+\lambda_1)f^{(4)} - \lambda_1 g'' - R_0 f f''' - R_0 M_n^2 f'' = 0\,, \tag{12}$$

$$G \coloneqq \lambda_3 g'' + \lambda_1(f'' - 2g) + R_0\lambda_2\left(\frac{1}{2}f'\mathrm{g} - f g'\right) = 0\,, \tag{13}$$

$$\Theta \coloneqq \left(1 + \frac{4}{3}N_r\right)\theta'' + \frac{1}{4}P_r E_c (f'')^2 - R_0 P_r f\theta' = 0\,, \tag{14}$$

$$\Phi \coloneqq \phi'' + R_0 S_c f \phi' = 0\,. \tag{15}$$

The dimensionless stretching Reynolds number is denoted by $R_0 = \rho S l^2/\mu$, the dimensionless parameter of magnetic field is denoted by $M_\mathrm{n} \coloneqq (\sigma_\mathrm{el} B_\mathrm{os}^2/\rho S)^{1/2}$, the dimensionless parameter of vortex viscosity is denoted by $\lambda_1 = \kappa/\mu$, the dimensionless parameter of micro-inertial density is denoted by $\lambda_2 = j/l^2$, the dimensionless parameter of spin gradient viscosity is denoted by $\lambda_3 = \alpha_3/\mu l^2$, the dimensionless Prandtl number is denoted by $P_\mathrm{r} = \mu c_\mathrm{p}/k$, the dimensionless parameter of radiation is denoted by $N_\mathrm{r} = 4\sigma T_2^3/k_\mathrm{a} k$, the dimensionless Eckert number is denoted by $E_\mathrm{c} = r^2 S^2/(T_1 - T_2)c_\mathrm{p}$, the dimensionless Schmidt number is denoted by $Sc = \nu/D_\mathrm{e}$, and the strength of the magnetic field is denoted by B_os.

The dimensionless variables presented in Equation (11) also modify the boundary conditions described in Equation (10), transforming them into the simpler form shown below [1,2]:

$$\begin{cases} f(-1) = 0, \;\; f'(-1) = -2, \;\; g(-1) = 0, \;\; \theta(-1) = 1, \;\; \phi(-1) = 1, \\ f(1) = 0, \;\; f'(1) = -2, \;\; g(1) = 0, \;\; \theta(1) = 0, \;\; \phi(1) = 0\,. \end{cases} \tag{16}$$

In conclusion, once Equations (12)–(15) are resolved together with the boundary conditions given in Equation (16), the Nusselt number which is denoted by N_u, the skin friction coefficient which is denoted by C_f, and wall couple stress which is denoted by C_g can be determined for both the top and bottom disks in the following manner [1,2]:

$$C_\mathrm{f} = -\frac{(1+\lambda_1)f''(\pm 1)}{2R_\mathrm{e}}, \quad C_\mathrm{g} = \frac{\lambda_3}{2R_\mathrm{e}}\mathrm{g}'(\pm 1), \;\; N_\mathrm{u} = -\theta'(\pm 1)\,. \tag{17}$$

In Equation (17), the local Reynolds number is denoted by $R_\mathrm{e} = \rho S l r/\mu$, the stretching parameter of the disks is denoted by S, the distance from the r-axis is denoted by l, the dynamic viscosity of the fluid is denoted by μ, and r is an arbitrary value for the radius of the disk.

3. Methodology

3.1. Description of the HAN method

The Hybrid Analytical and Numerical method (HAN method), first introduced by A. Ahmadi Azar, is an innovative semi-analytical technique specifically designed to address complicated systems of nonlinear differential equations. This method uniquely combines numerical and analytical approaches, making it highly versatile and flexible. The process begins with obtaining a precise numerical solution, which serves as the foundation for constructing an analytical framework. Unlike traditional methods, the HAN method is not limited to specific numerical techniques; it requires only an accurate numerical solution, allowing for broader applicability across diverse problems. This adaptability is one of its greatest strengths, as it enables the effective handling of highly nonlinear equations. By integrating numerical data into the development of an analytical solution, the HAN method bridges the gap between purely numerical and purely analytical approaches, offering a powerful tool for solving challenging mathematical problems in engineering, physics, and other applied sciences. Since its introduction, the HAN method has been successfully employed in numerous studies, demonstrating its capability to solve a wide range of nonlinear ordinary differential equations and solidifying its value in advancing research across various fields. Another strength of this method is that a power series with a much smaller number of terms than other semi-analytical solutions can be considered as an approximate analytical solution for the given nonlinear differential equation. To describe the HAN method, let us consider a non-linear differential equation of order m $(= 2, 3, ...)$ as follows:

$$\Gamma\left(u(\xi), u'(\xi), u''(\xi), \ldots, u^{(m)}(\xi)\right) = 0, \tag{18}$$

where $0 \leq \xi \leq b$ is an independent real variable, $u(\xi)$ a real-valued continuous function of the variable ξ, Γ a known function of the variables ξ, $u(\xi)$, and its derivatives of $u(\xi)$ with respect to ξ, i.e., $u^{(i)}(\xi) = \mathrm{d}^i u/\mathrm{d}\xi^i$ $(i = 1, \cdots, m)$ and $b \in \mathbb{R}^+ = (0, +\infty)$ a given positive real number. Suppose that $2m$ boundary conditions (BCs) of the Equation (18) at the boundary points $\{\xi = 0, \xi = b\}$ on the interval $[0, b]$ are as follows:

$$\begin{cases} u(\xi) = \Phi_{00}, \quad u'(\xi) = \Phi_{10}, \quad \ldots, \quad u^{(m-1)}(\xi) = \Phi_{(m-1)0}, \quad \text{when } \xi = 0\,, \\ u(\xi) = \Phi_{0b}, \quad u'(\xi) = \Phi_{1b}, \quad \ldots, \quad u^{(m-1)}(\xi) = \Phi_{(m-1)b}, \quad \text{when } \xi = b\,. \end{cases} \tag{19}$$

where $\Phi_{00}, \cdots, \Phi_{(m-1)0}, \Phi_{0b}, \cdots, \Phi_{(m-1)b}$ are known real numbers: $\Phi_{ij} \in \mathbb{R} = (-\infty, +\infty), i = 0,1,\cdots, m-1; j = 0, b$. In fact, the Equation (18) with $2m$ boundary conditions in Equation (19) is a boundary value problem (BVP). The existence and uniqueness of the solutions to this problem is an important theorem in the theory of differential equations. This theorem, known as "Picard's existence theorem is due to C-É. Picard (1856–1941). Let us suppose that the BVP, Equation (18), with its BCs in Equation (19), has a solution, and this is unique. This section aims to see how to solve analytically the m-order nonlinear Equation (18) with its BCs in Equation (19) by the HAN method. For this purpose, let's consider an approximate solution for the Equation (18) as a polynomial of degree n $(= 0, 1, \cdots)$ in terms of the variable ξ:

$$u(\xi) = P_n(\xi) := \sum_{i=0}^{n} a_i \xi^i\,, \tag{20}$$

where $n + 1$ coefficients $a_0, a_1, \ldots, a_n$ in the polynomial solution in Equation (20) are unknown real numbers: $a_i \in \mathbb{R} = (-\infty, +\infty), i = 0, 1, \cdots, n$. To find these unknowns, one needs $n + 1$ algebraic equations, such that these equations form a system of $n + 1$ equations for $n + 1$ unknowns. By solving this set of algebraic equations simultaneously, one can find the unknowns a_0, a_1, $\cdots$, a_n. Now, by substituting the power series of Equation (20) into the BCs of Equation (19) at the boundary points $\{\xi = 0, \xi = b\}$, yield the following algebraic equations for the unknowns a_0, a_1, $\cdots$, a_n:

$$\begin{aligned}
&u(0) = a_0 := \Phi_{00},\\
&u'(0) = a_1 := \Phi_{10},\\
&\quad\vdots\\
&u^{(m-1)}(0) = a_{m-1} := \Phi_{(m-1)0},\\
&u(b) = \sum_{i=0}^{n} a_i b^i := \Phi_{0b},\\
&u'(b) = \sum_{i=1}^{n} i a_i b^{i-1} := \Phi_{1b},\\
&\quad\vdots\\
&u^{(m-1)}(b) = \sum_{i=m-1}^{n} i(i-1)(i-2)\cdots\big(i-(m-2)\big)a_i b^{i-(m-1)} := \Phi_{(m-1)b}\,,
\end{aligned} \tag{21}$$

where

$$\Phi_{ij} := u^{(i)}(j) = \frac{\partial u^i}{\partial \xi^i}(\xi = j), \quad i = 0,1,\cdots,m-1; j = 0, b\,, \tag{22}$$

are $2m$ real numbers: $\Phi_{ij} \in \mathbb{R} = (-\infty, +\infty)$.

By using a numerical solution method (it is not limited to a specific method and can be any numerical method) for the Equation (18), it is possible to find $2m$ real numbers of Φ_{ij}s that appeared in the system of algebraic equations in Equation (21). By determining these numbers, Equation (21) will be a system of algebraic equations for the unknowns a_0, a_1, ..., a_n. in this way, $2m$ number of $2n+1$ algebraic equations needed to find the coefficients a_0, a_1, ..., a_n are provided. If we choose the number of terms in polynomial $P_n(\xi)$ sufficiently large, then this polynomial will be the solution of Equation (18) with high accuracy. So, for the polynomial solution of Equation (20) to be the solution of Equation (18) with high accuracy, we choose n as a large natural number. Then, $n+1$ is a large number, and consequently $n+1 > 2m$. This inequality shows that the number of the constructed algebraic equations from the BCs, $2m$, is less than the number of unknowns. Then, one needs $n+1-2m := k$ algebraic equations. By adding these equations to Equation (21), therefore, one has a system of $n+1$ equations for $n+1$ unknowns. In constructing $n+1-2m$ algebraic equations, we need the numerical solution of the Equation (18). Suppose that we have somehow reached the numerical solution. Using this numerical solution, the required algebraic equations can be made. For this purpose, we choose the distinct points ξ_0, ξ_1, $\cdots$, ξ_k on the interval $[0, b]$, such that $0 < \xi_1 < \xi_2 < \cdots < \xi_k < b$. Using the numerical solution of Equation (18), the function $u(\xi)$ and its derivatives from the first order to the $(m-1)$-order to the variable ξ at each point $\xi_1, \xi_2, \cdots, \xi_k$ can be determined. We note that the derivative of the l-th order ($l = 1,2,\cdots,m-1$) of the polynomial solution of Equation (20) to the variable ξ can be expressed by the following formula:

$$u^{(l)}(\xi)=\sum_{i=l}^{n} i(i-1)\cdots\big(i-(l-1)\big)a_i\xi^{i-l},\quad l=1{,}2,\cdots,m-1. \tag{23}$$

By substituting $\xi_1, \xi_2, \cdots, \xi_k$ in Equation (23), one has the following algebraic equations:

$$\begin{aligned}
&\xi_1\colon\ u^{(0)}(\xi_1)=\sum_{i=l}^{n} a_i{\xi_1}^{i} := \Phi_{01},\\
&\xi_1\colon\ u^{(l)}(\xi_1)=\sum_{i=l}^{n} i(i-1)\cdots\big(i-(l-1)\big)a_i{\xi_1}^{i-l} := \Phi_{l1},\ \ l=1{,}2,\cdots\\
&\ \ \vdots\\
&\xi_k\colon\ u^{(0)}(\xi_k)=\sum_{i=l}^{n} a_i{\xi_k}^{i} := \Phi_{lk},\\
&\xi_k\colon\ (\xi_k)=\sum_{i=l}^{n} i(i-1)\cdots\big(i-(l-1)\big)a_i{\xi_k}^{i-l} := \Phi_{lk},\quad l=1{,}2,\cdots,
\end{aligned} \tag{24}$$

These equations are called the approximate boundary conditions for the Equation (18). Then, by using the numerical solution of the given ODE and by choosing the real numbers $\xi_1, \xi_2, \cdots, \xi_k$ on the interval $[0,b]$, the real numbers Φ_{lk}, $l=0{,}1,\cdots,m-1$; $k=1,\cdots,(n+1)/m-2$, can be provided. For example, to have four numbers ξ_1, ξ_2, ξ_3, ξ_4 on the interval $[0,b]$, and for a second-order ODE, $\Gamma\big(u(\xi),u'(\xi),u''(\xi)\big)=0$, according to the equation between numbers n, m, k, i.e., $n=m(k+2)-1$, we have $n=11$. In this case, $k=4$, $m=2$, and $n=11$, the finite power series solution to the ODE, $\Gamma\big(u(\xi),u'(\xi),u''(\xi)\big)=0$ is a polynomial of degree $n=11$ in terms of the variable ξ as follows:

$$u(\xi)=P_{11}(\xi):=\sum_{i=0}^{11} a_i\xi^{i}=a_0+a_1\xi+\cdots+a_{11}\xi^{11}. \tag{25}$$

To find the unknowns a_0, a_1, ⋯, a_{11}, according to the Equations (21) and (23), we have the following system of twelve algebraic equations with twelve unknowns as BCs:

$$\begin{gathered}
\xi_0\colon u^{(0)}(\xi_0)=\sum_{i=0}^{11} a_i{\xi_0}^{i}=a_0:=\Phi_{00},\\
\xi_0\colon u^{(l)}(\xi_0)=\sum_{i=1}^{11} ia_i{\xi_0}^{i-1}=a_1:=\Phi_{l1},\\
\xi_1\colon u^{(0)}(\xi_1)=\sum_{i=0}^{11} a_i{\xi_1}^{i}=a_0+a_1\xi_1^1+a_2\xi_1^2+\cdots+a_{11}\xi_1^{11}:=\Phi_{01},\\
\xi_1\colon u^{(1)}(\xi_1)=\sum_{i=1}^{11} ia_i{\xi_1}^{i-1}=a_1+2a_2\xi_1+3a_3\xi_1^2+\cdots+11a_{11}\xi_1^{10}:=\Phi_{,01},\\
\vdots
\end{gathered} \tag{26}$$

$$\xi_5: u^{(0)}(\xi_5) = \sum_{i=0}^{11} a_i {\xi_5}^i = a_0 + a_1\xi_5^1 + a_2\xi_5^2 + \cdots + a_{11}\xi_5^{11} := \Phi_{05},$$
$$\xi_5: u^{(1)}(\xi_5) = \sum_{i=1}^{11} i a_i {\xi_5}^{i-1} = a_1 + 2a_2\xi_5 + 3a_3\xi_5^2 + \cdots + 11a_{11}\xi_5^{10} := \Phi_{15}. \tag{26}$$

where $\xi_0 = 0$ and $\xi_5 = b$. By using a numerical solution method, one can determine the twelve numbers Φ_{ij}, $i = 0,1; j = 0,1, \cdots, 5$. By substituting these determined numbers into the above system of equations (26) and then by solving this system, the unknowns $a_0, a_1, \cdots, a_{11}$ can be obtained simultaneously. In the final stage, putting a_0, a_1, $\cdots$, a_{11} in the polynomial Equation (25), the solution of the ODE, $\Gamma\big(u(\xi), u'(\xi), u''(\xi)\big) = 0$, can be found. This solution is a polynomial of degree $n = 11$ in terms of the variable $0 \le \xi \le b$ with the known coefficients. The HAN-method is a technique for solving a nonlinear differential equation with a numerical solution. By solving a system of equations with $n+1$ unknowns and $n+1$ Equation (21) that were made earlier, the coefficients of Equation (20) are determined, and then this obtained polynomial can be considered as the semi-analytical solutions of Equation (18). As mentioned earlier in this section, it should be considered that only a limited part of the Akbari-Ganji-method overlaps with the HAN-method and these two methods are completely different. The former version of the Akbari-Ganji-method is fully described in the study of Pattnaik et al. [81] while modified version of this method is described by many studies [64,68,70,72].

3.2. Application of the HAN-method

To apply the HAN-method for the Equations (12)–(15), first, the following polynomials with unknown constant coefficients should be assumed as the semi-analytical solutions:

$$f(\xi) = \sum_{i=0}^{12} a_i\xi^i = a_0 + a_1\xi^1 + a_2\xi^2 + \cdots + a_{12}\xi^{12}, \tag{27}$$

$$g(\xi) = \sum_{i=0}^{10} b_i\xi^i = b_0 + b_1\xi^1 + b_2\xi^2 + \cdots + b_{10}\xi^{10}, \tag{28}$$

$$\theta(\xi) = \sum_{i=0}^{10} c_i\xi^i = c_0 + c_1\xi^1 + c_2\xi^2 + \cdots + c_{10}\xi^{10}, \tag{29}$$

$$\phi(\xi) = \sum_{i=0}^{10} d_i\xi^i = d_0 + d_1\xi^1 + d_2\xi^2 + \cdots + d_{10}\xi^{10}. \tag{30}$$

In a special case, when in the Equations (12)–(15), the value of parameters $M_n = 1$, $S_c = 0.5$, $R_0 = 20$, $E_c = 0.2$, $N_r = 1$, $P_r = 0.7$, $\lambda_3 = 0.3$, $\lambda_2 = 0.2$, $\lambda_1 = 2$, and by applying the HAN-method, the analytical solutions of the Equations (12)–(15) are obtained. Based on Equations (27)–(30), there are 46 unknowns. So, we need 46 linear algebraic equations in terms of the unknowns of a_is, b_is, c_is, and d_is, to obtain these unknowns. The BCs in Equation (16) makes only ten equations as follows:

$$\begin{cases} f(\xi)=0,\ \dfrac{\mathrm{d}f(\xi)}{\mathrm{d}\xi}=-2,\ g(\xi)=0,\ \theta(\xi)=1,\ \phi(\xi)=1,\ \text{when } \xi=-1, \\ f(\xi)=0,\ \dfrac{\mathrm{d}f(\xi)}{\mathrm{d}\xi}=-2,\ g(\xi)=0,\ \theta(\xi)=0,\ \phi(\xi)=0,\ \text{when } \xi=1, \end{cases} \tag{31}$$

and the remaining 36 equations should be made through numerical solutions. The results of the numerical solution of the Equations (12)–(15), with the values of parameters $M_{\mathrm{n}}=1$, $S_{\mathrm{c}}=0.5$, $R_0=20$, $E_{\mathrm{c}}=0.2$, $N_{\mathrm{r}}=1$, $P_{\mathrm{r}}=0.7$, $\lambda_3=0.3$, $\lambda_2=0.2$, $\lambda_1=2$ are shown in **Table 1**:

Table 1. Results of numerical solution in Maple software.

ξ	$f(\xi)$	$g(\xi)$	$\theta(\xi)$	$\phi(\xi)$
−1	0	0	1	1
−0.8	−0.246005124491156	0.817889422276519	0.864417323523375	0.967184480779807
−0.6	−0.287412078985710	0.699224476135717	0.747139598839239	0.914803387876689
−0.4	−0.228582538070867	0.436491652089539	0.659933009990955	0.823375085853292
−0.2	−0.123414668423391	0.203695046637467	0.592730707383331	0.680935972701367
0	0	0	0.534632113764447	0.499999999998872
0.2	0.123414668424025	−0.203695046644449	0.476515794697461	0.319064027300319
0.4	0.228582538071048	−0.436491652086817	0.408964493290973	0.176624914147266
0.6	0.287412078985752	−0.699224476135717	0.319284654492353	0.0851966121235713
0.8	0.246005124491164	−0.817889422276190	0.189129334005668	0.0328155192202959
1	0	0	0	0

It is possible to look at the numerical solution results given in **Table 1** as approximate boundary conditions and create new equations from them. Considering that 36 equations need to be constructed, the approximate boundary conditions have been used to construct 36 equations in **Table 1**.

Considering the ten equations that were created by the boundary conditions of the problem and the 36 equations that were created by the approximate boundary conditions, a system of equations with 46 equations and 46 unknowns can be made, and by solving this system of equations, all the unknown coefficients of the Equations (12)–(15) are known. **Table 2** shows all the calculated coefficients.

Table 2. The semi-analytical solutions a_is, b_is and c_is, d_is of the polynomial solutions of Equations (27)–(30) by using Maple software.

i	a_i	b_i	c_i	d_i
0	0	0	0.5346321138	0.5000000000
1	0.6308526290	−0.9932581054	−0.2832663661	−0.9423864576
2	$1.314855659 \times 10^{-11}$	$-1.535799231 \times 10^{-10}$	0.00001313734819	$7.486085590 \times 10^{-11}$
3	−0.3361243916	−0.6268107312	−0.1789459199	0.9819150125
4	$-1.542107247 \times 10^{-10}$	$1.932409400 \times 10^{-9}$	−0.005556420643	$-7.351507187 \times 10^{-10}$
5	−0.2056198917	−0.1486907388	−0.07035631327	−1.008168042

Table 2. (*Continued*).

i	a_i	b_i	c_i	d_i
6	$6.358924750 \times 10^{-10}$	$-7.275123879 \times 10^{-9}$	-0.006849781331	$2.522186822 \times 10^{-9}$
7	-0.08199370720	1.443336356	-0.009636316660	0.6813602413
8	$-1.172739046 \times 10^{-9}$	$1.032999352 \times 10^{-8}$	-0.02330796936	$-3.427124023 \times 10^{-9}$
9	-0.02891848919	0.3254232194	0.04220491593	-0.2127207541
10	$9.889007828 \times 10^{-10}$	$-4.833699114 \times 10^{-9}$	0.001068920224	$1.566355064 \times 10^{-9}$
11	0.02180385067	-	-	-
12	$-3.109920437 \times 10^{-10}$	-	-	-

Therefore, the semi-analytical solutions of the Equations (12)–(15) are the following polynomials with known coefficients (given in **Table 2**):

$$\begin{aligned} f(\xi) = & -3.109920437 \times 10^{-10}\xi^{12} + 0.02180385067\xi^{11} + 9.889007828 \times 10^{-10}\xi^{10} \\ & -0.02891848919\xi^{9} - 1.172739046 \times 10^{-9}\xi^{8} - 0.08199370720\xi^{7} \\ & +6.358924750 \times 10^{-10}\xi^{6} - 0.2056198917\xi^{5} - 1.542107247 \times 10^{-10}\xi^{4} \\ & -0.3361243916\xi^{3} + 1.314855659 \times 10^{-11}\xi^{2} + 0.6308526290\xi, \end{aligned} \tag{32}$$

$$\begin{aligned} g(\xi) = & -4.833699114 \times 10^{-9}\xi^{10} + 0.3254232194\xi^{9} + 1.032999352 \times 10^{-8}\xi^{8} \\ & +1.443336356\xi^{7} - 7.275123879 \times 10^{-9}\xi^{6} - 0.1486907388\xi^{5} \\ & +1.932409400 \times 10^{-9}\xi^{4} - 0.6268107312\xi^{3} - 1.535799231 \times 10^{-10}\xi^{2} \\ & -0.9932581054\xi, \end{aligned} \tag{33}$$

$$\begin{aligned} \theta(\xi) = & \, 0.001068920224\xi^{10} + 0.04220491593\xi^{9} - 0.02330796936\xi^{8} \\ & -0.009636316660\xi^{7} - 0.006849781331\xi^{6} - 0.07035631327\xi^{5} \\ & -0.005556420643\xi^{4} - 0.1789459199\xi^{3} + 0.00001313734819\xi^{2} \\ & -0.2832663661\xi + 0.5346321138, \end{aligned} \tag{34}$$

$$\begin{aligned} \phi(\xi) = & \, 1.566355064 \times 10^{-9}\xi^{10} - 0.2127207541\xi^{9} - 3.427124023 \times 10^{-9}\xi^{8} \\ & +0.6813602413\xi^{7} + 2.522186822 \times 10^{-9}\xi^{6} - 1.008168042\xi^{5} \\ & -7.351507187 \times 10^{-10}\xi^{4} + 0.9819150125\xi^{3} + 7.486085590 \times 10^{-11}\xi^{2} \\ & -0.9423864576\xi + 0.5000000000, \end{aligned} \tag{35}$$

According to the known coefficients in **Table 2** and by substituting the semi-analytical solutions Equations (32)–(35) in the Equations (12)–(15), the following functions are obtained:

$$\begin{aligned} F(\xi) = & -0.72111048\xi - 510.5054373\xi^{9} + 9.208327727 \times 10^{-6}\xi^{10} \\ & +50.68002728\xi^{11} + 7.246234031 \times 10^{-7}\xi^{2} + 23.6729104\xi^{3} \\ & -6.846259567 \times 10^{-6}\xi^{4} - 188.6953981\xi^{5} - 2.553303752 \times 10^{-15}\xi^{21} \\ & +3.132740726 \times 10^{-7}\xi^{20} - 9.413076502\xi^{19} - 1.065495063 \times 10^{-6}\xi^{18} \\ & +18.84036847\xi^{17} + 34.47699268\xi^{15} - 1.134311440 \times 10^{-6}\xi^{14} \\ & +60.28961826\xi^{13} - 1.101479475 \times 10^{-8}, \end{aligned} \tag{36}$$

$$\begin{aligned} G(\xi) = {} & -3.955372750\times10^{-11} + 0.064479380\xi + 7.387427951\xi^{9} \\ & +1.150987074\times10^{-7}\xi^{10} + 8.269281386\xi^{11} - 2.739344998\times10^{-8}\xi^{12} \\ & +1.734175481\times10^{-7}\xi^{6} - 26.72537277\xi^{7} - 2.176380812\times10^{-7}\xi^{8} \\ & +4.451253930\times10^{-9}\xi^{2} - 1.987728644\xi^{3} - 5.154374818\times10^{-8}\xi^{4} \\ & +13.54304810\xi^{5} - 2.405187146\times10^{-17}\xi^{21} + 3.111526954\times10^{-9}\xi^{20} \\ & -0.0993367099\xi^{19} - 8.681084360\times10^{-9}\xi^{18} - 0.0194282808\xi^{17} \\ & -9.40604969\times10^{-9}\xi^{16} + 0.997925442\xi^{15} + 2.10391033\times10^{-9}\xi^{14} \\ & +3.251304946\xi^{13}, \end{aligned} \tag{37}$$

$$\begin{aligned} \Theta(\xi) = {} & -0.003452233\xi + 0.00006130762489 - 5.415773831\xi^{9} \\ & -0.4398051432\xi^{10} + 1.058580205\xi^{11} - 0.7311598925\xi^{12} \\ & -1.709032870\xi^{6} + 4.160236008\xi^{7} + 2.899239036\xi^{8} \\ & -0.01345753001\xi^{2} + 0.125044258\xi^{3} + 0.2974912040\xi^{4} \\ & -1.179098979\xi^{5} + 4.653959590\times10^{-11}\xi^{21} \\ & -0.003262919118\xi^{20} - 0.1159489481\xi^{19} + 0.2625816501\xi^{18} \\ & +0.1743739899\xi^{17} - 0.4002439803\xi^{16} + 0.5161009724\xi^{15} \\ & -0.6195609969\xi^{14} + 1.037467902\xi^{13}, \end{aligned} \tag{38}$$

$$\begin{aligned} \Phi(\xi) = {} & -0.053579667\xi + 1.497217118\times10^{-10} - 19.88694744\xi^{9} \\ & +7.869389009\times10^{-8}\xi^{10} - 0.2961980010\xi^{11} + 1.166591089\times10^{-7}\xi^{12} \\ & -9.807304522\times10^{-8}\xi^{6} + 26.43191200\xi^{7} - 3.87471243\times10^{-8}\xi^{8} \\ & -8.001195487\times10^{-9}\xi^{2} + 1.58753993\xi^{3} + 5.845206685\times10^{-8}\xi^{4} \\ & -11.14677643\xi^{5} - 4.871239625\times10^{-17}\xi^{21} + 9.369158776\times10^{-9}\xi^{20} \\ & -0.4174318401\xi^{19} - 4.427283003\times10^{-8}\xi^{18} + 1.593580042\xi^{17} \\ & +8.367944055\times10^{-8}\xi^{16} - 0.9086121950\xi^{15} - 1.418626638\times10^{-7}\xi^{14} \\ & +2.125878689\xi^{13}. \end{aligned} \tag{39}$$

According to **Figure 2**, by plotting the functions F, G, Θ, and Φ, that is, Equations (36)–(39), it is possible to validate the accuracy of the analytical results solved by the HAN-method:

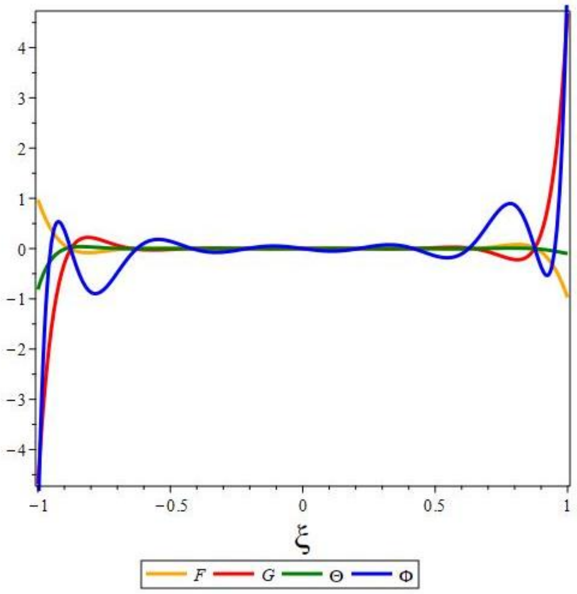

Figure 2. The accuracy of the results by the HAN-method.

3.3. Description of the modified Akbari-Ganji-method

The Akbari-Ganji-method was developed for the analytical solution of nonlinear differential equations. This semi-analytical method has been approximated the governing equations in many problems for which no exact analytical solutions exist. So far, many studies, used this method to solve non-linear and unsolvable mechanical engineering problems. However, due to the need for more accurate solutions, in this study, the Akbari-Ganji method is modified. To explain the main idea of this method, let us consider the general form of the differential equation of order-m as follows:

$$\Xi\colon\ \Gamma\left(u, u', u'', \dots, u^{(m)}\right) = 0; \quad u := u(\xi). \tag{40}$$

with the following BCs:

$$\begin{cases} u(\xi) = \Phi_{00},\ \ u'(\xi) = \Phi_{10}, \cdots,\ \ u^{(m-1)}(\xi) = \Phi_{(m-1)0}, & \text{when } \xi = 0, \\ u(\xi) = \Phi_{0b},\ \ u'(\xi) = \Phi_{1b}, \cdots,\ \ u^{(m-1)}(\xi) = \Phi_{(m-1)b}, & \text{when } \xi = b. \end{cases} \tag{41}$$

In Equation (41), $\{\xi = 0, \xi = b\}$ are boundary points. To solve Equation (40), the solution can be considered as a polynomial with degree n and constant and unknown coefficients:

$$u(\xi) = \sum_{i=0}^{n} a_i \xi^i = a_0 + a_1\xi^1 + a_2\xi^2 + \cdots + a_n\xi^n\,. \tag{42}$$

In Equation (42), the degree of the polynomial solution is assumed to be greater than the order of the differential equation in Equation (40). There is an $n + 1$ constant and unknown coefficient the Equation (42). To determine these coefficients, $n + 1$ equations must be made. The boundary conditions of the problem, i.e., Equation (41), can make some of these equations as follows:

$$\begin{aligned} & u(0) = a_0 := \Phi_{00}, \\ & u'(0) = a_1 := \Phi_{10}, \\ & \quad \vdots \\ & u^{(m-1)}(0) = a_{m-1} := \Phi_{(m-1)0}, \\ & u(b) = \sum_{i=0}^{n} a_i b^i := \Phi_{0b}, \\ & u'(b) = \sum_{i=1}^{n} i a_i b^{i-1} := \Phi_{1b}, \\ & \quad \vdots \\ & u^{(m-1)}(b) = \sum_{i=m-1}^{n} i(i-1)\cdots\left(i-(m-2)\right) a_i b^{i-(m-1)} := \Phi_{(m-1)b} \end{aligned} \tag{43}$$

where

$$\Phi_{ij} := u^{(i)}(j) = \frac{\partial u^i}{\partial \xi^i}(\xi = j), \quad i = 0,1,\cdots,m-1;\ j = 0, b \tag{44}$$

there are $2m$ real numbers: $\Phi_{ij} \in \mathbb{R} = (-\infty, +\infty)$. Equations made from the boundary conditions of the problem, as seen in Equation (43) are limited due to the assumption that $n > m$. But to build a system of $n + 1$ unknowns and $n + 1$ equations, more equations are needed. Therefore, the remaining equations can be created by replacing the approximate solution Equation (42) in Equation (40) as follows:

$$\Xi: \begin{cases} \Gamma\left(u(0), u'(0), u''(0), \ldots, u^{(m-1)}(0)\right) = 0, \\ \Gamma\left(u(b/2), u'(b/2), u''(b/2), \ldots, u^{(m-1)}(b/2)\right) = 0, \\ \Gamma\left(u(b), u'(b), u''(b), \ldots, u^{(m-1)}(b)\right) = 0, \end{cases} \tag{45}$$

$$\Xi': \begin{cases} \Gamma\left(u'^{(0)}, u''(0), u'''(0), \ldots, u^{(m-1)}(0)\right) = 0, \\ \Gamma\left(u'(b/2), u''(b/2), u'''(b/2), \ldots, u^{(m-1)}(b/2)\right) = 0, \\ \Gamma\left(u'(b), u''(b), u'''(b), \ldots, u^{(m-1)}(b)\right) = 0, \end{cases} \tag{46}$$

$$\Xi'': \begin{cases} \Gamma\left(u''^{(0)}, u'''(0), u''''(0), \ldots, u^{(m-1)}(0)\right) = 0, \\ \Gamma\left(u''(b/2), u'''(b/2), u''''(b/2), \ldots, u^{(m-1)}(b/2)\right) = 0, \\ \Gamma\left(u''(b), u'''(b), u''''(b), \ldots, u^{(m-1)}(b)\right) = 0. \end{cases} \tag{47}$$

Therefore, extracting as many equations as needed from Equations (45)–(47) is possible to make a system of algebraic equations containing $n + 1$ unknowns and $n + 1$ equations. In another step, by solving this system of algebraic equations, the coefficients a_1, a_2, …, a_n are obtained. By substituting these known coefficients in the polynomial Equation (42), the desired solution of ODE Equation (40) is obtained.

3.4. Application of the modified Akbari-Ganji-method

In this section, the modified Akbari-Ganji-method is explained to solve the equations governing the physics of the problem analytically. First, the following polynomials are approximate solutions for the system of ODEs of Equations (12)–(15), when the values of the parameters $M_{\mathrm{n}} = 1$, $S_{\mathrm{c}} = 0.5$, $R_0 = 20$, $E_{\mathrm{c}} = 0.2$, $N_{\mathrm{r}} = 1$, $P_{\mathrm{r}} = 0.7$, $\lambda_3 = 0.3$, $\lambda_2 = 0.2$, $\lambda_1 = 2$, are considered as follows:

$$f(\xi) = \sum_{i=0}^{13} a_i \xi^i = a_0 + a_1\xi^1 + a_2\xi^2 + \cdots + a_{13}\xi^{13}, \tag{48}$$

$$g(\xi) = \sum_{i=0}^{11} b_i \xi^i = b_0 + b_1\xi^1 + b_2\xi^2 + \cdots + b_{11}\xi^{11}, \tag{49}$$

$$\theta(\xi) = \sum_{i=0}^{11} c_i \xi^i = c_0 + c_1\xi^1 + c_2\xi^2 + \cdots + c_{11}\xi^{11}, \tag{50}$$

$$\phi(\xi) = \sum_{i=0}^{11} d_i \xi^i = d_0 + d_1\xi^1 + d_2\xi^2 + \cdots + d_{11}\xi^{11}. \tag{51}$$

According to the Equations (48)–(51), there are 50 unknown coefficients in the solutions, and to determine these coefficients, 50 equations must be made. The boundary conditions of the problem can only provide 10 of these equations as follows:

$$\begin{cases} f(\xi)=0, \quad \dfrac{\mathrm{d}f(\xi)}{\mathrm{d}\xi}=-2, \quad g(\xi)=0, \quad \theta(\xi)=1, \quad \phi(\xi)=1, \quad \text{when } \xi=-1, \\ f(\xi)=0, \quad \dfrac{\mathrm{d}f(\xi)}{\mathrm{d}\xi}=-2, \quad g(\xi)=0, \quad \theta(\xi)=0, \quad \phi(\xi)=0, \quad \text{when } \xi=1. \end{cases} \tag{52}$$

Due to the higher degree of polynomials in Equations (48)–(51) compared to the order of differential Equations (12)–(15), the number of constructed equations was not enough, and 40 other equations must be made. The numbers -1, -0.5, 0, 0.5, and 1 form the boundary points set of the problem in the modified Akbari-Ganji-method which is as follows:

$$\text{Boundary Points} = \text{B. P} = \{-1, -0.5, 0, 0.5, 1\}. \tag{53}$$

In the Mirgolbabaee et al. [82] study, the boundary points were only assumed to be -1 and 1 because, in the Akbari-Ganji-method, numbers -0.5 and 0.5 were not assumed. Using boundary points Equation (53) shows the difference between the modified Akbari-Ganji-method in this study. The B.P. Equation (53) can be used in making the other 40 equations as follows.

$$F\big(f(\text{B. P}), g(\text{B. P})\big) \rightarrow F\big(f(\text{B. P}), g(\text{B. P})\big) = 0, F'\big(f(\text{B. P}), g(\text{B. P})\big) = 0, \tag{54}$$

$$G\big(f(\text{B. P}), g(\text{B. P})\big) \rightarrow G\big(f(\text{B. P}), g(\text{B. P})\big) = 0, G'\big(f(\text{B. P}), g(\text{B. P})\big) = 0, \tag{55}$$

$$\Theta\big(f(\text{B. P}), \theta(\text{B. P})\big) \rightarrow \Theta\big(f(\text{B. C}), \theta(\text{B. P})\big) = 0, \Theta'\big(f(\text{B. C}), \theta(\text{B. P})\big) = 0, \tag{56}$$

$$\Phi\big(f(\text{B. P}), \phi(\text{B. P})\big) \rightarrow \Phi\big(f(\text{B. P}), \phi(\text{B. P})\big) = 0, \Phi'\big(f(\text{B. P}), \phi(\text{B. P})\big) = 0. \tag{57}$$

By using Equations (54)–(57), the remaining 40 equations can be made. In this way, an algebraic equation system including 50 equations and 50 unknowns is provided. By solving this system of algebraic equations by EES software, the unknown coefficients of polynomial Equations (48)–(51) are known. The results of these calculations are listed in **Table 3**.

Table 3. Coefficients of calculated semi-analytical solutions of $f(\xi)$, $g(\xi)$, $\theta(\xi)$, and $\phi(\xi)$ by using EES software.

i	a_i	b_i	c_i	d_i
0	1.305×10^{-09}	-1.503×10^{-09}	0.538	0.5
1	0.6333	−1.004	−0.2839	−0.9512
2	-2.633×10^{-09}	4.080×10^{-09}	−1.111 × 10−09	6.206×10^{-09}
3	−0.3388	−0.6784	−0.1798	1.004
4	2.744×10^{-10}	1.393×10^{-08}	−0.0176	-1.094×10^{-08}
5	−0.2071	0.4447	−0.06483	−1.084
6	3.158×10^{-09}	-3.530×10^{-08}	0.03249	1.179×10^{-08}
7	−0.07114	−0.7459	−0.03616	0.8653
8	-3.434×10^{-09}	2.523×10^{-08}	−0.07994	-6.729×10^{-09}
9	−0.05654	3.427	0.08456	−0.4226

Table 3. (*Continued*).

i	a_i	b_i	c_i	d_i
10	1.630×10^{-09}	-6.430×10^{-09}	0.0271	1.577×10^{-09}
11	0.04948	−1.444	−0.01995	0.08855
12	-3.006×10^{-10}	-	-	-
13	−0.009136	-	-	-

Therefore, Equations (48)–(51) with known coefficients in **Table 3** are as follows:

$$\begin{aligned} f(\xi) = {} & -0.00913586759 03062\xi^{13} - 3.0059935486316 \times 10^{-10}\xi^{12} \\ & +0.049479419881825\xi^{11} + 1.62959137088580 \times 10^{-9}\xi^{10} \\ & -0.056541511493550\xi^{9} - 3.43395702881180 \times 10^{-9}\xi^{8} \\ & -0.071135119727114\xi^{7} + 3.1584256271901 \times 10^{-9}\xi^{6} \\ & -0.20708488641248\xi^{5} + 2.7441666680975 \times 10^{-10}\xi^{4} \\ & -0.33884071588679\xi^{3} - 2.6326450840098 \times 10^{-9}\xi^{2} \\ & +0.63325868122841\xi + 1.3047692846982 \times 10^{-9}, \end{aligned} \tag{58}$$

$$\begin{aligned} g(\xi) = {} & -1.4439370475119\xi^{11} - 6.4300521802920 \times 10^{-9}\xi^{10} \\ & +3.42742904550680\xi^{9} + 2.5225974250684 \times 10^{-8}\xi^{8} \\ & -0.74586721719866\xi^{7} - 3.5298912095728 \times 10^{-8}\xi^{6} \\ & +0.44470574614560\xi^{5} + 1.3925998374323 \times 10^{-8}\xi^{4} \\ & -0.67840126764621\xi^{3} + 4.0797621819671 \times 10^{-9}\xi^{2} \\ & -1.0039292592957\xi - 1.5027699008770 \times 10^{-9}, \end{aligned} \tag{59}$$

$$\begin{aligned} \theta(\xi) = {} & -0.019949979396849\xi^{11} + 0.027102934710942\xi^{10} \\ & +0.084557599513564\xi^{9} - 0.079940426193195\xi^{8} \\ & -0.036155780661524\xi^{7} + 0.032489139997977\xi^{6} \\ & -0.064827401988362\xi^{5} - 0.017604748375972\xi^{4} \\ & -0.17975976695144\xi^{3} - 1.1111337095063 \times 10^{-9}\xi^{2} \\ & -0.28386467051539\xi + 0.53795310097138, \end{aligned} \tag{60}$$

$$\begin{aligned} \phi(\xi) = {} & 0.088550403451787\xi^{11} + 1.5765518305027 \times 10^{-9}\xi^{10} \\ & -0.42261174751715\xi^{9} - 6.7286923236797 \times 10^{-9}\xi^{8} \\ & +0.86531978712817\xi^{7} + 1.1793085932528 \times 10^{-8}\xi^{6} \\ & -1.0839867098965\xi^{5} - 1.0940578922658 \times 10^{-8}\xi^{4} \\ & +1.0039674300140\xi^{3} + 6.2057382125988 \times 10^{-9}\xi^{2} \\ & +0.95123916318038\xi + 0.49999999809390. \end{aligned} \tag{61}$$

By substituting the parameters $M_{\mathrm{n}} = 1$, $S_{\mathrm{c}} = 0.5$, $R_0 = 20$, $E_{\mathrm{c}} = 0.2$, $N_{\mathrm{r}} = 1$, $P_{\mathrm{r}} = 0.7$, $\lambda_3 = 0.3$, $\lambda_2 = 0.2$, $\lambda_1 = 2$and also the semi-analytical solutions Equations (58)–(61) in the system of ODEs Equations (12)–(15), the following functions are obtained:

$$\begin{aligned}F(\xi) = {} & 1.05\times 10^{-6}\xi + 1.617978297\times 10^{-7} - 2.864487108\xi^{23}\\ & -1.667514441\times 10^{-7}\xi^{22} + 24.46426562\xi^{21} + 1.412485108\times 10^{-6}\xi^{20}\\ & -71.40969308\xi^{19} - 4.665128944\times 10^{-6}\xi^{18} + 58.56010126\xi^{17}\\ & +7.166823992\times 10^{-6}\xi^{16} - 14.95208524\xi^{15} - 6.205967542\times 10^{-6}\xi^{14}\\ & +407.7001385\xi^{11} + 1.023646025\times 10^{-6}\xi^{12} + 51.12723700\xi^{13}\\ & +968.8314803\xi^{7} - 0.00003564085615\xi^{8} - 1156.866646\xi^{9}\\ & +0.00001283945909\xi^{10} - 0.00002209310958\xi^{4} - 293.9639348\xi^{5}\\ & +0.00004302281442\xi^{6} + 3.144794801\times 10^{-6}\xi^{2} + 29.3736218\xi^{3},\end{aligned}\tag{62}$$

$$\begin{aligned}G(\xi) = {} & -1\times 10^{-9}\xi + 1.264656650\times 10^{-9} - 0.2374491182\xi^{23}\\ & -9.50334838\times 10^{-9}\xi^{22} + 1.884919064\xi^{21} + 7.594561356\times 10^{-8}\xi^{20}\\ & -4.510551062\xi^{19} - 2.489325876\times 10^{-7}\xi^{18} + 0.603871120\xi^{17}\\ & +4.008168260\times 10^{-7}\xi^{16} - 5.093711742\xi^{15} - 2.899888176\times 10^{-7}\xi^{14}\\ & +72.91571319\xi^{11} - 1.200514615\times 10^{-7}\xi^{12} - 0.964474048\xi^{13}\\ & +83.69721252\xi^{7} - 8.268409477\times 10^{-7}\xi^{8} - 128.0173769\xi^{9}\\ & +5.666696327\times 10^{-7}\xi^{10} - 3.284691732\times 10^{-7}\xi^{4} - 22.35297628\xi^{5}\\ & +7.405153775\times 10^{-7}\xi^{6} + 3.857635990\times 10^{-8}\xi^{2} + 2.074823229\xi^{3},\end{aligned}\tag{63}$$

$$\begin{aligned}\Theta(\xi) = {} & -1\times 10^{-18} - 0.02806809701\xi^{23} + 0.1057565962\xi^{22}\\ & +0.2493513560\xi^{21} - 0.8125290153\xi^{20} - 0.7332496408\xi^{19}\\ & +2.125434747\xi^{18} + 0.5177206891\xi^{17} - 1.633310018\xi^{16}\\ & +0.07688241553\xi^{15} + 0.2069212252\xi^{14} + 4.268845670\xi^{11}\\ & -0.9537387143\xi^{12} + 0.9939434047\xi^{13} + 13.06567882\xi^{7}\\ & +13.52749523\xi^{8} - 14.76949872\xi^{9} - 4.223471658\xi^{10}\\ & +3.487965768\xi^{4} - 4.050784611\xi^{5} - 11.48225565\xi^{6}\\ & -0.3482685168\xi^{2} + 0.409178712\xi^{3},\end{aligned}\tag{64}$$

$$\begin{aligned}\Phi(\xi) = {} & -0.08898832371\xi^{23} - 4.368318235\times 10^{-9}\xi^{22} + 0.8294397323\xi^{21}\\ & +4.002490312\times 10^{-8}\xi^{20} - 2.986078961\xi^{19} - 1.556512418\times 10^{-7}\xi^{18}\\ & +4.949909265\xi^{17} + 3.346062434\times 10^{-7}\xi^{16} - 5.693260463\xi^{15}\\ & -4.799888970\times 10^{-7}\xi^{14} + 8.194318358\xi^{11} + 4.318955214\times 10^{-7}\xi^{12}\\ & +4.908856700\xi^{13} + 20.73435521\xi^{7} - 4.531249286\times 10^{-7}\xi^{8}\\ & -25.25068823\xi^{9} - 8.33815240\times 10^{-10}\xi^{10} - 1.180119054\times 10^{-7}\xi^{4}\\ & -25.25068823\xi^{9} - 8.33815240\times 10^{-10}\xi^{10} - 1.180119054\times 10^{-7}\xi^{4}\\ & -6.21444740\xi^{5} + 3.938015065\times 10^{-7}\xi^{6} + 1.16509320\times 10^{-8}\xi^{2}\\ & +0.61658411\xi^{3}.\end{aligned}\tag{65}$$

According to **Figure 3**, by plotting the functions F, G, Θ, and Φ, that is, Equations (62)–(65), it is possible to validate the accuracy of the analytical results solved by the modified AGM:

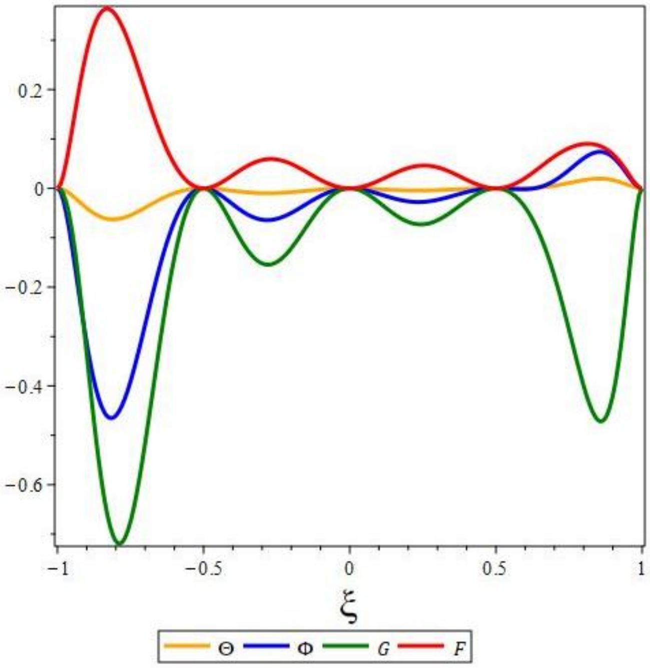

Figure 3. The accuracy of the results by the modified-AGM.

3.5. Validation process

In the validation process, the analytical results were obtained from two applied methods in a special case for Equations (12)–(15) when the values of the parameters $M_\mathrm{n} = 1$, $S_\mathrm{c} = 0.5$, $R_0 = 20$, $E_\mathrm{c} = 0.2$, $N_\mathrm{r} = 1$, $P_\mathrm{r} = 0.7$, $\lambda_3 = 0.3$, $\lambda_2 = 0.2$, and $\lambda_1 = 2$ have been compared with the results of Agarwal [1]. The comparison of results is shown in tables and graphs. The calculated profiles for axial, radial, microrotation, concentration, and temperature are illustrated in **Figures 4–8** and **Tables 4–9**. The tables and graphs used for validation confirm that the results of this study are accurate when compared to previous research.

Table 4. Comparison of calculated radial velocity when $M_\mathrm{n} = 1$, $S_\mathrm{c} = 0.5$, $R_0 = 20$, $E_\mathrm{c} = 0.2$, $N_\mathrm{r} = 1$, $P_\mathrm{r} = 0.7$, $\lambda_3 = 0.3$, $\lambda_2 = 0.2$, $\lambda_1 = 2$.

ξ	$f'(\xi)$			
	HAN-method	**Runge-Kutta**	**Modified-AGM**	**Reference [1]**
−1	−2.000000000	−2	−2	−2
−0.8	−0.6039874290	−0.604021502099537	−0.6070542988	−0.605730414
−0.6	0.1048968662	0.104900556292338	0.1043729063	0.0909617336
−0.4	0.4406972324	0.440698332661268	0.4417902710	0.4301777711
−0.2	0.5888353680	0.588833666382915	0.5909080012	0.5949989703
0	0.6308526290	0.630854360417168	0.6332586812	0.6292000000
0.2	0.5888353680	0.588833666383954	0.5909079992	0.5949989703
0.4	0.4406972324	0.440698332660745	0.4417902673	0.4301777711
0.6	0.1048968663	0.104900556292016	0.1043729020	0.0909617336
0.8	−0.6039874290	−0.604021502099592	−0.6070543008	−0.605730414
1	−2	−2	−2	−2

Table 5. Comparison of calculated axial velocity when $M_{\mathrm{n}} = 1$, $S_{\mathrm{c}} = 0.5$, $R_0 = 20$, $E_{\mathrm{c}} = 0.2$, $N_{\mathrm{r}} = 1$, $P_{\mathrm{r}} = 0.7$, $\lambda_3 = 0.3$, $\lambda_2 = 0.2$, $\lambda_1 = 2$.

ξ	$f(\xi)$			
	HAN-method	**Runge-Kutta**	**Modified-AGM**	**Reference [1]**
−1	0	0	0	0
−0.8	−0.2460051244	−0.246005124491156	−0.2465039339	−0.243911560
−0.6	−0.2874120790	−0.287412078985710	−0.2882691344	−0.284291985
−0.4	−0.2285825381	−0.228582538070867	−0.2293677608	−0.225792660
−0.2	−0.1234146684	−0.123414668423392	−0.1238738036	−0.124231180
0	0	0	0	0
0.2	0.1234146684	0.123414668424025	0.1238738060	0.124231180
0.4	0.2285825381	0.228582538071048	0.2293677625	0.225792660
0.6	0.2874120790	0.287412078985752	0.2882691353	0.284291985
0.8	0.2460051245	0.246005124491164	0.2465039341	0.243911560
1	0	0	0	0

Table 6. Comparison of calculated micro-rotation profile when $M_{\mathrm{n}} = 1$, $S_{\mathrm{c}} = 0.5$, $R_0 = 20$, $E_{\mathrm{c}} = 0.2$, $N_{\mathrm{r}} = 1$, $P_{\mathrm{r}} = 0.7$, $\lambda_3 = 0.3$, $\lambda_2 = 0.2$, $\lambda_1 = 2$.

ξ	$g(\xi)$			
	HAN-method	**Runge-Kutta**	**Modified-AGM**	**Reference [1]**
−1	0	0	0	0
−0.8	0.8178894223	0.817889422276519	0.8251948795	0.9384253169
−0.6	0.6992244761	0.699224476135717	0.7058893926	0.7958729497
−0.4	0.4364916521	0.436491652089539	0.4408197093	0.5517536048
−0.2	0.2036950467	0.203695046637467	0.2060785766	0.2011123512
0	0	0	0	0
0.2	−0.2036950467	−0.203695046644449	−0.2060785792	−0.2011123512
0.4	−0.4364916521	−0.436491652086817	−0.4408197105	−0.5517536048
0.6	−0.6992244760	−0.699224476135717	−0.7058893915	−0.7958729497
0.8	−0.8178894222	−0.817889422276190	−0.8251948775	−0.9384253169
1	0	0	0	0

Table 7. Comparison of calculated temperature profile when $M_{\mathrm{n}} = 1$, $S_{\mathrm{c}} = 0.5$, $R_0 = 20$, $E_{\mathrm{c}} = 0.2$, $N_{\mathrm{r}} = 1$, $P_{\mathrm{r}} = 0.7$, $\lambda_3 = 0.3$, $\lambda_2 = 0.2$, $\lambda_1 = 2$.

ξ	$\theta(\xi)$			
	HAN-method	**Runge-Kutta**	**Modified-AGM**	**Reference [1]**
−1	1	1	1	1
−0.8	0.8644173236	0.864417323523375	0.8670757642	0.8445318720
−0.6	0.7471395989	0.747139598839239	0.7504287808	0.7380952670
−0.4	0.6599330100	0.659933009990955	0.6633381810	0.6906250417
−0.2	0.5927307074	0.592730707383331	0.5961589877	0.6677569106

Table 7. (*Continued*).

ξ	(ξ)			
	HAN-method	**Runge-Kutta**	**Modified-AGM**	**Reference [1]**
0	0.5346321138	0.534632113764447	0.5379531010	0.6479362174
0.2	0.4765157947	0.476515794697461	0.4796946339	0.6294637420
0.4	0.4089644934	0.408964493290973	0.4118337130	0.6089844773
0.6	0.3192846545	0.319284654492353	0.3215882740	0.5529253049
0.8	0.1891293340	0.189129334005668	0.1904390477	0.3833875003
1	0	0	0	0

Table 8. Comparison of calculated concentration profile when $M_{\mathrm{n}} = 1$, $S_{\mathrm{c}} = 0.5$, $R_0 = 20$, $E_{\mathrm{c}} = 0.2$, $N_{\mathrm{r}} = 1$, $P_{\mathrm{r}} = 0.7$, $\lambda_3 = 0.3$, $\lambda_2 = 0.2$, $\lambda_1 = 2$.

ξ	$\boldsymbol{\phi}(\xi)$			
	HAN-method	**Runge-Kutta**	**Modified-AGM**	**Reference [1]**
−1	1	1	1	1
−0.8	0.9671844807	0.967184480779807	0.9698056259	0.7950729327
−0.6	0.9148033879	0.914803387876689	0.9178916174	0.6630816895
−0.4	0.8233750858	0.823375085853292	0.8260311037	0.5869060115
−0.2	0.6809359727	0.680935972701367	0.6825521057	0.5367816909
0	0.5000000000	0.499999999998872	0.4999999981	0.4985400090
0.2	0.3190640273	0.319064027300319	0.3174478910	0.4613553214
0.4	0.1766249142	0.176624914147266	0.1739688940	0.4136371083
0.6	0.0851966121	0.085196612123571	0.0821083813	0.3382232049
0.8	0.0328155193	0.032815519220295	0.0301943736	0.2019506869
1	0	0	0	0

Table 9. Comparison of Nusselt number (N_{u}), wall couple stress (C_{g}), and skin friction coefficient (C_{f}) calculated for upper and lower disks when $M_{\mathrm{n}} = 1$, $S_{\mathrm{c}} = 0.5$, $R_0 = 20$, $E_{\mathrm{c}} = 0.2$, $N_{\mathrm{r}} = 1$, $P_{\mathrm{r}} = 0.7$, $\lambda_3 = 0.3$, $\lambda_2 = 0.2$, $\lambda_1 = 2$ with different methods.

	HAN-method	**Runge-Kutta**	**Modified-AGM**
$N_{\mathrm{u}}(+1)$	1.098568314	1.09672856185007	1.102781042
$N_{\mathrm{u}}(-1)$	0.6204230168	0.630651895876009	0.6148246058
$C_{\mathrm{g}}(+1)$	1.412252920	1.335598593	1.339031852
$C_{\mathrm{g}}(-1)$	1.412252922	1.335598593	1.339031858
$C_{\mathrm{f}}(+1)$	13.88488130	13.89622017	13.82379755
$C_{\mathrm{f}}(-1)$	−13.88488130	−13.89622017	−13.82379756

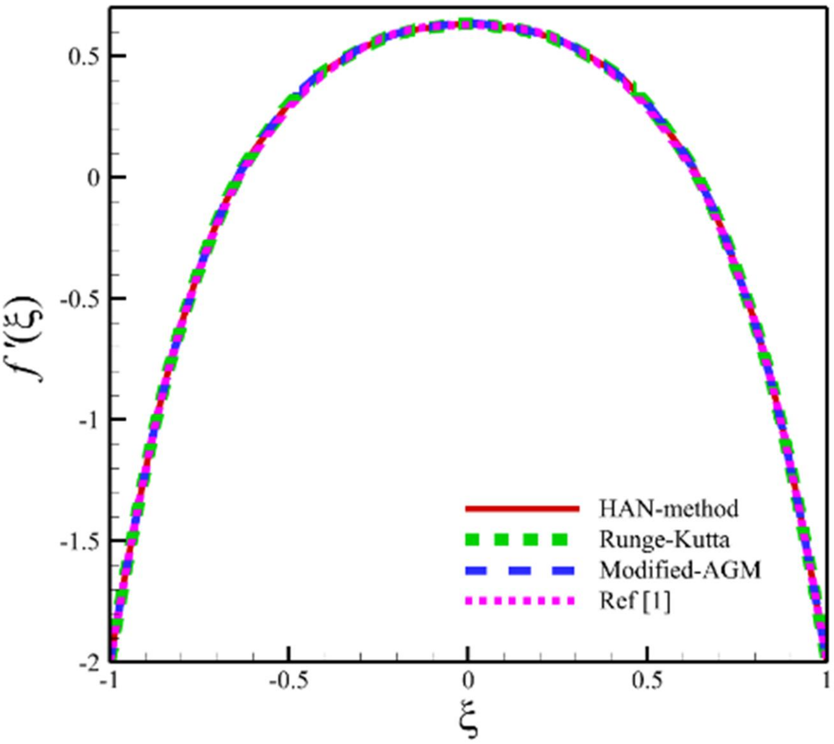

Figure 4. Comparison of calculated radial velocity when $M_{\mathrm{n}} = 1$, $S_{\mathrm{c}} = 0.5$, $R_0 = 20$, $E_{\mathrm{c}} = 0.2$, $N_{\mathrm{r}} = 1$, $P_{\mathrm{r}} = 0.7$, $\lambda_3 = 0.3$, $\lambda_2 = 0.2$, $\lambda_1 = 2$.

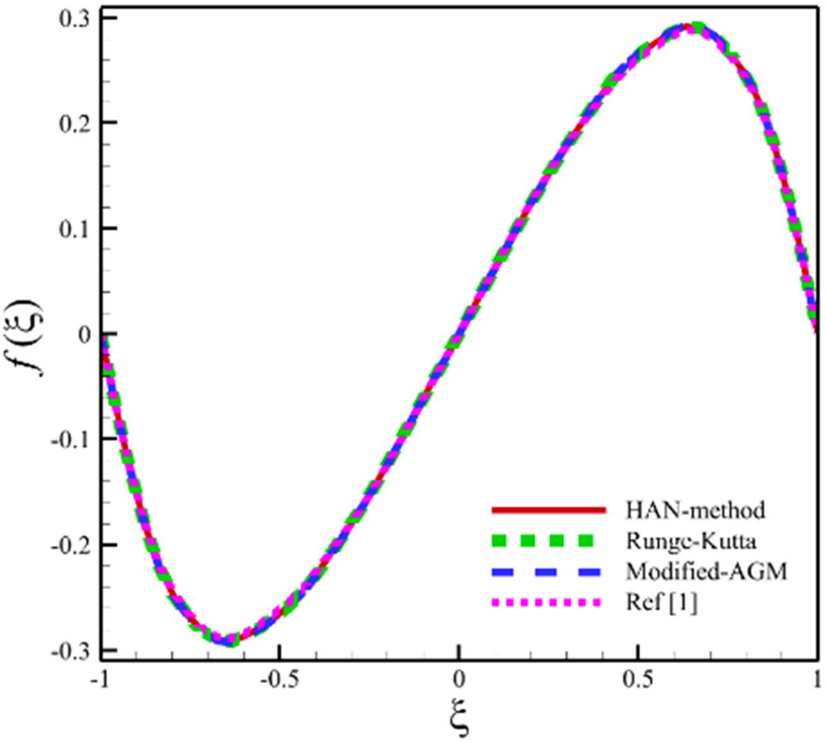

Figure 5. Comparison of calculated axial velocity when $M_n = 1$, $S_{\mathrm{c}} = 0.5$, $R_0 = 20$, $E_{\mathrm{c}} = 0.2$, $N_{\mathrm{r}} = 1$, $P_{\mathrm{r}} = 0.7$, $\lambda_3 = 0.3$, $\lambda_2 = 0.2$, $\lambda_1 = 2$.

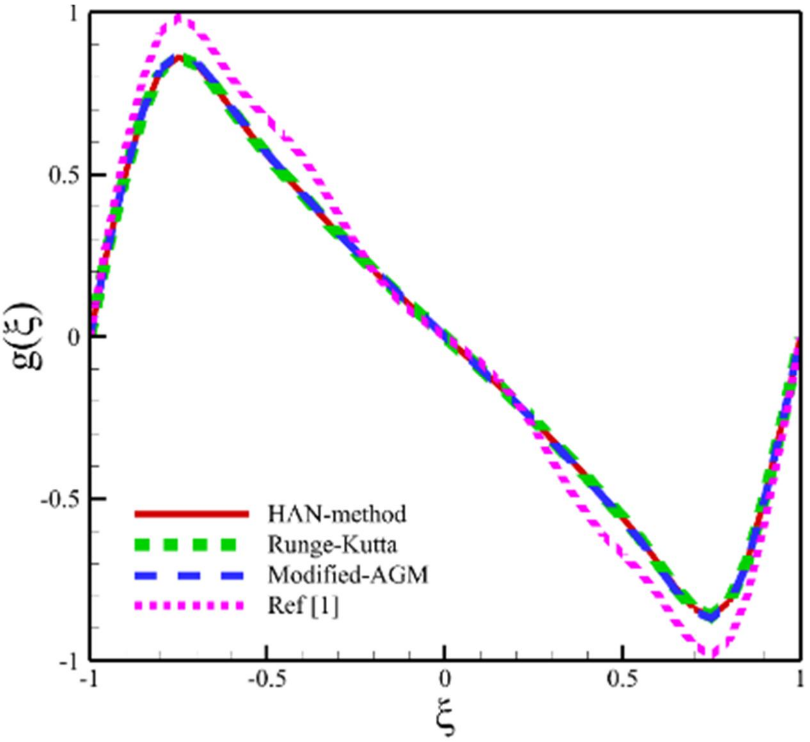

Figure 6. Comparison of calculated micro-rotation profile when $M_{\mathrm{n}} = 1$, $S_{\mathrm{c}} = 0.5$, $R_0 = 20$, $E_{\mathrm{c}} = 0.2$, $N_{\mathrm{r}} = 1$, $P_{\mathrm{r}} = 0.7$, $\lambda_3 = 0.3$, $\lambda_2 = 0.2$, $\lambda_1 = 2$.

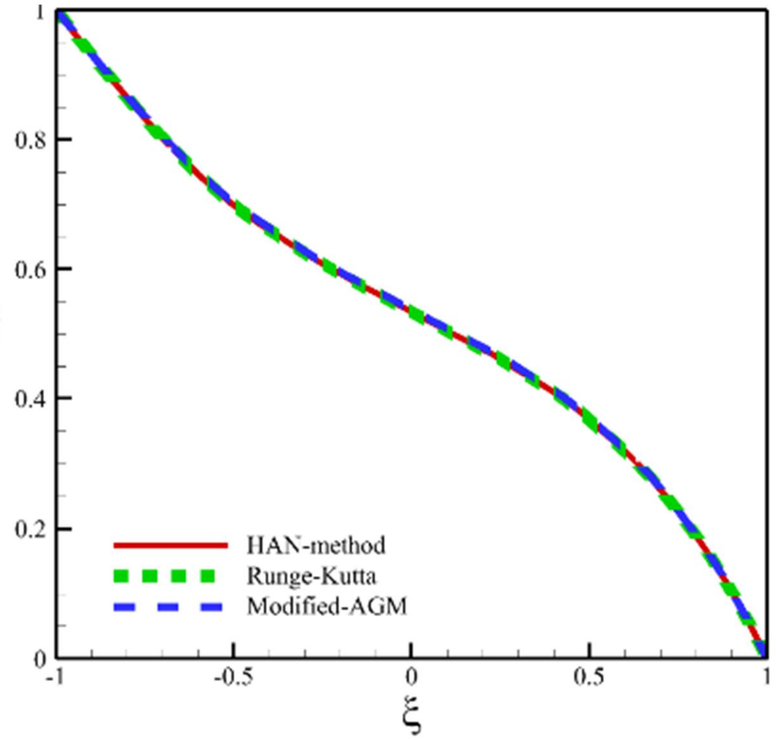

Figure 7. Comparison of calculated temperature profile when $M_{\mathrm{n}} = 1$, $S_{\mathrm{c}} = 0.5$, $R_0 = 20$, $E_{\mathrm{c}} = 0.2$, $N_{\mathrm{r}} = 1$, $P_{\mathrm{r}} = 0.7$, $\lambda_3 = 0.3$, $\lambda_2 = 0.2$, $\lambda_1 = 2$.

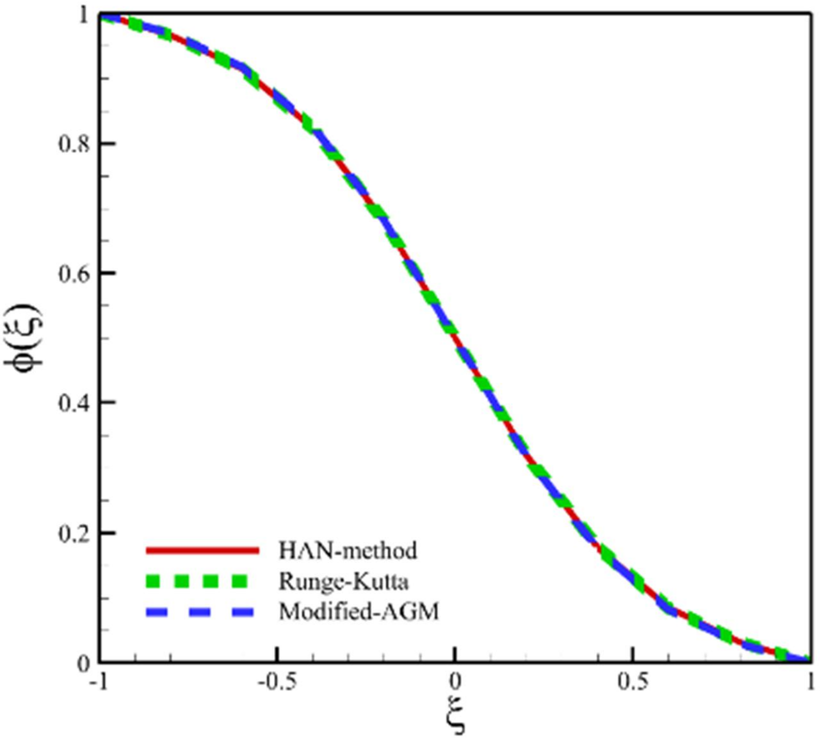

Figure 8. Comparison of calculated concentration profile when $M_{\mathrm{n}} = 1$, $S_{\mathrm{c}} = 0.5$, $R_0 = 20$, $E_{\mathrm{c}} = 0.2$, $N_{\mathrm{r}} = 1$, $P_{\mathrm{r}} = 0.7$, $\lambda_3 = 0.3$, $\lambda_2 = 0.2$, $\lambda_1 = 2$.

4. Results and discussions

After proving the correctness of the results of the two methods used in this research compared to the previous studies, the effect of changes in the physical parameters of Equations (12)–(15) is expressed on the axial, radial, concentration, temperature, and microrotation profiles. The effect of changing each of the parameters has been done separately. So, the effects of changes in parameters such as micropolar parameters, stretching Reynolds number, magnetic parameter, radiation parameter, Prandtl number, Eckert number, and Schmidt number on axial, radial, microrotation, temperature, and concentration profiles have been investigated, respectively.

Now, the results of examining the axial, radial, microrotation, temperature, and concentration contours for Equations (12)–(15) when the micropolar parameters λ_1, λ_2, and λ_3 are changed according to **Table 10**:

Table 10. Micropolar parameters in different cases.

Case number	λ_1	λ_2	λ_3
1	0	0	0
2	2	0.2	0.3
3	4	0.4	0.5
4	6	0.6	0.7
5	8	0.8	0.9
6	10	1.0	1.1

When the micropolar parameters were changed, other parameters were also constant and were equal to the values of $M_\mathrm{n} = 1$, $S_\mathrm{c} = 0.5$, $R_0 = 20$, $E_\mathrm{c} = 0.2$, $N_\mathrm{r} = 1$ and $P_\mathrm{r} = 0.7$. According to **Table 10**, the micropolar parameters were investigated in 6 different cases. The changes in these parameters affected all five quantities of axial velocity, radial velocity, microrotation, temperature, and concentration, as well as the 2D and 3D contours obtained from these changes, which are also shown in **Figures 9–18**. According to **Figures 9** and **10**, the axial velocity's maximum positive and negative values occur in case 6 and are equal to 0.367154015354 and -0.367154015355, respectively. The maximum positive axial velocity occurs when the value of ξ is equal to 0.591836734687163912, and the maximum negative value of the axial velocity occurs when the value of ξ is equal to -0.591836734773761197. According to **Figures 9** and **10**, the lowest value of the axial velocity is zero in all the cases in **Table 10** and exactly at three points of the upper disc $(\xi = 1)$ lower disc $(\xi = -1)$ and occurs between two disks $(\xi = 0)$. According to **Figures 11** and **12**, the maximum positive value of the radial velocity occurs in case 6 and has a value of 0.911191371136 and occurs in a place where the value of ξ is equal to -0.0204081632659887449. The maximum negative value of the radial velocity occurs on both disks and in all cases and has the value of -2. The minimum value of radial velocity calculated in all 6 cases is zero. Still, it happens in different places, which means that the place of minimum radial velocity is different in each case. According to **Table 10**, the minimum radial velocity in the first case occurs at $\xi = \pm 0.714783795486643614$, in the second case, at $\xi = \pm 0.640084929206338415$, in the third case, at $\xi = \pm 0.615927887799965768$, in the fourth case, at $\xi = \pm 0.603995651475552564$, in the fifth case, at $\xi = \pm 0.597038661803401371$, and in the sixth case, at $\xi = \pm\ 0.592472823036015117$. According to **Figures 13** and **14**, the maximum positive and negative values of microrotation occur in case 6 and are equal to 1.0699638786 and -1.0699638786, respectively. The maximum positive value of microrotation occurs when the value of ξ is equal to -0.71428571430603871, and the maximum negative value of microrotation occurs when the value of ξ is equal to 0.714285713365754971. According to **Figures 13** and **14**, the lowest amount of microrotation is zero in all the cases in **Table 10** and exactly occurs at three locations of the upper disk $(\xi = 1)$, the lower disk $(\xi = -1)$ and between two disks $(\xi = 0)$. According to **Figures 15–18**, the maximum temperature and concentration equal 1. In all the cases in **Table 10**, they occur when the value of ξ is equal to -1, and the minimum temperature and concentration are equal to -1, and they occur in all the cases in **Table 10** when the value of ξ is equal to 1.

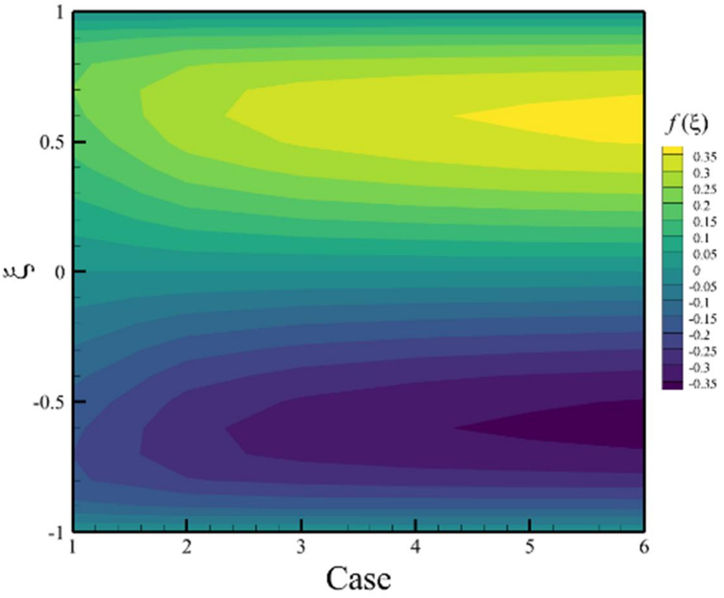

Figure 9. Two-dimensional contour of axial velocity in different cases of micropolar parameters.

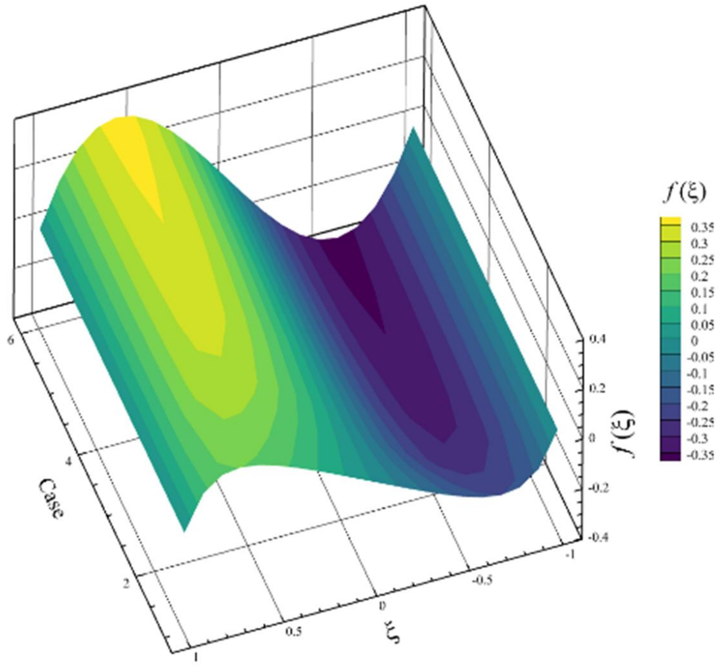

Figure 10. Three-dimensional contour of axial velocity in different cases of micropolar parameters.

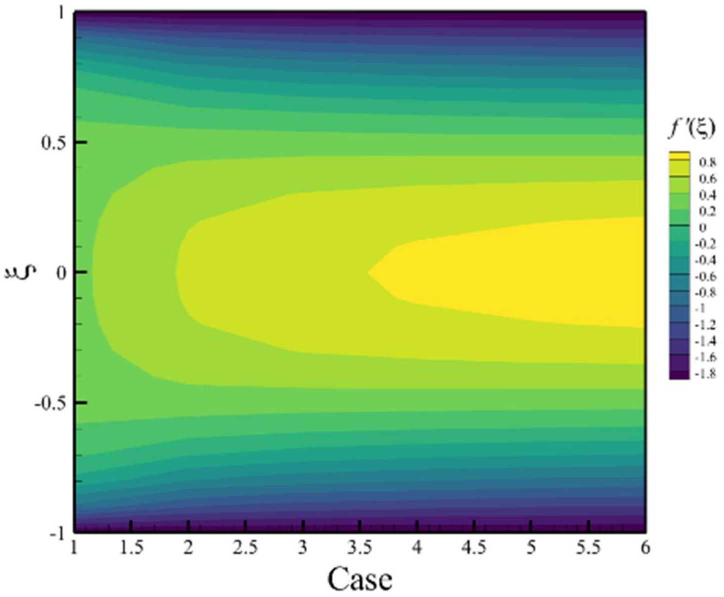

Figure 11. Two-dimensional contour of radial velocity in different cases of micropolar parameters.

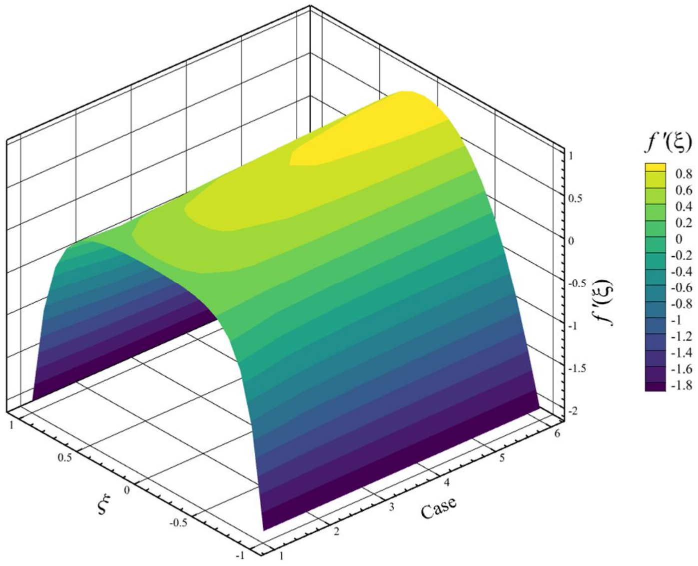

Figure 12. Three-dimensional contour of radial velocity in different cases of micropolar parameters.

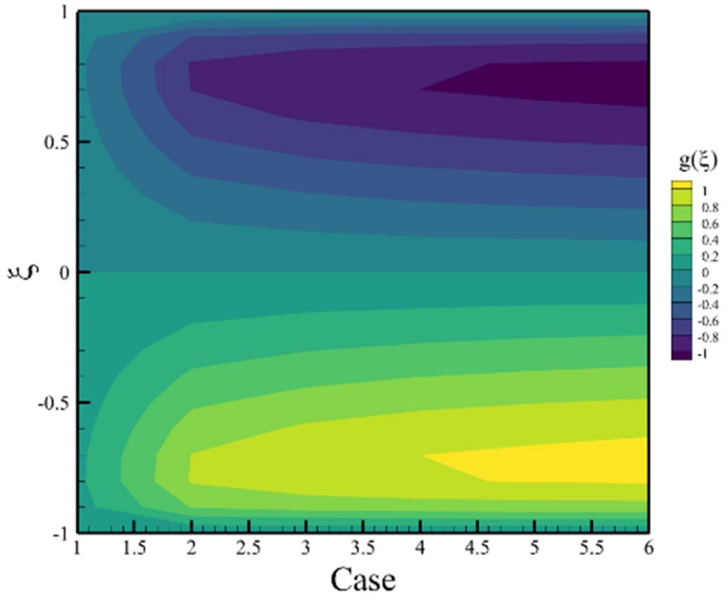

Figure 13. Two-dimensional contour of microrotation in different cases of micropolar parameters.

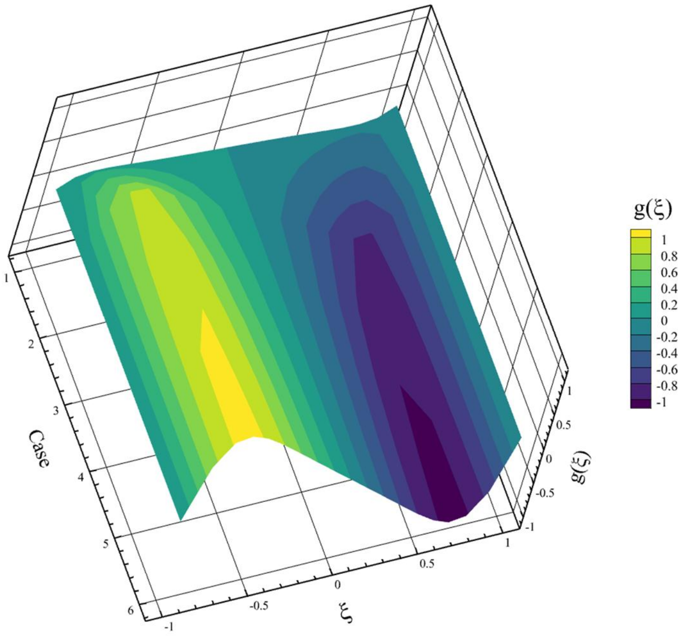

Figure 14. Three-dimensional contour of microrotation in different cases of micropolar parameters.

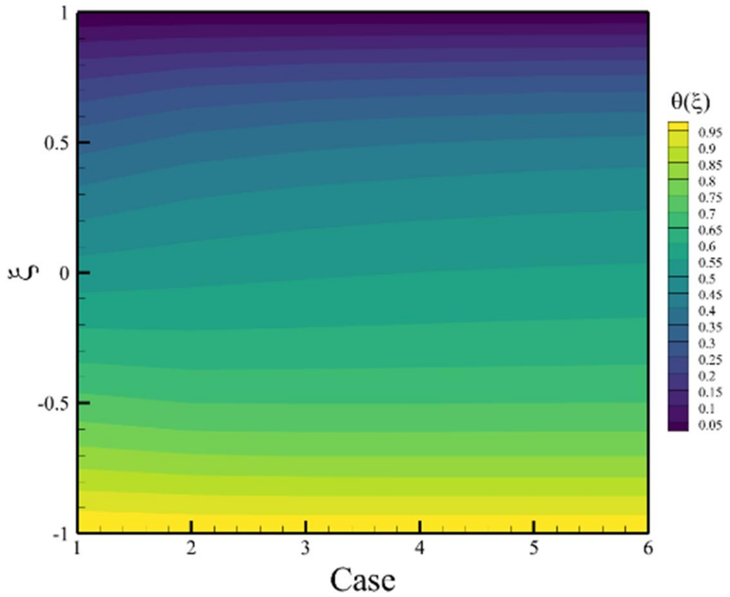

Figure 15. Two-dimensional contour of temperature in different cases of micropolar parameters.

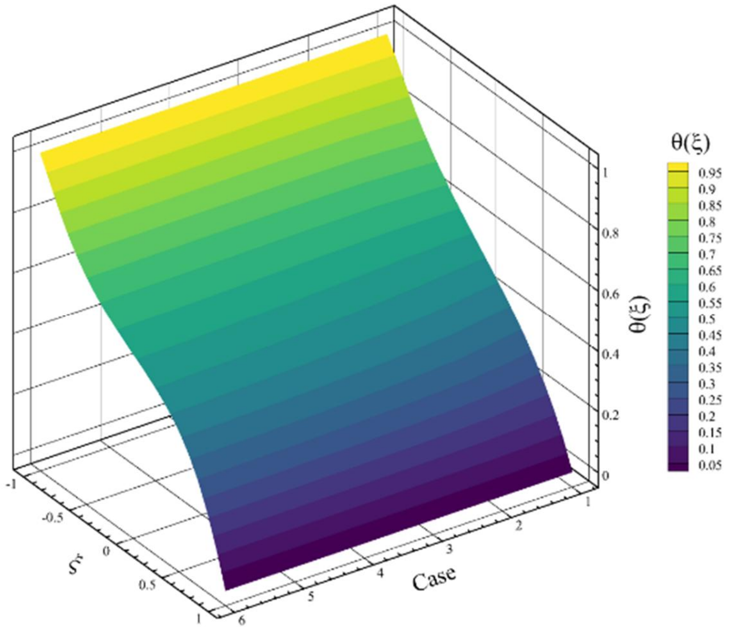

Figure 16. Three-dimensional contour of temperature in different cases of micropolar parameters.

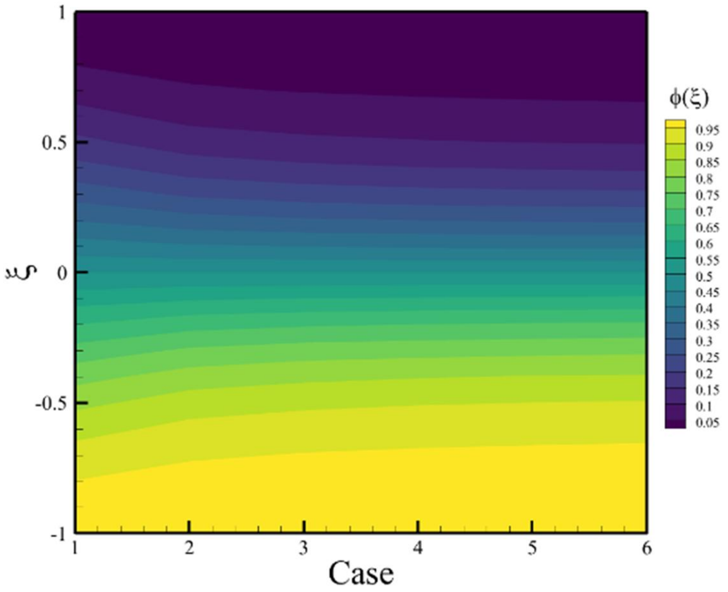

Figure 17. Two-dimensional contour of concentration in different cases of micropolar parameters.

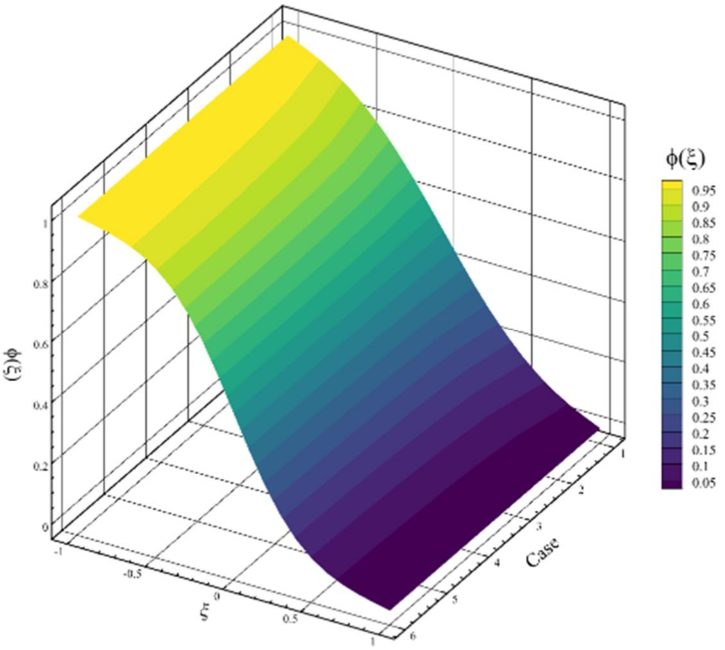

Figure 18. Three-dimensional contour of concentration in different cases of micropolar parameters.

Now, the results of the investigation of axial, radial, microrotation, temperature, and concentration contours for Equations (12)–(15), when the stretching Reynolds number was changed are discussed. When the stretching Reynolds number parameter was changed, the other parameters were constant and equal to the values of $M_{\mathrm{n}} = 1$, $S_{\mathrm{c}} = 0.5$, $E_{\mathrm{c}} = 0.2$, $N_{\mathrm{r}} = 1$, $P_{\mathrm{r}} = 0.7$, $\lambda_3 = 0.3$, $\lambda_2 = 0.2$, $\lambda_1 = 2$. The stretching Reynolds number parameter was investigated in 6 different cases. Changes in this parameter affected all five quantities of axial velocity, radial velocity, microrotation, temperature, and concentration, and the two-dimensional and three-dimensional contours resulting from these changes are also shown in **Figures 19–28**. According to **Figures 19** and **20**, the maximum positive and negative values of the axial velocity occurred when the value of the stretching Reynolds number was zero, 0.408437042705, and -0.408437042704, respectively. The maximum positive axial velocity occurs when the value of ξ is equal to 0.551020408126658312, and the maximum negative value of axial velocity occurs when the value of ξ is equal to -0.551020408397712713. According to **Figures 19** and **20**, the lowest value of the axial velocity is zero for each value of the stretching Reynolds number and happens exactly at the three points of the upper disc ($\xi = 1$), the lower disc ($\xi = -1$), and between the two discs ($\xi = 0$). According to **Figures 21** and **22**, the maximum positive value of the radial velocity occurs when the stretching Reynolds number is zero and has a value of 1.08743936914 and occurs at a point where the value of ξ is equal to -0.00502512566279166364. The maximum negative value of the radial velocity occurs on both disks and for each stretching Reynolds number, with a value of −2. The minimum calculated value of the radial velocity in every six stretching Reynolds numbers is assumed to be zero. Still, it happens in different places, which means that the location of the minimum radial velocity is different in every stretching Reynolds number. When the stretching Reynolds number is zero, the minimum radial velocity occurs at $\xi = \pm 0.567681247229664065$. When the stretching Reynolds number is assumed to be 10, the minimum radial velocity occurs at $\xi = \pm 0.608076355132214585$. When the stretching Reynolds number is assumed to be 20, the minimum radial velocity occurs at $\xi = \pm 0.640511670826334534$. When the stretching Reynolds number is assumed to be 30, the minimum radial velocity occurs at $\xi = \pm 0.665380422273169736$. When the stretching Reynolds number is assumed to be 50, the minimum radial velocity occurs at $\xi = \pm 0.703310792645532423$. According to **Figures 23** and **24**, the maximum positive and negative values of microrotation in the case that the stretching Reynolds number is assumed to be zero and are equal to 1.18125112872 and -1.18125112871, respectively. The maximum positive value of microrotation occurs when the value of ξ is equal to -0.628140703544759815, and the maximum negative value of microrotation occurs when the value of ξ is equal to 0.62814070251133014. According to **Figures 23** and **24**, the minimum amount of microrotation is zero for all assumed stretching Reynolds numbers. It is exactly at three points of the upper disk ($\xi = 1$), the lower disk ($\xi = -1$), and between the two disks ($\xi = 0$) that is happens. According to **Figures 25–28**, the maximum temperature and concentration are equal to 1. All assumed stretching Reynolds numbers occur when the value of ξ is equal to −1. The minimum temperature and concentration are equal to −1, and for all the assumed stretching, Reynolds numbers occur when the value of ξ is equal to 1.

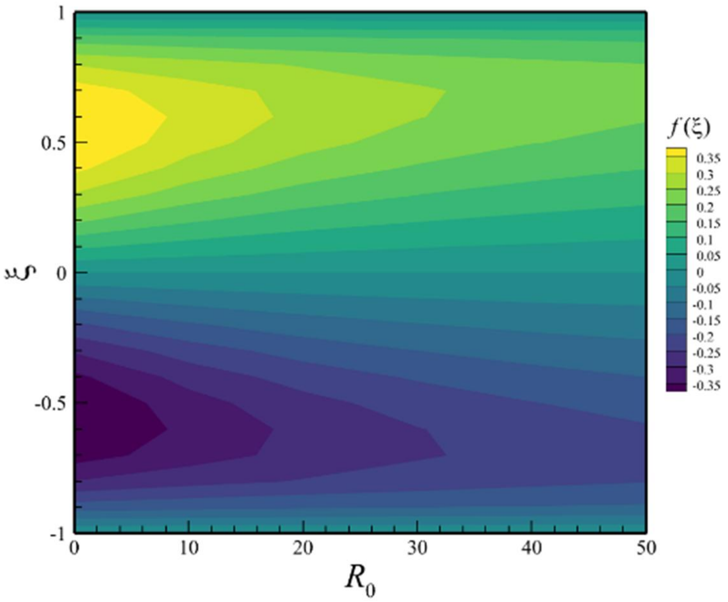

Figure 19. Two-dimensional contour of axial velocity at different values of the stretching Reynolds number.

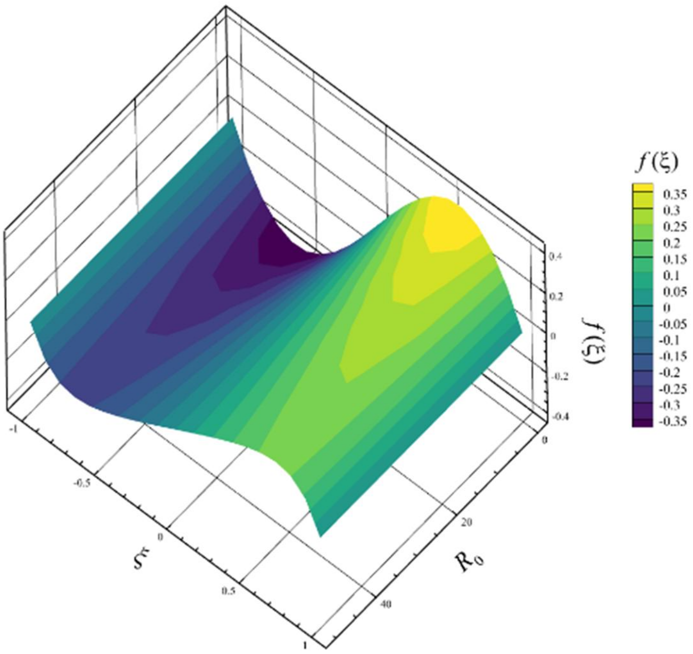

Figure 20. Three-dimensional contour of axial velocity at different values of the stretching Reynolds number.

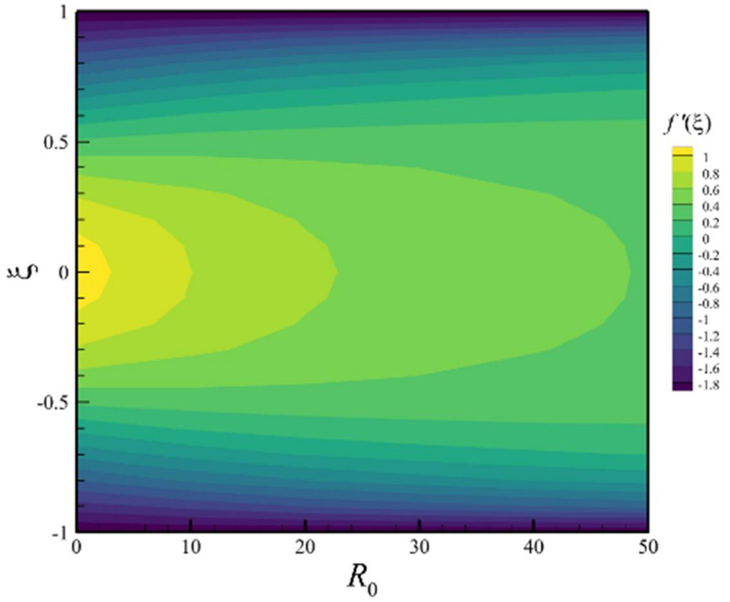

Figure 21. Two-dimensional contour of radial velocity at different values of the stretching Reynolds number.

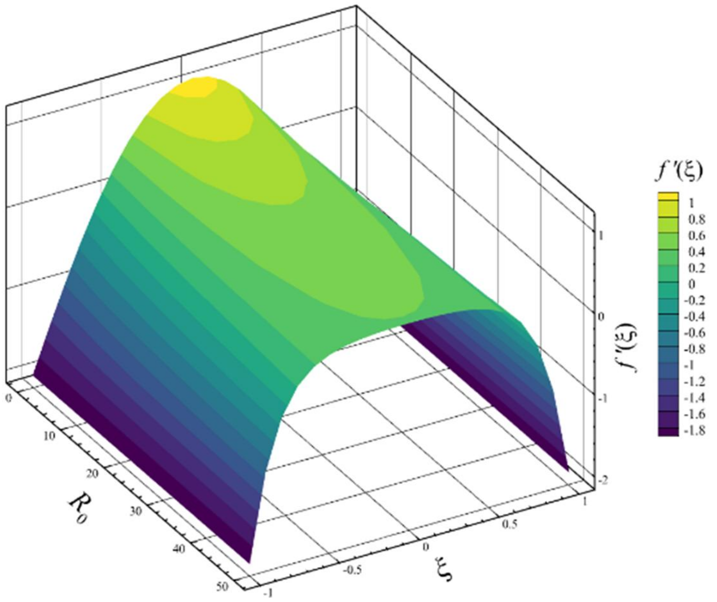

Figure 22. Three-dimensional contour of radial velocity at different values of the stretching Reynolds number.

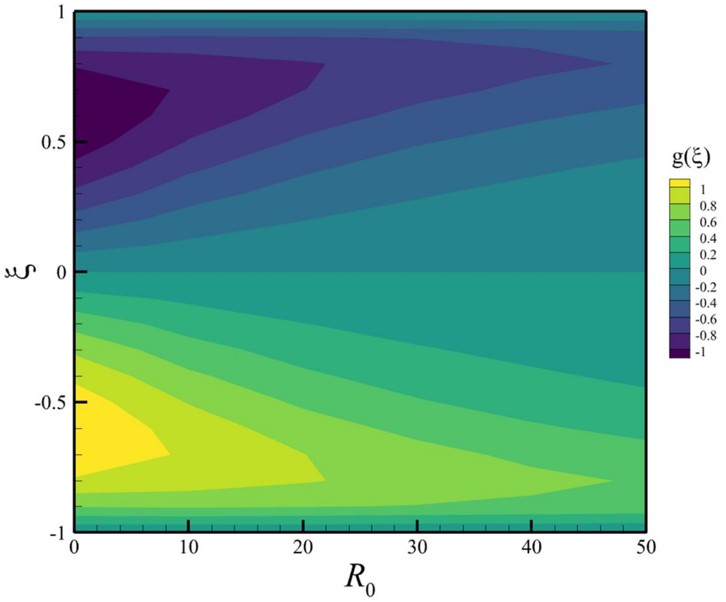

Figure 23. Two-dimensional contour of microrotation at different values of the stretching Reynolds number.

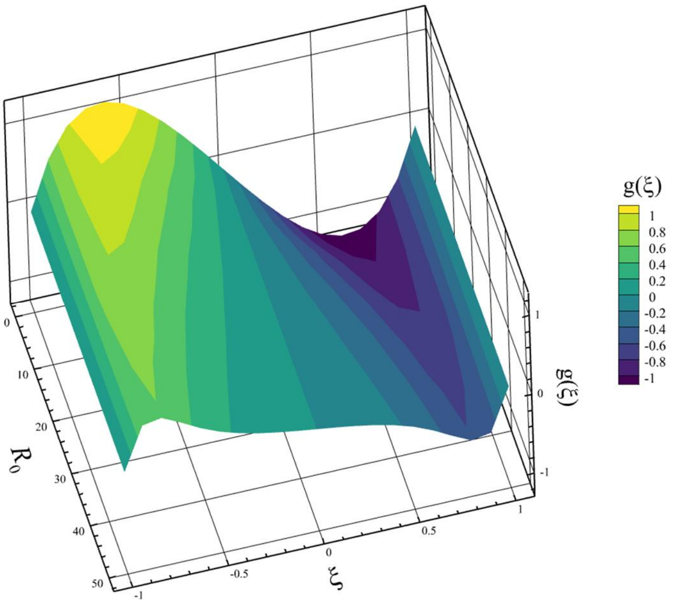

Figure 24. Three-dimensional contour of microrotation at different values of the stretching Reynolds number.

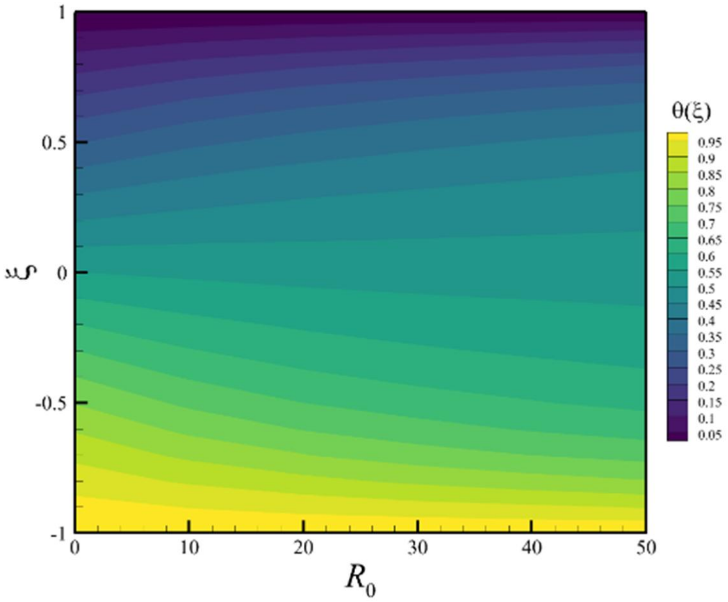

Figure 25. Two-dimensional contour of temperature at different values of the stretching Reynolds number.

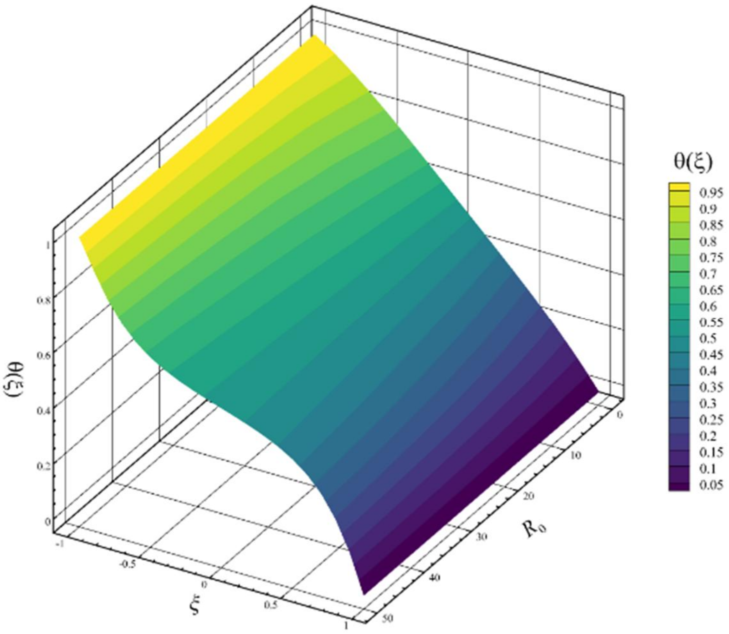

Figure 26. Three-dimensional contour of temperature at different values of the stretching Reynolds number.

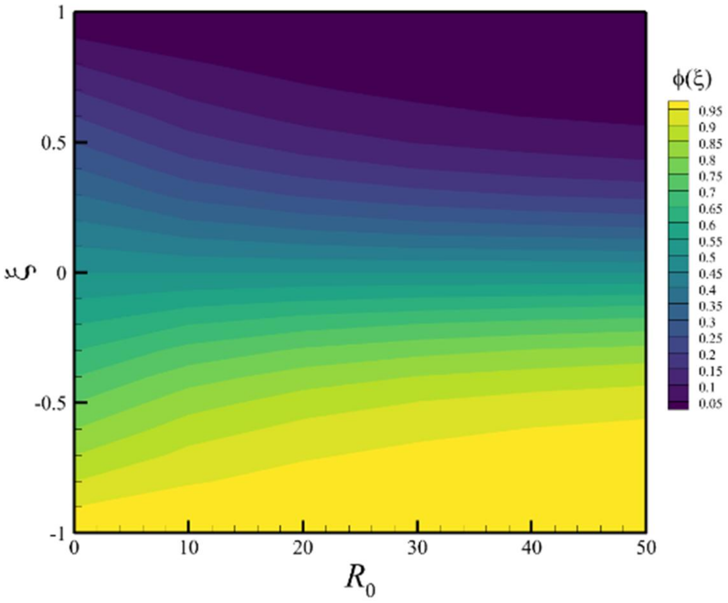

Figure 27. Two-dimensional contour of concentration at different values of the stretching Reynolds number.

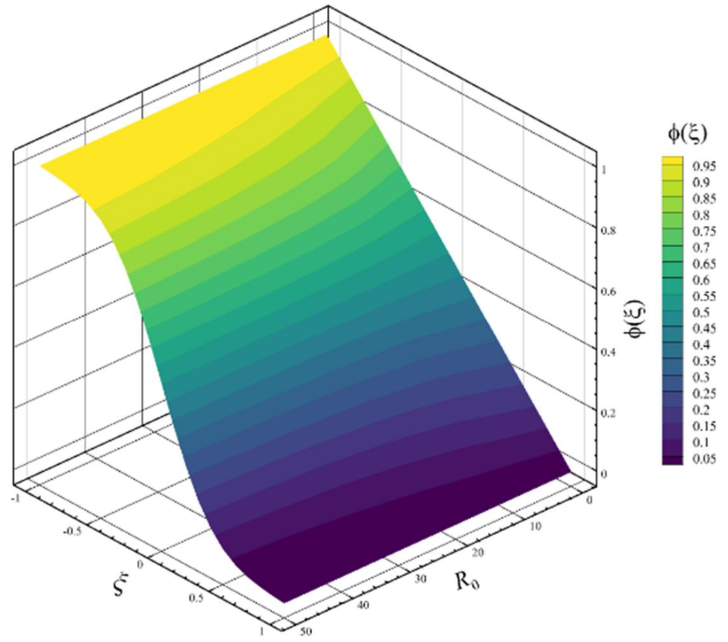

Figure 28. Three-dimensional contour of concentration at different values of stretching Reynolds number.

Now, the results of the investigation of axial, radial, microrotation, temperature, and concentration contours for Equations (12)–(15) when the magnetic parameter was changed are discussed. When the magnetic parameter was changed, the other parameters were constant and equal to the values of $S_c = 0.5$, $R_0 = 20$, $E_c = 0.3$, $N_r = 1$, $P_r = 2$, $\lambda_3 = 0.3$, $\lambda_2 = 0.2$, and $\lambda_1 = 2$. The magnetic parameter was investigated in 6 different cases, and the changes of this parameter affected all five quantities of axial velocity, radial velocity, microrotation, temperature, and concentration, and two-dimensional and three-dimensional contours resulting from these changes are also shown in **Figures 29–38**. According to **Figures 29** and **30**, the maximum positive and negative values of the axial velocity occurred when the value of the magnetic parameter was zero and were equal to 0.340651700237 and −0.340651700186, respectively. The maximum positive axial velocity occurs when the value of ξ is equal to 0.608040200808000031, and the maximum negative value of the axial velocity occurs when the value of ξ is equal to −0.608040201544712167. According to **Figures 29** and **30**, the lowest value of the axial velocity is zero for each value of the magnetic parameter and exactly happens at the three points of the upper disc ($\xi = 1$), the lower disc ($\xi = -1$), and between the two discs ($\xi = 0$). According to **Figures 31** and **32**, the maximum positive value of the radial velocity occurs when the magnetic parameter is zero and has a value of 0.813292009152 and occurs in a place where the value of ξ is equal to −0.00502512698202659848. The maximum negative value of the radial velocity occurs on both disks and for each magnetic parameter and has a value of −2. The minimum value of radial velocity calculated in all six magnetic parameters is assumed to be zero, but it happens in different places; that is, the location of minimum radial velocity is different in each magnetic parameter. According to **Figures 31** and **32**, in the case where the value of the magnetic parameter is zero, the minimum radial velocity occurs at $\xi = \pm 0.607429531034752723$. When the magnetic parameter is assumed to equal 0.5, the minimum radial velocity occurs at $\xi = \pm 0.616804860051527681$. When the magnetic parameter is assumed to equal 1, the minimum radial velocity occurs at $\xi = \pm 0.640511670824125412$. When the magnetic parameter is assumed to be equal to 1.5, the minimum radial velocity occurs at $\xi = \pm 0.669338517525361443$. In the case where the value of the magnetic parameter is assumed to equal 2, the minimum radial velocity occurs at $\xi = \pm 0.698644720773267114$. When the magnetic parameter is assumed to equal 2.5, the minimum radial velocity occurs at $\xi = \pm 0.724515125952562067$. According to **Figures 33** and **34**, the maximum positive and negative values of microrotation in the case where the magnetic parameter is assumed to be zero are 0.920228094121 and −0.920228094294, respectively. The maximum positive value of microrotation occurs when $\xi = -0.72864321608434357$, and the maximum negative value of microrotation occurs when $\xi = 0.728643208751884042$. According to **Figures 33** and **34**, the minimum amount of microrotation is zero for all the assumed magnetic parameters. It is exactly at three points of the upper disk ($\xi = 1$) and the lower disk ($\xi = -1$) and occurs between two disks ($\xi = 0$). According to **Figures 35–38**, the maximum temperature and concentration equal 1. For all assumed magnetic parameters, they occur when $\xi = -1$ is. The minimum temperature and concentration are equal to −1, and all the assumed magnetic parameters occur when $\xi = 1$.

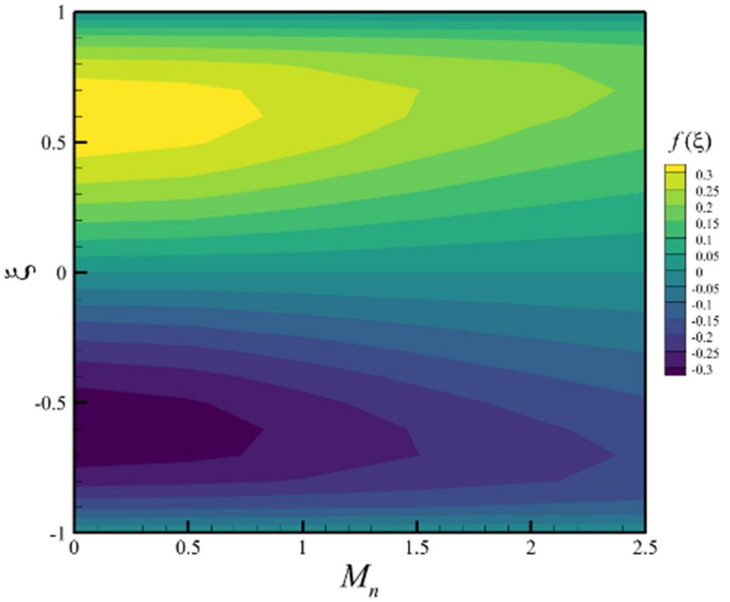

Figure 29. Two-dimensional contour of axial velocity in different values of the magnetic parameter.

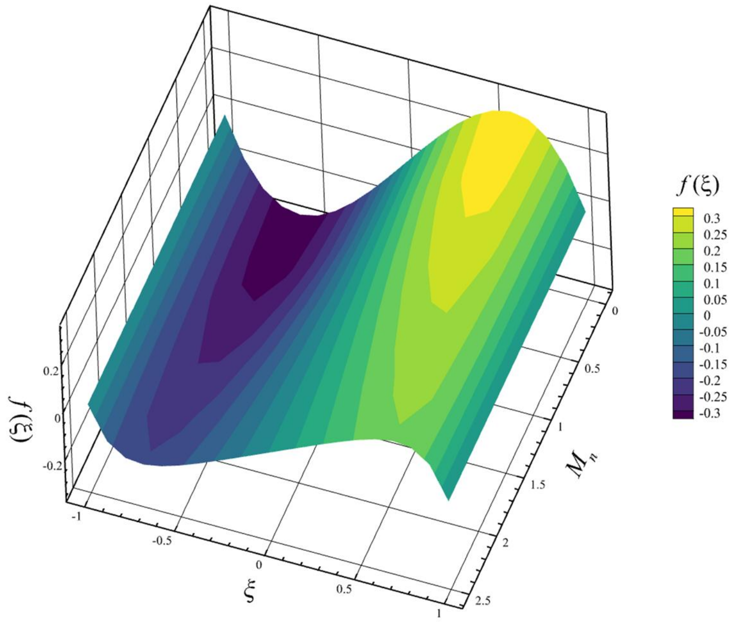

Figure 30. Three-dimensional contour of axial velocity in different values of the magnetic parameter.

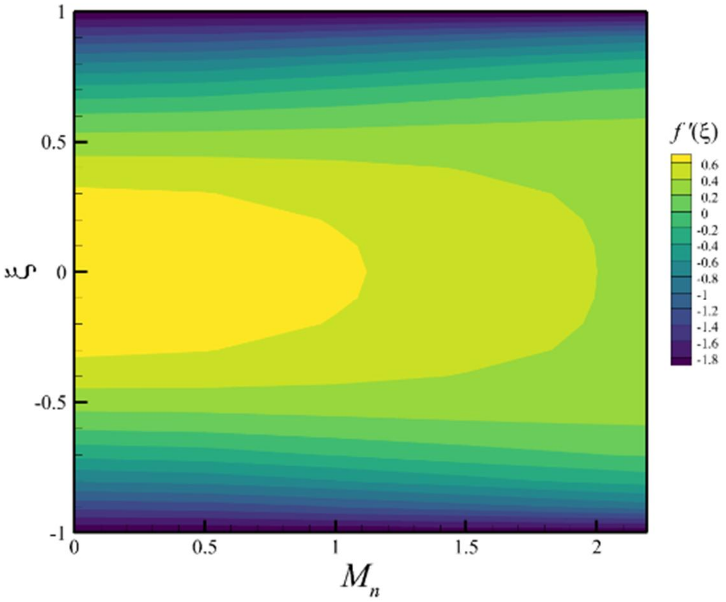

Figure 31. Two-dimensional contour of radial velocity in different values of the magnetic parameter.

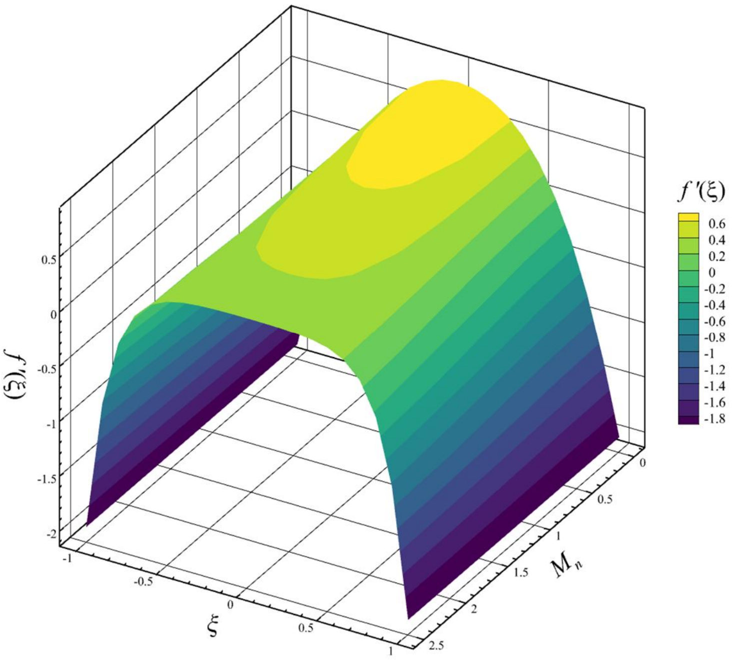

Figure 32. Three-dimensional contour of radial velocity in different values of the magnetic parameter.

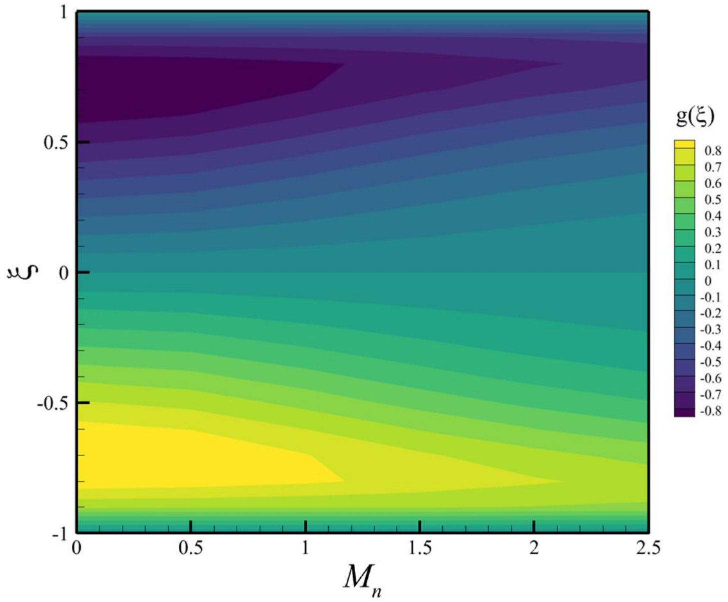

Figure 33. Two-dimensional contour of microrotation at different values of the magnetic parameter.

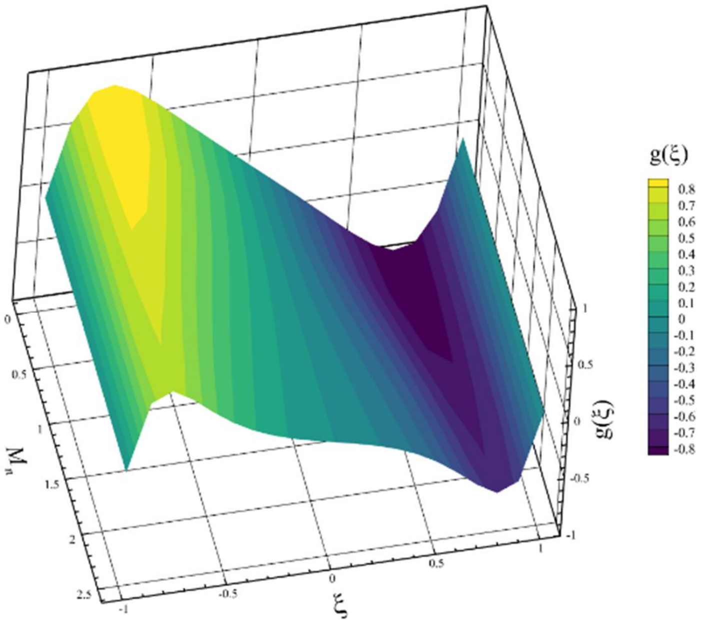

Figure 34. Three-dimensional contour of microrotation at different values of the magnetic parameter.

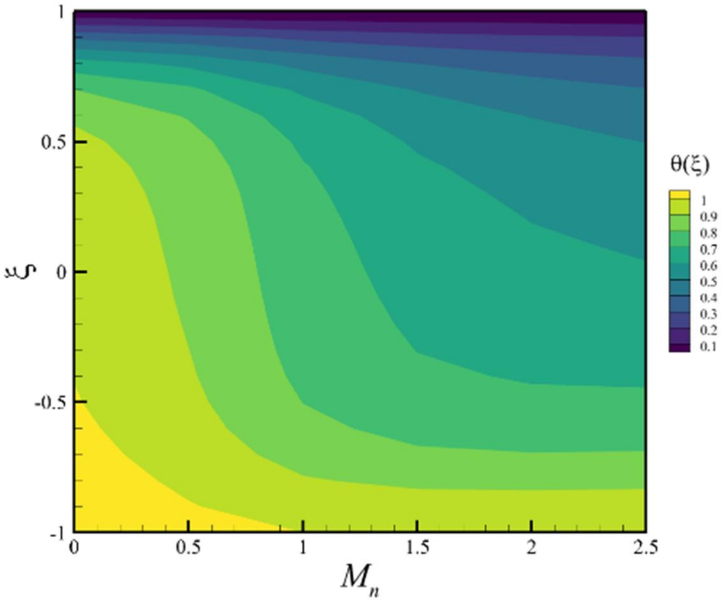

Figure 35. Two-dimensional contour of temperature at different values of the magnetic parameter.

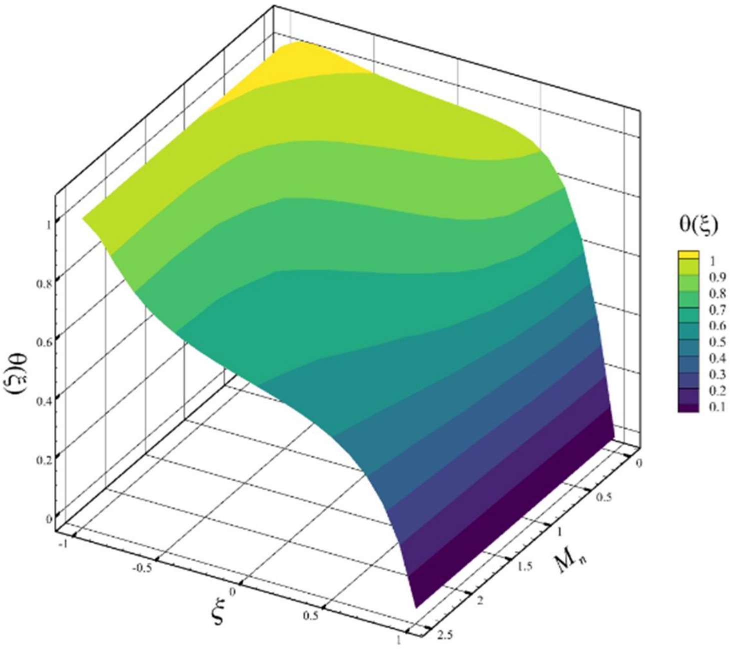

Figure 36. Three-dimensional contour of temperature in different values of the magnetic parameter.

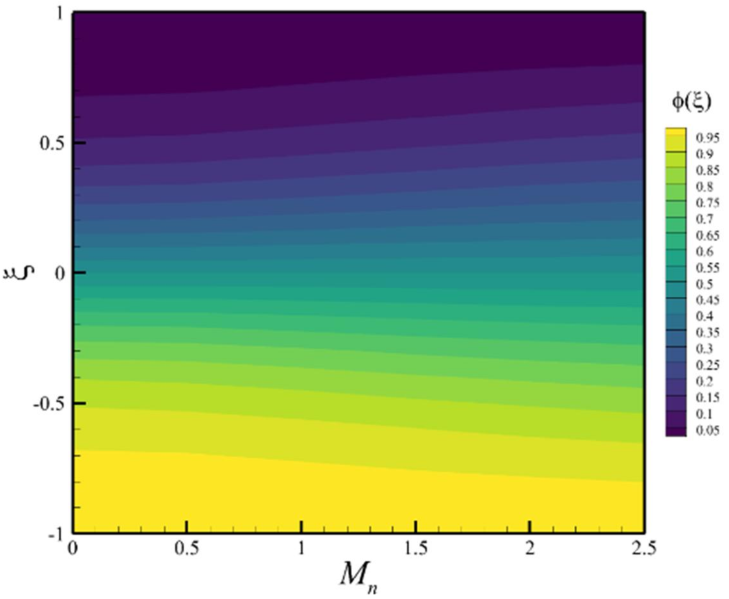

Figure 37. Two-dimensional contour of concentration in different values of the magnetic parameter.

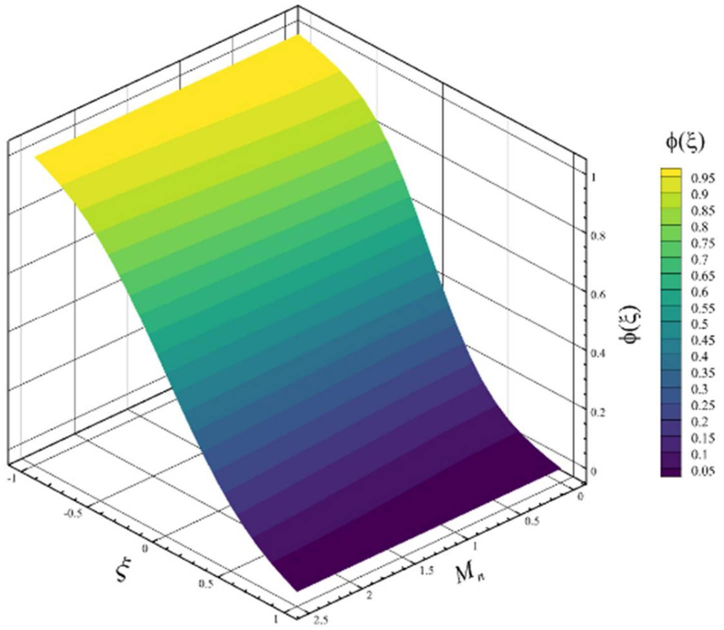

Figure 38. Three-dimensional contour of concentration in different values of the magnetic parameter.

Now, the results of the investigation of axial, radial, microrotation, temperature, and concentration contours for Equations (12)–(15) when the radiation parameter was changed are discussed. When the radiation parameter was changed, the other parameters were constant and equal to the values of $M_{\mathrm{n}} = 1$, $S_{\mathrm{c}} = 0.5$, $R_0 = 3$, $E_{\mathrm{c}} = 0.3$, $P_{\mathrm{r}} = 0.7$, $\lambda_3 = 0.3$, $\lambda_2 = 0.2$, $\lambda_1 = 2$. The radiation parameter was investigated in 6 different modes. The changes in this parameter only had a significant effect on temperature quantity. They had almost no effect on the four quantities of axial speed, radial velocity, microrotation, and concentration, and the resulting 2D and 3D temperature contours were shown in two **Figures 39** and **40**. The changes in the radiation parameter did not affect the quantity of the axial velocity, and the maximum positive and negative values of the axial velocity occurred for all the radiation parameters and are equal to 0.383953826907 and -0.383953826907, respectively. The maximum positive axial velocity occurs when the value of ξ is equal to 0.577889446943717244, and the maximum negative value of the axial velocity occurs when the value of ξ is equal to -0.577889448510863213. The lowest value of the axial velocity is zero for all radiation parameters. It occurs exactly at three points of the upper disk $(\xi = 1)$, the lower disk $(\xi = -1)$, and between the two disks $(\xi = 0)$. The radiation parameter changes did not affect the radial velocity quantity; the maximum positive and negative values of the radial velocity occurred for all the radiation parameters and are equal to 0.986765233308 and -2, respectively. The maximum positive radial velocity occurs when the value of ξ is equal to $-0.0050251257591163896 2$, and the maximum negative value of the radial velocity occurs when the value of ξ is equal to ±1. The lowest value of the radial velocity is zero for all radiation parameters and occurs when the value of ξ is equal to ±0.580466299484895809. The changes in radiation parameters did not affect the amount of microrotation, and the maximum positive and negative values of microrotation occurred for all radiation parameters and are equal to 1.11011447812 and -1.11011447812, respectively. The maximum positive microrotation occurs when the value of ξ is equal to -0.648241207908432315, and the maximum negative value of microrotation occurs when the value of ξ is equal to 0.648241203627465956. The lowest amount of microrotation is zero for all radiation parameters and occurs exactly at three points of the upper disk $(\xi = 1)$, the lower disk $(\xi = -1)$, and between the two disks $(\xi = 0)$. The changes in the radiation parameter did not affect the amount of concentration. The maximum concentration is equal to 1, and all the assumed radiation parameters occur when the value of ξ is equal to -1. The minimum concentration is equal to zero. It happens for all the assumed radiation parameters when the value of ξ equals 1. According to **Figures 39** and **40**, changes in the radiation parameter only significantly affect the quantity of temperature, and for all radiation parameters, the maximum temperature is equal to 1. It is assumed for all radiation parameters that when the value of ξ is equal to -1, it happens, and the minimum temperature is equal to zero. It happens for all assumed radiation parameters when the value of ξ is equal to 1.

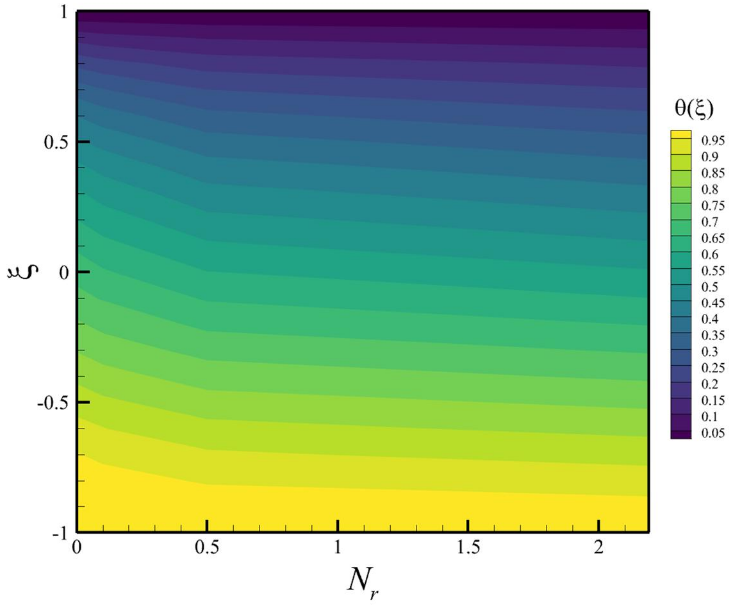

Figure 39. Two-dimensional contour of temperature in different values of radiation parameter.

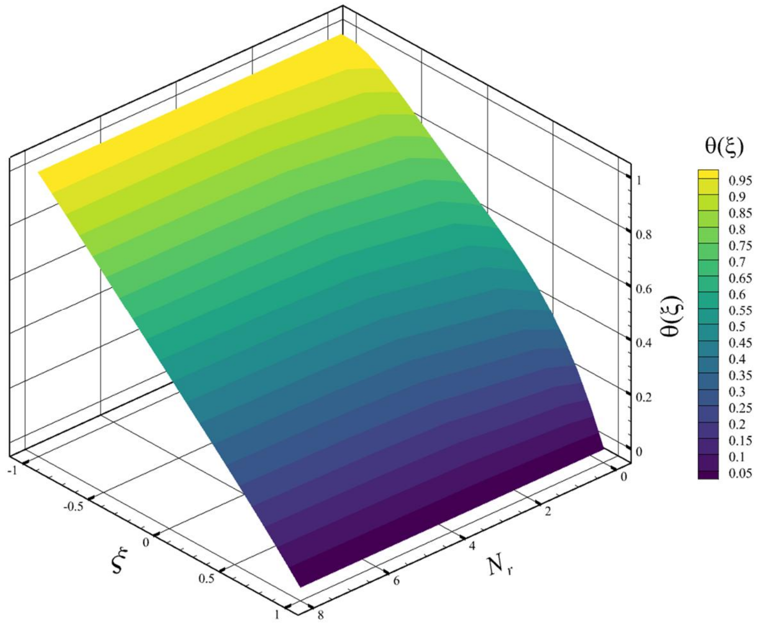

Figure 40. Three-dimensional contour of temperature in different values of radiation parameter.

Now, the results of the investigation of axial, radial, microrotation, temperature, and concentration contours for Equations (12)–(15) when the Prandtl number was changed are discussed. When the Prandtl number changed, other parameters were constant and equal to the values of $M_n = 1$, $S_c = 0.5$, $R_0 = 3$, $E_c = 0.2$, $N_r = 2$, $\lambda_3 = 0.3$, $\lambda_2 = 0.2$, $\lambda_1 = 2$. The Prandtl number was investigated in 6 different cases, and the changes of this parameter had a significant effect only on the quantity of temperature and the four quantities of axial velocity, radial velocity, microrotation, and concentration. It was almost unaffected, and the 2D and 3D contours obtained from these changes are also shown in **Figures 41** and **42**. The changes in the radiation parameter did not affect the quantity of the axial velocity. The maximum positive and negative values of the axial velocity occurred for all assumed Prandtl numbers, which were 0.383953826907 and −0.383953826907, respectively. The maximum positive axial velocity occurs when the value of ξ is equal to 0.577889446943606555, and the maximum negative value of the axial velocity occurs when the value of ξ is equal to −0.577889448511109238. The lowest value of the axial velocity is calculated for all the Prandtl numbers assumed to be zero and occurs exactly at the three points of the upper disk ($\xi = 1$), the lower disk ($\xi = -1$), and between the two disks ($\xi = 0$). Changes in the Prandtl number did not affect the quantity of the radial velocity, and the maximum positive and negative values of the radial velocity for all assumed Prandtl numbers are equal to 0.986765233307 and −2, respectively. The maximum positive radial velocity occurs when the value of ξ is equal to −0.00502512575474362705, and the maximum negative values of the radial velocity occurs when the value of ξ is equal to ±1. The lowest value of the radial velocity, for all assumed Prandtl numbers, is zero and occurs when the value of ξ is equal to ±0.580466299484894921. Changes in the Prandtl number did not affect the quantity of microrotation, and the maximum positive and negative value of microrotation for all assumed Prandtl numbers are equal to 1.11011447812 and −1.11011447812, respectively. The maximum positive microrotation occurs when the value of ξ is equal to −0.648241207908067829, and the maximum negative value of microrotation occurs when the value of ξ is equal to 0.648241203628162621. The minimum amount of microrotation, for all the assumed Prandtl numbers, is zero and occurs exactly at three points: the upper disk ($\xi = 1$), the lower disk ($\xi = -1$), and between the two disks ($\xi = 0$). Changes in the Prandtl number did not affect the amount of concentration, and for all the Prandtl numbers, the maximum concentration was assumed to be 1. It occurred when the value of ξ was -1, and the minimum concentration was equal to zero, and for all the Prandtl numbers, it was assumed that happens when the value of ξ is equal to 1. According to **Figures 41** and **42**, changes in the Prandtl number have a significant effect only on the quantity of temperature, and when the assumed Prandtl number is equal to 22, the maximum temperature is equal to 5.29149373452, and it happened where the value of ξ is equal to −0.206030151411750184. The minimum value of temperature for all assumed Prandtl numbers occurred when the value of ξ was equal to 1 and was equal to zero.

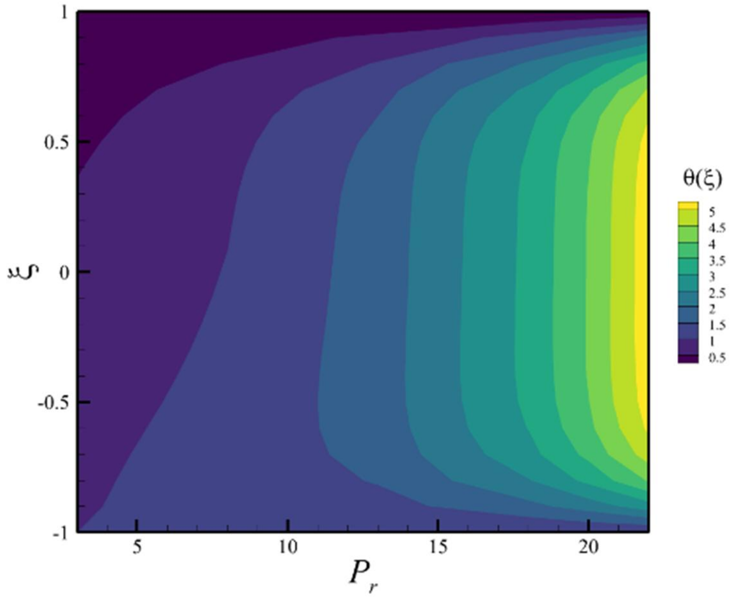

Figure 41. Two-dimensional contour of temperature at different values of the Prandtl number.

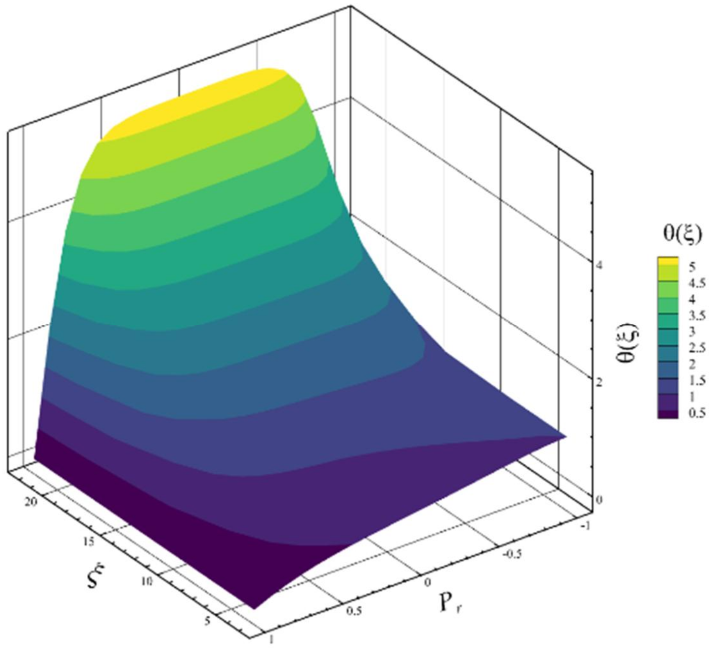

Figure 42. Three-dimensional contour of temperature at different values of the Prandtl number.

Now, the results of the investigation of axial, radial, microrotation, temperature, and concentration contours for Equations (12)–(15) when the Eckert number was changed are discussed. When the Eckert number changed, other parameters were constant and were equal to the values of $M_n = 1$, $S_c = 0.5$, $R_0 = 3$, $N_r = 1$, $P_r = 0.7$, $\lambda_3 = 0.3$, $\lambda_2 = 0.2$, $\lambda_1 = 2$. The Eckert number was investigated in 6 different cases, and the changes in this parameter had a significant effect on the quantity of temperature and the four quantities of axial velocity, radial velocity, microrotation, and concentration. It was almost unaffected, and the 2D and 3D contours obtained from these changes are also shown in **Figures 43** and **44**. The changes in Eckert number did not affect the quantity of axial velocity. The maximum positive and negative axial velocity values occurred for all assumed Eckert numbers, equal to 0.383953826907 and −0.383953826907, respectively. The maximum positive axial velocity occurs when the value of ξ is equal to 0.577889446942673635, and the maximum negative value of the axial velocity occurs when the value of ξ is equal to −0.577889448511718862. The lowest value of the axial velocity is calculated for all Eckert numbers assumed to be zero, and exactly at the three points of the upper disk $(\xi = 1)$, the lower disk $(\xi = -1)$ and between the two disks $(\xi = 0)$ occurs. The changes in Eckert number did not affect the quantity of radial velocity, and the maximum positive and negative value of radial velocity for all assumed Eckert numbers are equal to 0.986765233307 and −2, respectively. The maximum positive radial velocity occurs when the value of ξ is equal to −0.00502512575474362705, and the maximum negative value of the radial velocity occurs when the value of ξ is equal to ±1. The lowest value of the radial velocity, for all assumed Eckert numbers, is zero and occurs when the value of ξ is equal to ±0.580466299484894921. Changes in the Eckert number did not affect the amount of microrotation, and the maximum positive and negative values of the microrotation for all assumed Eckert numbers are equal to 1.11011447812 and −1.11011447812, respectively. The maximum positive microrotation occurs when the value of ξ is equal to −0.648241207908067829, and the maximum negative value of microrotation occurs when the value of ξ is equal to 0.648241203628162621. The minimum amount of microrotation, for all assumed Eckert numbers, is zero and occurs exactly at three points: the upper disk $(\xi = 1)$, the lower disk $(\xi = -1)$, and between two disks $(\xi = 0)$. Changes in the Eckert number did not affect the amount of concentration, and the maximum concentration is equal to 1. All the assumed Eckert numbers occur when the value of ξ is equal to -1 and the minimum concentration is equal to zero, and for all the assumed Eckert numbers, they happen when the value of ξ is equal to 1. According to **Figures 43** and **44**, changes in the Eckert number have a significant effect only on the quantity of temperature, and when the assumed Eckert number is equal to 2, the maximum temperature is equal to 1.20155355593, and it happened where the value of ξ is equal to −0.648241313576453315. The minimum temperature value for all assumed Eckert numbers occurred when the value of ξ was equal to 1 and was equal to zero.

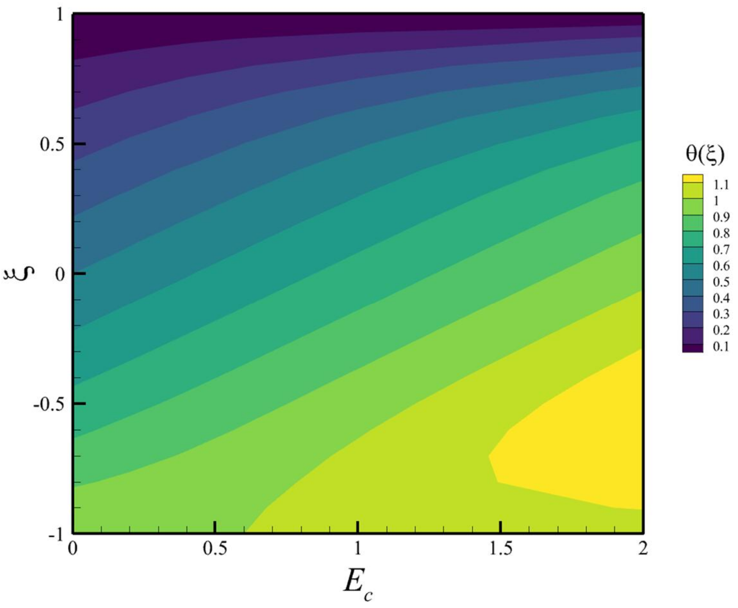

Figure 43. Two-dimensional contour of temperature at different values of the Eckert number.

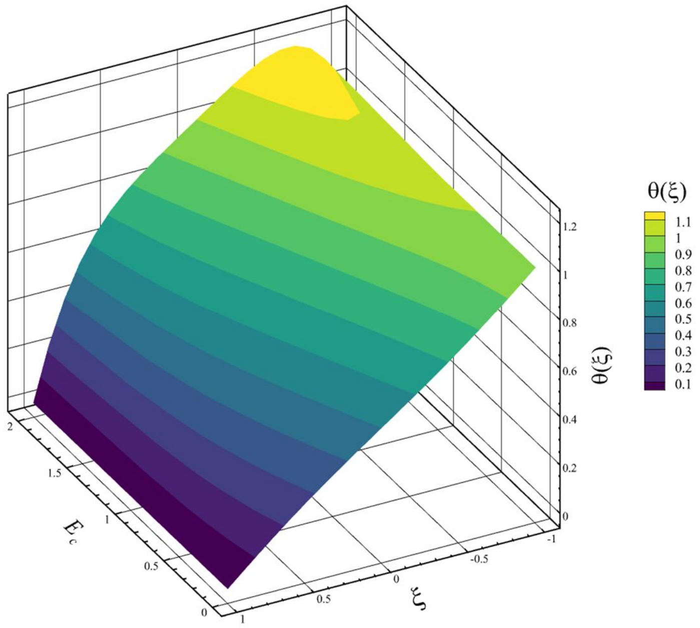

Figure 44. Three-dimensional contour of temperature at different values of the Eckert number.

Now, the results of the investigation of axial, radial, microrotation, temperature, and concentration contours for Equations (12)–(15) when the Schmidt number was changed are discussed. When the Schmidt number changed, the other parameters were constant and equal to the values of $M_n = 1$, $R_0 = 20$, $E_c = 0.2$, $N_r = 2$, $P_r = 3$, $\lambda_3 = 0.3$, $\lambda_2 = 0.2$, $\lambda_1 = 2$. The Schmidt number was investigated in 6 different cases, and the changes in this parameter had a significant effect on the quantity of concentration and the four quantities of axial velocity, radial velocity, microrotation, and temperature. It was almost unaffected, and the 2D and 3D contours obtained from these changes are also shown in **Figures 45** and **46**. Changes in the Schmidt number did not have much effect on the quantity of the axial velocity, and the maximum positive and negative value of the axial velocity occurred for all assumed Schmidt numbers and are equal to 0.289645614908 and −0.289645614907, respectively. The maximum positive axial velocity occurs when the value of ξ is equal to 0.63819095373231749, and the maximum negative values of axial velocity occurs when the value of ξ is equal to −0.638190955068300037. The lowest value of the axial velocity is calculated for all Schmidt numbers assumed to be zero and occurs exactly at the three points of the upper disk ($\xi = 1$), the lower disk ($\xi = -1$), and between the two disks ($\xi = 0$). Changes in the Schmidt number did not affect the quantity of the radial velocity, and the maximum positive and negative values for all assumed Schmidt numbers are equal to 0.630827168825 and −2, respectively. The maximum positive radial velocity occurs when the value of ξ is equal to −0.00502512563586887499, and the maximum negative value of the radial velocity occurs when the value of ξ is equal to ±1. The lowest value of the radial velocity, for all assumed Schmidt numbers, is zero and occurs when the value of ξ is equal to ±0.640511670822128121. Changes in the Schmidt number did not affect the amount of microrotation, and the maximum positive and negative values of microrotation for all assumed Schmidt numbers are equal to 0.82620738577 and −0.826207385766, respectively. The maximum positive microrotation occurs when the value of ξ is equal to −0.748743718610704767, and the maximum negative value of microrotation occurs when the value of ξ is equal to 0.748743718014597603. The minimum amount of microrotation, for all assumed Schmidt numbers, is zero and occurs exactly at three points: the upper disk ($\xi = 1$), the lower disk ($\xi = -1$), and between the two disks ($\xi = 0$). Changes in the Schmidt number did not affect the quantity of temperature, and the maximum temperature is equal to 1 for all assumed Schmidt numbers. They occur when the value of ξ equals −1, and the minimum temperature is zero for all assumed Schmidt numbers. It happens when the value of ξ is equal to 1. According to **Figures 45** and **46**, changes in the Schmidt number only significantly affect the quantity of concentration. For all assumed Schmidt numbers, the maximum concentration is equal to 1, and for all assumed Schmidt numbers, it happens when the value of ξ is equal to −1. The minimum concentration is equal to zero. All assumed Schmidt numbers happen when the value of ξ equals 1.

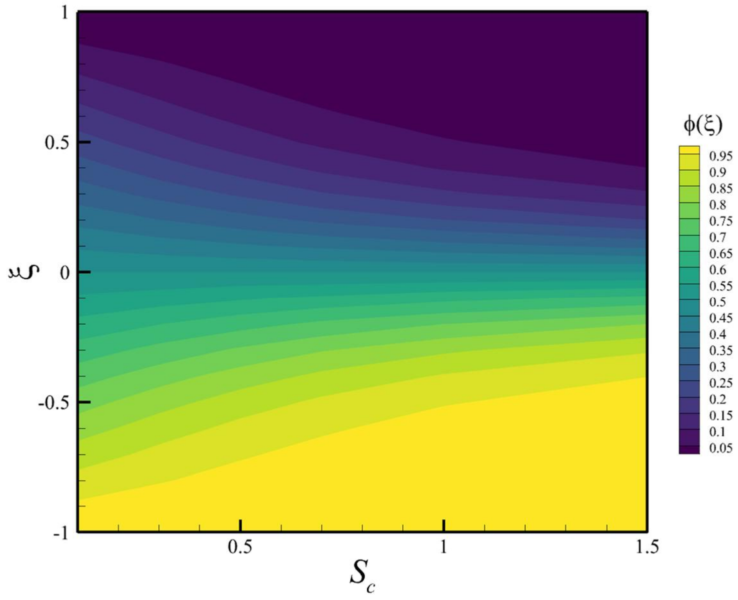

Figure 45. Two-dimensional contour of concentration at different values of the Schmidt number.

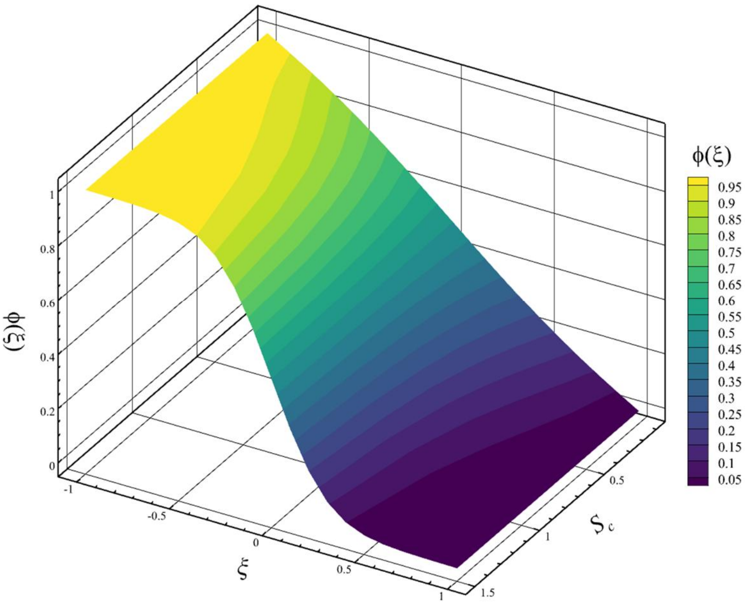

Figure 46. Three-dimensional contour of concentration at different values of the Schmidt number.

5. Conclusion

This study solved nonlinear equations governing heat and mass transfer in MHD micropolar fluid flow between stretching disks using two semi-analytical methods: the HAN method and modified AGM. These recently developed methods were applied innovatively, and their solutions were validated through three approaches: (1) substitution into governing equations with graphical verification; (2) comparison with existing analytical solutions; and (3) cross-validation between HAN and modified AGM results.

The problem addressed axisymmetric, incompressible, viscous MHD flow with heat and mass transfer. Similarity transformations reduced the PDE system to ODEs involving four dimensionless quantities $f(\xi)$, $g(\xi)$, $\theta(\xi)$, and $\phi(\xi)$ and their derivatives with nine parameters (e.g., Reynolds number, magnetic parameter, Prandtl number). Key findings include:

- Stretching Reynolds, magnetic, and micropolar parameters significantly influenced axial/radial velocity, microrotation, temperature, and concentration.
- Prandtl number ($3 \leq P_r \leq 22$) caused a 429% change in maximum temperature but did not affect other quantities.
- Eckert number (E_c = 1 → 2) led to a 16.5% increase in maximum temperature, with negligible impact elsewhere.
- Schmidt number ($0.1 \leq S_c \leq 1.5$) altered only concentration profile shape, not extrema.
- Radiation parameter ($0 \leq N_r \leq 8$) modified temperature graph shape without changing its maxima/minima.

The HAN method's ability to derive analytical expressions from numerical data and the modified AGM's independence from numerical solutions offer advantages over traditional techniques. Future work could extend this framework to analyze skin friction, Nusselt number, or microorganism density, broadening the physical insights.

Conflict of interest: The author declares no conflict of interest.

Nomenclature

Circular cylindrical coordinate system (m, rad, m)	r, θ, z	Components of the unit vector (-)	$\hat{\mathbf{e}}_1, \hat{\mathbf{e}}_2, \hat{\mathbf{e}}_3$
Velocity components ($\mathrm{m/s}$)	u, w	Stefan-Boltzmann constant ($\mathrm{W/m^2.K^4}$)	σ
Time (s)	t	Average absorption coefficient ($\mathrm{cm^{-1}}$)	k_a
Distance from r- axis (m)	l	Reactive flow ($\mathrm{kg/s^2.m^3}$)	$\dot{m}'''$
Velocity vector field ($\mathrm{m/s}$)	$\mathbf{V}$	Stretching parameter of the disks ($\mathrm{s^{-1}}$)	S
Pressure field (Pa)	p	Dimensionless temperature (-)	$\theta(\xi)$
Dynamic viscosity ($\mathrm{kg/m.s}$)	μ	Dimensionless concentration (-)	$\phi(\xi)$
Vortex viscosity	κ	Dimensionless axial velocity (-)	$f(\xi)$
Micro-inertia per unit mass	j	Dimensionless radial velocity (-)	$f'(\xi)$
Microrotation vector field ($\mathrm{m/s}$)	$\mathbf{N}$	Dimensionless micro-rotation velocity (-)	$g(\xi)$
Components of the microrotation ($\mathrm{m/s}$)	N_1, N_2, N_3	Stretching Reynolds number (-)	R_0
Fluid density ($\mathrm{kg/m^3}$)	ρ	Magnetic parameter (-)	M_n
Density vector field ($\mathrm{kg/m^3}$)	$\mathbf{J}$	Vortex viscosity (-)	λ_1
Sum of induced and imposed magnetic field	$\mathbf{B}$	Micro-inertial density (-)	λ_2
Gyro-viscosity coefficients	$\alpha_1, \alpha_2, \alpha_3$	Spin gradient viscosity parameter (-)	λ_3
Gradient operator (-)	$\boldsymbol{\nabla}$	Prandtl number (-)	P_r
Curl operator (-)	$\boldsymbol{\nabla} \times$	Radiation parameter	N_r
Temperature scalar field (K)	T	Eckert number (-)	E_c
Electrical conductivity of the fluid (S/m)	σ_el	Schmidt number (-)	Sc
Temperature of the lower disk (K)	T_1	Radius of the disk (m)	r
Temperature of the upper disk (K)	T_2	local Reynolds number (-)	R_e
Concentration scalar field ($\mathrm{mol/m^3}$)	C	Nusselt number (-)	N_u

Concentration of the lower disk ($\mathrm{mol/m^3}$)	C_1	Skin friction coefficient (-)	C_f
Concentration of the upper disk ($\mathrm{mol/m^3}$)	C_2	Wall couple stress (-)	C_g
Similarity variable (-)	ξ	Viscous dissipation function ($\mathrm{W/s.\,kg^{-1}\cdot m^{-2}}$)	Φ
Specific heat capacity at constant pressure ($\mathrm{J/kg\cdot K}$)	c_p	Thermal conductivity coefficient ($\mathrm{W/m\cdot K}$)	k
Radiant heat flux ($\mathrm{J/s}$)	q_rh	Diffusion coefficient/mass diffusivity ($\mathrm{m^2/s}$)	D_e
Strength of the magnetic field ($\mathrm{A/m}$)	B_os		

References

1. Agarwal R. Heat and mass transfer in electrically conducting micropolar fluid flow between two stretchable disks. Materials Today: Proceedings. 2021; 46: 10227-10238. doi: 10.1016/j.matpr.2020.11.614
2. Jalili P, Ahmadi Azar A, Jalili B, et al. Heat transfer analysis in cylindrical polar system with magnetic field: A novel Hybrid Analytical and Numerical Technique. Case Studies in Thermal Engineering. 2022; 40: 102524. doi: 10.1016/j.csite.2022.102524
3. Eringen AC. Simple microfluids. International Journal of Engineering Science. 1964; 2(2): 205-217. doi: 10.1016/0020-7225(64)90005-9
4. Eringen AC. Theory of Micropolar Fluids. Indiana University Mathematics Journal. 1966; 16(1): 1-18. doi: 10.1512/iumj.1967.16.16001
5. Eringen AC. Microcontinuum Field Theories: I. Foundations and Solids. Springer New York; 2012.
6. Lukaszewicz G. Micropolar Fluids: Theory and Applications. Birkhäuser Boston; 2012.
7. Turkyilmazoglu M. Analytic approximate solutions of rotating disk boundary layer flow subject to a uniform suction or injection. International Journal of Mechanical Sciences. 2010; 52(12): 1735-1744. doi: 10.1016/j.ijmecsci.2010.09.007
8. Turkyilmazoglu M. Purely analytic solutions of magnetohydrodynamic swirling boundary layer flow over a porous rotating disk. Computers & Fluids. 2010; 39(5): 793-799. doi: 10.1016/j.compfluid.2009.12.007
9. Turkyilmazoglu M. Analytic approximate solutions of rotating disk boundary layer flow subject to a uniform vertical magnetic field. Acta Mechanica. 2010; 218(3-4): 237-245. doi: 10.1007/s00707-010-0416-4
10. Sahoo B, Van Gorder RA, Andersson HI. Steady revolving flow and heat transfer of a non-Newtonian Reiner–Rivlin fluid. International Communications in Heat and Mass Transfer. 2012; 39(3): 336-342. doi: 10.1016/j.icheatmasstransfer.2011.12.007
11. Srivastava N. MHD Flow of the Micropolar Fluid between Eccentrically Rotating Disks. International Scholarly Research Notices. 2014; 2014: 1-7. doi: 10.1155/2014/317075
12. Iqbal MF, Ali K, Ashraf M. Heat and mass transfer analysis in unsteady titanium dioxide nanofluid between two orthogonally moving porous coaxial disks: a numerical study. Canadian Journal of Physics. 2015; 93(3): 290-299. doi: 10.1139/cjp-2014-0243
13. Kocic M, Stamenkovic Z, Petrovic J, et al. Heat transfer in micropolar fluid flow under the influence of magnetic field. Thermal Science. 2016; 20(suppl. 5): 1391-1404. doi: 10.2298/tsci16s5391k
14. Turkyilmazoglu M. Flow and heat simultaneously induced by two stretchable rotating disks. Physics of Fluids. 2016; 28(4). doi: 10.1063/1.4945651
15. Akhter S, Ashraf M, Ali K. MHD flow and heat transfer analysis of micropolar fluid through a porous medium between two stretchable disks using quasi-linearization method. Iran. J. Chem. Chem. Eng. 2017; 36(4).
16. Doh DH, Muthtamilselvan M. Thermophoretic particle deposition on magnetohydrodynamic flow of micropolar fluid due to a rotating disk. International Journal of Mechanical Sciences. 2017; 130: 350-359. doi: 10.1016/j.ijmecsci.2017.06.029
17. Hayat T, Javed M, Imtiaz M, et al. Convective flow of Jeffrey nanofluid due to two stretchable rotating disks. Journal of Molecular Liquids. 2017; 240: 291-302. doi: 10.1016/j.molliq.2017.05.024
18. Das A, Sahoo B. Flow of a Reiner-Rivlin fluid between two infinite coaxial rotating disks. Mathematical Methods in the Applied Sciences. 2018; 41(14): 5602-5618. doi: 10.1002/mma.5103
19. Tabassum M, Mustafa M. A numerical treatment for partial slip flow and heat transfer of non-Newtonian Reiner-Rivlin fluid due to rotating disk. International Journal of Heat and Mass Transfer. 2018; 123: 979-987. doi: 10.1016/j.ijheatmasstransfer.2018.03.040

20. Yao B, Lian L. A new analysis of the rotationally symmetric flow in the presence of an infinite rotating disk. International Journal of Mechanical Sciences. 2018; 136: 106-111. doi: 10.1016/j.ijmecsci.2017.12.023
21. Sahoo B, Shevchuk IV. Heat transfer due to revolving flow of Reiner-Rivlin fluid over a stretchable surface. Thermal Science and Engineering Progress. 2019; 10: 327-336. doi: 10.1016/j.tsep.2019.03.004
22. Yao B, Lian L. Series solution of the rotationally symmetric flow in the presence of an infinite rotating disk with uniform suction. European Journal of Mechanics - B/Fluids. 2019; 74: 159-166. doi: 10.1016/j.euromechflu.2018.11.012
23. Zangooee MR, Hosseinzadeh Kh, Ganji DD. Hydrothermal analysis of MHD nanofluid (TiO2-GO) flow between two radiative stretchable rotating disks using AGM. Case Studies in Thermal Engineering. 2019; 14: 100460. doi: 10.1016/j.csite.2019.100460
24. Das A, Sarkar S Flow analysis of Reiner-Rivlin fluid between two stretchable rotating disks. In: Recent Trends in Wave Mechanics and Vibrations: Select Proceedings of WMVC 2018 Springer Singapore; 2020. pp. 61-70. doi: 10.1007/978-981-15-0287-3_5
25. Naqvi SMRS, Kim HM, Muhammad T, et al. Numerical study for slip flow of Reiner-Rivlin nanofluid due to a rotating disk. International Communications in Heat and Mass Transfer. 2020; 116: 104643. doi: 10.1016/j.icheatmasstransfer.2020.104643
26. Usman M, Mehmood A, Weigand B. Heat transfer from a non-isothermal rotating rough disk subjected to forced flow. International Communications in Heat and Mass Transfer. 2020; 110: 104395. doi: 10.1016/j.icheatmasstransfer.2019.104395
27. Faraz N, Khan Y. Analytical solution of electrically conducted rotating flow of a second grade fluid over a shrinking surface. Ain Shams Engineering Journal. 2011; 2(3-4): 221-226. doi: 10.1016/j.asej.2011.10.001
28. Zhang X, Li M. Analysis of a semi-implicit and structure-preserving finite element method for the incompressible MHD equations with magnetic-current formulation. Communications in Nonlinear Science and Numerical Simulation. 2024; 128: 107677. doi: 10.1016/j.cnsns.2023.107677
29. Jalaal M, Nejad MG, Jalili P, et al. Homotopy perturbation method for motion of a spherical solid particle in plane couette fluid flow. Computers & Mathematics with Applications. 2011; 61(8): 2267-2270. doi: 10.1016/j.camwa.2010.09.042
30. Abdelmoneim M, Eldabe NT, Abouzeid MY, et al. Modified Darcy's law and couple stress effects on electro-osmotic flow of non-Newtonian nanofluid with peristalsis. International Journal of Applied Electromagnetics and Mechanics. 2023; 72(3): 253-277. doi: 10.3233/jae-220287
31. Hamad MAA. Analytical solution of natural convection flow of a nanofluid over a linearly stretching sheet in the presence of magnetic field. International Communications in Heat and Mass Transfer. 2011; 38(4): 487-492. doi: 10.1016/j.icheatmasstransfer.2010.12.042
32. Bejan A. A synthesis of analytical results for natural convection heat transfer across rectangular enclosures. International Journal of Heat and Mass Transfer. 1980; 23(5): 723-726. doi: 10.1016/0017-9310(80)90017-4
33. Ndlovu PL, Moitsheki RJ. Analytical Solutions for Steady Heat Transfer in Longitudinal Fins with Temperature-Dependent Properties. Mathematical Problems in Engineering. 2013; 2013: 1-14. doi: 10.1155/2013/273052
34. Mabood F, Khan WA, Ismail AIMd. MHD flow over exponential radiating stretching sheet using homotopy analysis method. Journal of King Saud University - Engineering Sciences. 2017; 29(1): 68-74. doi: 10.1016/j.jksues.2014.06.001
35. Talarposhti RA, Jalili P, Rezazadeh H, et al. Optical soliton solutions to the (2+1)-dimensional Kundu–Mukherjee–Naskar equation. International Journal of Modern Physics B. 2020; 34(11): 2050102. doi: 10.1142/s0217979220501027
36. Jalili B, Jalili P, Sadighi S, et al. Effect of magnetic and boundary parameters on flow characteristics analysis of micropolar ferrofluid through the shrinking sheet with effective thermal conductivity. Chinese Journal of Physics. 2021; 71: 136-150. doi: 10.1016/j.cjph.2020.02.034
37. Mahabaleshwar US, Maranna T, Pérez LM, et al. An effect of magnetohydrodynamic and radiation on axisymmetric flow of non-Newtonian fluid past a porous shrinking/stretching surface. Journal of Magnetism and Magnetic Materials. 2023; 571: 170538. doi: 10.1016/j.jmmm.2023.170538
38. Khan Y. A series solution of the boundary value problem arising in the application of fluid mechanics. International Journal of Numerical Methods for Heat & Fluid Flow. 2018; 28(10): 2480-2490. doi: 10.1108/hff-11-2017-0474
39. Ahmad A, Ishaq A, Khan Y. Influence of FENE-P fluid on drag reduction and heat transfer past a magnetized surface. International Journal of Modern Physics B. 2022; 36(23). doi: 10.1142/s0217979222501454
40. Khan Y, Majeed AH, Rasheed MA, et al. Dual solutions for double diffusion and MHD flow analysis of micropolar

nanofluids with slip boundary condition. Frontiers in Physics. 2022; 10. doi: 10.3389/fphy.2022.956737

41. Khan Y. Magnetohydrodynamic flow of linear visco-elastic fluid model above a shrinking/stretching sheet: A series solution. Scientia Iranica. 2017. doi: 10.24200/sci.2017.4305
42. Anusha T, Mahabaleshwar US, Hatami M. Navier slip effect on the thermal-flow of Walters' liquid B flow due to porous stretching/shrinking with heat and mass transfer. Case Studies in Thermal Engineering. 2021; 28: 101691. doi: 10.1016/j.csite.2021.101691
43. Ghadikolaei SS, Hosseinzadeh KH, Hatami M, et al. Investigation for squeezing flow of ethylene glycol ($C_2H_6O_2$) carbon nanotubes (CNTs) in rotating stretching channel with nonlinear thermal radiation. Journal of Molecular Liquids. 2018; 263: 10-21. doi: 10.1016/j.molliq.2018.04.141
44. Ghasemi SE, Hatami M, Sarokolaie AK, et al. Study on blood flow containing nanoparticles through porous arteries in presence of magnetic field using analytical methods. Physica E: Low-dimensional Systems and Nanostructures. 2015; 70: 146-156. doi: 10.1016/j.physe.2015.03.002
45. Fakour M, Vahabzadeh A, Ganji DD, et al. Analytical study of micropolar fluid flow and heat transfer in a channel with permeable walls. Journal of Molecular Liquids. 2015; 204: 198-204. doi: 10.1016/j.molliq.2015.01.040
46. Rashad A, Nafe M, Eisa D. 2D Radiative Casson-Carreau Hybrid Nanofluid Flow through a Circular Cylinder in a Darcy-Forchheimer Porous Medium. New Valley University Journal of Basic and Applied Sciences. 2023; 1(1): 1-19. doi: 10.21608/nujbas.2023.218751.1012
47. Rashad AM, Nafe MA, Eisa DA. Yield Stress Impact on Magnetohydrodynamic Jeffery Hybrid Nanofluid Flow Over a Moving Porous Surface: Buongiorno's Model. Journal of Nanofluids. 2023; 12(7): 1729-1738. doi: 10.1166/jon.2023.2057
48. Abdelhafez MA, Awad AA, Nafe MA, et al. Time-dependent viscous flow of higher-order reactive MHD Maxwell nanofluid with Joule heating in a porous regime. Waves in Random and Complex Media. 2021; 34(3): 1041-1061. doi: 10.1080/17455030.2021.1927237
49. Turkyilmazoglu M. Evidence of stretching/moving sheet-triggered nonlinear similarity flows: atomization and electrospinning with/without air resistance. International Journal of Numerical Methods for Heat & Fluid Flow. 2024; 34(9): 3598-3614. doi: 10.1108/hff-04-2024-0254
50. Turkyilmazoglu M. Two Models on the Unsteady Heat and Fluid Flow Induced by Stretching or Shrinking Sheets and Novel Time-Dependent Solutions. ASME Journal of Heat and Mass Transfer. 2024; 146(10). doi: 10.1115/1.4065674
51. Enamul, S. and Ontela, S., 2025. Entropy Analysis of Hall-Effect-Driven Ti− $CoFe_2O_4$/Engine Oil-Based Hybrid Nanofluid Flow Between Spinning Porous Disks with Thermal Convective Boundaries. JCIS Open, p.100134. https://doi.org/10.1016/j.jciso.2025.100134
52. Hussain, M., Shahid, S., Akbar, N.S. and Alaoui, M.K., 2025. Unsteady Flow and Heat Transfer Optimization of Viscous Fluid with Bioconvection over a Rotating Stretchable Disk and Gyrotactic Motile Microorganisms. Case Studies in Thermal Engineering, p.105796. https://doi.org/10.1016/j.csite.2025.105796
53. Lone, S.A., Bossly, R., Alduais, F.S., Al-Bossly, A., Khan, A. and Saeed, A., 2025. Thermal investigation of magnetized Casson hybrid nanofluid flow through two stretchable angular rotating disks with variable porosity and Cattaneo-Christov heat flux model: a numerical approach. Colloid and Polymer Science, 303(3), pp.529-546. https://doi.org/10.1007/s00396-024-05363-7
54. Mandal, S., Mukherjee, S., Shit, G.C. and Vajravelu, K., 2025. Entropy analysis of MHD flow in hybrid nanofluid over a rotating disk with variable viscosity and nonlinear thermal radiation. ZAMM ‐ Journal of Applied Mathematics and Mechanics/Zeitschrift für Angewandte Mathematik und Mechanik, 105(2), p.e202301027. https://doi.org/10.1002/zamm.202301027
55. Naveed Khan, M., Ahmad, S., Ahammad, N.A., Alqahtani, T. and Algarni, S., 2025. Numerical investigation of hybrid nanofluid with gyrotactic microorganism and multiple slip conditions through a porous rotating disk. Waves in Random and Complex Media, 35(2), pp.3789-3804. https://doi.org/10.1080/17455030.2022.2055205
56. Rauf, A., Ramesh, G.K., Fatima, S., Shehzad, S.A., Madhukesh, J.K. and Siddiq, M.K., 2025. Horizontal Magnetic Field Influence on Fluid Flow Across a Variable Thickness Rotating Disk With Stretching and Melting Phenomenon. Heat Transfer. https://doi.org/10.1002/htj.23285
57. Senbagaraja, P. and De, P., 2025. Sensitivity analysis on electro-osmotic flow of EMHD tangent hyperbolic nanofluid through porous rotating disk with variable thermal conductivity, Stefan blowing and thermal radiation. Multiscale and Multidisciplinary Modeling, Experiments and Design, 8(1), p.65. https://doi.org/10.1007/s41939-024-00648-4

58. Sultana, U., Mushtaq, M., Ahmad, I. and Muhammad, T., 2025. Porosity and heat transfer analysis of nanofluids due to rotating-stretching disk with Joule heating. Modern Physics Letters B, 39(01), p.2450404. https://doi.org/10.1142/S0217984924504049
59. Turkyilmazoglu, M. and Pop, I., 2025. Rheology of Bingham viscoplastic flow triggered by a rotating and radially stretching disk. International Journal of Numerical Methods for Heat & Fluid Flow. https://doi.org/10.1108/HFF-11-2024-0845
60. Usman, Kumar, R.V., Khan, W.A., AL‐lobani, E.M. and Massoud, E.E.S., 2025. Mathematical modeling and numerical simulations of convective heat transport in a stagnant flow of water‐based copper, aluminum oxide and MWCNTs nanofluid upon a stretching spinning disk. ZAMM‐Journal of Applied Mathematics and Mechanics/Zeitschrift für Angewandte Mathematik und Mechanik, 105(1), p.e202400476. https://doi.org/10.1002/zamm.202400476
61. Zada, J., Khan, A., Farooq, M., Alsubaie, A.S., Rezapour, S. and Inc, M., 2025. Computation of stretching disks fluid flow of hybrid nanofluid under the effect of variable magnetic field. ZAMM‐Journal of Applied Mathematics and Mechanics/Zeitschrift für Angewandte Mathematik und Mechanik, 105(1), p.e202400114. https://doi.org/10.1002/zamm.202400114
62. Azar, A.A., 2025. Semi-analytical solution for nonlinear Von Kármán swirling fluid flow via the hybrid analytical and numerical method. Mechanical Engineering Advances, 3(2), pp.2878-2878. https://doi.org/10.59400/mea2878
63. Jalili P, Azar AA, Jalili B, et al. The HAN method for a thermal analysis of forced non-Newtonian MHD Reiner-Rivlin viscoelastic fluid motion between two disks. Heliyon. 2023; 9(6): e17535. doi: 10.1016/jheliyon2023.e17535
64. Jalili B, Ahmadi Azar A, Esmaeili K, et al. A novel approach to micropolar fluid flow between a non-porous disk and a porous disk with slip. Chinese Journal of Physics. 2024; 87: 118-137. doi: 10.1016/j.cjph.2023.11.023
65. Ahmadi Azar A, Jalili B, Jalili P, et al. Investigating the effect of structural changes of two stretching disks on the dynamics of the MHD model. Scientific Reports. 2023; 13(1). doi: 10.1038/s41598-023-48988-4
66. Jalili P, Azar AA, Jalili B, et al. A Novel Analytical Investigation of a Swirling Fluid Flow and a Rotating Disk in the Presence of Uniform Suction. Arabian Journal for Science and Engineering. 2023; 49(8): 10453-10469. doi: 10.1007/s13369-023-08391-7
67. Jalili P, Azar AA, Jalili B, et al. Study of nonlinear radiative heat transfer with magnetic field for non-Newtonian Casson fluid flow in a porous medium. Results in Physics. 2023; 48: 106371. doi: 10.1016/j.rinp.2023.106371
68. Jalili B, Azar AA, Jalili P, et al. Analytical approach for micropolar fluid flow in a channel with porous walls. Alexandria Engineering Journal. 2023; 79: 196-226. doi: 10.1016/j.aej.2023.08.015
69. Jalili B, Ahmadi Azar A, Jalili P, et al. Investigation of the unsteady MHD fluid flow and heat transfer through the porous medium asymmetric wavy channel. Case Studies in Thermal Engineering. 2024; 61: 104859. doi: 10.1016/j.csite.2024.104859
70. Jalili P, Ahmadi Azar A, Jalili B, et al. A novel technique for solving unsteady three-dimensional brownian motion of a thin film nanofluid flow over a rotating surface. Scientific Reports. 2023; 13(1). doi: 10.1038/s41598-023-40410-3
71. Azar EA, Jalili B, Azar AA, et al. An exact analytical solution of the Emden–Chandrasekhar equation for self-gravitating isothermal gas spheres in the theory of stellar structures. Physics of the Dark Universe. 2023; 42: 101309. doi: 10.1016/j.dark.2023.101309
72. Jalili B, Azar AA, Liu D, et al. Analytical formulation of the steady-state planar Taylor–Couette flow constitutive equations with entropy considerations. Physics of Fluids. 2024; 36(11). doi: 10.1063/5.0239765
73. Khan KA, Vivas-Cortez M, Ishfaq K, et al. Exploring the numerical simulation of Maxwell nanofluid flow over a stretching sheet with the influence of chemical reactions and thermal radiation. Results in Physics. 2024; 60: 107635. doi: 10.1016/j.rinp.2024.107635
74. Basit MA, Imran M, Akgül A, et al. Mathematical analysis of heat and mass transfer efficiency of bioconvective Casson nanofluid flow through conical gap among the rotating surfaces under the influences of thermal radiation and activation energy. Results in Physics. 2024; 63: 107863. doi: 10.1016/j.rinp.2024.107863
75. Alzabut J, Nadeem S, Noor S, et al. Numerical analysis of Magnetohydrodynamic convection heat flow in an enclosure. Results in Physics. 2023; 51: 106618. doi: 10.1016/j.rinp.2023.106618
76. Gamachu D, Ibrahim W, Bijiga LK. Nonlinear convection unsteady flow of electro-magnetohydrodynamic Sutterby hybrid nanofluid in the stagnation zone of a spinning sphere. Results in Physics. 2023; 49: 106498. doi: 10.1016/j.rinp.2023.106498
77. Tshivhi KS, Tshehla MS. Heat source and radiation effects on MHD flow of Copper-Water nanofluid over exponential stretching surface with slip. Results in Physics. 2024; 58: 107463. doi: 10.1016/j.rinp.2024.107463

78. Leng Y, Li Y, Anwaar H, et al. Unraveling metachronal wave effects on heat and mass transfer in Non-Newtonian fluid. Case Studies in Thermal Engineering. 2024; 58: 104379. doi: 10.1016/j.csite.2024.104379
79. McChesney M. A Textbook of Magnetohydrodynamics. J. A. Shercliff. Pergamon Press, Oxford. 1965. 265 pp. Diagrams. 21s. The Journal of the Royal Aeronautical Society. 1966; 70(663): 453-453. doi: 10.1017/s0001924000058607
80. Devi SPAA, Devi RUU. On hydromagnetic flow due to a rotating disk with radiation effects. Nonlinear Analysis: Modelling and Control. 2011; 16(1): 17-29. doi: 10.15388/na.16.1.14112
81. Pattnaik PK, Panda S, Baithalu R, et al. Darcy-Forchheimer inertial drag on micropolar hybrid nanofluid flow through a channel: Akbari-Ganji method. Chaos, Solitons & Fractals. 2025; 194: 116197. doi: 10.1016/j.chaos.2025.116197
82. Mirgolbabaee H, Ledari ST, Ganji DD. Semi-analytical investigation on micropolar fluid flow and heat transfer in a permeable channel using AGM. Journal of the Association of Arab Universities for Basic and Applied Sciences. 2017; 24(1): 213-222. doi: 10.1016/j.jaubas.2017.01.002

Academic Publishing Pte. Ltd.

Add: 73 Upper Paya Lebar Road, #07-02B-01, Centro Bianco, Singapore 534818
Tel: +65 83184869
E-mail: editorial_office@acad-pub.com
Web: http://ojs.acad-pub.com/